



## City Research Online

### City, University of London Institutional Repository

---

**Citation:** Murali-Girija, M. (2020). Numerical simulation of cavitation in the presence of non-condensable gas using a three-phase model. (Unpublished Doctoral thesis, City, University of London)

This is the accepted version of the paper.

This version of the publication may differ from the final published version.

---

**Permanent repository link:** <https://openaccess.city.ac.uk/id/eprint/24807/>

**Link to published version:**

**Copyright:** City Research Online aims to make research outputs of City, University of London available to a wider audience. Copyright and Moral Rights remain with the author(s) and/or copyright holders. URLs from City Research Online may be freely distributed and linked to.

**Reuse:** Copies of full items can be used for personal research or study, educational, or not-for-profit purposes without prior permission or charge. Provided that the authors, title and full bibliographic details are credited, a hyperlink and/or URL is given for the original metadata page and the content is not changed in any way.

---

---

---

City Research Online:

<http://openaccess.city.ac.uk/>

[publications@city.ac.uk](mailto:publications@city.ac.uk)

---



# Numerical simulation of cavitation in the presence of non-condensable gas using a three-phase model

*By*

Mithun Murali-Girija

Thesis submitted for the fulfilment of the requirements  
for the Degree of Doctor of Philosophy



School of Mathematics, Computer Science & Engineering  
Department of Mechanical Engineering & Aeronautics

May 2, 2020

# Declaration

I hereby declare that the contents of this dissertation are original and have not been submitted in whole or in part for consideration for any other degree or qualification in this, or any other university. This dissertation is my own work, except where specific reference is made to a joint effort in the text and Acknowledgements accordingly.

I grant powers of discretion to the University Librarian to allow the thesis to be copied in whole or in part without further reference to me. This permission covers only single copies made for study purposes, subject to normal conditions of acknowledgement.

Mithun Murali Girija  
London, 2020

## Abstract

The interactions between liquid, vapour and gas (three-phases) play a vital role in determining the efficiency of many engineering equipments. To study these interactions, a three-phase model is developed using barotropic equations of state and implemented into the Navier-Stokes equations; the barotropic fluid is assumed to be in thermal and mechanical equilibrium with the air. The air's motion is simulated using two different approaches, a sharp interface capturing VOF technique and a diffused interface mixture model. Alongside the so-called three-phase model, an immersed boundary method (IBM) is also developed for modelling the complex geometry motions. Both these models are implemented into the Ansys Fluent solver using User Defined Functions (UDF's) and are validated against relevant experimental studies.

Several three-phase flow simulations have been performed, starting from simplified 2D simulations and moving to more complex industrial applications, such as Diesel injectors and gear pumps. Firstly, the three-phase model using the sharp interface VOF approach, in conjunction with the LES model for resolving turbulence, is used for studying the influence of in-nozzle flow on primary atomisation from an asymmetric step-nozzle. The results obtained from the simulation show a good correlation with the experimental observations.

The transient flow phenomena occurring during the opening, closing and dwelt time in fuel injectors are known to significantly contribute to excess exhaust emissions in engines. The three-phase model using the VOF approach with a model for wall-adhesion is used for predicting the flow development inside and outside of the orifices and the wall wetting during the start, end, dwelt time and the subsequent start of the injection cycle. The simulations are performed and validated in a six-hole VCO-type injector imposing realistic conditions of the valve movement, implemented using the immersed boundary method; this allows for simulations to be performed at zero lift during the dwelt time between successive injections.

The three-phase model using the mixture approach in conjunction with the IBM model is further used for simulating the effect of varying gas content in the fluid on cavitation occurring from an external gear pump. These simulations have revealed the importance of modelling contact between the gears in predicting the pump performance accurately. Moreover, it was observed that the main effect of increasing the NCG content in the fluid is a reduction in cavitation occurring inside the pump.

# Present Contributions

- A fully compressible multi-phase flow model has been developed and implemented in a 3-D flow solver of the Navier-Stokes equations. The model assumes mechanical and thermal equilibrium between liquid, vapour and air; a barotropic equation of state connects the pressure-density relation of the phases and it is referred to as a three-phase cavitation model. The inclusion of air as non-condensable gas (NCG) which is the third phase in the model, has allowed for the effects of dissolved air in fluids on cavitation development to be simulated.
- The model has been combined with an immersed boundary method able to handle complex moving geometries with solid-to-solid contact. Moreover, the three-phase model has also been combined with the Volume of Fluid (VOF) method for interface capturing and Large Eddy Simulation (LES) model for resolving turbulence. Thus, it represents a tool suitable for simulating complex flows realised in various hydraulic systems, such as fuel injectors and gear pumps.
- The numerical model has been used to study the effect of cavitation on primary atomization from a step nozzle and the results are validated against experimental data from (1). Depending on the pressure drop across the nozzle, different cavitation regimes such as cavitation inception, developing cavitation and hydraulic-flip have been predicted, in agreement with the relevant experiments; this has been the first time that predictions for this case have been obtained in the open literature.
- The model has been further applied to the simulation of the transient flow phenomena realised during the opening, closing and dwell time between successive injections of diesel fuel injectors for the first time. The inclusion of eccentric needle valve motion and wall adhesion has allowed prediction of fuel dribbling and external nozzle wall wetting to be simulated; predicted liquid distribution was found in qualitative agreement with experimental images available for such processes.

- The model was further applied to a parametric investigation of the impact of NCG on the performance of a gear pump utilised in the aviation industry. For the first time in the open literature, the study has considered the effect of non-condensable gas and contact between the gears to simulate more realistic conditions. The obtained results suggest that the contact between the gears and the % of NCG present in the liquid plays a major role in the cavitation and the subsequent performance of the pump.

# Acknowledgements

Undertaking this PhD has been a truly life-changing experience for me and it would not have been possible to do without the support and guidance that I received from many people. First of all, I would like to thank my supervisor Prof Gavaises for allowing me to join his research group and for trusting me with this research topic. Secondly, a big thanks go to Dr Koukouvini for the co-supervision and providing constant guidance. Without his guidance and feedback, this PhD would not have been achievable.

Special thanks to Mr Chatziarsenis and Ms Petrova for their administrative help and efforts in improving my soft skills. Thanks are due to the Rolls-Royce, especially Mr Andrew King, for providing me with required data that supported this research work and for introducing me to the internal CFD community within Rolls-Royce. I also express my gratitude to the European Union's Horizon 2020 research and innovation programme's CaFE project (Marie Skłodowska-Curie) for funding my research.

I would like to thank my colleagues and friends Dr Karathanassis, Dr Jadidbonab, Dr Malgarinos, Dr Naseri, Dr Rodriguez and my dear "soon to be Dr" friends Akis, Milad, Georgia, Alvaro, Max, Nikolaos, Theodoros, Konstantinos and Mahmoud for making my days at the office memorable.

Finally, my deep and sincere gratitude to my family for their continuous and unparalleled love, help and support. I am grateful to my wife Remya and my brother Jithin for always being there for me as a friend, my little son Ved for bringing happiness into my life. I am forever indebted to my father Muralidharan and my mother Girija for giving me the opportunities and experiences that have made me who I am and also my parents-in-law Somanadhan and Rajalakshmi for their continuous motivation.

# Contents

<b>1</b>	<b>Introduction</b>	<b>1</b>
1.1	Background and Motivation . . . . .	1
1.2	Cavitation in fuel injector nozzle . . . . .	1
1.3	Cavitation in pumps . . . . .	4
1.3.1	Gear Pumps . . . . .	5
1.4	Industrial relevance . . . . .	6
1.5	Aims . . . . .	7
1.6	Thesis structure . . . . .	9
1.7	Associated publications . . . . .	10
<b>2</b>	<b>Literature</b>	<b>11</b>
2.1	Cavitation and its influence on spray formation from an injector nozzle . . . . .	12
2.1.1	Relevant experimental studies on nozzle flow . . . . .	12
2.1.2	Relevant numerical studies on nozzle flow . . . . .	16
2.2	Cavitation in external gear pump . . . . .	22
2.2.1	Experimental evaluation of flow inside the gear pump . . . . .	22
2.2.2	Numerical evaluation of flow inside gear pump . . . . .	24
2.3	Immersed boundary model . . . . .	27
2.4	Literature gap and current contribution . . . . .	29
<b>3</b>	<b>Numerical Methodology</b>	<b>32</b>
3.1	Barotropic cavitation model (Two-phase) . . . . .	32
3.2	Three-phase cavitation model . . . . .	35

3.2.1	Volume of Fluid approach (VOF) . . . . .	35
3.2.2	Mixture approach . . . . .	38
3.3	Turbulence modelling . . . . .	39
3.3.1	Large eddy simulation (LES) . . . . .	40
3.3.2	Reynolds-Averaged Navier-Stokes (RANS) . . . . .	41
3.4	Immersed Boundary model (IBM) . . . . .	43
3.4.1	Immersed body motion . . . . .	44
3.4.2	Integration of IBM into turbulence equation . . . . .	47
<b>4</b>	<b>Numerical simulation of cavitation and primary atomization using the fully compressible three-phase model</b>	<b>48</b>
4.1	Simulation cases and setup . . . . .	49
4.2	Results and Discussion . . . . .	51
4.2.1	Comparison of in-nozzle cavitation and spray with experiments . . . . .	51
4.2.2	Half-cone angle . . . . .	52
4.2.3	Evolution of in-nozzle flow and liquid jet . . . . .	53
4.2.4	In-nozzle turbulence . . . . .	59
4.2.5	Effect of air entrainment on jet . . . . .	59
4.2.6	Time-averaged fields . . . . .	62
4.2.7	Surface area generation . . . . .	66
4.3	Chapter Summary . . . . .	67
<b>5</b>	<b>Numerical simulation of fuel dribbling and nozzle wall wetting on VCO injector with eccentric needle motion</b>	<b>70</b>
5.1	Problem description . . . . .	71
5.2	Validation of the model . . . . .	72
5.3	Results and discussion . . . . .	74
5.3.1	Start of Injection (SOI) . . . . .	76
5.3.2	End of Injection (EOI) . . . . .	78
5.3.3	Subsequent Start of Injection (SSOI) . . . . .	83
5.4	Chapter summary . . . . .	88



<b>6</b>	<b>Numerical simulation of three-phase flow in an external gear pump using immersed boundary approach</b>	<b>91</b>
6.1	Simulation Setup . . . . .	92
6.2	Results and Discussion . . . . .	92
6.2.1	Effect of gear contact . . . . .	96
6.2.2	Effect of gear RPM . . . . .	99
6.2.3	Effect of Non-condensable Gas . . . . .	103
6.3	Chapter summary . . . . .	104
<b>7</b>	<b>Conclusions and further work</b>	<b>107</b>
7.1	Conclusions . . . . .	107
7.2	Further work . . . . .	110
<b>A</b>	<b>Grid Resolution for LES simulation</b>	<b>112</b>
A.1	Validation of the estimated grid size for primary atomisation	112
<b>B</b>	<b>Comparison between the mixture and VoF approach for three-phase modelling and the influence of surface tension.</b>	<b>115</b>
<b>C</b>	<b>Validation of the immersed boundary model</b>	<b>118</b>
C.1	Oblique impact of water jet on a planar wall . . . . .	118
C.2	Multiphase flow in an expanding chamber . . . . .	118
C.3	Rotating cross . . . . .	120
C.4	Geometric conservativeness of the IBM model . . . . .	123
<b>D</b>	<b>Validation of the 3-phase mixture model approach</b>	<b>124</b>
D.1	Three-phase flow simulation on 2D Hydrofoil . . . . .	124
D.2	Three-phase flow simulation on 2D Step-Nozzle . . . . .	126
<b>E</b>	<b>Numerical simulation of 3-phase flow in 3D gear pump</b>	<b>132</b>

# List of Figures

1.1	Deposits on the external surface of a diesel fuel injector. <i>Image reproduced from the work of Gold et al. (2)</i> . . . . .	2
1.2	Schematic of cavitation inside a nozzle . . . . .	3
1.3	2D representation of an external gear pump. (source: <a href="http://processprinciples.com/2012/07/gear-pumps">http://processprinciples.com/2012/07/gear-pumps</a> ) . . . . .	6
2.1	Cavitation field distribution from cavitation start to the choked flow. Red: liquid only. Blue: gas only. Bright areas show fluctuation between liquid and gas phase, CS refers to start of cavitation and CC is the critical cavitation point Winklhofer et al. (3) . . . . .	13
2.2	: Cavitation mechanisms inside a diesel injector nozzle as reported by Naseri (4) . . . . .	16
2.3	Characteristic forms of cavitation observed in gear pump. (a) bubbles, (b) veil, (c) jet, (d) foam, (e) vortex, (f) plume. Reproduced from the work of Antoniak and Stryczek (5) . . . . .	23
2.4	(a) Schematic drawing showing flow past a generic body. The solid body occupies the volume $\Omega_s$ with boundary $\Gamma_b$ . The volume of the fluid is denoted by $\Omega_f$ . (b) Schematic of body immersed in a Cartesian grid on which the governing equations are discretized (Source: Mittal and Iaccarino (6)) . . . . .	28
3.1	Two-phase barotropic relation (plot in log scale) . . . . .	34
3.2	Immersed body representation using Lagrangian points (left) to mask function in Eulerian frame (right). . . . .	44
3.3	Schematic representation of wall distance calculation: (a) identifying the closest marker point to a given cell node n, (b) calculating the normal distance to the wall . . . . .	45

4.1	a) Step- Nozzle geometry as reported in Abderrezzak and Huang (1) b) Computational domain with boundary conditions; walls (grey), inlet (red), and outlet (blue). All dimensions are in millimetres. . . . .	49
4.2	Details of the computational mesh. . . . .	50
4.3	Comparison of in-nozzle cavitation and near-exit spray formation between experimental results from Abderrezzak and Huang (1) and current numerical study. (a, b) 2 bar (c, d) 3 bar (e, f) 5 bar inlet pressure. Iso-surfaces of mixture density at $100kg/m^3$ shown at a random time instant . . .	51
4.4	Spray cone angle for a) 2 bar, b) 3 bar and c) 5 bar injection pressure with transparent iso-surface of 95% of gas volume fraction and d) comparison with the experiments from Abderrezzak and Huang (1). . . . .	52
4.5	Instances of the evolution of in-nozzle cavitation and liquid jet disintegration at $p_{inj}=2bar$ . Iso-surfaces of 50% vapour (cyan) and 95% gas (white) volume fraction shown. The instances are chosen randomly over the evolution to highlight the main features. (The non-dimensional time is given in brackets) . . . . .	54
4.6	Instances of the evolution of in-nozzle cavitation and liquid jet disintegration at $p_{inj}=3bar$ . Iso-surfaces of 50% vapour (cyan) and 95% gas (white) volume fraction shown. The instances are chosen randomly over the evolution to highlight the main features. The thinning and widening of the liquid jet are highlighted using red and blue circles. (The non-dimensional time is given in brackets) . . . . .	56
4.7	Instances of the evolution of in-nozzle cavitation and liquid jet disintegration at $p_{inj}=5bar$ . Iso-surfaces of 50% vapour (cyan) and 95% gas (white) volume fraction shown. (The non-dimensional time is given in brackets) . . . . .	58
4.8	Instantaneous isosurface of Q-criteria showing vortex cores (value of $10^9$ ) coloured by non-dimensional velocity magnitude at $p_{inj}=2bar$ . (The jet interface close to the nozzle exit is shown in subset). . . . .	60

4.9	Instantaneous isosurface of Q-criteria showing vortex cores (value of $10^9$ ) coloured by non-dimensional velocity magnitude at $p_{inj}=3\text{bar}$ . (The jet interface close to the nozzle exit is shown in subset). . . . .	60
4.10	Instantaneous isosurface of Q-criteria showing vortex cores (value of $10^9$ ) coloured by non-dimensional velocity magnitude at $p_{inj}=5\text{bar}$ . (The jet interface close to the nozzle exit is shown in subset). . . . .	61
4.11	Contours of non-dimensional velocity magnitude with iso-lines of 95-99% gas volume fraction. a) Pictorial representation of the first spray widening event. (b, d) shows the widening of spray and c) shows the reduction in spray width. (the vectors shown are not up to scale they are used as an indicator of flow directions. . . . .	61
4.12	Contours of (a-c) average and (d-f) rms vapour volume fraction with iso-lines of mean and rms gas volume fractions respectively ranging from 0.1 - 0.5 at (a, d) 2bar, (b, e) 3bar and, (c, f) 5bar injection pressure. . . . .	62
4.13	Contours of mean and rms absolute pressure normalised with the injection pressure and iso-lines of gas volume fraction ranging from 0.1 - 0.5 at (a, d) 2bar, (b, e) 3bar and, (c, f) 5bar injection pressure. . . . .	63
4.14	Contours of average velocity magnitude and z-vorticity; (a, d) 2bar, (b, e) 3bar and, (c, f) 5bar injection pressure. (g-i) shows the mean streamwise velocity distribution and (j-l) shows the rms of streamwise velocity at Y0, Y2 and Y4 locations . . . . .	64
4.15	Instantaneous contours of (a,c) flow velocity in y-direction showing the flow separation of liquid from inlet edge and ambient gas from the exit edge of the bottom wall, (b) the instantaneous vorticity contours at 5bar injection pressure. . . . .	66
4.16	Non-dimensional surface area generation (an approximate measure of primary atomization) at different injection pressures. The region where integration is performed is highlighted in blue (in the inset). . . . .	68

5.1	a) VCO geometry and b) cross-section of the hexahedral mesh highlighting the mesh details near orifice entrance and exit. Telescopic refinement near the wall to ensure $y^+ \sim 1$ .	72
5.2	a) Needle lift profile and b) eccentricity in x (dashed) and y (dotted) direction as reported in Gold et al. (2). Start of Injection (solid blue), End of Injection (solid red) and Subsequent Start of injection (solid green). . . . .	72
5.3	Validation of the numerical model showing the liquid jet break-up during end of injection. (a, b, c) and (i, ii, iii) are the results from current simulation matching the experimental visualisation, (1, 2, 3) are the experimental results from Gold et al. (2) at $800\mu s$ ASOI, $1000\mu s$ ASOI and $1100\mu s$ ASOI. Isosurface of 90% gas volume fraction (red) and 50% vapour volume fraction (pink) is shown. . . . .	73
5.4	a) Single hole ECN Spray D nozzle, b) Needle motion profile as obtained from Manin et al. (7) for different injection pressure c) The hexahedral numerical mesh showing the extended circular chamber and d) IBM representation of the needle (in red). . . . .	74
5.5	Validation of the numerical model with the experimental results from Manin et al. (7) during the start of injection event . . . . .	75
5.6	Validation of the numerical model with the experimental results from Manin et al. (7) during the end of injection event	75
5.7	Evolution of diesel jet and formation of cavitation during the start of injection showing the development of geometry-induced cavitation and the stretching of string cavitation during the needle opening. Isosurfaces of 90% gas volume fraction (red) and 50% vapour volume fraction (pink) is shown. . . . .	76
5.8	Detailed view of swirling flow and string cavitation at selected needle lifts during SOI. Streamlines colored with velocity magnitude and the isosurface of 50% vapour volume fraction shown in cyan. . . . .	79

5.9	Dribble formation during start of injection from a nozzle filled with diesel. Correlation with the experimental observation from Gold et al. (2) shown in the subset of (i). Isosurface of 90% gas volume fraction is shown in red. Figures are shown selectively for Orifices 1 and 4. . . . .	80
5.10	Break-up of diesel jet and cavitation formation inside the orifice during end of injection. The sequence shows the cloud cavity stretching and the entrainment of gas after the needle closure. Isosurface of 90% gas volume fraction (red) and 50% vapour volume fraction (pink) is shown. . . .	81
5.11	Detailed view of swirling flow and string cavitation at selected needle lifts during EOI. Streamlines colored with velocity magnitude and the isosurface of 50% vapour volume fraction shown in cyan. . . . .	84
5.12	Isosurface of 90% gas volume fraction showing the disintegration of diesel jet during and after the needle closure. The swirling motion creating a membrane like structure and the formation of large ligaments and droplets later causing wall wetting is also shown. Figures are shown selectively for Orifices 1 and 4. . . . .	85
5.13	Evolution of diesel jet and formation of cavitation during subsequent start of injection shown using a view from the bottom of the injector. The presence gas bubbles inside the orifices and the ingestion of gas into the sac volume is depicted using isosurface of 90% gas volume fraction (red) and 50% vapour volume fraction (pink). . . . .	86
5.14	Comparison between SOI and SSOI at different needle lift showing the delay in jet formation due to the presence of entrained gas in the orifice. Isosurfaces of 90% gas volume fraction shown in red and 50% vapour volume fraction shown in pink. . . . .	87
5.15	Isosurface of 90% gas volume fraction showing the residual droplets and the newly formed droplets sticking to the wall due to adhesion during the subsequent start of injection. Figures are shown selectively for Orifices 1 and 4. . . . .	89
6.1	a) Line diagram of the gear pump from (8) and b) the computational mesh for immersed boundary simulation . . . . .	93

6.2	Modelling of a) tip clearances and b) clearance and the point of contact between the gears . . . . .	93
6.3	Comparison of the streamlines obtained by a) Castilla et al. (9) using TRPIV and b) the current numerical model using oil as working fluid, c) the velocity profile along line-A . . .	94
6.4	Comparison of the liquid volume fraction 1) at 500 RPM and 2) 1000 RPM; a) from the present simulation and b) from the experimental work of Stryczek et al. (10) to highlight cavitation occurring in the gap between gear teeth in the suction side. $T_g$ is the time for one gearing period . . .	95
6.5	Comparison of non-dimensional absolute gauge pressure over a gearing period with (a-e) clearance between the gears and (a' - e') with contact between gears. The contours in the subset shows (c'1) the condition before the second contact, (c'2) pressure rise during two contacts in the isolated region and (c'3) the condition after the release of the first contact. Note that c' and c'2 corresponds to the same gear position. The time interval between the contour plots from a-e are not uniform; they are chosen to highlight specific events over a period . . . . .	96
6.6	Comparison of non-dimensional velocity magnitude over a gearing period with (a-e) clearance between the gears and (a' - e') with contact between gears. The time interval between the contours from a-e are not uniform; they are chosen to highlight specific events over a period. . . . .	97
6.7	Comparison of vapour volume fraction over a gearing period with (a - e) clearance between the gears and (a' - e') with contact between gears. The time interval between the contours from a-e are not uniform; they are chosen to highlight specific events over a period . . . . .	98
6.8	Comparison of a) area integral of vapour volume fraction normalised using the total flow area b) inlet flow rate and c) outlet flow rate over two gearing periods . . . . .	99
6.9	Comparison of cavitation formation at 500 RPM (a-e), 1000 RPM (a' - e') and 2000 RPM (a'' - e'') represented as contours of vapour volume fraction over one gearing period. . .	101

6.10	Contours of z-vorticity near the gearing zone and tip clearances at a) 500 RPM b) 1000 RPM and c) 2000 RPM. The normalised velocity vector along with 50% vapour volume fraction (blue) highlighting the two-dimensional vortex structures and locations of cavitation are given in the subset	102
6.11	Comparison of a) area integral of vapour volume fraction normalized using the total flow area, b) inlet flow rate and c) outlet flow rate over two gearing periods at different gear RPM's	102
6.12	Representation of stairway pressure rise across inlet and outlet along the gear pockets at 500 RPM a) pressure contours with multiple locations along the line where the pressure is measured and b) the non-dimensional pressure at different points shown in (a)	102
6.13	Contours of pressure and velocity magnitude 1) 500 RPM 2) 1000 RPM and 3) 2000 RPM and a) $t/T_g=0$ ie. ( $\theta=0$ ) and b) $t/T_g=0.5$ ie. ( $\theta=0.5 \times 2\pi/11$ )	103
6.14	Comparison of the area integral of vapour volume fraction normalized using the total flow area over two gearing periods with different percentage of gas volume fraction at 2000 RPM.	104
6.15	Evolution of NCG and cavitation; (a-d) for 0% NCG, (a'-d') for 0.2% and (a''-d'') for 1% NCG content. The iso-lines of 50% vapour volume fraction shown in red lines. The instances are chosen randomly to highlight main features over a gearing period	105
A.1	LES resolution assessment (a) contour of the resolved over total turbulent kinetic energy at mid-span section and (b) along with vertical location at given locations, (c) Wall $y^+$ . All plots are for the extreme condition considered in this study ( $P_{inj}=5\text{bar}$ ).	113
A.2	Turbulent energy spectra at midsection of nozzle (left column) and 5mm downstream the nozzle-exit in spray region (right column) for (a, b) 2bar, (c, d) 3bar and (e, f) 5bar injection pressure.	113



B.1	Comparison between (a)mixture approach and (b) VoF approach for modelling atomization. Contours of mixture density normalized with the water density. . . . .	116
B.2	Instantaneous contours of (a) vorticity and (b) velocity magnitude from two-dimensional simulation using the mixture model (without surface tension effects). (c) The calculated Weber numbers at the highlighted regions. . . . .	116
C.1	Contours of a) velocity magnitude b) coefficient of pressure and c) liquid volume fraction. Flow is from right to left. The black line at $x=0$ is the immersed boundary representation of the planar wall and x-axis is the centre of the jet. . . . .	119
C.2	Comparison of pressure coefficient along the radial direction between the IBM and the exact solution from Taylor (11) . . . . .	120
C.3	Computational domain of the chamber with moving wall . . . . .	120
C.4	Comparison of IBM CFD simulation results with the 1-D model for an expanding chamber at $t = 60ms$ . . . . .	121
C.5	a) Computational domain and b) mesh used for rotating cross simulation . . . . .	121
C.6	Results showing comparison of instantaneous of velocity magnitude and 1% vapour volume fraction (in red) between (a-c) ALE approach and (d-f) immersed boundary approach, both from Örley et al. (12) and (g-i) current immersed boundary model; after $120^\circ$ , $240^\circ$ , and $360^\circ$ of rotation from the start . . . . .	122
C.7	Comparison of integral vapour volume fraction over time between ALE and IBM approach from Örley et al. (12) and with the current IBM model. . . . .	122
C.8	Calculated percentage error between the velocity and the target velocity. . . . .	123
D.1	Computational domain with hydrofoil geometry from the work of Dular and Coutier-Delgosha (13) . . . . .	124
D.2	Mean x-velocity profile at different locations a) $0mm$ , b) $16mm$ , c) $32mm$ , d) $48mm$ as shown in e). . . . .	125
D.3	Mean y-velocity profile at different locations a) $0mm$ , b) $5mm$ , c) $10mm$ , d) $15mm$ as shown in e). . . . .	125

D.4	Effect of NCG on the (a-d) mean u velocity (e-h) mean vapour volume fraction and (i-l) mean gas volume fraction. a, e, i) 0mm, b, f, j) 16mm, c, g, k) 32mm, d, h, l) 48mm as shown in e) . . . . .	128
D.5	Contours of mean vapour volume fraction for different gas volume fraction. . . . .	129
D.6	The computational domain with hexahedral numerical mesh showing the extended circular. The geometry is step-nozzle is obtained from the work of Sou et al. (14). . . . .	129
D.7	Evolution of liquid jet shown using contours of mixture density at different NCG%. (a-d) 0% NCG, (e-h) 0.001%, (i-l) 1% NCG . . . . .	130
D.8	Comparison of the liquid jet structure between the current simulation (a) and the results from Ghiji et al. (15)(b) . . . .	131
E.1	a) Gear pump geometry represented using iso-surface of 50% IBM masking function b) IBM representation of gears at the mid-plane c) Numerical hybrid mesh. . . . .	133
E.2	Validation of the cavitation prediction from the current study with the experimental results obtained by Rolls-Royce University Technology Centre at Loughborough University. 50% vapour volume fraction shown in cyan colour. . . . .	134
E.3	Evolution of vapour volume fraction during one gearing pitch. (a-e) 0% NCG and (i-v) 2% NCG. $T_g = 14xRPM/60$ is the term used to nondimensionalise time. 50% vapour volume fraction shown in cyan colour. . . . .	135
E.4	Comparison of the volume integral of vapour volume fraction normalized using the total flow volume over a gearing period with 0% and 2% of gas volume fraction at 6500 RPM. . . . .	136
E.5	Velocity contour during one gearing pitch. (a-e) 0% NCG and (i-v) 2% NCG. . . . .	136
E.6	Pressure distribution during one gearing pitch. (a-e) 0% NCG and (i-v) 2% NCG. . . . .	137
E.7	Velocity contour during one gearing pitch. (a-e) 0% NCG and (i-v) 2% NCG. . . . .	138

# List of Tables

3.1	Thermodynamic properties for water, vapour and gas at 20°C. . . . .	34
3.2	Properties of diesel, diesel-vapour and NCG at 60bars and 60°C. . . . .	34
4.1	Boundary conditions used for the simulation . . . . .	49
6.1	Mean and fluctuating outflow rate at different RPM . . . . .	103
6.2	Mean and fluctuating outflow rate for different gas content at 2000 RPM . . . . .	105

# List of abbreviations

CFD	Computational Fluid Dynamics
CFL	Courant–Friedrichs–Lewy
CICSAM	Compressive Interface Capturing Scheme for Arbitrary Meshes
EOI	End of Injection
EoS	Equation of State
FSI	Fluid Structural Interaction
HEM	Homogeneous Equilibrium Model
IBM	Immersed Boundary Model
LES	Large Eddy Simulation
NCG	Non Condensable Gas
RANS	Reynolds-averaged Navier–Stokes
RMS	Root mean square
RNG	Renormalization group
SST	Shear Stress Transport
SOI	Start of Injection
SSOI	Subsequent Start of Injection
UDF	User Defined Function
VCO	Valve Covered Orifice
VOF	Volume of Fluid
WALE	Wall-Adapting Local Eddy-viscosity

# Chapter 1

## Introduction

### 1.1 Background and Motivation

Cavitation is a phenomenon that occurs in various engineering systems operating with liquid as working fluid. They occur when the local pressure in the flow drops below the saturation pressure. In most of the engineering applications, cavitation is an undesirable phenomenon that needs to be addressed during the design. The occurrence of cavitation can lead to unintended energy loss, performance degradation or even result in catastrophic failure of the machinery. Studies on cavitation have been the subject of research interest for more than a century with applications spanning across areas such as pumps and turbines, fuel systems and more recently for biomedical applications. In this thesis, two industrial applications where cavitation is a major concern is addressed; fuel injectors and hydraulic pumps.

### 1.2 Cavitation in fuel injector nozzle

Internal combustion (IC) engines operating on fossil fuel oil provide about 25% of the world's power. Diesel engines offer the highest well-to-wheel thermal efficiency among all transportation concepts. Still, the higher level of emissions from internal combustion engines has perplexed the relative industries for past few decades; the well-known soot-NOX trade-off poses a difficult problem for the simultaneous reduction of these pollutants (see selectively (16; 17) among many others). The drastic advancements in IC engine technology that have brought pollutant levels down a 1000- fold in

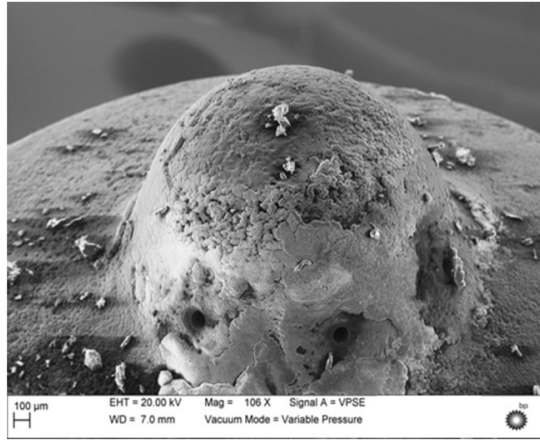


Figure 1.1: Deposits on the external surface of a diesel fuel injector. *Image reproduced from the work of Gold et al. (2)*

past decades (18) now make particulate emissions from tire and brake wear a larger problem than engine emissions (in both IC engine powered and electric vehicles). Today's emission issues are mainly related to insufficient oxygen due to local improper mixing, nozzle and piston wall wetting and fuel dribbling at the end of injection. Dribbling and wall wetting can lead to accumulation of carbonaceous deposit formation on the internal and external walls of an injector (see Fig. 1.1) and reduce combustion efficiency. On that front, the fuel injection system controls atomization and enables the mixing of air and fuel. Tremendous efforts have been made in the past three decades to study the flow inside and in the vicinity of the nozzle holes of diesel injectors both experimentally and numerically, as this is the key for further reducing emissions. Overall, remarkable improvements in injection strategies, such as increasing the injection pressure to a range of 3000 *bars* (19), controlling the injection-rate shaping and timing the injection (20), split or multiple injections (21; 22) and improved orifice geometry and orientation (23) are now standard practices.

The higher injection pressure and reduced orifice diameters of the modern injectors induces more cavitation inside the orifices. The fluctuating pressure field due to the cavitation increases the turbulent intensity and subsequently enhances the spray atomisation. Widening of the spray angle and enhanced atomisation are the major benefits of having cavitation inside the nozzle, both of which improves the efficiency of combustion. Although cavitation inside the nozzle is beneficial for atomisation, it also introduces some additional challenges. Their existence inside the orifice can block the effective flow area and thus significantly reduce the discharge

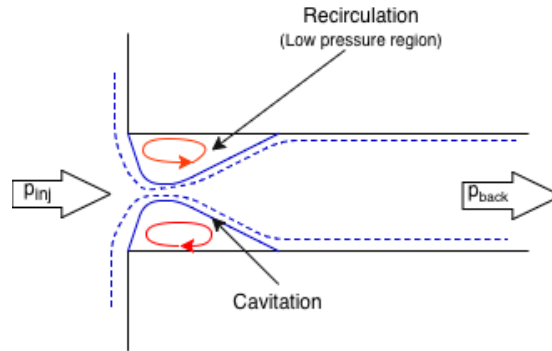


Figure 1.2: Schematic of cavitation inside a nozzle

through the orifice as shown in Fig. 1.2. In addition to that, the violent and repeated collapse of the vapour bubble inside the injector nozzle causes excessive noise and severe erosion problems even leading to catastrophic failures. Hence a fundamental understanding of the interaction between the cavitation and spray formation is vital for designing efficient injectors.

Detailed understanding of the impacts of cavitation on primary atomisation has not been possible through numerical methods to date. To numerically solve this interaction, a model that treats the in-nozzle cavitation and spray outside of the nozzle simultaneously is required. This means that the model should be able to solve three phases simultaneously (liquid, liquid vapour and gas). There are only very few numerical studies available that consider these interactions. Most of the existing studies either consider only the in-nozzle flow with cavitation without modelling the spray or only the spray is modelled while the in-nozzle cavitation is neglected, both requiring only a two-phase flow model. Hence, one of the aims of this thesis is to develop a model to handle three-phases for studying the interaction between cavitation and atomisation.

Past studies have also linked the influence of needle motion with flow pattern inside the injector and the spray formation. This is challenging both experimentally as well as numerically, thus limiting the number of studies available in the literature on this topic. Selectively the available experimental (24; 25; 26; 27; 28) and numerical (29; 30; 31; 32) studies with needle valve motion in diesel injectors provided a wealth of information on this topic. The off-axis motion of the needle valve is also found to have a significant impact on the spray especially at low and medium needle lifts as observed by (33). The flow phenomena taking place during the very short time scales ( $\sim 100 \mu s$ ) of the opening and closing of the needle valve controlling the injection process represent the major issue for emissions.

In particular, fuel dribbling, which is the formation of poorly atomized unintended fuel jet after the closure of the needle valve, represents an unknown flow mechanism. Although a reasonable amount of research has been done with transient needle motion to study the spray penetration and atomization during the needle opening and closing phases, modelling of the complete needle closure after the End of Injection (EOI) and the flow field during dwell has not been thoroughly studied. The slow-moving droplets after the end of injection can cause wetting of the surface of the injector's exit wall. When the liquid droplets come in contact with the surface, the surface tension causes them to contract and leave them in the near nozzle region leading to wetting of the surface (2). The surface wetting of the injector wall was found to have a greater influence on the initial droplet formation and subsequent accumulation of the deposits. The limitations in the understanding of the occurrence of this phenomenon due to experimental limitations on real-sized nozzles and numerical challenges in modelling complete needle closure (solid-to-solid contact) is the major reason why fuel dribbles remain as an unsolved problem.

### 1.3 Cavitation in pumps

The modern design requirements for compact pumps with greater performance would need the pumps to be operated at higher rotational speeds. Higher rotational speed causes higher flow acceleration near the pump rotor causing the local pressure to drop further producing more cavitation within the pump. Cavitation has also long been identified as a major cause of fluid-borne noise in pumps. Higher noise levels from the pumps are not welcomed in many industries especially aerospace and naval. Cavitation in pumps can lead to degradation of its performance or even catastrophic failures of the machine. Hence, the physics of cavitation must be properly understood and controlled while designing pumps.

Cavitation occurring in pumps is a complex phenomenon and have been an area of research interest for several decades. The traditional and the most acceptable way of studying cavitation in pumps is through experiments. However, experimental studies with the existing instrumentation technology pose several limitations in obtaining detailed flow visualisation and also in the arrangements and the number of probes for data collection due to moving parts. This is where the application of numerical studies becomes handier. Through appropriate refinements and assumption, a numerical model can provide better visualisation of the flow physics at



any selected location in a relatively cheaper way. Many different models exist in the literature for modelling cavitation in different types of pumps. The accuracy of each model depends on the assumptions involved in the model. Adding more complex flow physics into the numerical model can bring the model close to the real flow. However, it introduces additional numerical complexities.

The dynamics of cavitation become more complex when non-condensable gas (NCG) is present in the liquid. It is known that the presence of impurities in the liquid can significantly decrease the tensile strength of the liquid leading to different dynamics of cavitation. The presence of imperfections in the form of NCG in the liquid is often unavoidable. According to Henry's law, the amount of gas dissolved in the liquid is proportional to the partial pressure of the gas phase. Thus, the gas dissolved in the liquid at higher pressure can come out of the solution when it is exposed to lower pressure. For example, a fuel pump used in an aircraft fuel system. The fuel tanks in aircraft are vented to the atmosphere. When the tanks are exposed to the lower pressure at higher altitudes, the gas dissolved in the fuel at sea level pressure (which is higher than the pressure at altitude) comes out of the solution. During pump operation, the fuel with the NCG flows into the pump and is found to alter the predicted or expected performance of the pump. However, the behaviour of the pump in the presence of NCG is not very well understood. With a proper understanding of the influence of NCG, more efficient pumps can be developed. Hence one of the objectives of this thesis is to study the effect of non-condensable gas on cavitation occurring in a pump. An external gear pump with two counter-rotating spurs gears of equal dimensions is considered as the reference geometry.

### 1.3.1 Gear Pumps

Gear pumps are rotary displacement machines commonly used in a wide range of automotive, aviation and other industrial hydraulic applications due to their versatility along with their simplistic design and high structural reliability. A gear pump consists of two rotating gears; a drive gear which receives its power from a drive shaft and a driven gear. They work on the fundamental principle of volumetric displacement and can operate over a wide range of conditions by varying their size and rotational speed. A two-dimensional representation of an external gear pump is shown in Fig. 1.3. When the gear rotates, the low pressure created by the expanding volume between the teeth pulls the fluid from the inlet. This fluid volume

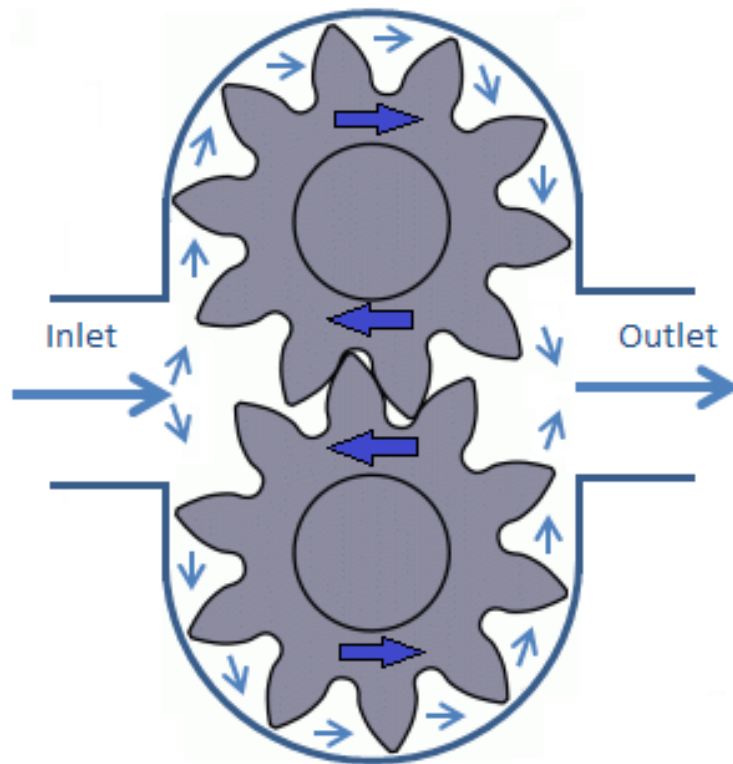


Figure 1.3: 2D representation of an external gear pump.  
(source: <http://processprinciples.com/2012/07/gear-pumps>)

that is trapped between the teeth is then transported between the teeth and casing to the high-pressure side. At the pressure side, the meshing of the gears leads to a reduction in volume and the trapped fluid is pushed out. The hydraulic impedance at the outlet causes the outlet pressure to rise when the fluid is pushed out.

## 1.4 Industrial relevance

One of the expected outcomes of this applied research is to develop and validate the numerical model that can be applied for industrial applications. For the validations to be convincing to industry, evaluations must be performed with realistic geometries and conditions comparable to their environment. Moreover, the computational cost must be practical for industrial applications.

The developed three-phase cavitation model in combination with the im-

mersed boundary approach will offer the flexibility for modelling complex realistic engineering scenarios such as the interaction between gas and cavitation, modelling contact between solids etc. Such scenarios are often unavoidable in practical applications like gear pumps, fuel injectors, and also in many biomedical applications. The numerical models developed in this thesis are validated using realistic geometries (such as diesel injectors, gear pump) with operating conditions which are relevant to the industry. With the simplistic approach for modelling cavitation using barotropic equations and the application of the IBM for modelling complex geometries and their motion, a considerable reduction in computational cost without compromising much on accuracy can be achieved compared to conventional modelling approaches using transport equation based cavitation model or a body-fitted grid with mesh motion for moving geometries. An indicative measure of the computation expense using the current modelling approach is provided in Chapter 6 where the gear pump is studied. With the numerical model validated against practical engineering problems and the reduced computational cost will make the current study more appealing to the industries. The model is currently being used to support research activities in industries that design and manufacture diesel injectors and aerospace pumps.

## 1.5 Aims

Keeping industry in mind, the present work aims to develop a numerical model to predict cavitation in the presence of non-condensable gas for industrial multiphase flow applications. The main objectives are summarised below:

- To develop a numerical model that can handle three phases (liquid, vapour and gas) and offer flexibility to be applied for different industrial applications.
- Provide closure to the three-phase model using two different approaches; a diffused interface mixture model and a sharp interface VOF model, suitable for modelling different scenarios.
- Incorporate the compressibility of the phases into the three-phase model by employing barotropic equations of state alongside appropriate models for turbulence, such as LES and  $k - \omega - SST$ .
- Implementation of an immersed boundary approach for modelling

complex geometric motion with the capability to model the surface-to-surface contact.

- Validation of the three-phase and the immersed boundary models against the experimental results from the literature.
- Application of the validated models for simulating cases of industrial interest such as,
  - \* studying the effect of cavitation on primary atomisation,
  - \* the effect of eccentric needle motion on atomisation from a VCO nozzle,
  - \* the dribble formation and wall wetting during the start of injection, end of injection, dwell time from a VCO nozzle,
  - \* the effect of NCG and contact between the gears on cavitation occurring in a gear pump.

## 1.6 Thesis structure

In Chapter 2 a detailed review of literature related to the current study is presented. The numerical method used, including the governing equations, the implementation of the three-phase model and the immersed boundary model is described in Chapter 3. In Chapter 4, Chapter 5 and Chapter 6 the results and discussions from the simulation conducted on different industrial applications are presented. The major conclusions drawn from the study and the scope for future work is presented in Chapter 7. Finally, some relevant results from the numerical studies conducted as a predecessor/successor for the results presented in Chapters 4 to 6 is provided in Appendices A to E.

## 1.7 Associated publications

The portion of the work presented in this thesis is published in International scholarly publications as follows:

**Chapter 4:** The results presented in this chapter is published in:

- M. G. Mithun, P. Koukouvnis, I. K. Karathanassis, M. Gavaises, Simulating the Effect of In-Nozzle Cavitation on Liquid Atomisation Using a Three-Phase Model, in: J. Katz (Ed.), Proceedings of the 10th International Symposium on Cavitation (CAV2018), ASME, New York, NY, ISBN 9780791861851
- M. G. Mithun, P. Koukouvnis, M. Gavaises, Numerical simulation of cavitation and atomization using a fully compressible three-phase model, *Physical Review Fluids* 3(6) (2018) 064304, ISSN 2469-990X, doi: 10.1103/PhysRevFluids.3.064304

**Chapter 5:** The result presented in this chapter is published in:

- M. Gold, R. Pearson, J. Turner, D. Sykes, V. Stetsyuk, G. de Sercey, C. Crua, M. G. Mithun, F. Koukouvnis, M. Gavaises, Simulation and Measurement of Transient Fluid Phenomena within Diesel Injection, 1-15, doi:10.4271/2019-01-0066.
- M. Gavaises, M.G. Mithun, F. Koukouvnis, M. Gold, R. Pearson, Numerical simulation of fuel dribbling and nozzle wall wetting, submitted to *Physical Review Fluids* (under review).

**Chapter 6:** Part of the results presented in this chapter is published in:

- M. G. Mithun, P. Koukouvnis, I. K. Karathanassis, M. Gavaises, Numerical simulation of three-phase ow in an external gear pump using immersed boundary approach, *Applied Mathematical Modelling* ISSN 0307904X, doi:10.1016/j.apm.2019.03.022.

## Chapter 2

# Literature

The co-existence of three phases (namely; liquid, liquid vapour and gas) can be observed in many engineering applications. Their interactions play a vital role in determining the efficiency of the machinery. For example, to study the atomisation from an injector, it is necessary to consider the cavitation inside the nozzle and air inside the combustion chamber. Similarly, the performance of a fuel pump is influenced by the amount of non-condensable gas present in the fuel. The presence of non-condensable gas in the fluid can change the properties (density) of the mixture, therefore alter the cavitation and turbulence levels in the flow. At the same time, the increased compressibility of the gas can protect the fluid machinery from cavitation erosion to a certain extent. With these interactions offering both favourable and unfavourable effects and along with the complex physics involved, it is difficult to determine their influence on the performance of the machinery. Hence, it is vital to study these interactions in detail for designing efficient engineering solutions.

In this chapter, a review of the literature related to the numerical simulations presented in Chapters 4 to 6 is given. The results presented can be broadly classified into two categories; one that studies the effect of cavitation on the primary atomisation from both, simplified step-nozzle as well as a valve covered orifice (VCO), while the other one study the effect of non-condensable gas on cavitation occurring in gear pumps. To facilitate these studies, several fundamental numerical models have been implemented, such as the cavitation model, three-phase model and an immersed boundary model. The state of the art in these fundamental models are also covered briefly in this review.

## 2.1 Cavitation and its influence on spray formation from an injector nozzle

Fuel injectors are one of the major components of combustion engines as they control fuel delivery, atomization, mixing, and to a large extent the combustion process. Atomization, in particular, is known to be influenced by the in-nozzle flow. In order to obtain a better understanding of the nature of the in-nozzle flows, many experimental studies have been performed for idealised flow conditions and simplified configurations of injectors. These studies provided clarity about specific flow features to be considered in models for predicting spray atomization. One of the major in-nozzle parameters that affect spray atomization is the formation of cavitation. In most of the engineering problems, the formation of cavitation is undesirable as the collapse of the cavity leads to erosion and mechanical damages. In general, the decrease in density of the mixture in the presence of cavitating will also affect the performance of the machinery. On the contrary, cavitation inside a fuel injector nozzle is found to be beneficial for combustion. This is due to the enhanced turbulence caused by the cavitation that improves the atomization of the spray (34; 35; 36).

### 2.1.1 Relevant experimental studies on nozzle flow

Due to the complex interaction between the in-nozzle flow and spray, many experimental studies in the past were focused on correlating the spray characteristics such as measured spray angle, break-up length, drop size etc. with parameters such as injection velocity, injection pressure, ambient gas density, nozzle geometry etc. Many such studies were conducted by (37; 38; 39; 40; 41; 42; 43; 44) among others. They all observed that with the formation of cavitation inside the orifice, the spray cone angle increases and the jet breakup length decreases. The turbulence in the flow is enhanced by the formation of cavitation and the impulse during the collapse of the vapour cavity produces more perturbation on the liquid jet surface enhancing the atomization. The existence of cavitation inside the orifice is also identified as a contributor to the reduction in discharge coefficient observed from the orifice (39; 45; 46). In addition to the flow parameters, the geometric features of the orifice also influence the cavitation and spray characteristics. Bergwerk (38) observed that the flow inside the orifice is very sensitive to the surface imperfections especially in small scale nozzles. The influence of the inlet radius/chafer on delaying the formation of cavitation was reported by (39; 45). Many researchers including (38; 39) observed a form of singularity called "hydraulic-flip" at large Cavitation number. Hydraulic flip is an anomalous behaviour where the flow separates from the inlet



corner and flows undistributed through the nozzle while the liquid in the nozzle is surrounded by the downstream gas. The formation of the hydraulic-flip has adverse effects on atomization.

So far it has been established that the in-nozzle flow has a strong influence on the spray atomization and this understanding has led the researchers to focus on the in-nozzle flow features in more detail. Despite this being a topic of intensive research, the detailed flow features inside the diesel injector nozzle that influence the spray formation is not yet well understood. This is impeded by several factors such as the extremely smaller size of the nozzle, high injection pressure and flow velocities, extremely transient nature of the needle movement, short injection duration etc.; thus, limiting the experimental visualization inside the nozzle. To overcome these challenges, experimentalists employed simplified representation of the injectors such as a step nozzle or single-hole injectors or even scaled-up version of real injectors with and without needle motion; all designs have been manufactured using transparent material for enabling flow visualization. With the advancement in instrumentation technologies, these studies laid the foundation in the understanding of the in-nozzle flow features.

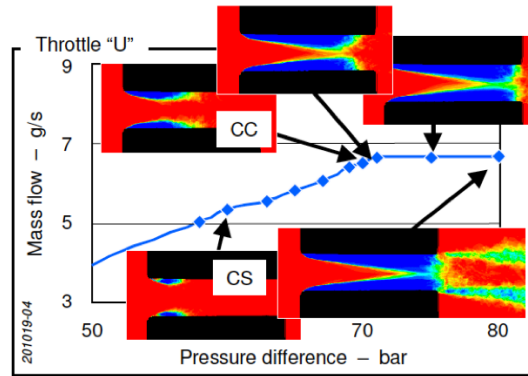


Figure 2.1: Cavitation field distribution from cavitation start to the choked flow. Red: liquid only. Blue: gas only. Bright areas show fluctuation between liquid and gas phase, CS refers to start of cavitation and CC is the critical cavitation point Winklhofer et al. (3)

Experimental investigations on a simplified 2D step-nozzle to study the flow feature inside the nozzle were conducted by (3; 47; 48; 1) among many others. Winklhofer et al. (3) observed that the mass flow rate through the injector increases with the increase in pressure difference until there is cavitation formation inside the orifice. After the inception of cavitation, a further increase in pressure difference increases the cavitation and thereby reducing the mass flow rate through the nozzle until it is fully choked. They termed the cavitation number at which the cavitation induced choking starts as "critical cavitation

number”.

Sou et al. (47) used high-speed cameras to visualize the cavitation inside a 2D step-nozzle and its effect on the jet formation. They classified different patterns of cavitation observed into four regimes namely; no-cavitation regime, developing cavitation, supercavitation and hydraulic-flip. They concluded that the jet formed outside of the nozzle depends on the cavitation regimes, a wavy jet is observed during no-cavitation and developing cavitation, an enhanced spray formation is observed during supercavitation and a flipping jet is observed during the hydraulic-flip.

Suh and Lee (48) investigated the influence of cavitating flow on the nozzle with different length-to-width ratios. Similar to (47), they classified the cavitation regimes into different regions, turbulent flow region, cavitating flow region and hydraulic-flip region. They observed that the cavitation has a significant effect on spray characteristics as long as it has not reached the hydraulic-flip condition. They concluded that the cavitation generated in the nozzle enhances the spray atomization and so will be the effect of longer orifice length.

Experiments on an asymmetric rectangular nozzle to study the macroscopic characteristics of cavitation-driven atomization was conducted by (1). The cavitation and the spray formation near the nozzle were studied using high-speed visualization. The asymmetric geometry used in this study produced asymmetric cavitation from the top and bottom walls of the nozzle allowing them to visualize the differences in the top and bottom interfaces of the spray. Their observation once again confirmed that the cavitation has a positive impact on atomization.

The strong connection between the nozzle flow and the resulting spray was also observed on enlarged and real-sized sac/VCO injector nozzles by (41; 46; 42; 49; 50). With high injection pressures and velocities realized in the modern common rail injection system, different cavitation patterns formed at the inlet are found to extend towards the exit, benefiting the spray atomization (46; 49; 50), an observation which is consistent with the observation from a step-nozzle.

Soteriou et al. (49) conducted experiments on different types of nozzles ranging from simple circular geometry to sac type multi-hole injectors and valve covered orifices, to study the effect of geometry on cavitation and the subsequent effect of cavitation on the spray characteristics. They characterized cavitation into three distinctive regions, i.e., a separated boundary layer inner region, a mainstream flow, and an attached boundary layer inner region. Their experiments have identified a new form of flow singularity namely; the ”partial hydraulic-flip” in a VCO nozzle. In partial hydraulic-flip, the air in the chamber, which is at a higher pressure than the vapour pressure, enters the injector hole from the exit and occupies the upper part of the injector hole previously

occupied by the cavitation. Partial hydraulic-flips are more likely to occur in real diesel injectors.

The formation of "supercavitation" (where the vapour cavity from the inlet reaches the exit) on a real sized transparent nozzle with an increase in injection pressure was observed by (46). They observed that the discharge coefficient and the spray angle level up at a value and does not change further with the increase in injection pressure once supercavitation is reached. They found that at supercavitating condition, the jet formed at the exit is asymmetric and tend to break much quicker. Many other experimental studies over the years have established the influence of in-nozzle cavitation on spray characteristics (51; 52; 53; 54).

The experimental studies conducted by (53; 54; 55) have identified two distinctive forms of cavitation inside the injector nozzle, geometric cavitation and vortex or "string-type" cavitation. Geometric cavitation is initiated by the sharp inlet corners where the flow accelerates as it enters the orifice. On the other hand, the vortex or string-type cavitation is observed in the bulk of the liquid where the vortical structures are formed (52; 56). A pictorial representation of the cavitation types observed in an injector nozzle as illustrated by (4) is shown in Fig. 2.2.

The geometric cavitation is also referred to as "cloud cavitation". The vapour cavity formed at the inlet grow in size and form a cavity cloud that is periodically broke-off by the re-entrant jet motion. The periodic shedding of vapour cloud due to the re-entrant jet was also observed by (57). This periodic shedding enhances the flow turbulence and improves the atomization upon reaching the orifice exit (58). The mechanism of the re-entrant jet is explained in detail by (59) using a step nozzle. The transient development of the cloud produced by the hole cavitation itself has been held responsible for the variation in transient flow rate through each injection hole even from a symmetric injector nozzle. This transient behaviour induces transient vortices to be formed inside the sac volume. The string-type cavitation is formed in the low-pressure core of these vortices and is more transient than the geometrically induced cavitation.

Similar observations using direct imaging techniques on a real-sized VCO injector nozzle under actual transient realistic operating conditions were presented by (60). They found that the cavitation patterns during the pilot injection are very similar to those during the main injection. Since the full development of the flow structures is completed in a very short time compared to injection duration, while the pressure in the nozzle tip is still building up, the effect of actual rail pressure is to just accelerate the already developed cavitation structures along the hole. This means that the injection pressure does not play a major role in the dynamics of different cavitation patterns. However, the influence of

back-pressure is more evident in the cavitation patterns.

In a recent experimental study, (61) focused on expanding the understanding of the string cavitation from their previous work (62), particularly on the hole-to-hole interaction of cavitation strings. They found that the spacing between the orifice holes also plays a significant role in vortex cavitation found in the nozzle.

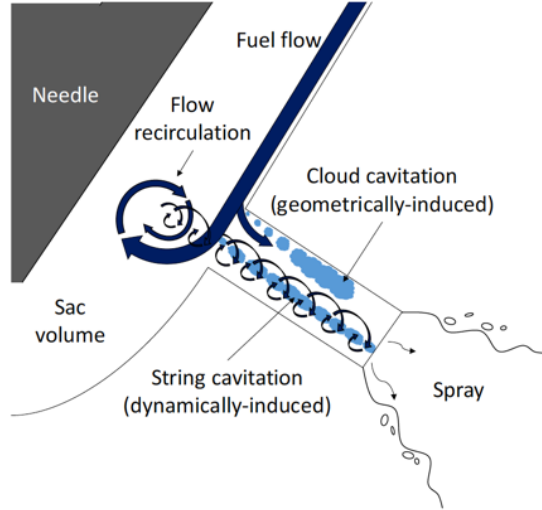


Figure 2.2: : Cavitation mechanisms inside a diesel injector nozzle as reported by Naseri (4)

### 2.1.2 Relevant numerical studies on nozzle flow

Numerous studies have addressed experimentally the formation and development of turbulence and cavitation inside fuel injectors and their effect on atomization as described in the previous section. Despite considerable improvement in instrumentation technology, experimentation of the internal nozzle flow and spray breakup is challenging. Most of the relevant studies focus on scaled-up or simplified designs of real-size nozzles. Still, quantification of the liquid volume fraction and differentiation between the vapour and gaseous cavitation are open questions. In contrast, numerical simulations, despite the high resolution required for capturing the very small turbulent and interfacial area scales, can provide insight regarding the flow dynamics at a resolution that cannot be obtained with today’s experimental techniques.

Along these lines, one of the important factors to consider is the effect of turbulence on cavitation formation and development. Most of the relevant studies have utilised the Reynolds Averaged Navier-Stokes (RANS) equations for mod-

elling turbulence owing to its simplicity and affordable CPU times. However, RANS models do not resolve the smaller vortices developing in the flow and thus, can significantly underestimate the formation and extent of cavitation (63). Fixes such as the model of Reboud et al. (64) that compensate to a certain extent the increase of turbulent viscosity predicted by RANS turbulence models, do not have global validity. On the other hand, Large Eddy Simulations (LES) can be used to obtain a more accurate flow field, though at an increased computational cost. In LES, large-scale turbulence is resolved, while scales below the grid size must be modelled. The comparative study of (63) involving different RANS and LES models suggests that RANS models fail to predict incipient cavitation when the pressure difference between inlet and outlet is low but LES can predict the formation of cavitation due to small vortices developing in the flow investigated.

Many different models have been developed for modelling cavitation; widely utilised approaches include the heterogeneous "multi-fluid" model, the homogeneous "mixture" model and the "single-fluid" model. The multi-fluid approach can model non-equilibrium conditions between the phases *i.e.* each phase can have a different temperature, pressure and velocity (65; 66). The interaction between the phases is modelled using interphase exchange terms. In 'homogeneous' approaches, the slip velocity between the phases is neglected; this can be justified by the fact that even in the most extreme cases, the relative velocity between the two phases does not exceed 10% of the local velocity magnitude and only in very localised areas. The most widely utilised mixture approaches employ a transport equation for the mass/volume fraction of the secondary phase. In this type of models, the phase-change rate is controlled using a source term which is typically derived from the Rayleigh-Plesset (R-P) equation, as shown in (67; 68; 69; 70). A detailed review of such models can be found in (71; 72). The single-fluid approach for modelling cavitation uses an equation of state (EoS), which relates the density and speed of sound with pressure and temperature. This simpler approach does not require any transport equation for the secondary phase. A subset of this model is the barotropic model in which the density is assumed as a function of pressure alone. A barotropic model assumes pressure equilibrium and infinite mass transfer between the phases. Hence, it is also known as homogeneous equilibrium model. One limitation of such models is that they cannot predict the baroclinic torque  $((\nabla\rho \times \nabla p)/\rho^2)$ , since the density variation is aligned with the pressure variation (73). Another challenge in modelling cavitation using barotropic models is defining an appropriate EoS for the mixture, which includes air in addition to liquid and vapour. Despite these limitations, barotropic models are widely used for complex simulations due to their simplicity and numerical stability (74; 63).

The break-up of liquid jet occurs when the disruptive forces exceed the stabilising forces, such as surface tension and viscous force. The disruptive forces arise from many internal and external factors such as liquid turbulence, cavitation in the nozzle and aerodynamic forces from the surrounding gas (75). During injection, a race between the disruptive and stabilising forces produce instabilities which under certain condition get amplified leading to the disintegration of the liquid jet forming droplets. The break-up process that occurs near to the nozzle exit (prior to the formation of droplets) is frequently referred to as primary atomization. There have been many attempts to study numerically the atomization process in the past; the numerical complexity is arising from the multi-phase nature of the flow, the interaction between the phases and the sudden variation in fluid properties across the interface. The numerical models developed in this front can be broadly classified into two main categories, one employing the Eulerian-Lagrangian (E-L) and the other using Eulerian-Eulerian (E-E) framework. In the E-L approach, the spray is represented as parcels containing a finite number of uniform droplets which are transported using Lagrangian formulation; the continuous gas phase is represented using Eulerian conservation equations. The coupling between the phases is achieved through source terms for mass, momentum and energy exchange. One of the major limitations of the E-L model is its sensitivity to the mesh resolution, especially in the dense spray region (76). Different methodologies to circumvent the grid sensitivity can be found in (77; 78; 79). On the other hand, the E-E models treat both phases as a continuum and solve conservation equations in the Eulerian framework. This approach provides better predictions in the dense spray region. Several studies employing the E-E framework can be found in (80; 81; 82) among many others. The Eulerian-Lagrangian spray atomization (ELSA) (79; 83) and the Coupling Interface (ACCI) (84), implemented in AVL FIRE Code, take advantage of both the E-L and E-E approaches by coupling them (85; 86; 87). Another popular approach for modelling atomization is by employing a method that tracks the liquid-gas interface, such as the VoF, level-set or a coupled level-set/VoF (88; 89). Such models are useful for modelling primary atomization where many topological changes such as interface pinching and merging occur and the interface motion are to be tracked accurately.

In order to numerically study the effect of in-nozzle flow on primary atomization, a model that can handle the transport and interaction between the three phases present, namely; liquid, vapour and air, is required. There are only very few studies available in the literature which deal with such problems. These models represent extensions of cavitation models accommodating for the additional gas phase. Along these lines, the cavitation model of (90) was extended to an eight-equation, two-fluid model to include non-condensable gas by (91).

This model was then used to study the cavitating liquid jet problem in a two-dimensional step-nozzle. Another three-phase model based on the homogeneous mixture approach can be found in (92). This model represents an extension of the single-fluid cavitation model of (74) to a closed-form barotropic two-fluid model and has been employed in LES simulations of a 3D step-nozzle. The authors reported three mechanisms responsible for the break-up of the liquid jet: turbulent fluctuations caused by the collapse of the cavity near the nozzle’s exit plane, air entrainment into the nozzle and cavitation collapse events near the liquid-gas interface. An alternative approach for modelling the co-existence of three-phases is by employing the Volume of Fluid (VoF), with a high-resolution interface capturing scheme such as the one of (93); this approach can be advantageous for modelling atomization. There are about five studies available in the literature that attempted to link a two-phase VoF model with a cavitation model for studying the in-nozzle effects on atomization (94; 95; 96; 97). These models differ in the way cavitation is resolved. A linear barotropic model similar to the one presented in (98) was combined with VoF for modelling atomization in a gasoline injector by (95). A comparative study between two transport-based cavitation models (68; 69) and employing VoF can be found in (97) for a single-hole solid cone injector. Further studies that assume the phases to be incompressible can be found in (96; 94). A Eulerian-Eulerian cavitation model with VoF was used to study cavitation and liquid jet breakup in a step-nozzle by (96). The incompressible assumption in this study was justified by the low-pressure conditions used.

With the influence of the in-nozzle flow on atomisation being established, and the importance of having a compressible three-phase model for simultaneous simulation of in-nozzle and near exit flow being understood, the other important area of research is the influence of needle motion. Past studies have also linked the influence of needle motion on the flow pattern inside the injector and the spray formation. However, this is a challenging task for both experimental techniques mainly using high energy X-rays (25; 27; 28; 24; 26) and real size optical nozzles (99; 100) as well as numerical simulations (101; 63; 102). Early one-dimensional models have considered transient effects in fuel systems, including the motion of the needle valve (103) while many later studies have included the motion of the needle valve in diesel injectors; see selectively (30; 29; 32). The needle motion in these studies is typically implemented using a moving mesh algorithm. A moving mesh approach for the needle motion was used for studying flow dynamics in a diesel injector with three different types of hole geometries (cylindrical,  $k$ ,  $k - s$ ) by (104). Their study concluded that the  $k - s$  type offers better fluid dynamic efficiency and less risk to cavitation erosion. Some other studies that considered needle movement in a multi-hole injector

can be found in (105; 33; 106; 29). A cut-cell based remeshing approach, implemented in the CONVERGE solver is used for studying the development of flow inside a 5-hole diesel injector under the influence of "on-axis" and "off-axis" needle motion by (33). A significant impact of the needle off-axis motion has been observed at low and medium lifts. The resulting mass flow rate, as well as the liquid jets emerging from the orifices, show noticeable sensitivity to the needle off-axis motion. A cut-cell based immersed boundary method for modelling the needle motion, without considering the effect of wobble is presented by (106; 107) with a primary focus on the developed turbulent structures. It is evident that a reasonable amount of research in diesel spray has been done with transient needle motion to study the spray penetration and atomization during the needle opening and closing phases. However, in none of the studies, neither a complete needle closure, representing the end of injection is modelled, nor the flow field after the End of Injection (EOI) is simulated. All past studies have assumed needle closure when the clearance between the needle and the sac wall reaches a specified minimum value to avoid discontinuity in the computational domain and to maintain numerical stability.

Using High-speed Mie-scatter and shadowgraphy imaging techniques, Kook et al. (108) studied the liquid-phase penetration and vaporization during quasi-steady and transient conditions realized after EOI. They found that the liquid penetration length decreases after the EOI compared to quasi-steady conditions due to the reduction in mass flow rate. They also formulated a one-dimensional model to explain the formation of entrainment waves from the nozzle towards the jet after the needle valve closure. The formation of this wave was also observed by other researchers (109; 110). This wave can travel till the tip of the liquid-phase and results in the liquid jet to recede towards the injector or to break the liquid spray (109). One of the sources of NOX and soot emission from an IC engine is the rich mixture formed by wall-wetting due to excessive jet penetration and poorly atomized liquid that leaves the nozzle (dribble) at the EOI (111). Fuel dribble is the formation of poorly atomized unintended fuel jet after the closure of the needle valve. The limitations in the understanding of the occurrence of this phenomenon due to experimental limitations on real size nozzles is the major reason why fuel dribbles remain as an unsolved problem.

In one of the initial experimental studies, Han et al. (112) performed spray visualization to investigate spray structures from a mini sac and a VCO nozzle using a high-pressure common rail system. They observed large liquid ligaments and droplets with a low velocity that were visible up to 0.32 *ms* for low pressures in the range of 300 *bars*. However, at higher injection pressures (1350 *bars*), their size and lifetime were shortened. Eagle and Musculus (113) utilized high-speed digital cinematography to observe the spatial and temporal evolu-



tion of the dribble after the EOI. They identified three main types of dribble formation; immediate dribble, late-cycle dribble and blow-down dribble. They also discussed the effect of different parameters such as nozzle geometry, fuel type, ambient pressure and temperature, rail pressure, injection schedules on dribble formation. They concluded that the dribble can exist in a wide range of operating conditions including different nozzle types and geometries. In a recent investigation, Moon et al. (114) used X-ray phase-contrast imaging technique to study the needle dynamics and in- and near-nozzle flow characteristics associated with fuel dribble of a three-hole mini-sac type injector. They observed high shot-to-shot variations in dribble formation from the injector hole and inconsistent air ingestion which they attributed to the hole-to-hole flow variations. Two modes of dribbling process were reported, one with a faster breakup and short residence time, and the other one with a large residence time where the dripping of undistributed liquid columns is observed. It was concluded that there is a strong connection between ingested air and dribble formation and the major factor that influence the dribble formation is the needle closure velocity.

So far, the EOI behaviour and dribble formation for an injector nozzle have only been studied experimentally; only a few studies have included simulations. Battistoni et al. (115) studied the end of injection process from a single hole injector using a two-phase three-components mixture model to simulate cavitation while considering the presence of non-condensable gas. They used a Cartesian cut-cell grid generated during run time to incorporate the needle motion. To model the needle closure, they switched to two disconnected domains when the needle lift drops below  $10\mu m$  and the simulation is continued for  $3000\mu s$  to cover the relevant flow dynamics. They observed the formation of cavitation inside the sac due to sudden pressure drop when the needle closes, and the pressure recovery caused by the pull-back of the liquid into the nozzle reabsorbs the vapour. In (116), the authors utilized the volume of fluid (VOF) approach with a  $k - \omega - SST$  turbulence model to study the full injection process of a real size multi-hole injector. To seal the high-pressure zone from the low-pressure zone at needle closure, they modelled an interface which acts as a "wall" when needle lift is below  $0.5\mu m$  and as an "interior" all other times. They observed dripping of fuel from the nozzle after EOI with the nozzle almost filled with liquid fuel when the outlet pressure was set to  $60 bar$ . Whereas at  $1 bar$  outlet pressure, the fuel was almost emptied from the nozzle replaced by the air from the combustion chamber. Since their primary objective was to study the in-nozzle flow with transient needle motion, the fuel dribble was not studied in detail. Both studies did not consider the compressibility of the phases and they assumed needle motion in the axial direction only. However, the off-axis wobbling motion of the needle was found to produce hole-to-hole flow variation

and swirling motion which affects the liquid jet structure at close to the opening and closing conditions (117; 118).

## 2.2 Cavitation in external gear pump

### 2.2.1 Experimental evaluation of flow inside the gear pump

The advancements in instrumentation technology have enabled the experimental evaluation of the flow inside the gear pumps plausible. In the last few decades, the visualisation techniques such as strobe photography and Particle Image Velocimetry (PIV) have become popular among researchers for studying the flow characteristics inside the pump. A study on the visualisation of flow inside the gear pump using strobe photography technique was conducted by (119). They captured the averaged images of cavitation formation in the gear meshing region over several meshing cycles. They observed the formation of cavitation due to vaporisation even when the fluid is highly saturated with air content. For a pump operating with relatively high air content, they observed the release of air due to vortex cavitation over a range of operating conditions. One of the key purposes of their experimental study was to validate their numerical model.

In the past few decades, the PIV techniques have been applied to study a large number of flow problems. The application of Digital PIV (DPIV) as a quantitative measuring method for the flow in turbo-machines was presented by (120). In PIV, tracer particles are introduced in the flow that follows fluid motion, typically solid or water. A laser light sheet is then used to illuminate the particles in a planar region of the flow and a digital camera captures the images of the plane. By using two consecutive particle images, the two components of velocity can be estimated on that plane. By increasing the image acquisition rate, a better resolution of the velocity and the flow evolution can be obtained. The technique of resolving the velocity time series from the particle images is called as Time-Resolved Particle Image Velocimetry (TRPIV).

The TRPIV technique was used to study the turbulence inside the gear pump by (121). To avoid the gears being damaged by the usage of conventional PIV tracers such as solid particles or water, they utilised air bubbles as the tracer material. By keeping the size of the air bubble under  $100 \mu m$  and their count in the interrogation area below 20, they minimised the problems related to buoyancy and the compressibility of the mixture that can arise due to the introduction of air bubbles into the liquid. They found that at high enough Reynolds number, the integral time scale of turbulence obtained from the autocorrelation is almost the same as the gearing period. A similar TRPIV approach using air bubbles as the tracer was also used by (122) to investigate

the flow inside the suction chamber of an external gear pump. This study was focused on obtaining detailed flow patterns inside the suction chamber under two different rotational velocities. They observed the existence of two stable vortices during all gearing period in the upper part of the chamber and a more complex region with formation of a critical point and a vortex core that move and evolve with the gear motion in the gearing zone. They reported the formation of critical point as an indication of three-dimensionality of the flow inside the suction chamber. Another visualisation study on the flow process inside the inlet chamber of the gear pump is presented by (10). They investigated the flow features in the pump with and without the relief grooves, to compare their effects. Additionally, the effect of parameters such as rotational speed, inlet pressure and oil temperature were also studied. They found that the interaction of the gears with the inlet/outlet chambers and bridge results in cavitation, with more pronounced effects found in inlet chamber and bridge location when the trapped volume is connected with the inlet chamber. They found that with the inlet pressure increasing from  $-0.075\text{Mpa}$  value to  $+0.05\text{Mpa}$ , the intensity of cavitation reduces from the third degree to first degree, with the third degree being full cavitation featuring cavitation vortex generated in the working fluid and the first degree being the beginning of the cavitation where a single bubble appears in the working fluid. Similarly, a decrease in rotation speed or an increase in oil temperature was also found to reduce the degree of cavitation. Their visualisation study also identified the usefulness of relief grooves in limiting the cavitation.

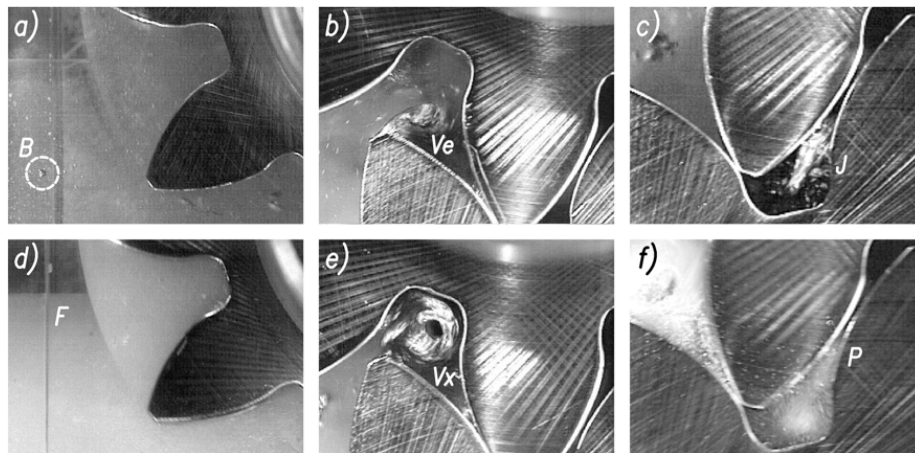


Figure 2.3: Characteristic forms of cavitation observed in gear pump. (a) bubbles, (b) veil, (c) jet, (d) foam, (e) vortex, (f) plume. Reproduced from the work of Antoniuk and Stryczek (5)

More recently, Antoniuk and Stryczek (5) presented another study which

made the visualisation of the flow in all characteristic areas of the pump possible by making the body of their pump using a transparent material (PMMA). Based on the operating conditions, they observed three forms of cavitation occurring independently inside the pump, namely; cavitation bubble ( $B$ ), cavitation veil ( $Ve$ ) and cavitation jet ( $J$ ) as shown in Fig. 2.3(a-c) respectively. Depending on the operating condition, these forms of cavitation can take extreme forms. By significantly lowering the inlet pressure the cavitation bubbles ( $B$ ) will change into a foam ( $F$ ) (Fig. 2.3d). If the rotation speed of the pump increases, a veil ( $Ve$ ) will transform into a cavitation vortex ( $Vx$ ) (Fig. 2.3e). Lowering the inlet pressure as well as increasing the pump speed will also affect the appearance of the jet ( $J$ ). The reduced pressure in the chamber will facilitate the transformation of the bubbles ( $B$ ) into cavitation foam ( $F$ ) and eventually this accompanying foam ( $F$ ) will make the jet ( $J$ ) look less clear and resemble a plume ( $P$ ), as shown in Fig. 2.3f. A detailed description of the flow streams at inlet and outlet chambers as well as at the inlet and outlet bridges are presented in (5). Their study was limited to low and medium pressure ratios (in the range of 10 *bar*) due to the structural limitation of the transparent material.

### 2.2.2 Numerical evaluation of flow inside gear pump

The initial numerical studies in this front were based on graphical (123) or theoretical approaches (124; 125). Other numerical studies focusing on modelling gear pumps are also available; however, modelling of such a pump is not so trivial despite the pump's simple design. With the recent advancement in engineering and computational technologies, more advanced models capable of performing complex, CFD simulations have been developed. One of the popular but simple approaches for modelling gear pump using lumped parameters can be found in (126; 127). In their model (HYGESim), the fluid dynamics and the mechanical gear motion are modelled using AMESim<sup>®</sup>, and the lateral gaps are modelled using CFD, and these models are coupled together with many other sub-models to include cavitation, material erosion and the lateral motion of the gears.

On the other hand, a complete CFD simulation of the gear pump poses a major challenge concerning numerical meshing of gears with small clearances and solid-to-solid contact between the gears. Besides, the modelling requires a dynamic mesh that can adapt to the rotation of the gears without losing the mesh quality. These issues in mesh handling have been a research focus for the past few decades. A superposition method where the stationary and moving regions are meshed separately and the data is interpolated between these meshes during the simulation was employed by (128). The interpolation between the mesh was a critical step in their method. An Arbitrary Lagrangian-Eulerian

(ALE) approach using a pseudo-pressure operator for describing the nodal velocity is presented in (129). They applied their model on a two-dimensional lobe pump and an external gear pump with an incompressible flow assumption. One limitation of this model according to (130) was the limited control over the mesh in the clearance region due to the automatic re-meshing. An alternative method called FMALE (fixed mesh ALE) was proposed by (130), in which the evolving geometry is meshed apriori as opposed to re-meshing in the classical ALE. They employed 10 different meshes over a gearing period and used an algorithm for interpolating the data between the time-steps. This approach ensured that the mesh quality is maintained. However, the limitation of this model was that the time-step size is directly related to the number of mesh instances considered in a period. To have smaller time-steps, more mesh instances are required which is expensive; on the other hand, if fewer mesh instances are used, a larger time-step is needed and therefore the interpolation between the mesh at two consecutive time-instants can lead to numerical errors. Even though the primary objective of their study was to estimate the suction side pressure distribution to avoid cavitation, no cavitation model was used. The occurrence of cavitation was linked to the pressure values below the fluid's vapour pressure, as obtained from the single-phase analysis. In another study, a dynamic mesh approach using an unstructured mesh that deforms and re-mesh to accommodate the gear motion as implemented in Ansys Fluent<sup>®</sup> was employed by (131). This approach can be expensive if the mesh count is large and smaller time-step values are used, which is typically the case for gear pumps where frequent adaptation of the mesh is required to maintain the mesh quality. A hybrid between the deform/re-mesh approach of (131) and the mesh replacement approach of (130) was employed by (9). Their study was focused on the flow field in the inlet chamber. They performed two-dimensional simulations using both laminar and RANS flow approximations with various two-equation turbulence models. They concluded that the modelling of contact between the teeth and a proper choice of turbulence model is essential to capture the flow fluctuations which are responsible for the pressure ripples, noise and vibration. A three-dimensional simulation of the external gear pump using OpenFOAM toolkit was recently reported by (132). Since this study was dedicated to mesh manipulation and modelling gear contacts, cavitation and turbulence were not taken into account. Another custom made approach that is focused on flow simulations in compressors can be found in (133; 134; 135). The numerical algorithm they developed is implemented in to a meshing solver called SCORG which has the capability to work alongside many commercial CFD solvers.

Despite its importance, none of the works described above considers the effect of cavitation in their studies. One of the first CFD work to consider cavitation

in a gear pump was reported by (136). They considered a two-dimensional gear pump to study the influence of different parameters such as suction chamber geometry and gear RPM on cavitation and volumetric efficiency. They compared their results obtained using different cavitation models with experimental results to test the applicability of each model. In a follow-up work, the effect of operating pressure on pump performance in the presence of cavitation was studied by (137). They reported that the impact of suction side cavitation on the outlet flow and pressure ripples observed at the outlet for low pressure (10 *bar*) disappear when a mean pressure jump of 100 *bar* is applied. However, no significant change in the inlet flow and morphology of cavitation is observed with the increase in operating pressure. In their study, unlike the approach of (9), where a tiny wall was defined to model the contact between the gears that will deform with the gear rotation until the new mesh replaces it, the authors of (137) modelled the gear contact by increasing the dynamic viscosity to a higher value at the contact location. According to (137), the approach of (9) produces numerical errors when cavitation is considered. CFD simulations using one-dimensional and three-dimensional gear pumps for improving the porting design and for reducing cavitation erosion in an external gear pumps were conducted by (138). A recent study considering cavitation in the numerical analysis of a 3D gear pump can be found in (139). They used the commercial code PumpLinx<sup>®</sup> for their simulation and validated their results against the experimental data from the pump manufacturer. Their cavitation model was based on the work of (140) which consider the effect of a finite amount of non-condensable gas. To have a better prediction of the volumetric efficiency, the authors have considered all the leakage paths and grooves in their model. However, they did not consider the contact between the gears. Recently, the SCORG solver was combined with the pressure based algorithm implemented in Star-CCM+ for predicting cavitation in twin-screw pumps by (141). They employed a combination of VOF method and the Scherr-Sauer model for predicting cavitation. Their meshing strategy allowed the modelling of small clearances, hence were able to predict the leakage flows. They reported a slight increase in volumetric efficiency due to the reduction in leakage when cavitation is present in the clearances.

It has been pointed out in the literature by many authors e.g. (136; 142) that the interpolations involved while using a traditional re-meshing/deforming approach or a mesh replacement approach could lead to numerical errors especially while solving for multi-phase flows and with high gear RPM. Moreover, they are computationally expensive due to the small time-step requirements for maintaining the mesh quality in small clearances. To overcome these complexities, approaches such as overset mesh, which uses a background mesh and many component meshes have been employed in the past (143) for simulat-

ing turbo-machinery. Even though this approach ensures better mesh quality, the numerical errors arising from the interpolation of data between the base and component mesh cannot be avoided. From the personal experience of the authors, modelling clearance between the gears is also challenging since the data interpolation requires at least four overlapping cells between the background and component mesh. An alternate approach that is becoming increasingly popular for such simulations is the immersed boundary method. This approach was initially utilized for biological applications (144) with flexible geometries. Later, this approach was modified and used for rigid body simulations by other researchers (145; 146). A detailed review of the immersed boundary approaches can be found in (147; 6). In a recent study, the immersed solid approach implemented in Ansys CFX<sup>®</sup> was employed by (142) for modelling a three-dimensional gear pump operating at very high speed (10,000 RPM). They claim that the use of this method simplified their numerical simulation setup and reduced the computation time to a great extent. Their model was validated against the experimental data for flow rate measurements. They concluded that the dominant geometrical parameters that influence the pump flow rate are the tip and the lateral clearances. The limitation of their work is that it was not applied in multiphase or variable density flows. More recently, a numerical algorithm for reducing the computational cost while finding the optimum parameter for cavitation optimisation in a double-suction centrifugal pump was conducted by (148). They proposed an optimisation algorithm which claims to reduce the time for NPSHr by at least 44.4%. They used the Zwart-Gerber-Belamri model implemented in CFX for modelling cavitation with frozen-rotor approach for modelling the rotor motion.

## 2.3 Immersed boundary model

The immersed boundary method (IBM) has emerged in recent years as an alternative to traditional body-conforming mesh method for simulating fluid flows over complex and moving objects. The method was first introduced by (144) to simulate cardiac mechanics and associated blood flow. One distinguishing feature of this approach is the ability to perform the entire simulation on a fixed Cartesian grid. By imposing the effect of the immersed body on the flow through fluid equations, the requirement to conform the grid to the complex geometries and issues related to the moving boundaries such as mesh distortions and mesh interpolation errors due to deforming-mesh and re-meshing can be eliminated.

A schematic of the simulation of flow past a solid body is shown in Fig. 2.4. A conventional approach would be to generate a mesh that conforms to the body.



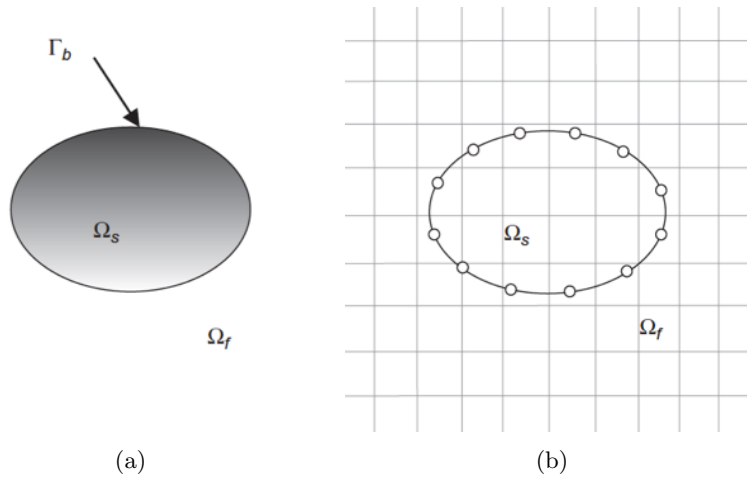


Figure 2.4: (a) Schematic drawing showing flow past a generic body. The solid body occupies the volume  $\Omega_s$  with boundary  $\Gamma_b$ . The volume of the fluid is denoted by  $\Omega_f$ . (b) Schematic of body immersed in a Cartesian grid on which the governing equations are discretized (Source: Mittal and Iaccarino (6))

This is achieved in two steps, first, a surface grid is generated and then using this surface mesh as a boundary condition, a volume mesh is generated. This method is challenging if the geometry is complex and involves complex motion. On the other hand, in an immersed boundary approach, the surface grid for the geometry would still be generated, however, the volume grid generated will be with no regards to this surface grid. This means that the solid boundary would cut through the volume grid. Since the volume grid does not conform to the geometry, applying boundary conditions in this approach would require modification to the governing equations in the vicinity of the boundary.

The application of boundary condition for an immersed boundary approach is not straight forward. Two different approaches for applying the boundary conditions of an immersed body is presented by (6). The first approach is the continuous forcing approach, where the forcing function is incorporated into the continuous governing equations applied to the entire domain before discretization. The second approach, which is the discrete forcing approach, the 'forcing' is introduced after the equations are discretized. The continuous forcing approach is well suited for simulating flows with elastic bodies. Successful application of this approach can be found in (149; 150). However, the general formulation for the continuous forcing approach is not suitable for modelling rigid bodies. Different modifications to this model have been applied in the past to utilize this methodology for rigid bodies. Beyer and Leveque (151) provided a solution by using a spring to attach the solids to an equilibrium location



with a restoring force. A similar feedback forcing strategy to control the velocity near the objects, which behaves as a system of springs and dampers were proposed by (145; 152). They introduced artificial constraints which are ad-hoc and are large enough to ensure the no-slip boundary conditions near the wall. However, large values make it too stiff and result in instabilities and impose stringent requirements for time step size and CFL number (145). Other studies using continuous forcing approach for rigid bodies can be found in the work of (153; 154; 112; 147). The discrete forcing approaches are not as practical as the continuous forcing approach. However, it enables a sharp representation of the immersed boundary which is especially desirable for high Reynolds number flows. It also allows direct control over the numerical accuracy, stability, and discrete conservations of the solver. The successful implementation of this type of approach can be found in (155; 156). It is apparent that the choice of either of these approaches is purely problem-dependent. A detailed explanation of these approaches and the mathematical formulation can be found in the work of (6). In recent years, the immersed boundary approach has been utilized to model pumps (157; 142; 158; 159) and fuel injectors (92; 2) due to their simplicity and reduced computational cost.

## 2.4 Literature gap and current contribution

From the detailed literature review presented above, it has been established that the primary atomisation from an injector is influenced by the cavitation occurring inside the nozzle. To model the influence of the in-nozzle flow on atomization, a model that can solve simultaneously the in-nozzle and out of nozzle flow is required. The thorough literature review conducted on this topic has revealed that there are only less than five numerical studies available in the literature where the cavitation and atomisation are solved simultaneously while considering the compressibility of the fluid. Hence, in this study, a numerical model for modelling coexistence of three phases and consider the compressibility of all the phases using non-linear barotropic relations is developed. Such consideration for compressibility is essential to capture the non-linear effects of the flow even when phase change is not dominant. In this model, the liquid compressibility is modelled using a modified Tait equation, which can predict the water density and speed of sound with a minimum deviation (up to 0.001% for density and 3.8% for the speed of sound) from the experimental data (160). As far as modelling the compressibility of the vapour phase is concerned, even though the vapour formation occurs below the saturation pressure, where compression can be considered to be negligible, the expansion of the vapour at this lower pressure plays an important role in the accuracy of the numerical

model (161). An isentropic gas relationship is utilized for modelling the pure vapour and gas phase. The compressibility of the mixture phase is modelled using the Wallis speed of sound correlation. All three-phase models available in the literature, either consider the phases to be incompressible or assume linear compressibility, which results in a much higher speed of sound for the mixture phase ( $\sim 136$  m/s compared to the 0.8 m/s using the present non-linear model at 50% vapour volume fraction with same fluid properties). According to (162), during the phase change, the speed of sound should have a value between the frozen speed of sound, 3 m/s, and the equilibrium speed of sound, 0.08 m/s (163), which is achieved using the developed three-phase model.

The transient flow phenomena occurring during the opening, closing and dwell time in fuel injectors are known to significantly contribute to excess exhaust emissions in engines; this is due to the formation of large droplets dribbling and wetting the injector's wall, resulting to poor combustion, deposits and unburned hydrocarbon emissions. Despite their importance, combination of adverse thermodynamic conditions,  $\mu\text{m}$ -scales of nozzle hole orifices,  $\mu\text{s}$ -time scales of the events, highly compressible flow phenomena leading to air entrainment and formation/collapse of cavitation, all contribute to a rather complex environment; up to now, no study is available linking the in-nozzle flow during the opening/closing of the needle valve with the detailed mechanism of the nozzle wall wetting.

The existing models are challenged by the wall-to-wall contact during the needle closure. Some kind of switching techniques that creates a fictitious wall between the needle and nozzle wall when the lift is below a certain limit are commonly employed. To overcome this challenge, a novel immersed boundary method is developed which allows the modelling of complete needle closure without any numerical difficulties. To model the phenomenon of wall wetting, a wall adhesion model has been implemented in the solver. Along with these, the application of the three-phase model using the VOF approach allows the tracking of dribbles and droplet formed within and outside the orifice after the needle closure.

Furthermore, the literature review on gear pumps has revealed that there is a huge gap in the literature particularly in the understanding of flow behaviour inside the gear pump. This is predominantly due to the experimental limitations in the visualising the flow inside a real metallic pump and if a transparent gear pump is used, it is limited to pressures much lower than the realistic operating pressures. On the other hand, the numerical investigations are primarily limited due to the complex mesh manipulation required to capture the gear motion. The traditional dynamic meshing or an overset meshing approach introduces difficulties in modelling cavitation and fluid compressibility due to the

complex interpolations involved both in manipulating the mesh as well as the field variables. In addition to that, it is impossible to model contact between the gears using such approaches. The existing approaches employ tricks such as introducing a fictitious wall or ramping up the viscosity in the region where the gears are in contact. Moreover, there is no numerical study available in the literature that can predict the effect of non-condensable gas on cavitation. Hence, the study presented in this thesis is focused on addressing all these limitations; introducing an immersed boundary method for modelling the gears which has the capability to model the contact between the gears, and a compressible three-phase model using a mixture approach that can be used for studying the effect of NCG on gear pump performance.

## Chapter 3

# Numerical Methodology

In this chapter, the governing equations and numerical methods used for the simulations presented in this thesis are described. The two main contributions of this thesis in terms of numerical methodology includes the development of a novel approach for modelling fully compressible three-phase flows and an immersed boundary approach for modelling complex geometric motion. Two different approaches are used in this study for modelling the co-existence of three phases. The first approach is using a barotropic model in combination with the Volume of Fluid similar to the one proposed by (164) where different phases are modelled as immiscible fluids with a sharp interface between them. The other approach combines the barotropic model with a diffused interface mixture model where different phases can coexist in a computational cell. The governing equations for the mass and momentum conservation are formulated according to the two approaches as mentioned above. The numerical implementation of the immersed boundary approach used for modelling the moving geometries is also presented in this chapter. The basic numerical formulation for the VoF and the mixture approach used in this thesis is the same as implemented in the Ansys Fluent solver. The major contributions of this work includes the development of sub-models for three-phase cavitation, immersed boundary method, and corrections for turbulent viscosity, all implemented in to Ansys Fluent using user defined functions (UDF's) and the methodology to combine these capabilities with physics such as wall adhesion and surface tension.

### 3.1 Barotropic cavitation model (Two-phase)

A single fluid approach using barotropic equations of state is utilized for modelling cavitation in this study. The model is based on the assumption of homogeneous equilibrium with infinite mass transfer rate between the phases. The

homogeneous mixture assumption implies that both phases are uniformly mixed, with no-slip between them and no clear interface can be defined between the phases. The equilibrium assumption means that there is thermodynamic equilibrium between the phases which implies that heat and mass transfer across the interface will be at an infinite rate. Cavitation is associated with an abrupt change in the density of the fluid locally as a function of both temperature and pressure. However, in this study, a barotropic model which assumes the fluid density as a function of pressure alone is used. This model is implemented into the Ansys Fluent using a User Defined Function (UDF).

The cavitation model used in this study is a piecewise function employing three different equations corresponding to liquid, liquid-vapour mixture, and the pure vapour phases. A modified form the Tait equation of state is used for modelling liquid ( $\rho \geq \rho_l$ ). the pure vapour phase ( $\rho < \rho_v$ ) is modelled using the isentropic gas equation, and the equation of the two-phase mixture ( $\rho_v \leq \rho \leq \rho_l$ ) is derived by integrating the Eq. (3.1) with respect to the mixture density for an isentropic process, using the Wallis speed of sound Eq. (3.2) (162).

$$c^2 = \left( \frac{\partial p}{\partial \rho} \right)_s \quad (3.1)$$

$$\frac{1}{c_{lv}^2 \rho_{lv}} = \frac{\alpha_l}{c_l^2 \rho_l} + \frac{\alpha_v}{c_v^2 \rho_v} \quad (3.2)$$

where,  $c$  is the speed of sound and  $\alpha$  is the volume fraction. The subscript  $lv, v$  and  $l$  corresponds to the mixture, vapour and liquid phases respectively and the subscript  $s$  refers to an isentropic process. Combination of the individual equations of state with the assumption of the homogeneous equilibrium results in the equation for a two-phase mixture Eq. (3.3).

$$p = \begin{cases} B \left[ \left( \frac{\rho}{\rho_l} \right)^N - 1 \right] + p_{sat,l} & \rho \geq \rho_l \\ \frac{c_v^2 c_l^2 \rho_l \rho_v (\rho_v - \rho_l)}{c_v^2 \rho_v^2 - c_l^2 \rho_l^2} \ln \left( \frac{\rho}{c_l^2 \rho_l (\rho_l - \rho) + c_v^2 \rho_v (\rho - \rho_v)} \right) + p_{ref} & \rho_v \leq \rho \leq \rho_l \\ C_{vap} \rho^\kappa & \rho \leq \rho_v \end{cases} \quad (3.3)$$

In Eq. (3.3),  $B$  is the bulk modulus,  $p_{sat,l}$  is the saturation pressure and  $N$  is the stiffness of the liquid. The parameter  $p_{ref}$  in the mixture equation is tuned to ensure a continuous variation of density between the liquid and mixture phases.  $C_{vap}$  is the constant of the isentropic process and  $\kappa$  is the heat capacity ratio for the vapour phase. The densities  $\rho_l$  and  $\rho_v$  corresponds to the density of the pure liquid and vapour phase at saturation. In Fig. 3.1, the behaviour of the equation of state presented in Eq. (3.3) is plotted in a logarithmic scale of pressure and density. The plot also shows the speed of sound variation with

Table 3.1: Thermodynamic properties for water, vapour and gas at 20°C.

Liquid properties			Vapour properties			Gas properties		
$B$	3.07	GPa	$C_{vap}$	27234.7	Pa/(kg/m <sup>3</sup> ) <sup>n</sup>	$C_{gas}$	75267.8	Pa/(kg/m <sup>3</sup> )
$N$	1.75	–	$\kappa$	1.327	–	$\gamma$	1.4	–
$\rho_l$	998.16	kg/m <sup>3</sup>	$\rho_v$	0.0173	kg/m <sup>3</sup>			
$C_l$	1483.26	m/s	$C_v$	97.9	m/s			
$P_{sat,l}$	4664.4	Pa	$P_{sat,v}$	125	Pa			
$\mu_l$	1.02	mPa.s	$\mu_V$	9.75	$\mu$ Pa.s	$\mu_g$	17.8	$\mu$ Pa.s

Table 3.2: Properties of diesel, diesel-vapour and NCG at 60bars and 60°C.

Diesel properties			Vapour properties			Gas properties		
$B$	0.19	GPa	$C_{vap}$	17036	Pa/(kg/m <sup>3</sup> ) <sup>n</sup>	$C_{gas}$	75267.8	Pa/(kg/m <sup>3</sup> )
$N$	1.75	–	$\kappa$	1.022	–	$\gamma$	1.4	–
$\rho_l$	880.7	kg/m <sup>3</sup>	$\rho_v$	0.143	kg/m <sup>3</sup>			
$c_l$	1253	m/s	$c_v$	129.1	m/s			
$p_{sat,l}$	54.9	kPa	$p_{sat,v}$	2336	Pa			
$\mu_l$	4.64	mPa.s	$\mu_v$	7.0	$\mu$ Pa.s	$\mu_g$	17.8	$\mu$ Pa.s

the mixture density. The thermodynamic relationship for the speed of sound of pure liquid and vapour phases are derived from the respective pressure density relationship given in Eq. (3.3) and differentiating them using Eq. (3.1).

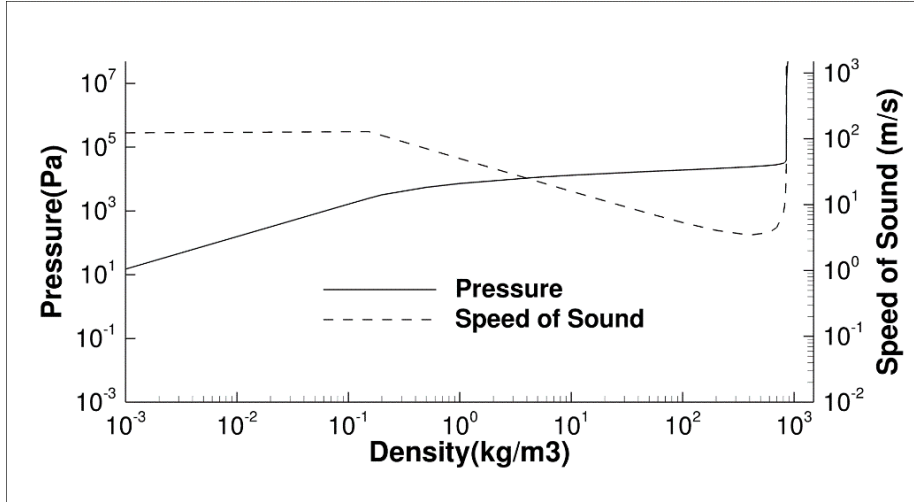


Figure 3.1: Two-phase barotropic relation (plot in log scale)

The values of the constants used in Eq. (3.3) depends upon the working fluid used. In this thesis, water at 20°C and Diesel at 60°C are used as working fluid, for which the barotropic constants are presented in Tables 3.1 and 3.2 respectively.

## 3.2 Three-phase cavitation model

In a three-phase model, in addition to the pure liquid and vapour phases, the effect of non-condensable gas (NCG) is also modelled. The properties of the air at ambient temperature and pressure is used for modelling NCG in this study. The NCG in this study is modelled using a barotropic equation of state (isentropic gas equation) which assumes density as a function of pressure alone (see Eq. (3.4)).

$$p = C_{gas}\rho^\gamma \quad (3.4)$$

where,  $C_{gas}$  is the constant of the isentropic process for gas and  $\gamma$  is the heat capacity ratio for the gas phase.

The pressure density relationship for the NCG is similar to that of the pure vapour phase, but with a different value for the heat capacity ratio ( $\gamma = 1.4$ ) and the constant of the isentropic process ( $C_{gas}$ ).

To close the three-phase system, the barotropic cavitation model is combined with the equation of the NCG. To achieve this, two different approaches are used, one using a volume of fluid approach and the other using a mixture approach. Both these approaches based on the Eulerian framework are explained along with the governing equation in the following sections. It should be emphasised here that in the current approach, the non condensable gas is modelled as free gas and does not participate in the phase change process. This means that the mass exchange between NCG and liquid phase is assumed to be zero and hence the nucleation phenomenon and its subsequent effect on cavitation cannot be captured.

### 3.2.1 Volume of Fluid approach (VOF)

A VOF approach is well suited for modelling two or more immiscible fluids where the position of the interface between the two fluids are of interest. In the VOF approach, the volume fraction ( $\alpha$ ) of the secondary fluid in a computational cell is tracked throughout the domain.

In this thesis, the three-phase model using the VOF approach is used for studying the liquid jet atomisation from nozzles in the presence of cavitation. An implicit formulation is used for the discretisation of the VOF equation. The three-phase flow modelled using the VOF approach considers a cavitating fluid as the primary phase and the non-condensable gas (NCG) as the secondary phase. To track the interface between the two phases, an advection equation for the secondary phase volume fraction as given in Eq. (3.5) is first solved and then the volume fraction of the primary phase is calculated using the constraint

given in Eq. (3.6), which implies that in each control volume the volume fraction of all phases sum to unity.

$$\frac{1}{\rho_g} \left[ \frac{\partial(\alpha_g \rho_g)}{\partial t} + \nabla \cdot (\alpha_g \rho_g \bar{\mathbf{u}}_g) = \sum (\dot{m}_{lv-g} - \dot{m}_{g-lv}) \right] \quad (3.5)$$

$$\alpha_{lv} + \alpha_g = 1 \quad (3.6)$$

The volume fraction ( $\alpha$ ) is a scalar quantity which takes a value between 0 and 1, with 0 being the cavitating fluid (subscript  $lv$ ) and 1 being the gas phase (subscript  $g$ ) in this thesis. Any value between 0 and 1 means that the cell contains an interface between the two fluids. In this thesis, the mass transfer between the two fluids (i.e. cavitating fluid and the NCG) are assumed to be zero, hence the term  $\sum (\dot{m}_{lv-g} - \dot{m}_{g-lv})$  in Eq. (3.5) will equate to zero.

The field variables and properties of the flow are then represented as the volume-averaged values of the volume fraction at each cell in the computational domain. The mixture density  $\rho$  and the mixture viscosity  $\mu$  at each cell in the domain is calculated as,

$$\rho_m = (1 - \alpha_g) \rho_{lv} + \alpha_g \rho_g \quad (3.7)$$

$$\mu = (1 - \alpha_g) \mu_{lv} + \alpha_g \mu_g \quad (3.8)$$

where  $\rho_{lv}$  is the density of the cavitating fluid and  $\rho_g$  is the density of the NCG as described in the previous section. Once the densities and viscosities are calculated, the volume fraction of the pure vapour phase ( $\alpha_v$ ) is computed using the relation,

$$\alpha_v = \frac{(\rho_l - \rho_{lv})}{(\rho_l - \rho_v)} \quad (3.9)$$

Once all the mixture properties such as density and viscosity are calculated, a single set of momentum equations for the mixture phase is solved. The resulting velocity field is then shared among all the phases. The momentum equation given in Eq. (3.10) is related to all the phases through the mixture properties  $\rho$  and  $\mu$ .

$$\frac{\partial(\rho U_i)}{\partial t} + \frac{\partial(\rho U_j U_i)}{\partial x_j} = -\frac{\partial p}{\partial x_i} + \frac{\partial}{\partial x_j} (\sigma_{ij} + \tau_{ij}) + \rho g + F + f_\sigma \quad (3.10)$$

In the above equation,  $p$  is the pressure,  $F$  includes all body forces,  $g$  is acceleration due to gravity,  $f_\sigma$  is the surface tension force,  $\sigma_{ij}$  is the stress



tensor due to molecular viscosity and  $\tau_{ij}$  is the Reynolds stress tensor. The definition of the stress tensors is provided later in this thesis where turbulence modelling is explained.

An implicit formulation as given in Eq. (3.11) is used in this thesis to discretise the volume fraction equation.

$$\frac{\alpha_g^{n+1}\rho_g^{n+1} - \alpha_g^n\rho_g^n}{\Delta t} + \sum_f (\rho_g^{n+1}u_f^{n+1}\alpha_{g,f}^{n+1}) = \left[ \sum (\dot{m}_{lg} - \dot{m}_{gl}) \right] V \quad (3.11)$$

where  $n + 1$  is the current timestep,  $n$  is the previous timestep,  $\alpha_g^{n+1}$ ,  $\alpha_g^n$ ,  $\rho_g^{n+1}$ ,  $\rho_g^n$  are the gas volume fraction and the gas density at the current and previous timesteps respectively, the subscript  $f$  refers to the values at the cell face and  $V$  is the cell volume. Since the volume fraction at the current timestep depends on other quantities at the current timestep, the transport equation is solved iteratively for each secondary phase volume fraction at each timestep. The discretization of the face fluxes is performed using the compressive scheme within Ansys Fluent, which is a second-order reconstruction method, with slope limiter values ranging between 0 and 2. In the present study, a limiter value of 2 is used, which corresponds to the compressive interface capturing scheme for arbitrary meshes (CICSAM) of (93).

An important interfacial factor that can impact the study of primary atomization is the surface tension between the liquid and gas. The continuum surface force (CSF) approach taken from the work of (165) is used for modelling surface tension which is included as an additional source term ( $f_\sigma$ ) to the momentum equations of the VOF model, which is defined as:

$$f_\sigma = \sigma \frac{\rho\beta\nabla\alpha}{\frac{1}{2}(\rho_l + \rho_g)} \quad (3.12)$$

where  $\beta$  is the curvature of the interface which is defined as the divergence of a unit normal as given in Eq. (3.13) and Eq. (3.14),

$$\beta = -\nabla \cdot \hat{n} \quad (3.13)$$

$$\beta = \nabla \cdot \left( \frac{\nabla\theta}{|\nabla\theta|} \right) \quad (3.14)$$

To model the droplet impingement on a solid surface, the wettability of the wall needs to be accounted for, an approach similar to the one presented in (165) is used. The contact angle that the fluid is assumed to make with the wall is used to adjust the surface normal in cells near the wall. The surface normal at the live-cell next to the wall  $\hat{n}$  is rotated according to the prescribed angle  $\theta_w$

(which is an assumed value depending on the fluids involved) as:

$$\hat{n} = \hat{n}_w \cos\theta_w + \hat{n}_t \sin\theta_w \quad (3.15)$$

where  $\hat{n}_w$  and  $\hat{n}_t$  are the unit vectors normal and tangent to the wall. The combination of the contact angle and the calculated surface normal on the cell above the wall determines the local curvature of the surface which is used to adjust the surface tension force.

An additional source term related to the implementation of the immersed boundary approach is also introduced to the momentum equation to model the moving geometry. The formulation of this source term is described later in the section where the immersed boundary approach is presented.

### 3.2.2 Mixture approach

Another approach for modelling the three-phase flow is by utilising the homogeneous mixture model. Similar to the VOF model, the mixture model uses the single-fluid approximation and solves only for a single set of momentum equation, a continuity equation for the mixture and a transport equation for the secondary phase. However, the mixture model differs from the VOF in the aspects that it assumes the phases to be inter-penetrating and also allows the modelling of slip between the phases through algebraic expressions. In this thesis, a homogeneous approximation is made which allows both phases to be in the same velocity.

The continuity equation for the mixture phase is defined as,

$$\frac{\partial}{\partial t} (\rho) + \nabla \cdot (\rho \bar{u}) = 0 \quad (3.16)$$

where the mixture density ( $\rho$ ) is calculated similar to Eq. (3.7) and the mass averaged velocity ( $\bar{u}$ ) is calculated as,

$$\bar{u} = \frac{\sum \alpha_g \rho_g \bar{u}_g}{\rho} \quad (3.17)$$

The mixture momentum equations are then formulated by summing all the individual momentum equations of the phases.

$$\frac{\partial}{\partial t} (\rho \bar{u}) + \nabla \cdot (\rho \bar{u} \bar{u}) = -\nabla p + \nabla \cdot (\sigma_{ij} + \tau_{ij}) + F + \rho g + \nabla \cdot \left( \sum \alpha_g \rho_g \bar{u}_{dr,g} \bar{u}_{dr,g} \right) \quad (3.18)$$

where  $\bar{u}_{dr,g}$  is the drift velocity for the gas phase which is assumed zero in this study,  $\sigma_{ij}$  is the stress tensor due to molecular viscosity and  $\tau_{ij}$  is the shear stress

due to turbulent viscosity. The mixture viscosity in the term  $\sigma_{ij}$  is computed using the mixing law described in Eq. (3.8) and the term  $\tau_{ij}$  is computed by employing different turbulence models which will be explained in the following section.

The transport equation for the volume fraction of the secondary phase (gas phase in this study) can then be defined from the continuity equation for the gas phase which is similar to the equation presented in Eq. (3.5)

$$\frac{\partial}{\partial t}(\rho_g \alpha_g) + \nabla \cdot (\rho_g \alpha_g \bar{u}) = \sum (\dot{m}_{lv-g} - \dot{m}_{g-lv}) \quad (3.19)$$

An enhanced numerical treatment is enabled for both the VOF and mixture-based model in the solver for providing better numerical stability at start-up and during calculation for the compressible flows. This is achieved by providing additional diagonal dominance to the matrix of the equation by controlling the rate of change of pressure between iterations.

### 3.3 Turbulence modelling

Turbulence is a property of the flow in which the physical quantities as well as the pressure, and velocity components undergo fluctuations in space and time. The turbulent diffusion caused by the turbulent agitation can produce substantial amplification to the mass, momentum, and energy transfer across the control volume boundary. Turbulent flows span a wide range of scales, with energy supplied by the macro-scales and dissipated as heat by viscosity at micro-scales; a process known as "Energy cascading". The length scale at which the energy is dissipated as heat is known as the Kolmogorov micro scale, where the viscosity becomes dominant.

Turbulence in the flow is identified as one of the major contributors in both cavitating flows as well as the flow atomisation, hence an important parameter to consider in this study. A range of computational models exists in the modern CFD codes to resolve the turbulence phenomena. This is because no one model fits all scenarios. Approaches like Direct Numerical Solutions (DNS) can resolve all turbulent scales without any models, however, they are limited to small and simple applications due to the computational cost, hence not suitable for design purpose. On the other hand, the turbulence models based on averaged Navier-Stokes (N-S) equations which are computationally much less expensive, are more popular for engineering simulations. There are two classes of turbulence models based on averaged N-S equations; a) Scale Resolving Simulation (SRS) and b) Reynolds Averaged Navier-Stokes (RANS) equation. In the present study, models based on both SRS and RANS approach has been utilised as appropriate.

The implementation of these turbulence models into the governing equations and the three-phase model is described in following subsections.

### 3.3.1 Large eddy simulation (LES)

Large-eddy simulations (LES) is one of the most popularly used SRS models. It is based on the concept of resolving only the large-scale eddies, which are problem dependent while the more universal smaller scales are modelled using an eddy viscosity model. The scales that are resolved and modelled are classified based on the filtering of Navier-Stokes equation over a finite spatial region (typically grid volume). Only the turbulence larger than the filter width is resolved. The filtering operation is defined as;

$$\bar{\Phi} = \int_{-\infty}^{+\infty} \Phi(\vec{x}') G(\vec{x} - \vec{x}') d\vec{x} \quad (3.20)$$

$$\int_{-\infty}^{+\infty} G(\vec{x} - \vec{x}') d\vec{x} = 1 \quad (3.21)$$

where  $G$  is the spatial filter.

The filtered form of the momentum equation employed for the LES is given by,

$$\frac{\partial(\rho\bar{U}_i)}{\partial t} + \frac{\partial(\rho\bar{U}_j\bar{U}_i)}{\partial x_j} = -\frac{\partial p}{\partial x_i} + \frac{\partial}{\partial x_j}(\sigma_{ij} + \tau_{ij}^{LES}) + \rho g + F \quad (3.22)$$

The term  $\tau_{ij}^{LES}$  in Eq. (3.22) is the additional subgrid-scale stress tensor arising from the filtering operation, which is defined as,

$$\tau_{ij}^{LES} = \bar{\rho}\bar{U}_i\bar{U}_j - \bar{\rho}U_iU_j \quad (3.23)$$

The subgrid-scale stress tensor  $\tau_{ij}^{LES}$  is an unknown term that requires modelling. The Eq. (3.23) is then split into two parts, the isotropic and deviatoric parts as,

$$\tau_{ij}^{LES} = \underbrace{\tau_{ij}^{LES} - \frac{1}{3}\tau_{kk}\delta_{ij}}_{\text{deviatoric}} + \underbrace{\frac{1}{3}\tau_{kk}\delta_{ij}}_{\text{isotropic}} \quad (3.24)$$

The deviatoric part in the above equation is solved using a compressible form of Smagorinsky model,

$$\underbrace{\tau_{ij}^{LES} - \frac{1}{3}\tau_{kk}\delta_{ij}}_{\text{deviatoric}} = -2\mu_t \left( S_{ij} - \frac{1}{3}S_{kk}\delta_{ij} \right) \quad (3.25)$$

By using Eq. (3.25) into Eq. (3.24):, the sub-grid scale stress can be written as,

$$\tau_{ij}^{LES} = -2\mu_t \left( S_{ij} - \frac{1}{3} S_{kk} \delta_{ij} \right) + \frac{1}{3} \tau_{kk} \delta_{ij} \quad (3.26)$$

where  $S_{ij} = \frac{1}{2} \left( \frac{\partial \bar{U}_i}{\partial x_j} + \frac{\partial \bar{U}_j}{\partial x_i} \right)$  is the strain rate tensor and  $\mu_t$  is the sub-grid scale turbulent viscosity.

Several formulations exist for modelling the eddy viscosity  $\mu_t$ . A wall-adaptive local eddy viscosity model (WALE) by (166) is used in the present study. The eddy viscosity  $\mu_t$  in the WALE model is defined as,

$$\mu_t = \rho L_s^2 \frac{(S_{ij}^d S_{ij}^d)^{\frac{3}{2}}}{(S_{ij} S_{ij})^{\frac{5}{2}} + (S_{ij}^d S_{ij}^d)^{\frac{5}{4}}} \quad (3.27)$$

$$L_s = \min \left( \kappa d, C_w V^{\frac{1}{3}} \right) \quad (3.28)$$

where  $\kappa$  is the von Karman constant,  $V$  is the volume of the computational cells from which the local grid size is estimated, and  $C_w$  is the WALE constant which takes a value of 0.325. The term  $L_s$  in Eq. (3.28) is the mixing length of the subgrid-scale which is defined based on the distance to the closest wall  $d$ . This term also ensures the asymptotic behaviour ( $y^3$ ) of the turbulent viscosity near the wall. The deficiency of the Smagorinsky model in achieving zero eddy viscosity in pure laminar shear flows can be rectified by the application of the WALE model. The formulation of the WALE automatically provides zero eddy viscosity for laminar shear flows thereby allowing correct treatment of laminar zones in the domain. Thus, this model is well suited for wall-bounded flow simulations as it has been pointed out by (167).

### 3.3.2 Reynolds-Averaged Navier-Stokes (RANS)

A much simpler and relatively less expensive model compared to the LES is the RANS turbulence model. In this class of turbulence models, the flow velocity is decomposed into its mean and fluctuating components. The Navier-Stokes equations are then re-written in terms of these decomposed velocities and a density-weighted averaging is applied on the equations (Favre averaging) to obtain an averaged Navier-Stokes equation for compressible flows. The resulting averaged equations are then solved for the average velocity field.

$$\frac{\partial (\bar{\rho} \tilde{u}_i)}{\partial t} + \frac{\partial (\bar{\rho} \tilde{u}_i \tilde{u}_j)}{\partial x_j} = -\frac{\partial (\bar{p} \delta_{ij})}{\partial x_j} + \frac{\partial}{\partial x_j} (\bar{\tau}_{ij} - \bar{\tau}_{ij}^{T_{ur}}) + \bar{\rho} g + F \quad (3.29)$$

The term  $\tau_{ij}^{Tur}$  in Eq. (3.29) is the additional stress term due to Favre averaging of the governing equation, known as the Favre-averaged Reynolds stress tensor which is defined as,

$$\tau_{ij}^{Tur} = -\overline{\rho u_i'' u_j''} \quad (3.30)$$

The Favre-averaged stress term incorporates the effect of the unresolved turbulent fluctuations (i.e., unresolved by the mean flow equations) on the mean flow. This stress term introduces 6 new unknowns leading to a closure problem. Thus, appropriate turbulence models are required to provide necessary closure for the problem by specifying the turbulent stress in terms of mean flow solution quantities.

The two-equation  $k - \omega - SST$  model of (168) based on Boussinesq eddy viscosity hypothesis was chosen among the other available RANS turbulence models for the RANS simulations presented in this thesis. This is mainly due to its ability to predict the flow separation and reattachment better compared to the other two-equation models. In this model, the Boussinesq hypothesis is used to relate the mean velocity gradients to the shear stress,

$$-\overline{\rho u_i' u_j'} = \mu_t \left( \frac{\partial u_i}{\partial x_j} + \frac{\partial u_j}{\partial x_i} \right) - \frac{2}{3} \left( \rho k + \mu_t \frac{\partial u_k}{\partial x_k} \right) \delta_{ij} \quad (3.31)$$

where  $k$  is the kinetic energy and  $\mu_t$  is the turbulent viscosity which is defined as,

$$\mu_t = \frac{\rho k}{\omega} \frac{1}{\max \left( \frac{1}{a^*}, \frac{F_2 \sqrt{S_{ij}:S_{ij}}}{a_1 \omega} \right)} \quad (3.32)$$

where  $a^*$  is the correction for low Reynolds number flow, the constant  $a_1=0.31$ ,  $F_2$  is a blending factor and  $S_{ij}$  is the strain rate tensor (168).

Unlike the other two-equation models, the  $k - \omega - SST$  accounts for the transport of the turbulent shear stress in the definition of the turbulent viscosity. The transport equation for the turbulent kinetic energy ( $k$ ) and the specific dissipation rate ( $\omega = \frac{\varepsilon}{k}$ ) are given below,

$$\frac{\partial (\rho k)}{\partial t} + \frac{\partial (\rho k u_i)}{\partial x_i} = \frac{\partial}{\partial x_j} \left( \Gamma_k \frac{\partial k}{\partial x_j} \right) + G_k - Y_k + S_k \quad (3.33)$$

$$\frac{\partial (\rho \omega)}{\partial t} + \frac{\partial (\rho \omega u_i)}{\partial x_i} = \frac{\partial}{\partial x_j} \left( \Gamma_\omega \frac{\partial \omega}{\partial x_j} \right) + G_\omega - Y_\omega + S_\omega \quad (3.34)$$

where the terms  $G$ ,  $\Gamma$  and  $Y$  represents the turbulent generation, effective diffusivity and the dissipation of both  $k$  and  $\omega$  respectively. The terms  $S_k$  and  $S_\omega$  corresponds to the user-defined source terms for  $k$  and  $\omega$  equations respectively, which in this thesis represents the contribution from the immersed boundary

implementation.

In addition to the correction already implemented for the eddy-viscosity ( $\mu_t$ ) in the  $k - \omega - SST$  model, in the present study, an additional correction for the density term ( $\rho$ ) in the equation of eddy viscosity is also applied. This correction is to compensate for the mixture compressibility in the two-phase mixture region and to allow for stronger shear flows to develop (169). The mixture density ( $\rho$ ) in Eq. (3.32) is replaced with a function  $f(\rho)$  which is defined as,

$$f(\rho) = \rho_v + (1 - \alpha)^{10} (\rho_l - \rho_v) \quad (3.35)$$

where the subscripts  $v$  and  $l$  represents the saturated vapour and liquid conditions respectively.

### 3.4 Immersed Boundary model (IBM)

To mimic the complex motion of the geometries, an immersed boundary approach has been developed and implemented into Ansys Fluent using User Defined Functions. The IBM approach makes the modelling of wall-to-wall contact (e.g.: to model the needle closure, the contact between two gears in a gear pump etc.) and the complex motion of the geometry easier where the canonical body-fitted grids with remeshing/deforming approaches can be computationally expensive and inefficient. In an IBM approach, the presence of the body is represented using an additional forcing term (source term) in the momentum equation.

The IB method used in this work is based on the continuous forcing approach (144; 6) where the forcing term ( $F = f_{IB}$ ) is added to the continuous form of momentum equation. The term  $f_{IB}$  is the source term that forces the flow to follow the boundaries of the immersed body. This force is proportional to the difference in flow velocity ( $\bar{u}$ ) and the target body velocity ( $\bar{U}_{IB}$ ); which is the velocity of the immersed body. The formulation of the forcing term is given in Eq. (3.36);

$$f_{IB} = -\frac{\rho_m C}{dt} \alpha_{IB} (\bar{u} - \bar{U}_{IB}) \quad (3.36)$$

In the above equation,  $C$  is an arbitrary coefficient which can be tuned to adjust the strength of the immersed body velocity ( $C = 1$  in this study),  $dt$  is the time step and  $\alpha_{IB}$  is the masking function which takes a value of 1 if the cell is inside the immersed body (solid) and 0 if the cell is outside (fluid). Any value between 0 and 1 refers to a cell which is partially occupied by the wall (see Fig. 3.2). For calculating the mask function in each cell, the wall normal distance (signed

distance) of each cell nodes from the immersed boundary points needs to be estimated. This is done by looping over all cell nodes, and identifying the IB point with the minimum distance (see the graphical representation given in Fig. 3.3). The formulation of this can be represented using Eq. (3.37):

$$d_{n,IB} = (\bar{x}_n - \bar{x}_{IB}) \cdot n_{IB} \quad \text{if } \min(|\bar{x}_n - \bar{x}_{IB}|) \quad (3.37)$$

where  $\bar{x}_n$  and  $\bar{x}_{IB}$  are the coordinates of the cell node and immersed boundary point,  $n_{IB}$  is the normal to the wall. The distance from the immersed body to the cell is estimated as the average of node distances, for the nodes belonging to that particular cell using Eq. (3.38):

$$d_{c,IB} = \frac{\sum_n d_{n,IB}}{n} \quad (3.38)$$

where  $n$  is the number of nodes in the selected cell.

After estimating the distance function using Eq. (3.37), the mask function  $\alpha_{IB}$  in Eq. (3.36) is calculated using,

$$\alpha_{IB} = \frac{\sum_n [-\min(d_{n,IB}, 0)]}{\sum_n |d_{n,IB}|} \quad (3.39)$$

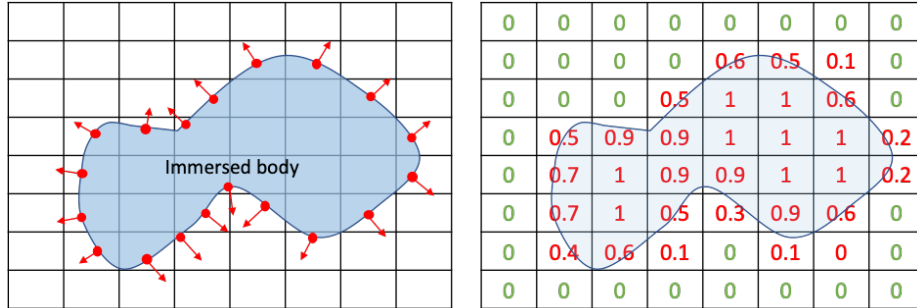
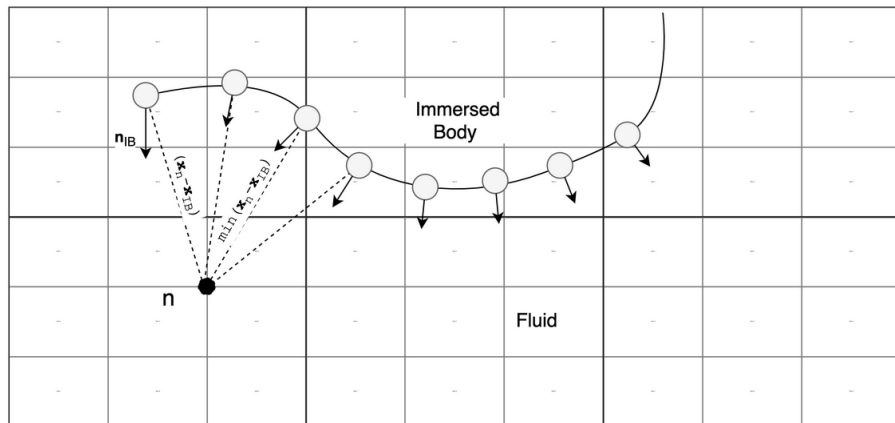


Figure 3.2: Immersed body representation using Lagrangian points (left) to mask function in Eulerian frame (right).

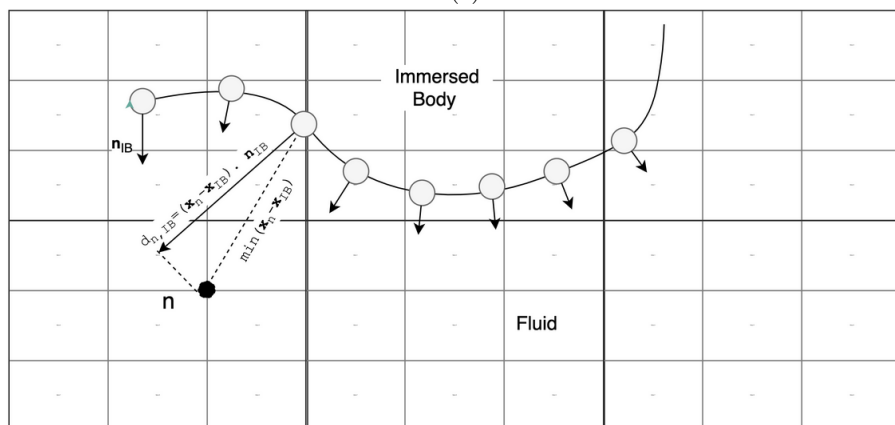
### 3.4.1 Immersed body motion

The first step in the IBM approach is to convert the geometry into a triangulated surface consisting of several triangular elements such as an *.stl* file, using any numerical meshing software. The barycentre location of each cell and their corresponding surface normal are then computed. These barycentre points and the corresponding surface normal are then used to represent the immersed body. These coordinates of the barycentre points and the surface normal at each of





(a)



(b)

Figure 3.3: Schematic representation of wall distance calculation: (a) identifying the closest marker point to a given cell node  $n$ , (b) calculating the normal distance to the wall

these points are then imported into the solver using a user-defined function. This serves as the initial known position of the immersed body for the first time-step. The initial masking function  $\alpha_{IB}$  and the forcing term  $f_{IB}$  are then calculated as described in the previous section and introduced into the momentum equation. At each time-step, when the immersed body has moved the new orientation of the immersed body is updated based on the motion type and the variables  $d_{n,IB}$ ,  $d_{c,IB}$ ,  $\alpha_{IB}$  and  $f_{IB}$  are recalculated. A typical motion of the body involves translational and/or rotational motion which are described using the following equations,

For translation motion:

$$\vec{x}_{IB}^{new} = \vec{x}_{IB}^{old} + \vec{d}x \quad (3.40)$$

$$\vec{x}_{IB,CM}^{new} = \vec{x}_{IB,CM}^{old} + \vec{d}x \quad (3.41)$$

$$\vec{n}_{IB}^{new} = \vec{n}_{IB}^{old} \quad (3.42)$$

For rotational motion:

$$\vec{x}_{IB}^{new} = \vec{x}_{IB,CM}^{new} + RM(\theta) (\vec{x}_{IB}^{old} - \vec{x}_{IB,CM}^{new}) \quad (3.43)$$

$$\vec{n}_{IB}^{new} = \vec{x}_{IB,CM}^{new} + RM(\theta) (\vec{n}_{IB}^{old} - \vec{n}_{IB,CM}^{new}) \quad (3.44)$$

$$RM_x(\theta) = \begin{bmatrix} 1 & 0 & 0 \\ 0 & \cos(\theta) & -\sin(\theta) \\ 0 & \sin(\theta) & \cos(\theta) \end{bmatrix}; \quad RM_y(\theta) = \begin{bmatrix} \cos(\theta) & 0 & \sin(\theta) \\ 0 & 1 & 0 \\ -\sin(\theta) & 0 & \cos(\theta) \end{bmatrix};$$

$$RM_z(\theta) = \begin{bmatrix} \cos(\theta) & \sin(\theta) & 0 \\ -\sin(\theta) & \cos(\theta) & 0 \\ 0 & 0 & 1 \end{bmatrix} \quad (3.45)$$

In the above equations, the subscript  $IB, CM$  represents the centre of mass of the immersed body and  $RM(\theta)$  is the rotation matrix where  $\theta = |\omega| dt$ .

The Eqs. (3.40) to (3.45) are modified accordingly to suit the motion required for the geometry. For example, the gear pump simulation in Chapter 6 requires only the rotational motion at a prefixed angular velocity  $\omega_z$ , whereas the eccentric motion of the needle valve in Chapter 5 requires only the translation motion in all three directions to be specified. In this thesis, neither the

flow-induced motion of the immersed body due to the fluid forces nor any form of structural deformation due to the flow-induced loads is considered.

When the immersed body is in motion, the Eulerian cells inside the immersed body should also have the same velocity as the body. This is enforced using the following formulation.

$$\vec{U}_{IB} = \frac{d\vec{x}}{dt} + \omega_{IB} \times (\vec{x}_c - \vec{x}_{IB,CM}) \quad (3.46)$$

where  $\omega_{IB}$  is the angular velocity of the body and  $\vec{x}_c$  is the cell centre.

Although the immersed boundary method implemented here satisfies the continuity near the solid wall, it is impossible to guarantee absolutely no penetration of flow through the walls, as the forcing term is proportional to the fluid velocity. Hence a different perspective is used for checking the correctness of the model; the mismatch between the velocity and the target velocity in cells marked as walls is evaluated in the domain. In all of the cases presented in this thesis, this error is less than 2%, hence it is acceptable for practical applications. The validation of the immersed boundary model is provided in Appendix C.

### 3.4.2 Integration of IBM into turbulence equation

In this thesis, the IBM approach is only used with  $k - \omega - SST$  turbulence model. It is to be noted that, this is not a limitation of the model, the IB model presented in this thesis can also be used in combination with other RANS and LES turbulence models.

The source terms in the turbulence equations, Eqs. (3.33) and (3.34) are defined such that it satisfies the conditions of  $k = 0$  and  $\omega \rightarrow \infty$  (higher value of  $10^{15}$  in this study) close to the wall where there is less turbulence. This is achieved by defining the source terms for turbulent kinetic energy ( $k$ ) and specific dissipation ( $\omega$ ) as,

$$S_k = -\frac{\rho_m C}{dt} \alpha_{IB} (k - 0) \quad (3.47)$$

$$S_\omega = -\frac{\rho_m C}{dt} \alpha_{IB} (\omega - 10^{15}) \quad (3.48)$$

## Chapter 4

# Numerical simulation of cavitation and primary atomization using the fully compressible three-phase model

In this chapter, the application of the fully compressible three-phase (liquid, vapour, and air) model for simulating the in-nozzle cavitation effects on liquid atomization is presented. The numerical model employs a combination of the homogeneous equilibrium barotropic cavitation model with an implicit sharp interface capturing volume of fluid (VOF) approximation. The numerical predictions are validated against the experimental results obtained for injection of water into the air from a step nozzle, which is designed to produce asymmetric cavitation along its two sides. Simulations are performed for three injection pressures, corresponding to three different cavitation regimes, referred to as cavitation inception, developing cavitation, and hydraulic flip. Due to the lack of experimental data, a quantitative comparison between the numerical and experimental prediction have not been possible. Hence, the model validation is achieved by qualitative comparison of the cavitation, spray pattern, and spray cone angles. The flow turbulence in this study is resolved using the large-eddy simulation approach.

Table 4.1: Boundary conditions used for the simulation

Inlet pressure ( $p_{in}$ ) <sub>abs</sub> in bar	Mean Velocity of water in the nozzle $V_n$ in m/s	Reynolds number
2.0	13.5	64586
3.0	18.3	89540
5.0	25.9	126727

## 4.1 Simulation cases and setup

Computations have been performed on the step-nozzle configuration of (1) for which experimental data for the in-nozzle flow and the near-nozzle atomization are available. The geometry of the nozzle and the computational domain is shown in Fig. 4.1.

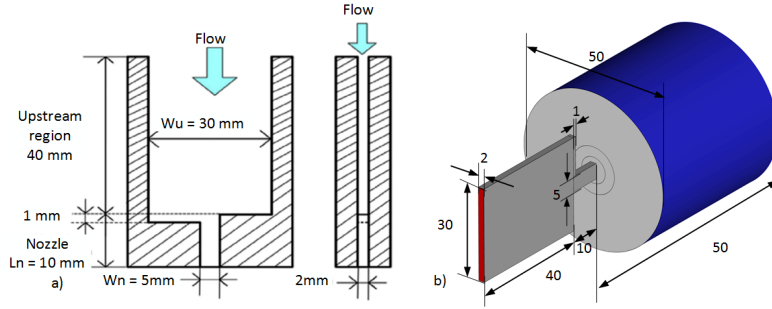


Figure 4.1: a) Step- Nozzle geometry as reported in Abderrezzak and Huang (1) b) Computational domain with boundary conditions; walls (grey), inlet (red), and outlet (blue). All dimensions are in millimetres.

In order to visualize the evolution of the liquid jet, the flow field is initialized with zero velocity throughout the domain while constant pressures are applied at the inlet and outlet boundaries. The extended cylindrical region at the exit is initialized with 100% gas volume fraction ( $\alpha_g = 1$ ) to model the presence of ambient air.

Pressurized tap water at 293 K is injected through the nozzle to ambient air at 1 bar and then gravitated to a buffer tank. In order to model the injection into ambient air, a cylindrical section with length 10 times the width of the nozzle passage is included. The nozzle has a non-uniform inlet with a step of 1 mm on one side, to trigger an asymmetry to cavity formation. The absolute value of the inlet and outlet pressure are set corresponding to the experimental conditions presented in (1). The absolute pressure at the outlet is fixed at 1 bar and the inlet total pressure is adjusted to match different static pressures between inlet and outlet. The boundary conditions used for the current simulations are listed in Table 4.1. It should be noted that since the flow rate measurements were

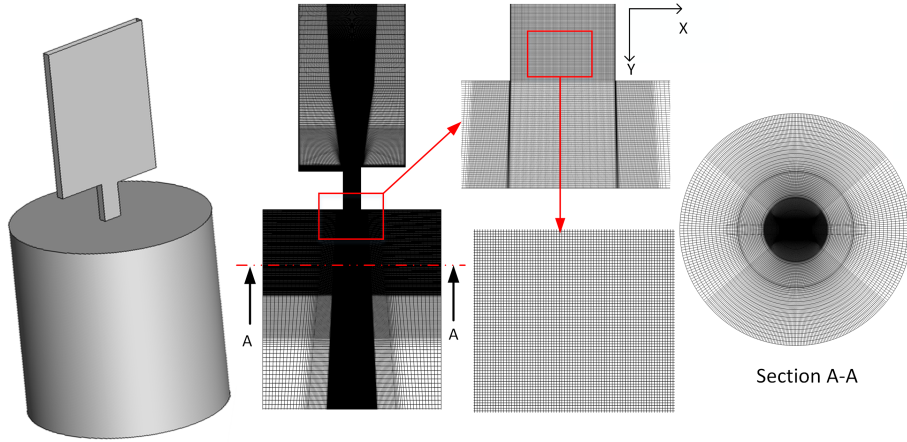


Figure 4.2: Details of the computational mesh.

not reported in the reference paper and the pressure measurements are reported further upstream, a correction of  $0.5 \text{ bar}$  is applied at the computational inlet to compensate for the pressure drop in the inlet tubing system. The inlet pressure is calibrated such that the cavitation regimes are matched between the experiments and computations.

The computational mesh used for the simulation is shown in Fig. 4.2. A block-structured mesh with appropriate refinement near the walls is used to ensure  $y^+ < 1$ . The initial estimate of the mesh resolution for LES simulation is calculated based on the Kolmogorov (Eq. (4.1)) and Taylor time (Eq. (4.2)) and length (Eq. (4.3)) scales (refer to (170; 29; 63; 52)):

$$\mu_k = (\nu^3/\epsilon)^{\frac{1}{4}} \sim 0.84\mu\text{m} \quad (4.1)$$

$$\tau_\mu = (\nu/\epsilon)^{\frac{1}{2}} \sim 0.7\mu\text{s} \quad (4.2)$$

$$\gamma_g = \sqrt{10}Re^{-0.5}L \sim 48\mu\text{m} \quad (4.3)$$

In the above equations,  $\nu$  is the kinematic viscosity of water ( $\sim 10^{-6} \text{ m}^2/\text{s}$ ),  $\epsilon$  is the turbulent dissipation calculated as  $u^3/L$ , with  $u$  being the average velocity through the nozzle and  $L$  the characteristic length (width of nozzle =  $5 \text{ mm}$ ). In order for the mesh resolution to be sufficient for all the inlet pressures values considered, the flow parameters (such as average velocity) at the extreme condition is used. In this study, an average velocity of  $22.2 \text{ m/s}$  corresponding to a pressure difference of  $5 \text{ bar}$  across inlet and outlet as reported in (1) is considered.

Based on these calculations, the spatial resolution at the core of the nozzle is kept equal to  $40\mu\text{m}$  and the near-wall resolution is kept to  $1.8\mu\text{m}$  resulting

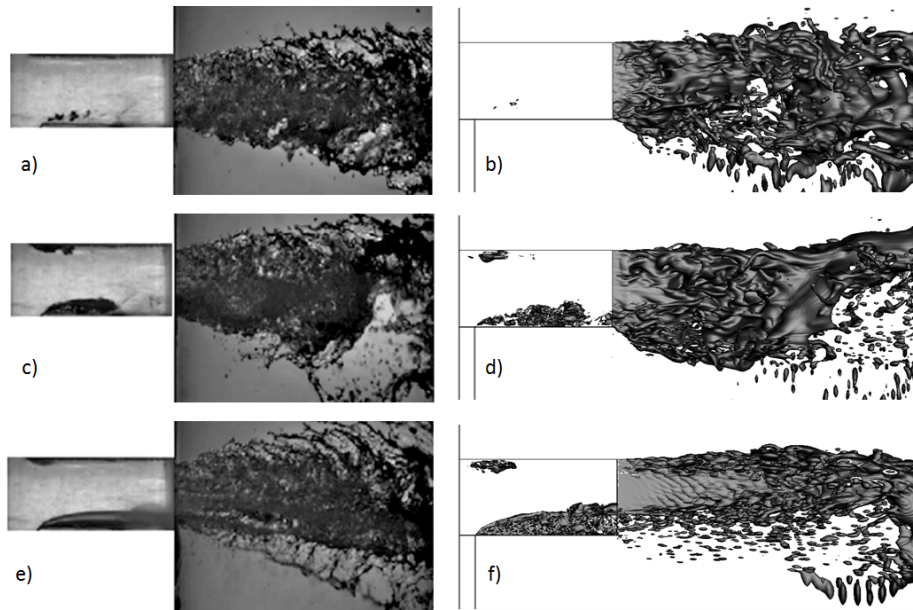


Figure 4.3: Comparison of in-nozzle cavitation and near-exit spray formation between experimental results from Abderrezzak and Huang (1) and current numerical study. (a, b) 2 bar (c, d) 3 bar (e, f) 5 bar inlet pressure. Iso-surfaces of mixture density at  $100\text{kg}/\text{m}^3$  shown at a random time instant

in 5-8 elements in the viscous sub-layer. With the estimated spatial resolution ( $< 48\mu\text{m}$ ) in the core and near the exit of the nozzle, the total mesh count in the domain sums to  $\sim 15$  million cells. The time resolution is controlled by using an adaptive time-stepping method so as to maintain the Courant - Friedrichs - Lewy (CFL) number to be less than 0.8 throughout the computational domain.

In the results that follow, the variables are made non-dimensional based on the mean velocity inside the nozzle corresponding to each condition (reported in Table 4.1) and the width of the nozzle ( $W_n$ ). Using this approach the non-dimensional time takes the form ( $\tau = tV_n/W_n$ ).

## 4.2 Results and Discussion

### 4.2.1 Comparison of in-nozzle cavitation and spray with experiments

A comparison of the in-nozzle flow and the near-exit spray formation between the experimental results from (1) and the present computations are shown in Fig. 4.3. The results are presented for three different injection pressure condi-

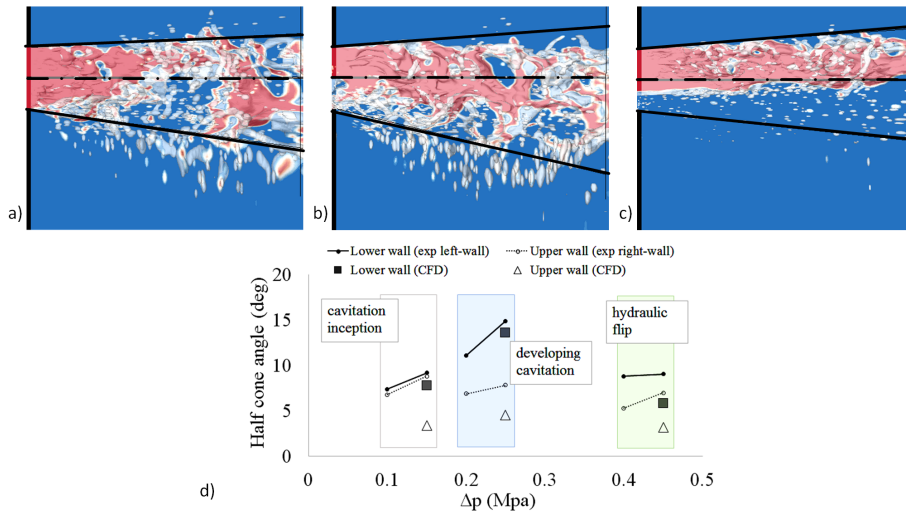


Figure 4.4: Spray cone angle for a) 2 bar, b) 3 bar and c) 5 bar injection pressure with transparent iso-surface of 95% of gas volume fraction and d) comparison with the experiments from Abderrezzak and Huang (1).

tions, each corresponding to three different cavitation regimes. The first condition considered in this study corresponds to the case where cavitation inception occurs (at 2 bar injection pressure). The inception of vapour cavity is observed from the lower wall with very little or no cavitation from the upper wall. The results presented in Fig. 4.3 confirm that the liquid jet atomises faster on the cavitating side of the step-nozzle as more ligaments and droplets forming on this side. Looking to the second condition at 3 bar, the cavity formed at the inlet corner of the lower wall extends up to 70% of the nozzle length while cavity formation is also seen from the upper wall (see Fig. 4.3(c,d)). Under this condition, periodic shedding of vapour clouds is observed from both corners. With the increase in the intensity of cavitation, a wider jet with finer droplets is formed. Compared to the experiments, the numerical simulation also shows the entrainment of ambient air moving backwards inside the orifice. As the injection pressure is further increased to 5 bar, hydraulic-flip is observed, as the liquid is completely separated from the lower wall allowing for ambient gas to flow inside the nozzle, as depicted in Fig. 4.3(e and f). The qualitative comparison shows a good match between the experimental results and simulations for all conditions.

#### 4.2.2 Half-cone angle

Figure 4.4 shows the half cone angle measured for the spray for the three conditions presented in this study. The half-cone angle is the maximum angle measured between the nozzle axis and the outer edge of the spray. It can be



noticed from this figure that the cone angle on the lower wall is larger than that on the upper wall, primarily due to cavitation. This angle increases with an increase in injection pressure. This is again related to the increase in cavitation. During the hydraulic-flip, the cavitation disappears from the lower wall and a drastic reduction in the cone angle can be observed in Fig. 4.4c. A comparison with the results presented in (1) shows a good correlation of the half cone angles from the lower wall. On the other hand, the cone angle predicted for the upper wall is always lower compared to the experimental values for all conditions presented. However, the trend of increasing cone angle with increasing injection pressure and a break down at hydraulic flip remains consistent with what is observed in the experiments (see Fig. 4.4d). The reason for the variation between the simulation and experiments could be due to the difference in the way the cone angle is measured during experiment and simulation; also, these could be due to the variation in the geometric features, for example, a curvature at the exit plane of the experimental geometry can lead to a wider spray as compared to the sharp edges considered in the CFD model.

### 4.2.3 Evolution of in-nozzle flow and liquid jet

In this section, results are presented to show the in-nozzle flow effects on liquid jet evolution and atomization. The three conditions representing three cavitation regimes, namely, cavitation inception, developing cavitation and hydraulic flip are given in (Figs. 4.5 to 4.7). Results are further supported from the presentation of the iso-surfaces of the turbulent structure represented by the second invariant of velocity gradient tensor (Q-criterion) (171; 172) given in Fig. 4.8 - 4.10) for the three flow conditions, respectively. Positive values of the Q-criterion can be used for identifying vortices and the local rotational areas. The iso-surface of the Q-criterion with a value of  $10^9 s^{-2}$  coloured with velocity magnitude is plotted to identify the evolution of vortical structures inside the nozzle.

Cavitation inception is the condition at which the cavitation first occurs; the 2 bar case can be considered representative of this change in the flow (see, Fig. 4.5). As the flow progresses, the formation of a small vapour cavity can be observed from the sharp corner of the lower wall. This is then convected by the flow towards the nozzle exit and mostly collapses within the nozzle. Only a negligible amount of vapour formation is observed from the upper wall at this pressure condition. Turning now to the emerging jet evolution, during the early stages of injection, the formation of a mushroom-shaped liquid can be observed at the leading-edge due to the Rayleigh-Taylor instability caused by the density difference (173; 174). Further, the interaction between the large inertia liquid

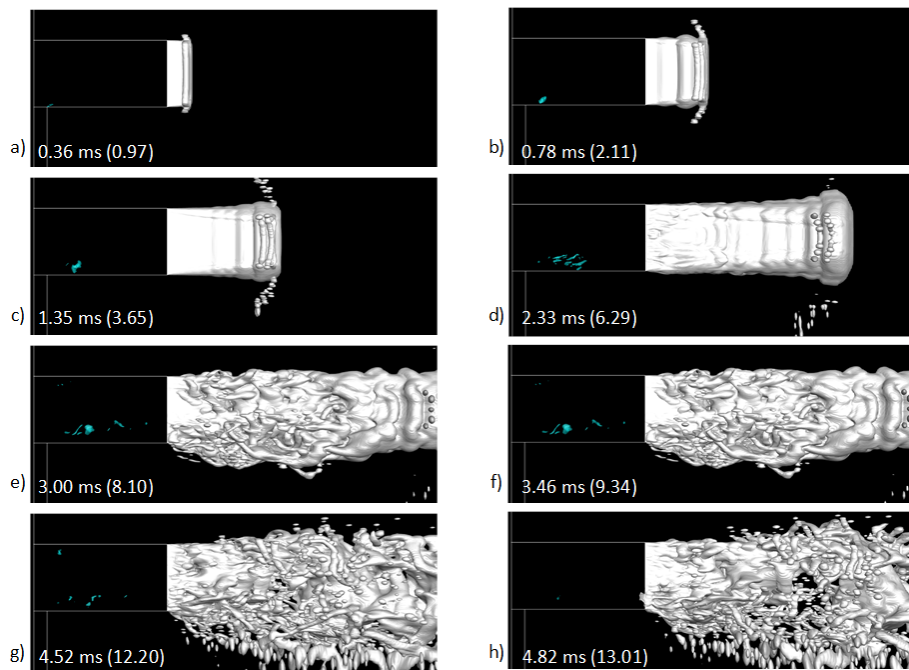


Figure 4.5: Instances of the evolution of in-nozzle cavitation and liquid jet disintegration at  $p_{inj}=2\text{bar}$ . Iso-surfaces of 50% vapour (cyan) and 95% gas (white) volume fraction shown. The instances are chosen randomly over the evolution to highlight the main features. (The non-dimensional time is given in brackets)

moving outwards and the ambient gas, shearing the liquid due to the pressure gradient at the jet front also assist in the mushroom formation (175). As the flow progresses, the mushroom grows in size and a larger recirculation zone of gas is created behind it. This recirculation initiates the necking of the jet behind the mushroom, which leads to the formation of droplets (Fig. 4.5 b-c). The formation of liquid droplets is first observed from the edge of the mushroom and later from the core of the liquid jet. The small circumferential waves seen around the liquid jet are initiated by the aerodynamic Kelvin-Helmholtz (K-H) instability developing at the liquid-air interface. It has been reported that the influence of aerodynamic forces on the primary breakup of the liquid jet is negligible if the density ratio (ratio of liquid over air density) is greater than 500. In such flow, the breakup is primarily due to the liquid turbulence (176). In the present study, the density ratio is 1000; with almost no cavitation occurring at this pressure condition, the breakup of the liquid jet can be primarily attributed to liquid turbulence. The turbulent structures inside and outside the nozzle are depicted in Fig. 4.8 by plotting the Q-criterion. The interaction of the turbulent structures with the liquid jet surface initiating the disruption of the liquid core can be seen while comparing two time instances, one at an early stage when turbulent structures are still inside the nozzle where the liquid surface only shows K-H waves (Fig. 4.5c and Fig. 4.8b) and another instance when the turbulent structures leave the nozzle and interact with the liquid-air interface, where the interface becomes irregular leading to the formation of ligaments (Fig. 4.5d and Fig. 4.8c). The collapse of the vapour clouds that are convected beyond the nozzle exit further assists in the disintegration of the liquid; formation of liquid ligaments can be observed in Fig. 4.5e onwards. Due to the asymmetry in the geometry creating more cavity formation from the lower wall, the formed spray is spreading more in the direction of the lower wall. Widening of spray cone angle with increasing cavitation has been observed in other experimental studies; see for example (1),(177),(178).

A developing cavitation with the periodic shedding of vapour cavities is seen when the injection pressure is increased to 3bar; the process is depicted in Fig. 4.6. As expected, the cavitation from both walls increases with an increase in injection pressure. The sheet cavity formed from the sharp inlet edge of the bottom wall quickly transforms into small vortices, which are then transported by the flow. The variation in vortex transport velocity causes these vortices to merge to form cavity clouds, at approximately  $1/3^rd$  downstream from the nozzle inlet. This can be seen in Fig. 4.6(b-d). The merging of the vortices in a similar way was also observed for flow over a hydrofoil (179) and was reported as highly erosive when they collapse close to the wall surface. The clouds shedding from the lower wall can travel till the nozzle exit or even further beyond the

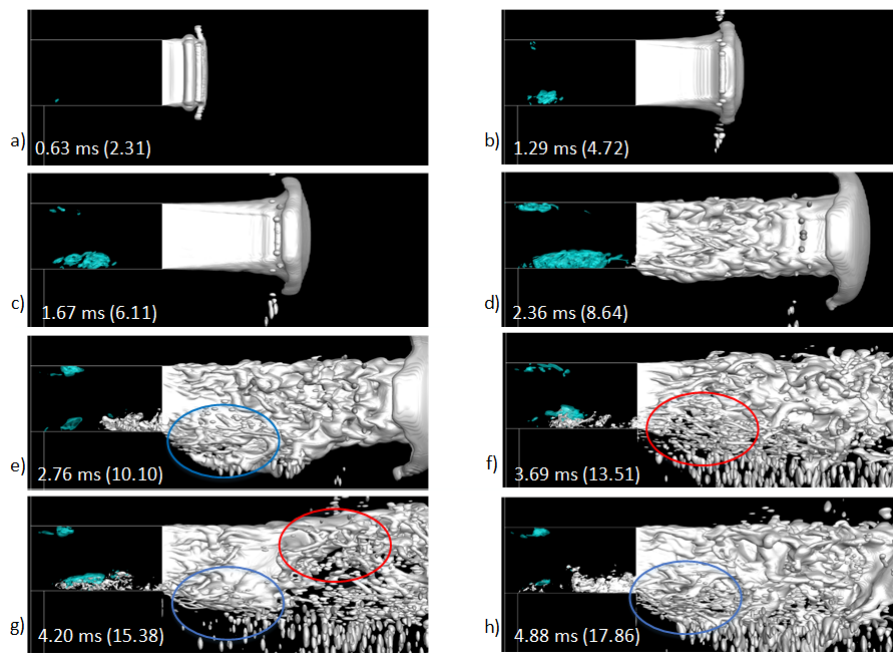


Figure 4.6: Instances of the evolution of in-nozzle cavitation and liquid jet disintegration at  $p_{inj}=3\text{bar}$ . Iso-surfaces of 50% vapour (cyan) and 95% gas (white) volume fraction shown. The instances are chosen randomly over the evolution to highlight the main features. The thinning and widening of the liquid jet are highlighted using red and blue circles. (The non-dimensional time is given in brackets)

exit into the chamber before collapsing. When the cloud reaches the nozzle exit, the low pressure inside the cloud pulls the ambient air into the nozzle pushing the liquid away from the wall, as shown in Fig. 4.6(d, e). A similar phenomenon of air entrainment into the nozzle from the chamber was reported in the experimental work of (180) in a multi-hole injector. However, it was attributed to the low-pressure core of the liquid vortex that pulls the air into the nozzle; whereas in the present study, it is attributed to the low-pressure at the exit due to the presence of vapour cloud similarly to (96) and (92). The increase of shear force at the liquid-air interface due to the upstream movement of the air pulls the liquid jet outwards, causing a wider spray opening inside the chamber, as shown in Fig. 4.6e with blue circles. Later, due to the reduction in the effective flow area at the nozzle exit caused by the entrained air, a narrower jet is created, a trace of which is highlighted with a red circle in Fig. 4.6(f, g). This process is further illustrated in Fig. 4.11. The reduction in flow area is compensated by an increase in bulk flow velocity in this region. The restricted flow causes the pressure to build up upstream and this pushes the air back, see Fig. 4.6(e to g). During this event, the momentum of the jet is increased and widening of the liquid jet can be observed again in Fig. 4.6g (highlighted with blue circle). A similar observation was also made by (96), where the dynamic change in the spray cone angle is reported over time. In short, during developing cavitation, a periodic phenomenon of air entering and leaving the nozzle have been observed along with two events of spray widening and one event causing a reduction in spray width. The early evolution of the jet under this condition is like the previous 2 *bar* case. The formation of a mushroom-shaped jet front and the initial droplet formation from its circumference can be also observed under this condition. However, the mechanism of the jet atomization, in this case, is primarily due to cavitation and air entrainment. Due to the increased velocity of the jet, the disintegration of liquid jet occurs earlier and closer to the nozzle exit.

At 5 *bar* injection pressure, complete separation of the liquid flowing over the sharp edge corner of the lower wall is observed (Fig. 4.7). This condition is typically known as "hydraulic-flip". The higher injection pressure forces the flow to accelerate more around the nozzle inlet resulting in more vapour generated from both walls. Unlike the other two conditions presented, the formation of a sheet cavity can be seen from both walls at this pressure condition. The sheet cavity formed from the upper walls grows roughly up to 40% of the channel length until the re-entrant jet moving upstream cuts the sheet structure to form vapour clouds, Fig. 4.7(d, e). On the other hand, the cavity sheet formed from the lower wall grows and extends until the nozzle exit without shedding. As the cavity sheet reaches the exit, ambient air enters the nozzle, as observed in the

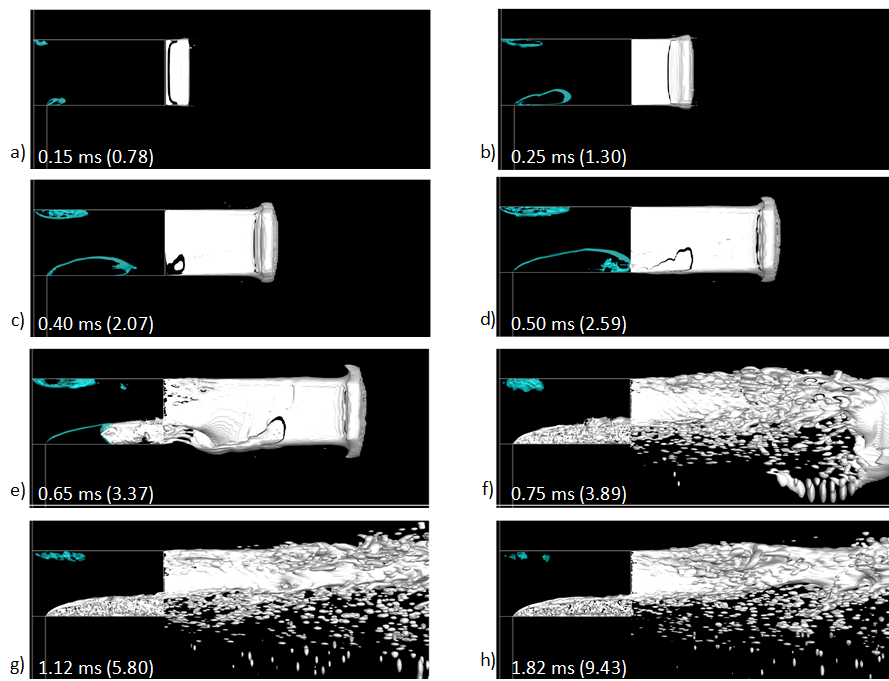


Figure 4.7: Instances of the evolution of in-nozzle cavitation and liquid jet disintegration at  $p_{inj}=5\text{bar}$ . Iso-surfaces of 50% vapour (cyan) and 95% gas (white) volume fraction shown. (The non-dimensional time is given in brackets)

previous 3bar injection pressure case. This time, air penetrates till the leading edge of the lower wall, fully replacing the liquid from the wall. However, here the entrained air is not pushed back by the flow and is continuously present inside the nozzle. The presence of air suppresses cavitation from the lower wall. The liquid jet formed at this condition remains intact for a longer distance with the mushroom shape formation occurring further downstream compared to aforementioned conditions. The disintegration of the liquid jet, in this case, is primarily due to cavitation; this is first observed when the vapour cloud collapses inside the jet. The width of the liquid jet reduces drastically with the liquid core inclined more towards the upper wall due to the partial hydraulic-flip, meaning hydraulic-flip occurring only on one wall. A similar observation was also made by (48) in their experimental study on a step-nozzle with the same length to width ratio as the current one ( $L/W = 1.8$ ) when partial hydraulic-flip occurs.

#### 4.2.4 In-nozzle turbulence

The influence of turbulence on the atomization is demonstrated using the Q-criterion with a value of  $10^9 s^{-2}$ , coloured with the non-dimensional velocity magnitude for the three injection pressures considered. The initial formation of spanwise vortices, stretching of vortices in the longitudinal direction and its subsequent transformation into hairpin vortices can be seen in Figs. 4.8 to 4.10. To highlight the influence of turbulence on jet disintegration, a picture of the jet interface corresponding to that time is given as a subset of (b, c). The (Figs. 4.8 to 4.10)(a, b) corresponds to an early time instant where the in-nozzle turbulent structures are within the nozzle. At this condition, the jet interface only shows evidence of K-H waves. When the turbulent structures leave the nozzle, it interacts with the interface producing more disturbances on the interface initiating disintegration of the jet as can be seen from (Figs. 4.8 to 4.10)c. The presence of the entrained air in the nozzle close to the bottom wall produces more turbulence in this region, Fig. 4.9d and Fig. 4.10d.

#### 4.2.5 Effect of air entrainment on jet

This section describes the process of air entrainment, primarily focusing on the events leading to widening and narrowing of the spray at  $p_{inj}=3 \text{ bar}$ . During one air entrainment cycle, two events causing an increase in the spray width and one event causing a reduction in spray width are observed. The first widening events occur during the air entrainment into the nozzle and the other during the push-back from the nozzle. These events are depicted in Fig. 4.11 using contours of velocity magnitude at selected time instances. As described above, the presence of the low-pressure vapour cloud at the nozzle exit pulls the ambient air into the

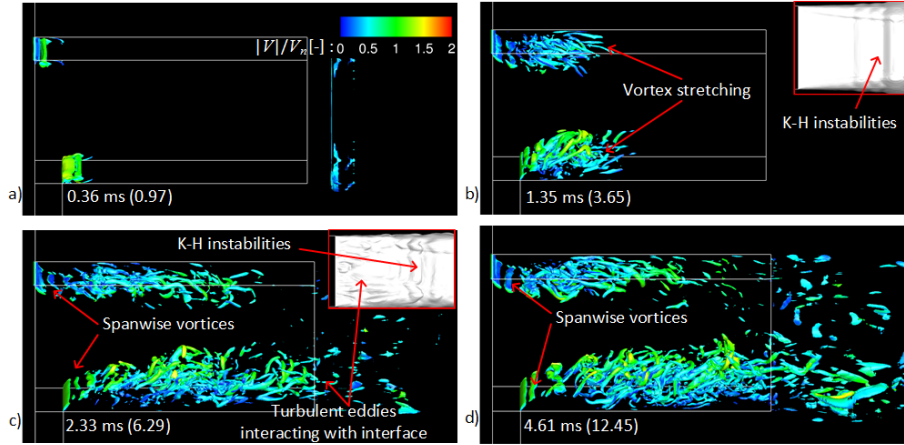


Figure 4.8: Instantaneous isosurface of Q-criteria showing vortex cores (value of  $10^9$ ) coloured by non-dimensional velocity magnitude at  $p_{inj}=2\text{bar}$ . (The jet interface close to the nozzle exit is shown in subset).

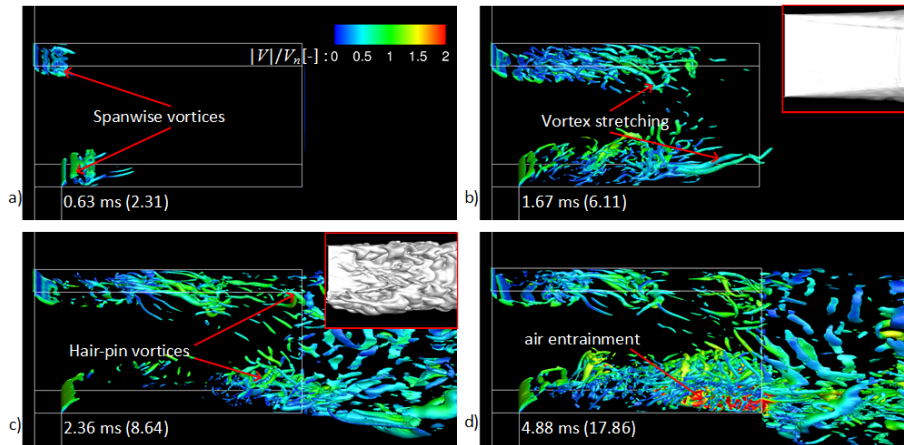


Figure 4.9: Instantaneous isosurface of Q-criteria showing vortex cores (value of  $10^9$ ) coloured by non-dimensional velocity magnitude at  $p_{inj}=3\text{bar}$ . (The jet interface close to the nozzle exit is shown in subset).



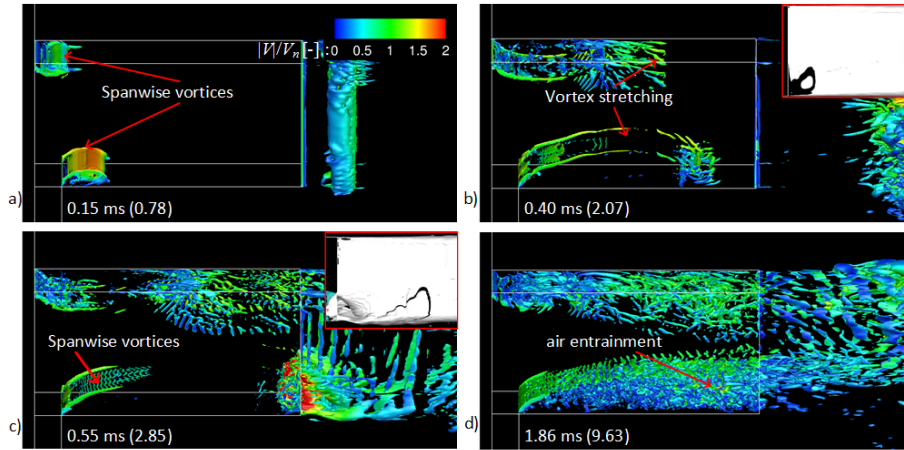


Figure 4.10: Instantaneous isosurface of Q-criteria showing vortex cores (value of  $10^9$ ) coloured by non-dimensional velocity magnitude at  $p_{inj}=5\text{bar}$ . (The jet interface close to the nozzle exit is shown in subset).

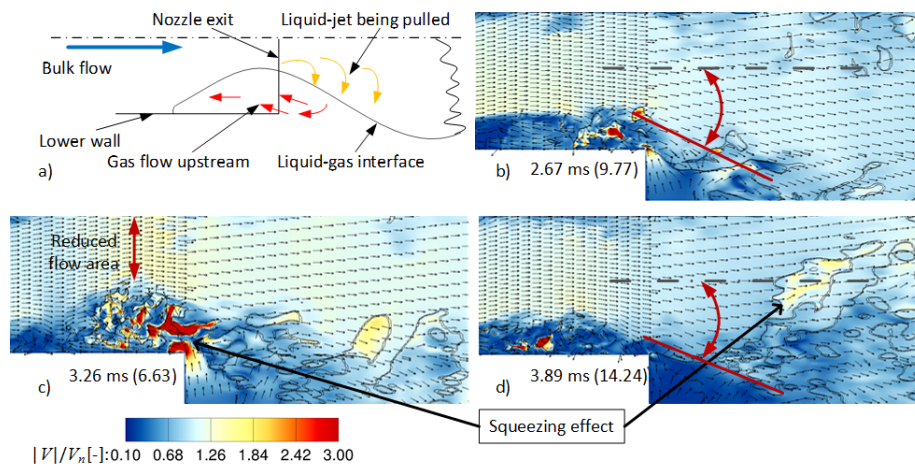


Figure 4.11: Contours of non-dimensional velocity magnitude with iso-lines of 95-99% gas volume fraction. a) Pictorial representation of the first spray widening event. (b, d) shows the widening of spray and c) shows the reduction in spray width. (the vectors shown are not up to scale they are used as an indicator of flow directions).

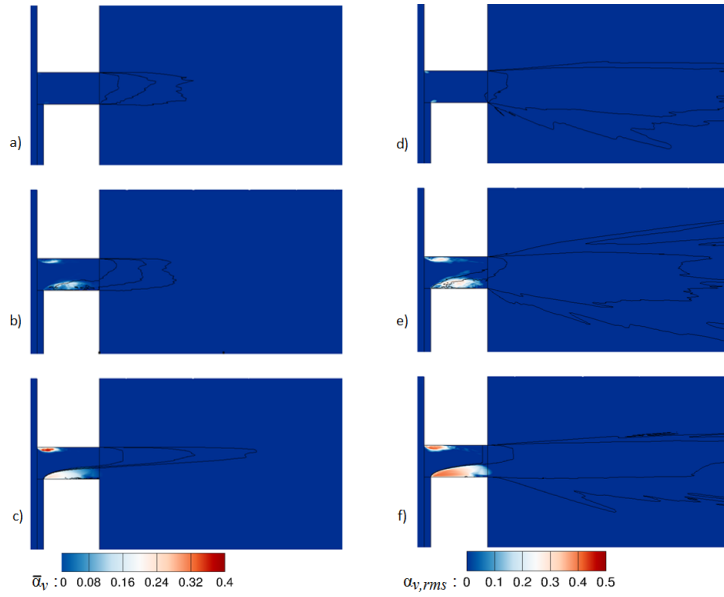


Figure 4.12: Contours of (a-c) average and (d-f) rms vapour volume fraction with iso-lines of mean and rms gas volume fractions respectively ranging from 0.1 - 0.5 at (a, d) 2bar, (b, e) 3bar and, (c, f) 5bar injection pressure.

nozzle by displacing the liquid away from the wall. The increase in shear force at the liquid-air interface due to the upstream movement of the air pulls the liquid jet away from the nozzle axis, increasing the spray angle, as can be seen from Fig. 4.11b; a pictorial representation of this process is also given in Fig. 4.11a. Figure 4.11c shows a condition when the air occupies the maximum width of the channel during the pushed-out event, while the entrained air shifts the liquid to a maximum distance away from the bottom wall, causing a constriction in the flow and a narrower jet formation. The widening of the spray is again observed when the air is pushed back by the flow. The liquid quickly fills the recovered flow area creating an additional component of velocity in the downward direction thereby increasing the spray angle, shown in Fig. 4.11d. The process of air entrainment and push-out occurs over a time-period of approximately 1.1 *ms* (computed based on two cycles) and the process is repeated over time. The high-velocity pockets observed in the velocity field is the result of air getting squeezed by the liquid-air interface. The squeezing effect during the atomization was also observed by (96).

#### 4.2.6 Time-averaged fields

Figure 4.12 shows the average and rms field for the vapour volume fraction obtained from the statistics collected over 3 *ms*. The vapour volume fraction

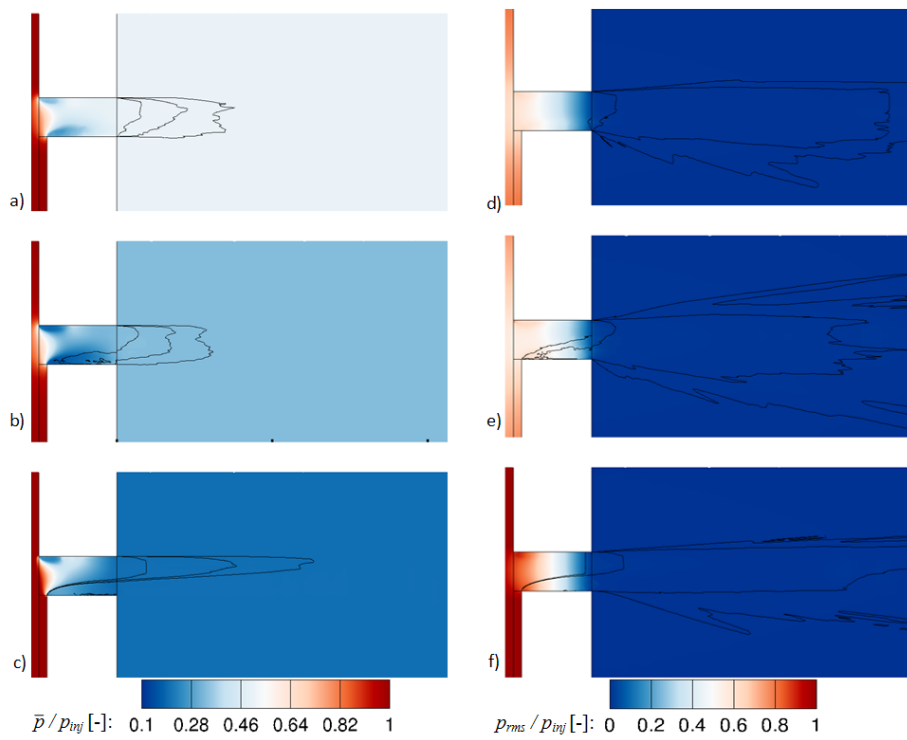


Figure 4.13: Contours of mean and rms absolute pressure normalised with the injection pressure and iso-lines of gas volume fraction ranging from 0.1 - 0.5 at (a, d) 2bar, (b, e) 3bar and, (c, f) 5bar injection pressure.

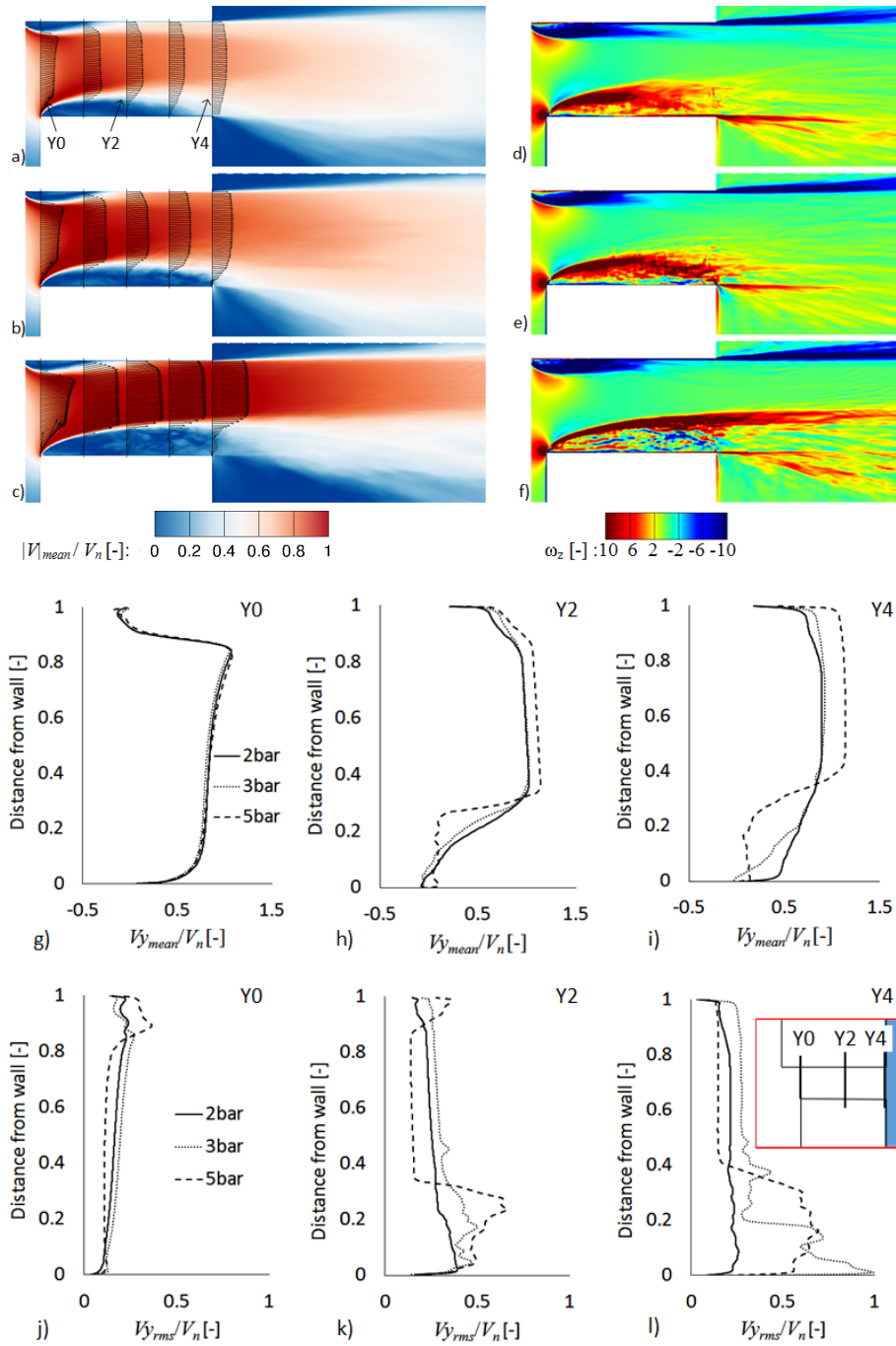


Figure 4.14: Contours of average velocity magnitude and z-vorticity; (a, d) 2bar, (b, e) 3bar and, (c, f) 5bar injection pressure. (g-i) shows the mean streamwise velocity distribution and (j-l) shows the rms of streamwise velocity at Y0, Y2 and Y4 locations

clearly shows an increase in average cavitation development with a rise in injection pressure. There is only a negligible amount of vapour cavity formation at 2 *bar* injection pressure (with a max volume fraction of 0.02 near the inlet edge). From 3 *bar* to 5 *bar*, an increase in the intensity and the spread of cavitation is visible, due to the increased acceleration of the flow near the inlet corner. The predicted rms values of the vapour volume fraction are larger than the mean values, which implies a highly fluctuating cavity. Similar observations can also be made for the gas entrainment into the nozzle, with no entrainment at all at  $p_{inj}=2$  *bar* to almost 70% towards the inlet at 3 *bar* and up to the inlet at 5 *bar*. The constriction caused by the entrained gas causes the pressure to build upstream and results in increased flow velocity as can be seen in Figs. 4.13 and 4.14. The non-dimensional mean and fluctuating velocity profile calculated at three locations (nozzle inlet Y0, mid-nozzle Y2, and nozzle exit Y4) are shown in Fig. 4.14(g-l). The flow recirculation due to the separated flow from the upper wall is captured as negative values at the top edge of Y0 for all the pressure conditions. The asymmetry in the nozzle results in the velocity distribution inclined more towards the upper wall, thus forcing the separated boundary layer from this wall to reattach quickly, before it reaches the mid-channel. Whereas, the flow separated from the bottom wall reattach at about  $1/10^{th}$  before the nozzle exit for 2 *bar* and almost at the exit for 3 *bar*. At 5 *bar*, the separated shear layer from the bottom wall never reattaches. The velocity profile observed for 5 *bar* injection pressure shows a different behaviour compared to the other cases. The averaged field show a wavy vertical profile up to 20% of the nozzle width at the mid-plane (Y2) and the mean velocity at the exit plane (Y4), close to the bottom wall is lesser than the other cases, Fig. 4.14(h, i). This is due to the upstream motion of the entrained air during hydraulic-flip. Similarly, the entrainment of the gas also produces highly fluctuating velocity field near the bottom wall which is evident from the rms velocity profile shown in Fig. 4.14(j-l) with maximum fluctuations occurring at 3 *bar* injection pressure near the nozzle exit.

The instantaneous field of the flow velocity and the vorticity at the mid-span (*z*-plane) of the nozzle for 5 *bar* injection pressure are shown in Fig. 4.15, highlighting the mid and the near exit region of the nozzle. A closer look at the figure reveals that in addition to the water getting separated from the inlet, the air entering the nozzle through the exit also separates from the exit corner and reattach to the wall before reaching the mid-section of the nozzle. This creates a recirculation zone of air near the nozzle exit leading to the velocity distribution shown in Fig. 4.14i. The shear force between the liquid jet, the entrained gas and small droplets created in the near-wall separated region enhances turbulent production and a large number of smaller eddies are generated as can be seen

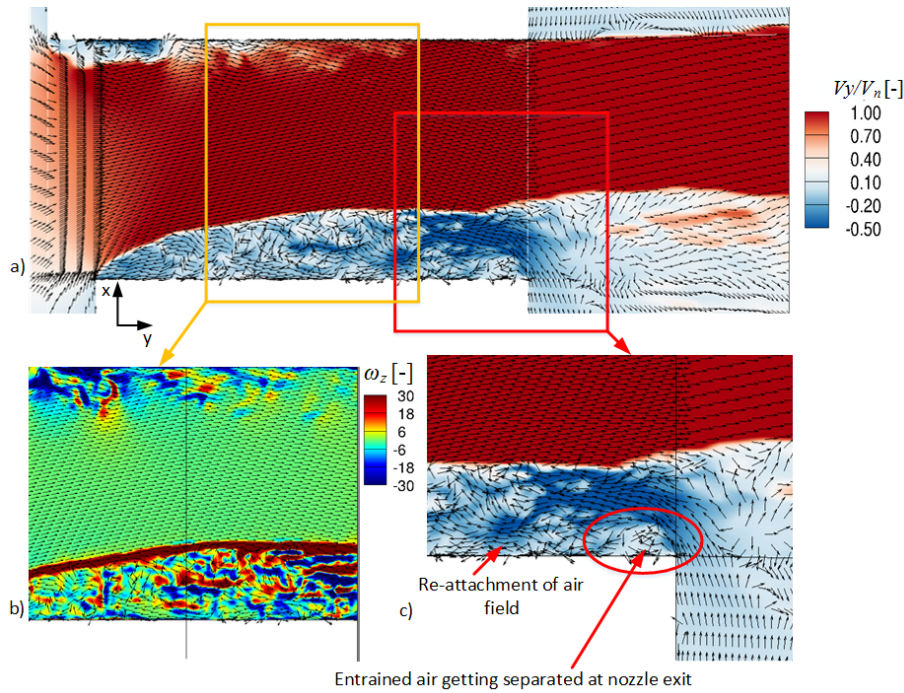


Figure 4.15: Instantaneous contours of (a,c) flow velocity in y-direction showing the flow separation of liquid from inlet edge and ambient gas from the exit edge of the bottom wall, (b) the instantaneous vorticity contours at 5bar injection pressure.

from Fig. 4.15b and the mean vorticity contours shown in Fig. 4.14f. The wavy velocity profile inside the separated shear layer in Fig. 4.14h is the result of the continuous presence of these counter-rotating eddies.

#### 4.2.7 Surface area generation

The quantification of the primary atomization is achieved by integrating the surface area of 50% gas volume fraction over a volume of interest as a function of time. The results obtained from the integration is plotted against the non-dimensional time ( $\tau = tV_n/l_{ref}$ ) for the three cavitation regimes in Fig. 4.16. The surface area is non-dimensionalized using the cross-sectional area of the nozzle. The integration is performed over the region shown in "blue" (i.e. up to six times nozzle width ( $W_n$ ) downstream from the nozzle exit), where the mesh is refined enough to capture the primary atomization. At the start of injection, only the leading edge of the jet is exposed to ambient air and the surface area calculated is close to zero. The increase in surface area is observed at two different rates (two different slopes of the curve). The initial slope of the curves corresponds to the increase in surface area generation due to the formation and

expansion of the mushroom and the exposure of the liquid core to the ambient air due to liquid penetration with time. Further increase in the slope is observed at the start of the liquid core disintegration (observed at  $\tau \sim 2.48$  for 5 *bar*,  $\tau \sim 7.74$  for 3 *bar* and  $\tau \sim 6.89$  for 2 *bar*). The surface area increases until the jet front reaches the end of the blue region (up to which integration is performed), after which the curve drops due to the front mushroom leaving out of the integration domain (line L1). For 5 *bar* injection pressure, the start of air entrainment occurs at the non-dimensional time  $\tau \sim 2.48$  where the liquid bulk disintegration starts (where the slope increases) and the flow go into complete flip at  $\tau \sim 4.25$ . At this time instant, the jet front is still within the integrating region and the surface area continue to increase due to the combined effect of primary atomization, the expansion of the mushroom front and the jet penetration (up to L1 where  $\tau \sim 6.21$ ). As the jet front leaves the domain ( $\tau \sim 6.21$ ), there is a sudden drop in the surface area. The surface area calculated after this time can be directly related to the primary atomization. Since there are no significant changes observed in the flow field at 5 *bar* after hydraulic-flip, the integral surface area remains almost steady thereafter. Similar characteristics for the curves are also observed for the other two cases, both showing two slopes, one corresponding to the expansion of the leading-edge mushroom and jet penetration and the other due to the additional surface area generation arising from the disintegration of the liquid core. Since the cavitation and the air entrainment, occurring at 5 *bar* and 3 *bar* injection pressures promote atomization, a much steeper slope is observed at these conditions compared to 2 *bar* where less cavitation and no air entrainment occurs. The start and end of the air entrainment occurring at 3 *bar* injection pressure are highlighted in the figure as SoAE and EoPO (Start of Air Entrainment and End of Push-Out), respectively. Unlike the previous case of 5 *bar* injection, at 3 *bar* injection pressure, the air entrainment is a cyclic process. As pointed out earlier, the air entrainment cycle improves the atomization and as a result, a rise in surface area is again observed from SoAE-2 till EoPO-2 during the second entrainment cycle. From Fig. 4.16, for the three conditions considered, it can be concluded that the developing cavitation (3 *bar*) is the most favourable and hydraulic flip is the least favourable condition for primary atomization.

### 4.3 Chapter Summary

A numerical framework for modelling the co-existence of three-phases namely liquid, vapour and non-condensable gas has been developed. The model was



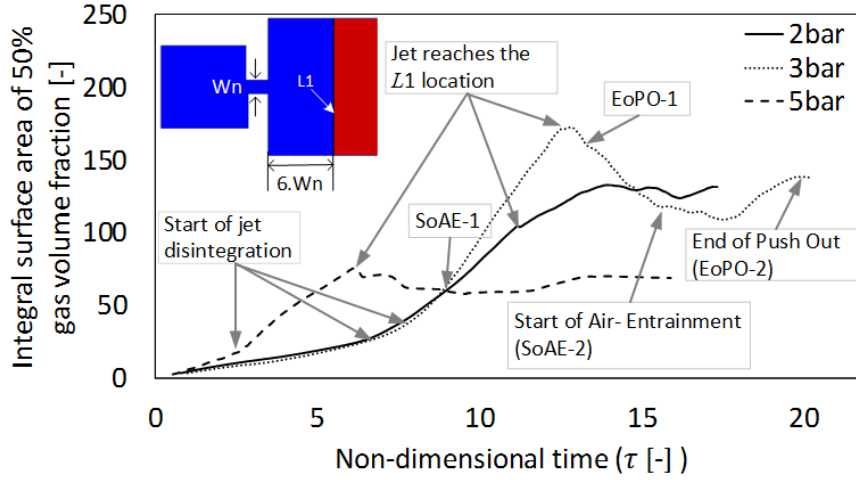


Figure 4.16: Non-dimensional surface area generation (an approximate measure of primary atomization) at different injection pressures. The region where integration is performed is highlighted in blue (in the inset).

utilised to study the effect of in-nozzle flow parameters, such as cavitation, on primary atomization of a liquid jet. A homogeneous equilibrium based barotropic approach is used for modelling cavitation, combined with a sharp interface Volume of Fluid (VoF) method to complete the three-phase system. A wall adaptive LES was used for resolving turbulence.

The results from the simulations have been compared with the experimental results from (1) for three different cavitation regimes, namely cavitation inception, developing cavitation and hydraulic flip. From the analysis, it has been observed that the disintegration of the liquid jet is influenced mainly by four factors: in-nozzle cavitation, the entrainment of air into the nozzle, the turbulence generated and partially due to the aerodynamic instabilities. The formation of the droplets is first observed from the mushroom edge due to Rayleigh-Taylor instabilities and later from the liquid core due to the combined effect of cavitation, turbulence and Kelvin-Helmholtz instabilities. Liquid ligaments are formed when the vapour cloud collapses near the liquid-air interface. At cavitation inception, the atomization is primarily due to liquid turbulence and aerodynamic instabilities. Whereas at developing cavitation, in addition to the above parameters, the cavitation and the air entrainment into the nozzle plays the major role. The air entrainment into the nozzle is periodic when developing cavitation occurs. During one entrainment cycle, the spray cone angle is increased twice improving the atomization. Due to the asymmetry in the nozzle geometry, a partial hydraulic flip occurs at 5 bar injection pressure, suppressing the vapour formation from the lower wall completely. At this condition, the atomization



and the subsequent spray cone angle is drastically reduced.

From the observed results for three cavitation regimes considered, it can be concluded that the developing cavitation is the most favourable condition for effective atomization and wider spray. However, merging of vortices forming highly erosive potential vapour clouds has also been observed at this condition. Hence, there should be a trade-off between the cavitation-assisted atomization and erosion while designing an efficient nozzle. This study provides new insights in the less explored area of atomization by providing a framework for simultaneous simulation of the in-nozzle flow and primary atomization by utilising a barotropic model for cavitation, a surface tracking model for atomization and LES model for turbulence resolution.

## Chapter 5

# Numerical simulation of fuel dribbling and nozzle wall wetting on VCO injector with eccentric needle motion

In this chapter, the application of the combination of the compressible 3-phase model and the immersed boundary model (IBM) for simulating the dribble formation and the wall wetting during the start of injection (SOI), end of injection (EOI), dwell time and the subsequent start of injection (SSOI) is studied. The Navier-Stokes equations are numerically solved in a six-hole VCO type injector imposing realistic conditions of the valve movement and considering in addition to the axial motion of the needle valve, a time-dependent eccentric motion. The valve motion is simulated using the immersed boundary method; this allows for simulations to be performed at zero lift during the dwell time between successive injections, where the needle remains closed. Moreover, the numerical model utilises a fully compressible 3-phase (liquid, vapour, air) barotropic model, where the barotropic fluid, is in thermal and mechanical equilibrium with the air. The air's motion is simulated with an additional transport equation coupled with the VOF interface capturing method able to resolve the near-nozzle atomisation and the resulting impact of the injected liquid on the oleophilic nozzle wall surfaces. Mathematical models are also included for considering the surface tension and wall-adhesion. The  $k - \omega - SST$  model with the correction

for turbulent viscosity is used for resolving turbulence.

The outline of this chapter is as follows. A description of the problem including the meshing, operating and boundary conditions are discussed in Section 5.1. After that the validation of the numerical model is presented in Section 5.2, the result and discussions for the injection scenarios considered (start of injection, end of injection, dwell time and the subsequent start of injection) are presented in Section 5.3. In the final section (Section 5.4), a summary of the chapter is provided.

## 5.1 Problem description

The simulations are performed on a 6-hole valve covered orifice (VCO) with eccentric needle motion. The geometry of the VCO and the details about the computational domain and numerical grids are shown in Fig. 5.1. The computational domain is extended at the outlet body of the injector in order to model the combustion chamber in the vicinity of the nozzle exit; this is initialized with 100% NCG at the beginning of the simulation. The inlet and outlet boundaries are applied with a constant absolute pressure of 1600 *bars* and 60 *bars*, respectively. The computational domain is discretized using hexahedral elements with telescopic boundary layer refinements near the wall to maintain the  $y^+$  values close to 1 suitable for  $k - \omega - SST$  model. The computational domain is split into two regions: one within the interior of the injector nozzle and the other which is exterior to the injector where the diesel is injected. Since the main focus of this study is to predict the dribble formation and wall surface wetting caused by the dribbles near the orifice exit at needle closure, special attention was given to the mesh resolution near the needle seat and the orifice exit. In particular, a resolution of  $0.5\mu m$  is applied near the needle seat and  $1.75\mu m$  near the orifice walls. In addition to that, the mesh near the exit is refined using a non-conformal mesh as shown in the subset of Fig. 5.1b. The resolution at the core of the orifice is in the range of  $5\mu m$ . The same resolution is used in the near nozzle region which allows liquid fragments larger than  $5\mu m$  to be simulated. To minimise the computational cost, the nozzle downstream is meshed with larger aspect ratio elements which could influence the shape of the droplets. With these refinements, the total mesh count is approximately 10 millions cells with  $\sim 6$  million inside the injector and  $\sim 4$  million cells outside of the injector. On the other hand, the resolution for the temporal discretisation is chosen such that the Courant number is in the range of unity ( $CFL \sim 1$ ). In the present study, the motion of the needle in three dimensions are pre-defined and their profile is shown in Fig. 5.2. The data file with the time series is interpolated by the immersed boundary model to extract the location of the needle

at any time instant. The physical properties of the diesel used are given in Table 3.2.

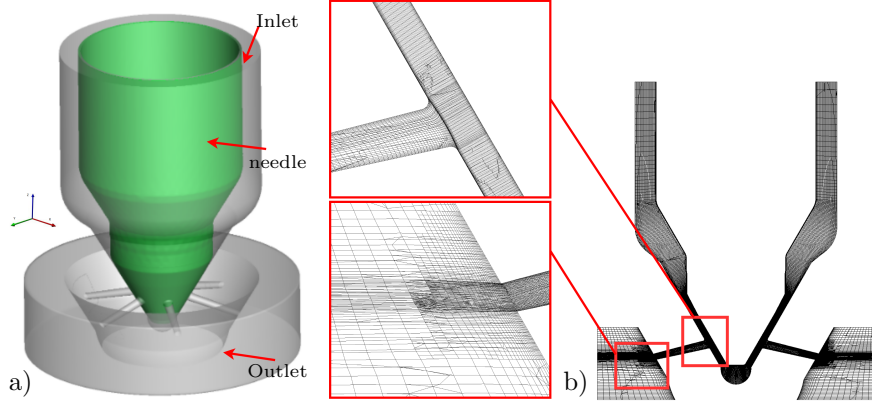


Figure 5.1: a) VCO geometry and b) cross-section of the hexahedral mesh highlighting the mesh details near orifice entrance and exit. Telescopic refinement near the wall to ensure  $y^+ \sim 1$

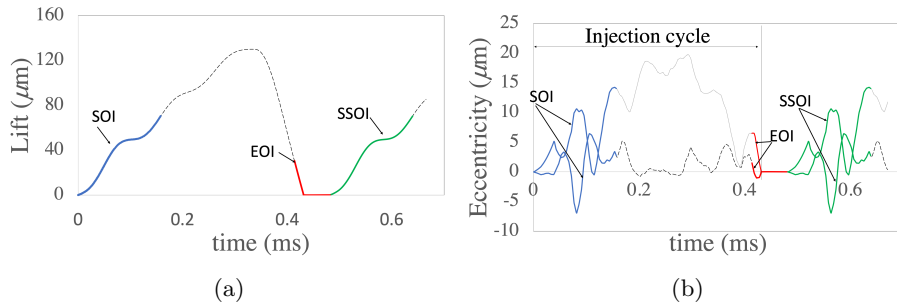


Figure 5.2: a) Needle lift profile and b) eccentricity in x (dashed) and y (dotted) direction as reported in Gold et al. (2). Start of Injection (solid blue), End of Injection (solid red) and Subsequent Start of injection (solid green).

## 5.2 Validation of the model

The validation of the three-phase model with the experimental results of primary atomization from a step-nozzle is presented in the previous chapter (also published; see (102; 181)). Further, the numerical results from the VCO nozzle simulations are compared with the experimental visualization from (2). The comparison between the numerical and experimental studies show a good correlation between them (see Fig. 5.3).

In addition to that, the applicability of the numerical model with moving geometry is further validated against the experimental data obtained for a single

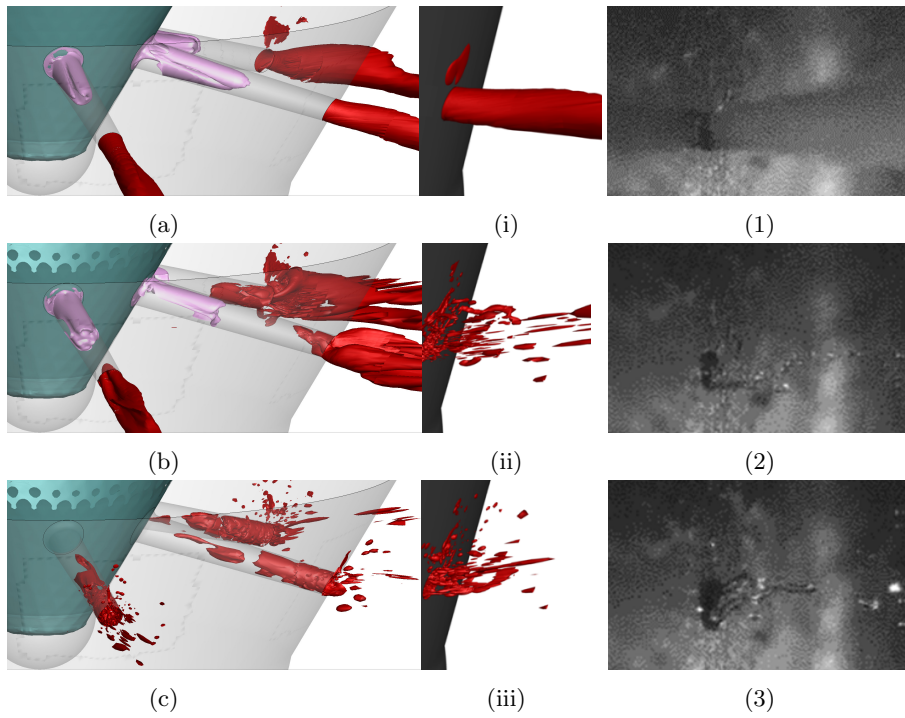


Figure 5.3: Validation of the numerical model showing the liquid jet break-up during end of injection. (a, b, c) and (i, ii, iii) are the results from current simulation matching the experimental visualisation, (1, 2, 3) are the experimental results from Gold et al. (2) at  $800\mu s$  ASOI,  $1000\mu s$  ASOI and  $1100\mu s$  ASOI. Isosurface of 90% gas volume fraction (red) and 50% vapour volume fraction (pink) is shown.

hole nozzle (7); these correspond to a modified single-hole transparent nozzles manufactured with the same hole inlet radius and diameter as in Engine Combustion Network Spray D nozzle with the body and needle geometry of an ECN Spray A nozzle. The nozzle geometry used for this purpose is shown in Fig. 5.4. The nozzle is imposed with an upstream pressure of 500 bar and a downstream pressure of 1 bar. The needle motion profile used by the authors of (7) is shown in Fig. 5.4b. The results are validated against the experimental observations during the start of injection transients. To replicate the experimental conditions, the model is initialized with diesel fuel inside the nozzle and ambient gas inside the circular chamber.

The qualitative validation of the events during the start and end of injection shown in Figs. 5.5 and 5.6 is in good match with the experimental results. The numerical model predicts the retraction of the liquid and the formation of the leading-edge umbrella during the start of injection (Fig. 5.5), and the bulk cavitation and gas pullback during the end of injection (Fig. 5.6) as observed in the experiment.

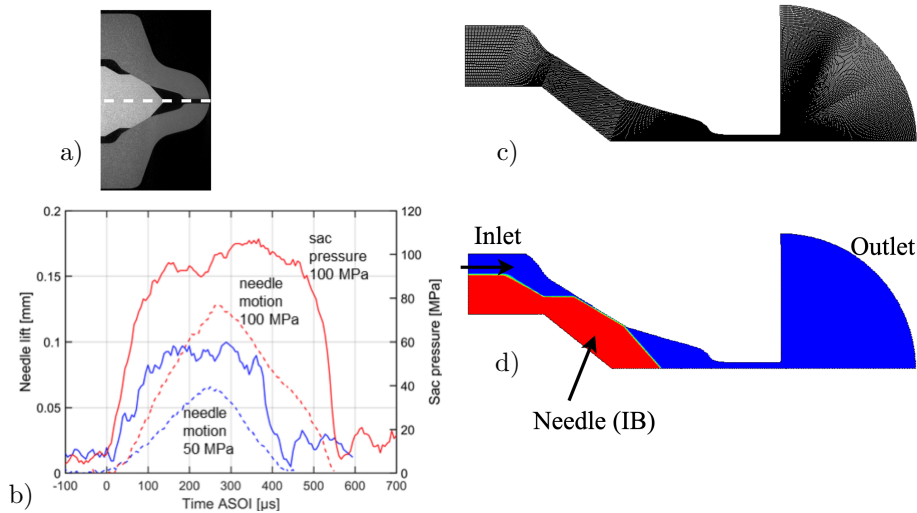


Figure 5.4: a) Single hole ECN Spray D nozzle, b) Needle motion profile as obtained from Manin et al. (7) for different injection pressure c) The hexahedral numerical mesh showing the extended circular chamber and d) IBM representation of the needle (in red).

### 5.3 Results and discussion

In this section, the obtained results are presented for the three conditions considered during the operation of the injector nozzle. The dynamics of the flow

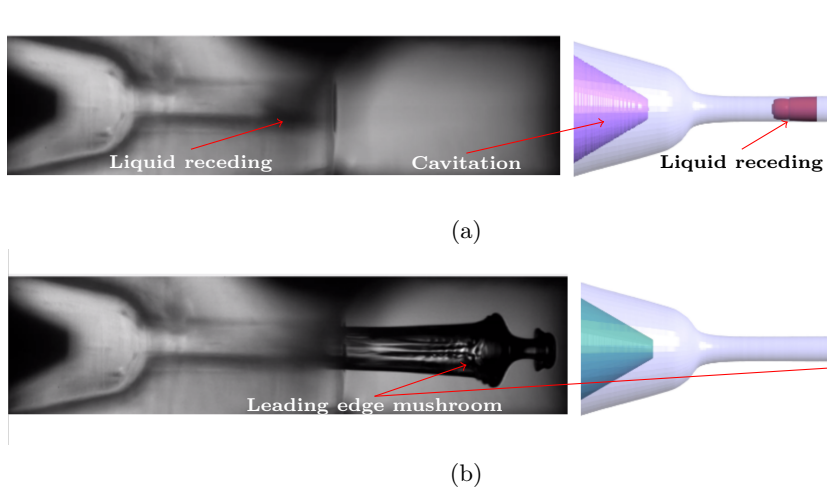


Figure 5.5: Validation of the numerical model with the experimental results from Manin et al. (7) during the start of injection event

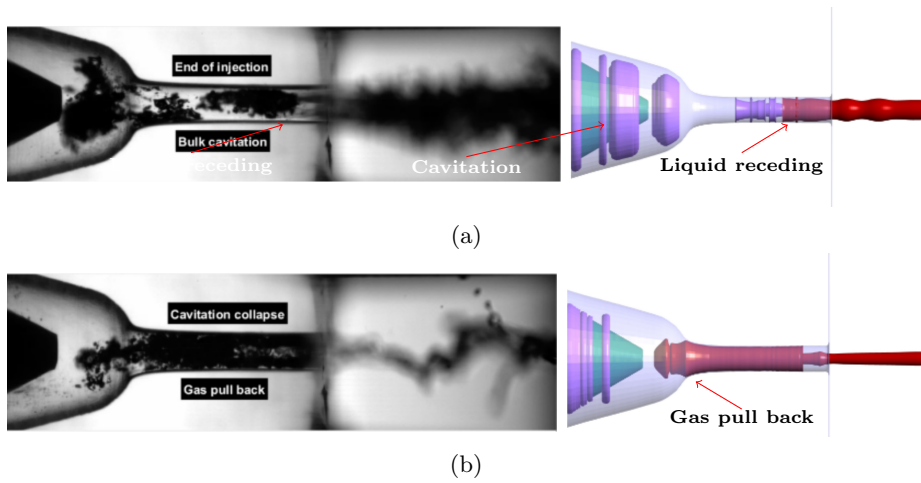


Figure 5.6: Validation of the numerical model with the experimental results from Manin et al. (7) during the end of injection event

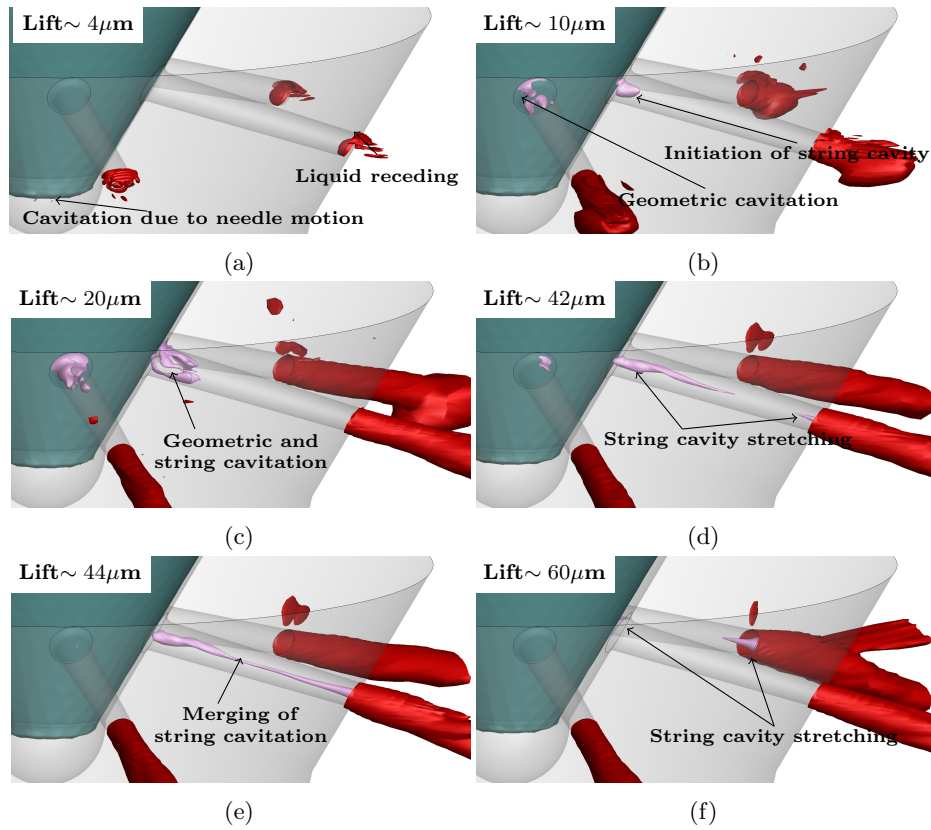


Figure 5.7: Evolution of diesel jet and formation of cavitation during the start of injection showing the development of geometry-induced cavitation and the stretching of string cavitation during the needle opening. Isosurfaces of 90% gas volume fraction (red) and 50% vapour volume fraction (pink) is shown.

inside the orifices and the development of the spray during the start of injection from a clean nozzle is presented first. The flow during the end of injection and after the needle closure (dwelt), which shows the near-nozzle fuel dribbles is presented next, followed by the simulation of the subsequent start of injection.

### 5.3.1 Start of Injection (SOI)

In this section, the flow development inside and outside the nozzle orifice during the start of injection is presented. During the start of injection, the nozzle orifice is assumed to be filled with diesel and the gas is present only in the engine chamber. The needle rests on its seat sealing the flow between the inlet and outlet. The SOI simulation is performed for a needle lift upto  $70\mu\text{m}$  starting from a fully closed condition as depicted in Fig. 5.2 following the solid blue line.

When the needle lifts from its initially closed position, the suction created



due to the sudden acceleration of the needle pulls in a small amount of air from the combustion chamber into the orifice (Fig. 5.7a), forming a concave liquid front inside the orifice. The sudden opening of the needle also produces local counter-rotating vortices just below the needle valve, resulting in the formation of cavitation bubbles at this location, also shown in Fig. 5.7a. With the further lifting of the needle valve, the fuel slowly recedes into the orifice. The backward flow of the air stops and the forward motion of the fuel towards the orifice exit starts when the needle lift reaches approximately  $5\mu m$  for this specific nozzle design. At this low lift, the high pressure at the inlet produces highly accelerated flow in the gap between the needle and nozzle walls, which is sufficient to generate cavitation at the inlet edge (see Fig. 5.7b at  $10\mu m$ ). At the same time, the formation of a mushroom-headed jet can also be seen outside the orifices (Fig. 5.7b). The penetration of the liquid jet into the combustion chamber and the formation of cavitation occurring in each orifice correspond to different rates, due to the hole-to-hole flow variations caused by the eccentric needle motion. Further lifting of the needle valve induces a highly swirling flow inside the orifice holes and result in the formation of vortex cavitation in addition to geometric-induced cavitation realized at the hole inlet, as can be seen from Fig. 5.7c onwards. Both the vorticity-induced and geometry-induced cavitation stretch and merge along the orifice axis resulting in the formation of string cavities as the needle lifts further (Fig. 5.7d and Fig. 5.8b). Two types of string vortices are particularly noted, one that originates from the orifice inlet towards the outlet and the other which starts from the air downstream towards the upstream direction, as highlighted in Fig. 5.7(d, f); a similar formation of string cavitation from an enlarged VCO was also observed by (51) in their experimental study. The two string vortices from both ends stretch towards each other and merge to form a single long string cavity starting from the needle towards the combustion chamber, as shown in Fig. 5.7e. A more detailed view along with the streamlines showing the swirling flow and the formation of string cavitation at the core of this vortices is shown in Fig. 5.8. These string cavities are dynamic and are observed in pairs simultaneously from orifices O-3, O-5 and O-4, O-6 at different needle lifts, starting from  $\sim 40\mu m$ . Two such instances showing the development of string cavities from orifice pairs are given in Fig. 5.8(b, c). The simulation of SOI is terminated at  $\sim 70\mu m$  needle lift where the cavitation does not appear inside the nozzle any further and no large scale oscillations appear on the diesel jet.

Focusing on the flow outside of the nozzle, when the needle lifts-off from its seat, the high injection pressure at the inlet forces the diesel fuel to flow out of the orifice into the combustion chamber. As the flow progresses, the diesel jet forms a leading-edge umbrella with surface instabilities in the form of spike-like

structures emanating from the head of the umbrella, as it can be seen from Fig. 5.9i and also evident from the microscopic images obtained by (2) (in the subset of Fig. 5.9i). The downward inclination of the orifices (see the subset of Fig. 5.9a) induces higher acceleration at the upper half of the orifice compared to the lower half, causing an umbrella front to be stretched more in the upper half. As the needle valve lifts further, allowing more flow into the nozzle, the diesel jet penetrates into the chamber against the air, forming large ligaments and droplets from its periphery. The initial droplets formed are larger in size and non-spherical in shape. It is observed that some of these initial droplets formed lose their momentum and tend to stick to the nozzle wall, due to wall adhesion, as shown throughout in Fig. 5.9. When the slow-moving liquid droplets come in contact with the oleophilic surface of the nozzle, the surface tension causes them to contract and leave them in the near nozzle region leading to surface wetting. This phenomenon is captured in the present study using a wall adhesion model, as proposed by Brackbill et al. (165) which specify a fixed contact angle as a dynamic boundary condition to the outer wall of the nozzle. Sticking of these droplets to the wall is observed near all six orifice exits. However, the number of droplets sticking, and the duration of their existence are different for each orifice, due to hole-to-hole variations in the flow. These droplets remain as a residual fuel from the injection and act as a locally rich mixture near the wall.

### 5.3.2 End of Injection (EOI)

The red solid lines in the profile shown in Fig. 5.2 represents the region for which the end of injection simulation is performed. The downward motion of the needle is performed until its complete closure; the simulation is further continued for  $50\mu s$  at the closed condition in order to capture the phenomena occurring after the needle closure.

The dynamics of flow during the EOI is shown in Fig. 5.10 to Fig. 5.12 using iso-surfaces of vapour volume fraction and the NCG inside and outside of the nozzle orifices. As the needle valve closes, the rapid deceleration of the liquid jet and the reduction in the diesel supply causes the continuous liquid jet to break and form poorly atomized large fuel ligaments. The closure of the needle creates a highly swirling flow inside and outside the orifice along its axis, as it can be seen from Fig. 5.10 and Fig. 5.11 for selected orifices; the streamlines plotted in Fig. 5.11 clearly shows the swirling motion present in the orifices. This swirling motion and the continuous reduction in diesel flow rate due to the needle closure causes the jet to form a membrane-like structure with diesel droplets starting to form at its periphery (see selectively Fig. 5.10(b-d) and Fig. 5.12i). The centrifugal force of the swirling jet pushes the droplets away

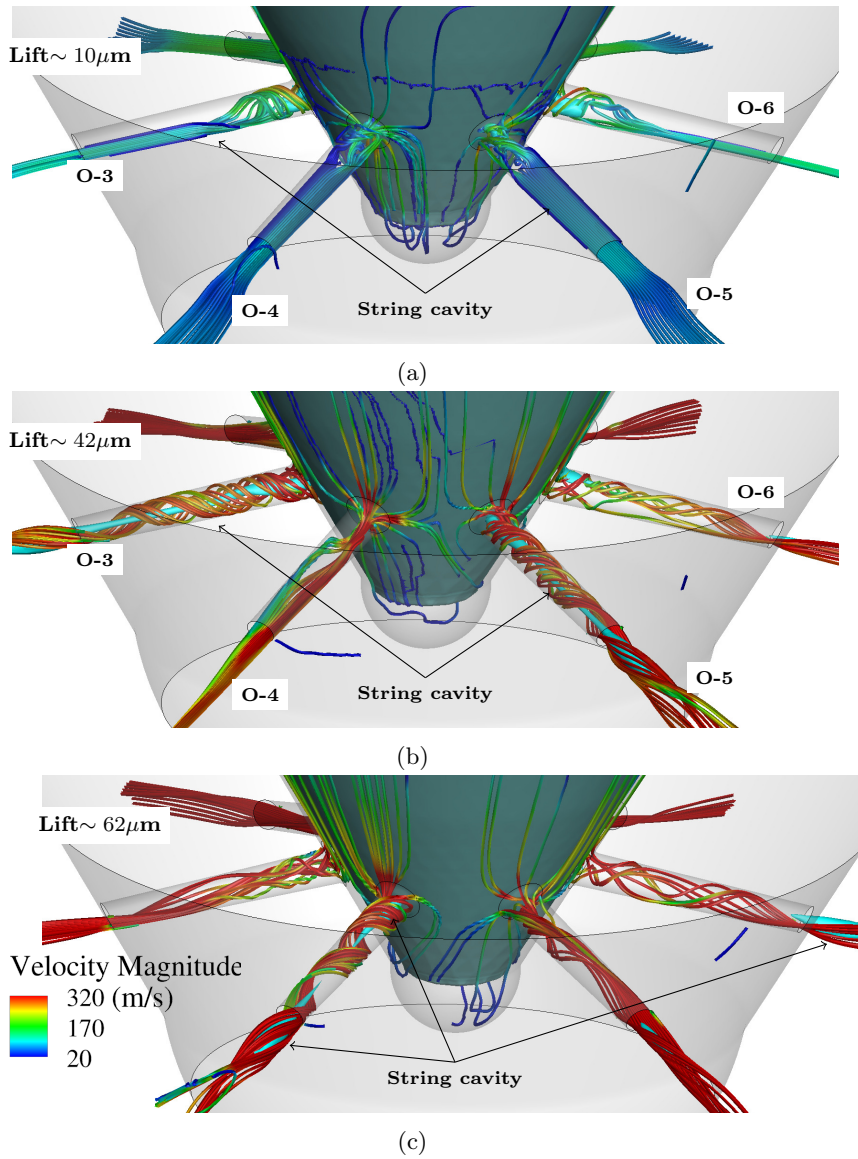


Figure 5.8: Detailed view of swirling flow and string cavitation at selected needle lifts during SOI. Streamlines colored with velocity magnitude and the isosurface of 50% vapour volume fraction shown in cyan.

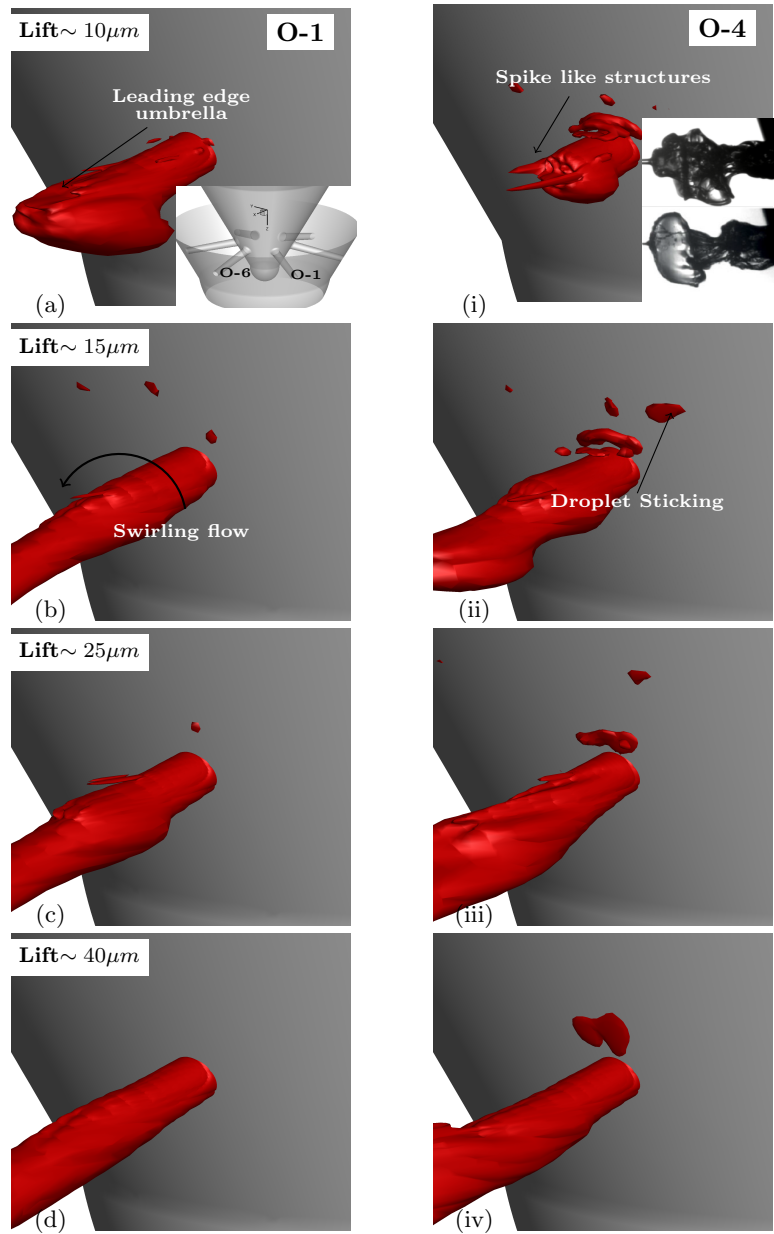


Figure 5.9: Drizzle formation during start of injection from a nozzle filled with diesel. Correlation with the experimental observation from Gold et al. (2) shown in the subset of (i). Isosurface of 90% gas volume fraction is shown in red. Figures are shown selectively for Orifices 1 and 4.

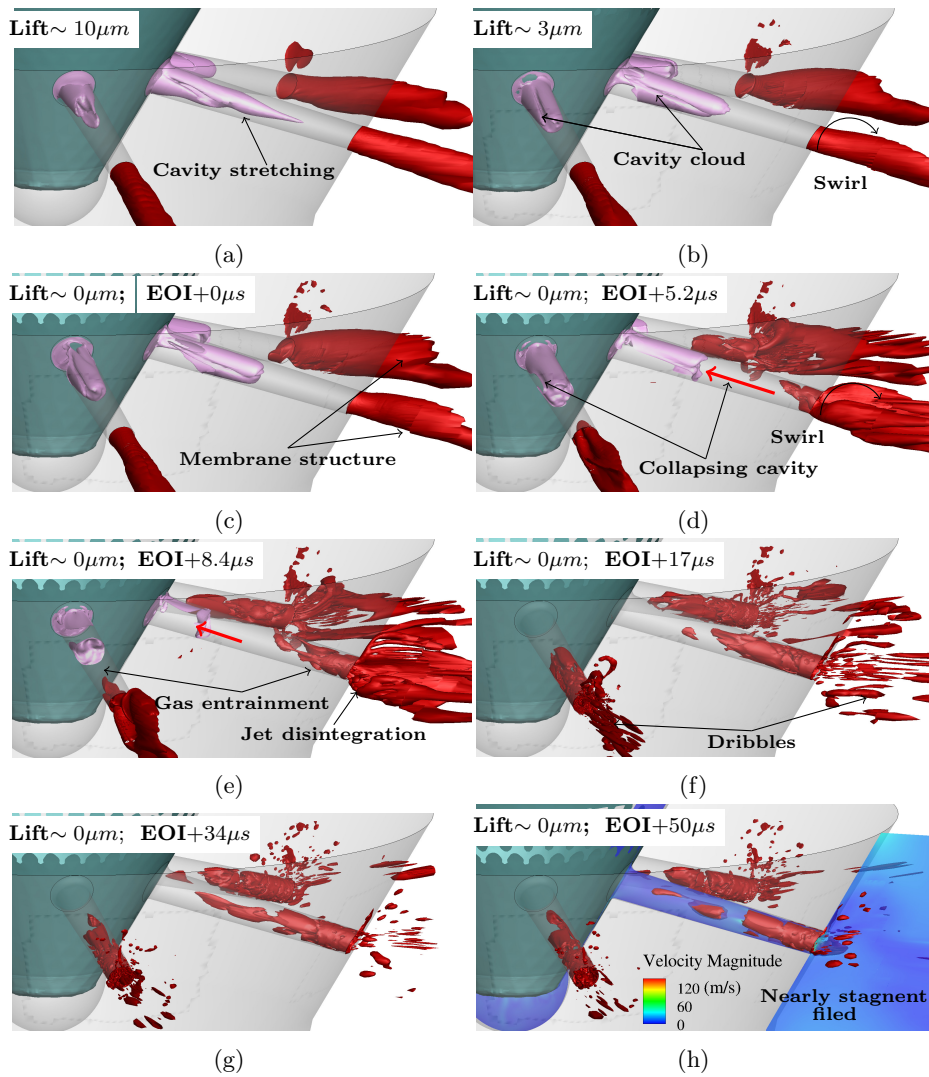


Figure 5.10: Break-up of diesel jet and cavitation formation inside the orifice during end of injection. The sequence shows the cloud cavity stretching and the entrainment of gas after the needle closure. Isosurface of 90% gas volume fraction (red) and 50% vapour volume fraction (pink) is shown.

from the jet axis. Depending on the local flow conditions, these droplets hit the wall of the nozzle and remain attached to the wall due to the wall adhesion causing wall-wetting, similar to that observed during the SOI. However, the number of droplets formed and the number of droplets sticking to the wall is much higher than those observed during the SOI. The formation of cavitation inside the orifice is also similar to that observed at SOI. Until  $\sim 30\mu\text{m}$  needle lift, the variations in the flow features inside the orifices are negligible as the influence of needle closure is still not evident. As the needle valves continue to close, a rapid deceleration of the flow is observed. At  $\sim 30\mu\text{m}$  needle lift, the geometric-induced cavitation starts to appear at the inlet of the injection holes. With further closure of the needle, the development of both geometric and vortex-induced cavitation, their merging and stretching along the orifice axis is observed. When the needle valve approaches its seat, i.e. at lift near  $\sim 10\mu\text{m}$  and below, a severe drop in the pressure is observed near the needle, with the minimum pressure reaching in the range of  $\sim 1000\text{ pa(abs)}$ ; this is much lower than the vapour pressure of the diesel fuel considered, thus forming localized cavitation zones near the orifice inlet; see Fig. 5.10(a, b). Unlike the narrow string cavitation formed during the SOI, the cavitation formed during the EOI is a more pronounced cavity cloud that covers almost the entire cross-section of the orifice, as can be seen from Fig. 5.10(a, b). The eccentric motion of the needle becomes more evident below this needle lift. With the needle valve covering some of the orifices more compared to the other due to its eccentric motion, the disintegration of the liquid jet from these orifices occurs earlier than from those which are less covered by the valve; this is evident while comparing the spray formation from orifices O-1 and O-4 in Fig. 5.12. Even when the flow is completely cut-off by the needle closure (EOI+0 $\mu\text{s}$ ), the liquid inside the orifices continue to flow outwards but slowed down from the pressure of the surroundings. Once the liquid bulk has lost its momentum, the back-pressure from the combustion chamber pushes the ruptured liquid inside the orifices back towards the inlet, recovering the pressure inside and collapsing the vapour cavities, as it can be observed from Fig. 5.10d onwards. Behind the ruptured residual liquid, large pockets of gas from the chamber also enters the orifices. The receding of the diesel, as well as the entrainment of gas into the orifice, is seen until the vapour cavity present in the orifice is completely collapsed, after which the entrained gas is found to oscillate due to the fluctuating pressure field. Such a pressure field oscillation after the end of injection was also reported by (7) on a single hole nozzle injector with supporting evidence in the form of slow-motion videos. The complete collapse of vapour cavities from the nozzle occurs about 17 $\mu\text{s}$  after the EOI in this particular nozzle; by then 50% of the orifice length is filled with the gas from the combustion chamber. After  $\sim 34\mu\text{s}$ ,

the velocity field becomes almost stagnant with only negligible flow oscillations inside the orifices and relatively small movement of droplets observed outside the orifices. The EOI simulation is stopped at  $\sim 50\mu s$  after the needle closure when the flow became stagnant everywhere in the computational domain; this can be seen from the contour of the velocity magnitude shown at a mid-plane of the orifice in Fig. 5.10(h). The compressible gas inside the orifices influences the subsequent injection process. The presence of gas voids inside the orifice before the start of injection was also observed by (100) in their experimental visualization from a real-size, multi-hole, transparent, sac-type injector. They reported that the bubble patterns observed are not repeatable and they can be found either as a single large or as multiple smaller bubbles. Given sufficient time, with repeated injection cycles, these bubbles can coalesce and form a large void that can occupy most of the sac volume.

### 5.3.3 Subsequent Start of Injection (SSOI)

The subsequent injection after the end of the previous injection cycle starts from a completely closed needle position where the liquid droplets are almost stagnant (at EOI+50 $\mu s$ ). The lift profile for this stage of injection is shown with the solid green lines in Fig. 5.2. At the SSOI, the orifice is partially filled with gas from the previous injection. The eccentricity in needle motion causing the orifices in the upper half being partially covered is evident from Fig. 5.13a. The formation of cavitation under the needle valve created due to vortices generated during the sudden opening of the valve can also be seen in Fig. 5.13a. As the needle lifts-off from its seat, the suction created by the needle motion pulls some gas that is already present inside the orifice further towards the needle valve and also into the sac volume. By comparing the instances shown in Fig. 5.13(a, b), the ingestion of the gas into the sac can be traced. The presence of gas inside the sac volume during the start of injection was also observed by (100; 111) in their experimental studies. The suction of the gas into the sac continues until about 11 $\mu m$  needle lift, after which the gap between the needle valve and the sac wall is sufficient to induce forward flow from each orifice pushing the gas back into the chamber, an instance is shown in Fig. 5.13c at 15 $\mu m$  needle lift. With the further lifting of the needle valve, the forward flow is established and the formation of a cavitating vortex from the orifice inlet can be observed. In addition to the cavitating string, during SSOI a string of expanding gas from the orifice inlet coexist with the vapour string, as it can be seen from Fig. 5.13d. Unlike the string cavities that extend toward the orifice exit as observed during SOI, the formation of the vapour and gaseous strings during SSOI does not seem to stretch more than  $\sim 30\%$  of the orifice length. In addition to that, the



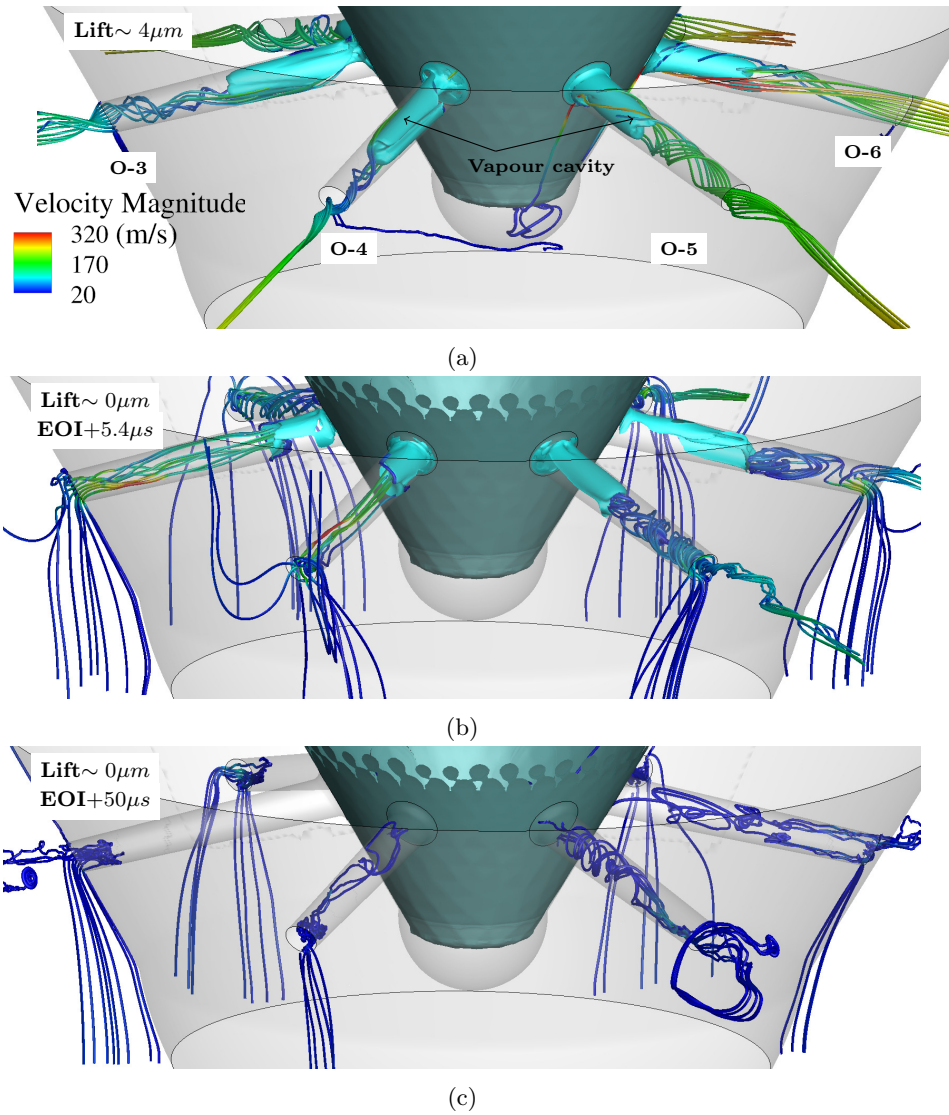


Figure 5.11: Detailed view of swirling flow and string cavitation at selected needle lifts during EOI. Streamlines colored with velocity magnitude and the isosurface of 50% vapour volume fraction shown in cyan.



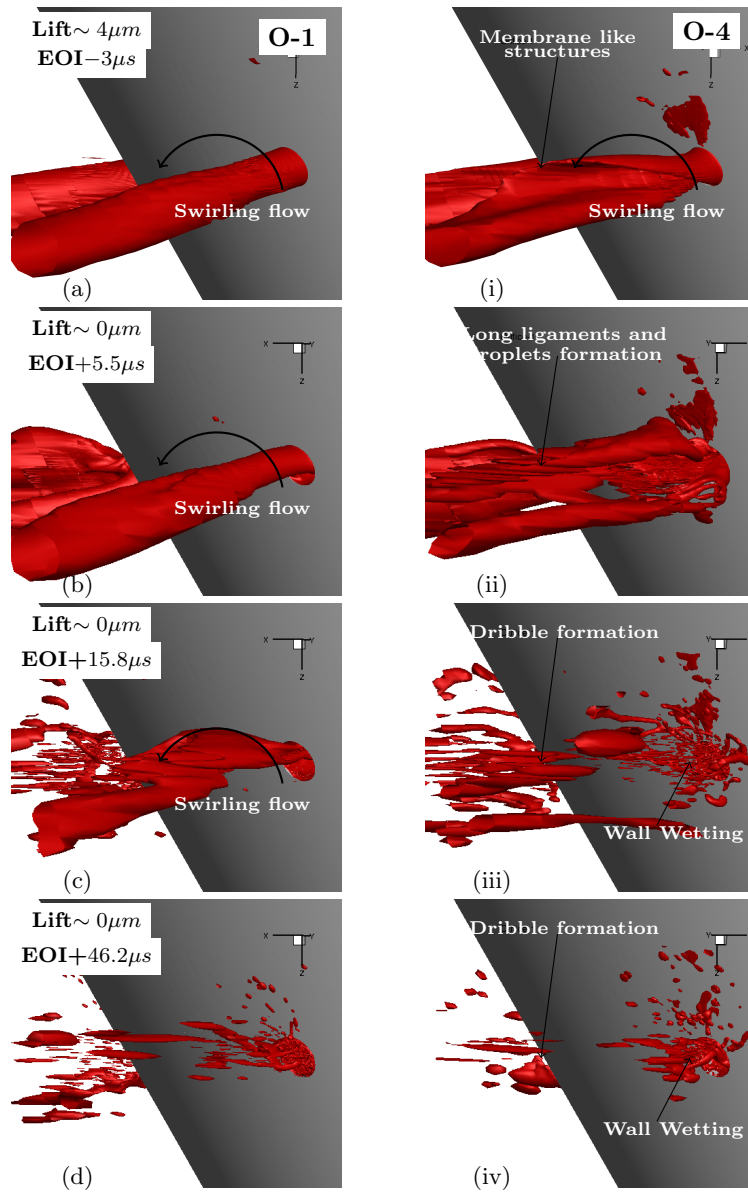


Figure 5.12: Isosurface of 90% gas volume fraction showing the disintegration of diesel jet during and after the needle closure. The swirling motion creating a membrane like structure and the formation of large ligaments and droplets later causing wall wetting is also shown. Figures are shown selectively for Orifices 1 and 4.

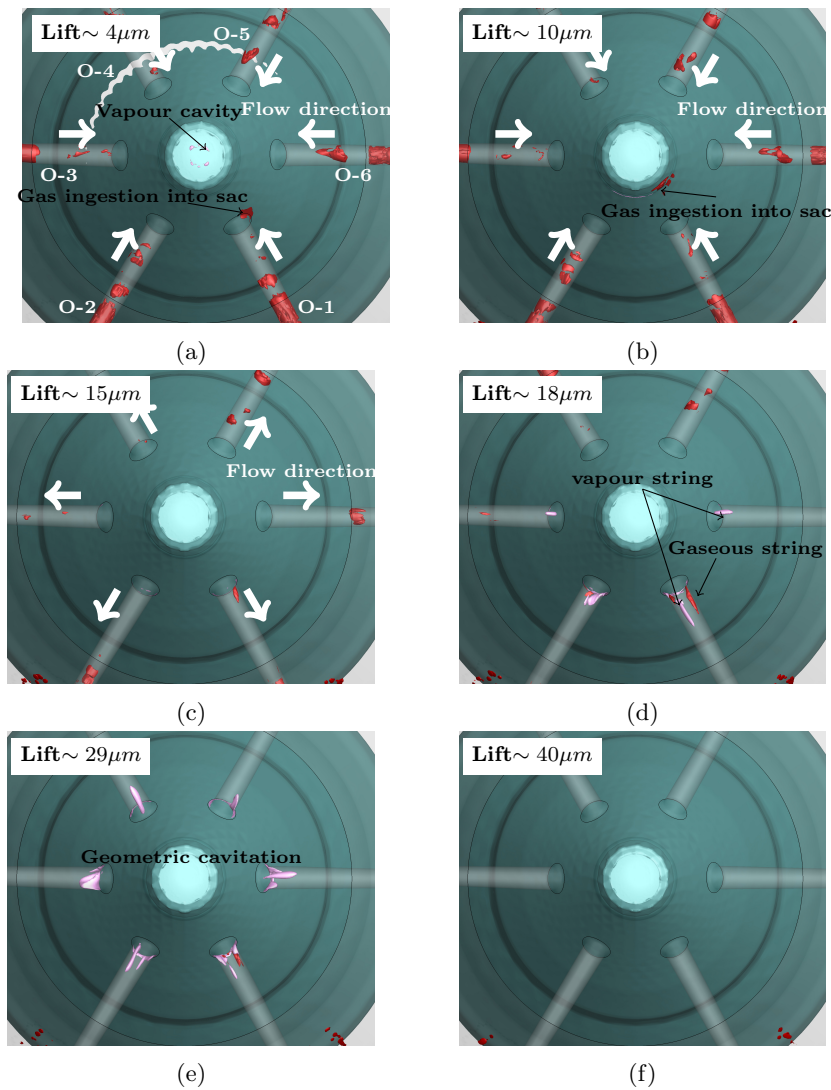


Figure 5.13: Evolution of diesel jet and formation of cavitation during subsequent start of injection shown using a view from the bottom of the injector. The presence gas bubbles inside the orifices and the ingestion of gas into the sac volume is depicted using isosurface of 90% gas volume fraction (red) and 50% vapour volume fraction (pink).

formation of string cavity that originated from the combustion chamber towards the orifice inlet during SOI is also not observed during SSOI. The cavitation inside the orifices disappears completely when the needle lift is about  $40\mu\text{m}$  for this particular design, which is much earlier compared to the SOI. This could be attributed to the recovery of local pressure due to expansion of the gas present inside the orifice when the pressure drops, thus limiting the cavitation formation at the orifice inlet compared to SOI and EOI. A comparison of flow

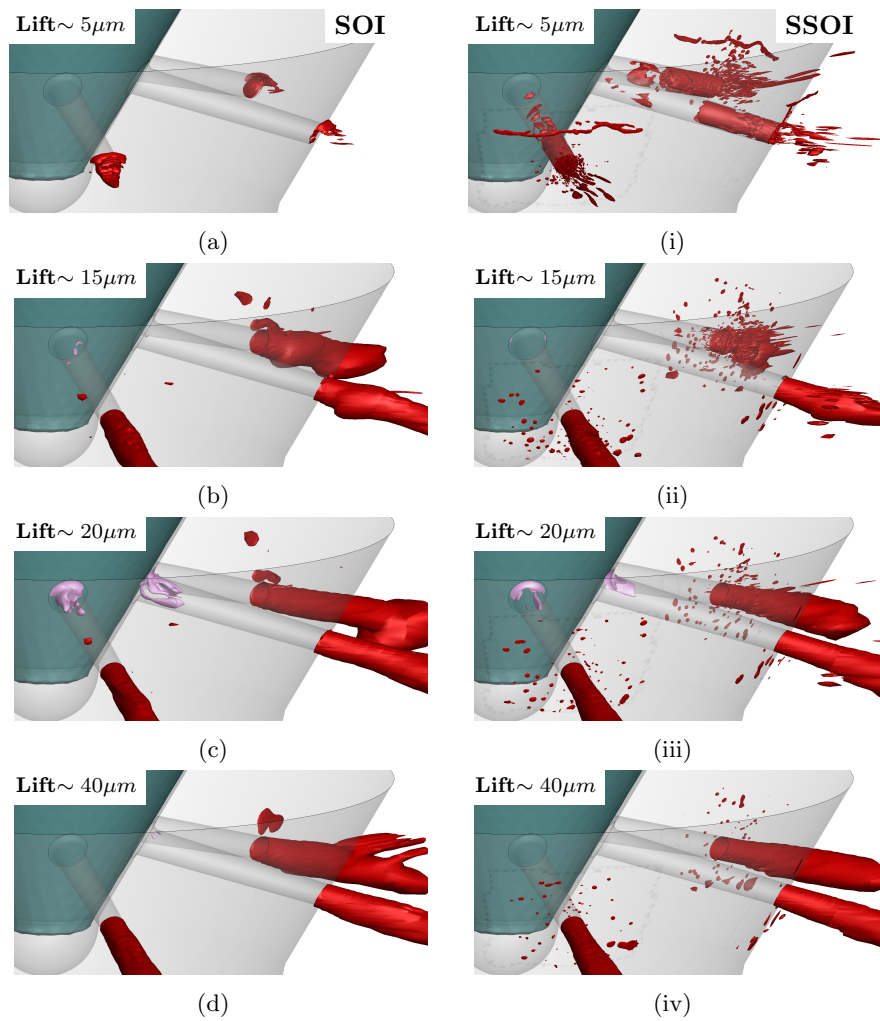


Figure 5.14: Comparison between SOI and SSOI at different needle lift showing the delay in jet formation due to the presence of entrained gas in the orifice. Isosurfaces of 90% gas volume fraction shown in red and 50% vapour volume fraction shown in pink.

field between SOI and SSOI at different needle lifts is given in Fig. 5.14. It can be confirmed from this figure that the presence of the compressible gas inside the orifice delays the penetration of the diesel jet from the nozzle and limits cavitation. However, due to earlier disappearance of cavitation, the fluctuations in the periphery of the diesel jet also disappear earlier during SSOI compared to SOI where cavitation exists for a longer period.

On the nozzle wall surface, which is in contact with the combustion chamber, the number of droplets sticking is much higher compared to that seen during SOI situation. This is primarily due to the residue from the previous injection being present inside and near the orifice exit. As the needle lifts-off from its seat, the swirling flow forces more droplets onto the wall as liquid dribbles and agglomerates, forming larger droplets and ligaments; this can be seen in Fig. 5.15(a, i) along with the formation of the spike-like structure at the periphery of the diesel jet. A delay in the formation of diesel jet can also be observed while comparing the orifices O-1 and O-4 in Fig. 5.15(b, ii) which is influenced both by the eccentricity as well as the entrained gas. With the further lifting of the needle valve, the flow from all orifices becomes established and the droplets and ligaments formed at its periphery continue to stick to the wall as before causing wall-wetting. The diesel jet becomes fully established above  $\sim 45\mu m$ . With the lifting of the needle, the number of droplets sticking to the wall also decreases. It is noted that the size and number of droplets present on and near the wall during SSOI are much larger compared to the SOI at all needle lifts. The simulation was terminated after the needle reaching a lift of  $\sim 60\mu m$ . It is expected that over multiple injection cycles, some of these droplets sticking on the wall may either merge and form large droplets before escaping from the wall or may evaporate from the wall at higher temperatures present inside the chamber.

## 5.4 Chapter summary

The transient flow phenomena such as fuel dribbling and external nozzle wall wetting occurring during the opening, closing and dwell time and the subsequent opening of the needle valve has been simulated and validated against available experimental data. The Navier-Stokes equations have been numerically solved utilising a fully compressible 3-phase (liquid, vapour, air) barotropic model; the barotropic fluid was assumed to be in thermal and mechanical equilibrium with the air, which has been simulated with an additional transport equation coupled with the VOF interface capturing method able to resolve. A six-hole injector has been simulated imposing realistic conditions of the valve movement and considering in addition to its axial motion, a time-dependent eccentric motion.

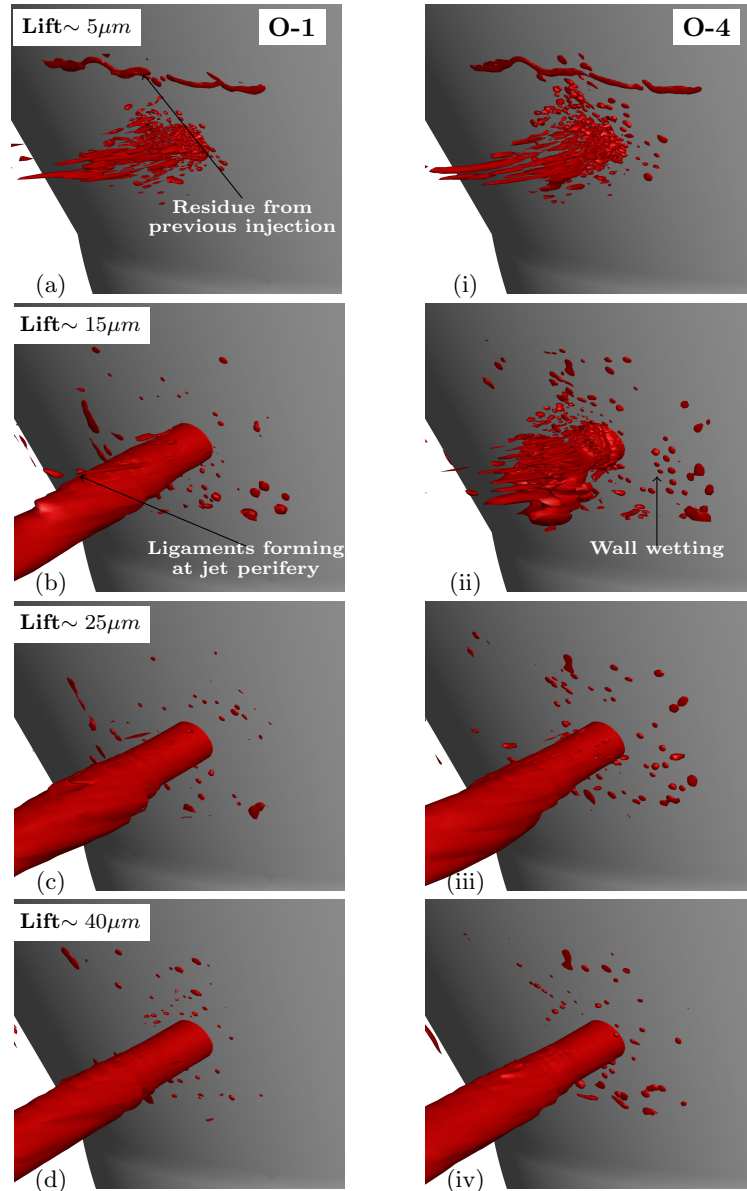


Figure 5.15: Isosurface of 90% gas volume fraction showing the residual droplets and the newly formed droplets sticking to the wall due to adhesion during the subsequent start of injection. Figures are shown selectively for Orifices 1 and 4.

The valve motion has been simulated utilising the immersed boundary method; that has allowed for predictions to be obtained at zero valve lift during the dwell time between successive injections, where the needle remains closed. The model predicted the formation of vortex (or so-called string) cavities stretching from the needle surface till the orifice exit, along with the formation of small droplets and ligaments at the near nozzle exit region. The eccentric needle motion was found to be responsible for the formation of strong swirling flows inside the orifices, which not only contributes to the breakup of the injected liquid jet into ligaments but also to their backwards motion towards the external wall surface of the injector. After their splash, the liquid fragments have been found to stick to the wall due to adhesion, in agreement with relevant experimental observations. Model predictions suggest that such nozzle wall wetting phenomena are more pronounced during the closing period of the valve and the re-opening of the nozzle, due to the residual gases trapped inside the nozzle, and which contribute to the pure atomisation of the injected fluid upon re-opening of the needle valve in subsequent injection events.

## Chapter 6

# Numerical simulation of three-phase flow in an external gear pump using immersed boundary approach

This chapter presents the application of the three-phase model along with an immersed boundary model for predicting cavitation occurring in a gear pump. Combination of these models is capable of overcoming numerical challenges such as modelling the contact between the gears and simulating the effect of NCG in cavitation. The model accounting for the effect of NCG also has broader applicability, since gas dissolved in liquids can come out of the solution when exposed to low pressures; this plays a significant role in the pump performance and cavitation erosion. Here the simulation results are presented for the gear pump at different operating conditions including the contact between gear, gear RPM and different %'s of NCG; their effects on performance and cavitation is demonstrated. In this study, the turbulence in the flow is modelled using the  $k - \omega - SST$  model with proper correction for the turbulent viscosity (169) to circumvent the overestimation of turbulent dissipation in the two-phase region, which is a typical problem in two-equation turbulence models.

The structure of this chapter is as follows: In the next section, the details about the numerical setup for the gear pump simulation is described. The major findings from the simulations are then shown in the results and discussion section

with the main conclusions summarised at the end.

## 6.1 Simulation Setup

Simulations have been performed for a 2D gear pump; the pump geometry used for the simulation, shown in Fig. 6.1a is publicly shared by (8). For simulation, this geometry is simplified at the curved shoulders at the inlet and outlet, replacing it with sharp edges while keeping everything else the same. The most difficult features in a gear pump simulation are the modelling of small clearances and the contact between the gears while maintaining a reasonable mesh quality. In the present simulation, the application of the IB method has made the implementation of these tasks more manageable. To model the contact between the gears, the gears are rotated by a small angular position so as to make the gear surfaces touch each other before exporting the coordinate positions of the gears into immersed boundary code. In Fig. 6.2, the clearances between the gears and between the gears and casing along with the contact between gears are highlighted using immersed boundary points superimposed on the background mesh. An additional refinement for the numerical mesh is provided at the location where the two gears come in contact as highlighted in Fig. 6.1. This refinement ensures sufficient grid elements in the clearances to capture the leakage flow between the gears. With this refinement and the addition of boundary layer refinement to limit the  $y^+$  values below 5 in most of the domain for the extreme condition considered, the total mesh count reaches up to 0.5 million cells.

Constant absolute pressure boundary conditions have been applied to the inlet and outlet boundaries. In all the cases considered in this study, a relatively low-pressure jump is applied between the inlet and outlet ( $\sim 10$  bar), similar to the numerical study of (136).

All simulations have been performed using 2 CPU's with 8 cores each (16 cores) having a clock speed of  $1.95GHz$  on a Linux cluster. The elapsed wall-clock time for one pitch rotation of the gears at 2000 RPM was approximately 6 hours.

## 6.2 Results and Discussion

Due to the two-dimensional approximation used in this study, the volumetric efficiency and the flow rates reported may not replicate the values observed in a real gear pump since the leakage paths, side porting and the relief grooves cannot be modelled in two dimensions. However, since the primary objective



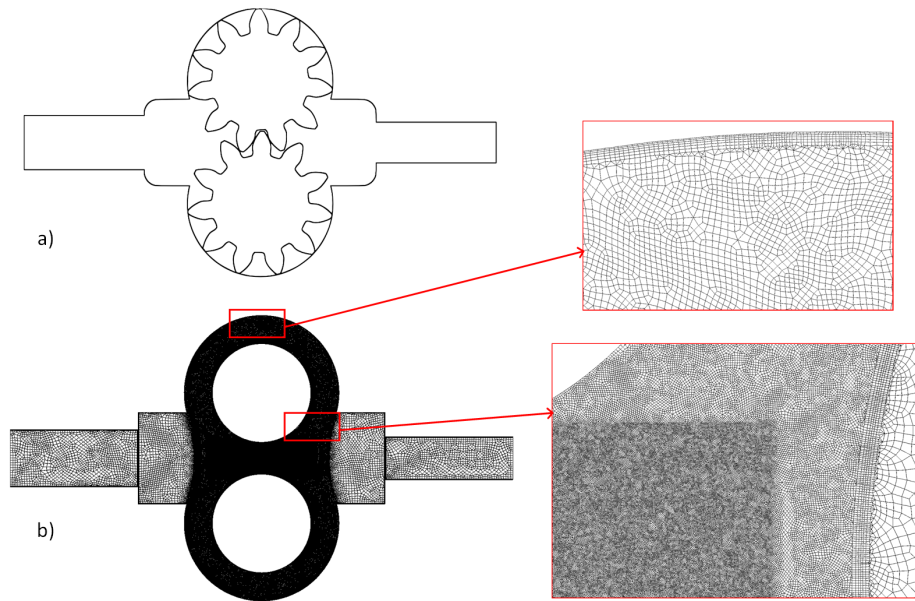


Figure 6.1: a) Line diagram of the gear pump from (8) and b) the computational mesh for immersed boundary simulation

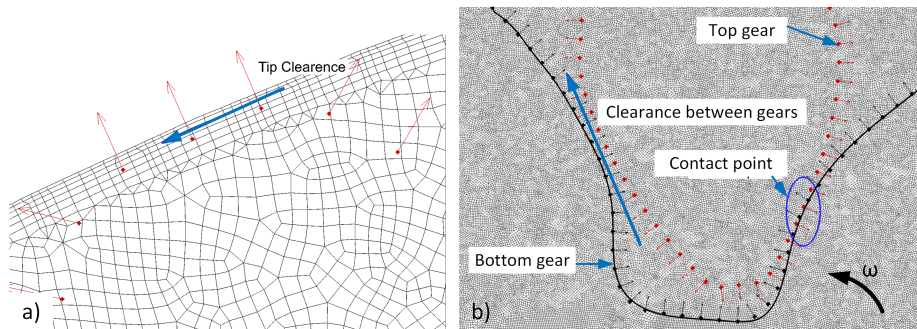


Figure 6.2: Modelling of a) tip clearances and b) clearance and the point of contact between the gears

of this work is to present a numerical model that can handle three-phases in conjunction with an immersed boundary method for complex gear motion, the approximations used for simplifying the problem can be justified. Validation of the numerical model is performed on two different cases, a two-dimensional rotating cross (see the Appendix C) and also with some experimental works on gear pump available in the literature.

In Fig. 6.3, the streamlines observed by (9) using TRPIV are compared with the current numerical study. The flow field and the velocity profile plotted in Fig. 6.3 shows a good correlation with the experimental values. In addition to this, a qualitative comparison is also made for the cavitation predictions

at two different gear RPM's as shown in Fig. 6.4. It can be observed that the locations of the cavitation predicted from the simulations correlate very well with the vortex core observed in the gap between the teeth at the suction chamber observed in the experimental work of (10) for both the cases considered.

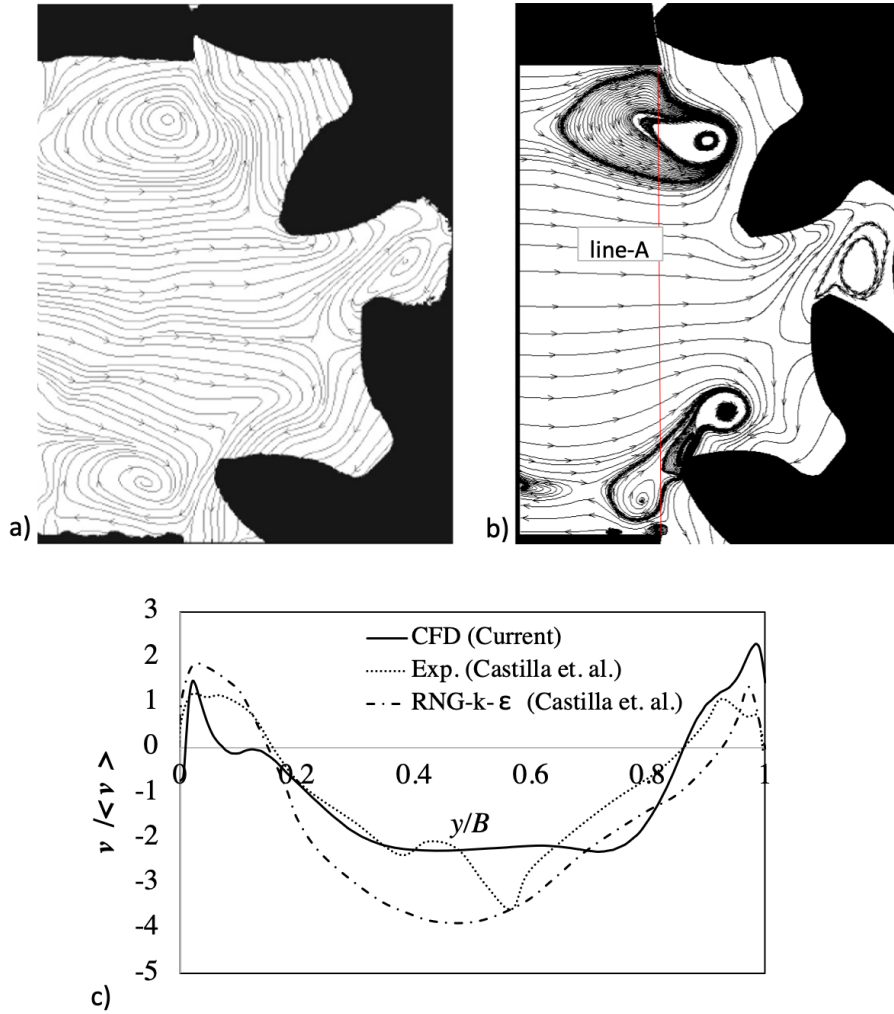


Figure 6.3: Comparison of the streamlines obtained by a) Castilla et al. (9) using TRPIV and b) the current numerical model using oil as working fluid, c) the velocity profile along line-A

In the results that follow, the pressure is made non-dimensional using the inlet pressure of 1 bar, time using the term  $T_g$  defined as  $T_g = 11 \cdot RPM/60$ , and the non-dimensional velocity is defined as  $V/(r_g\omega_z)$ , where  $r_g$  is the radius of the gear and  $\omega$  is the angular velocity in rad/sec.

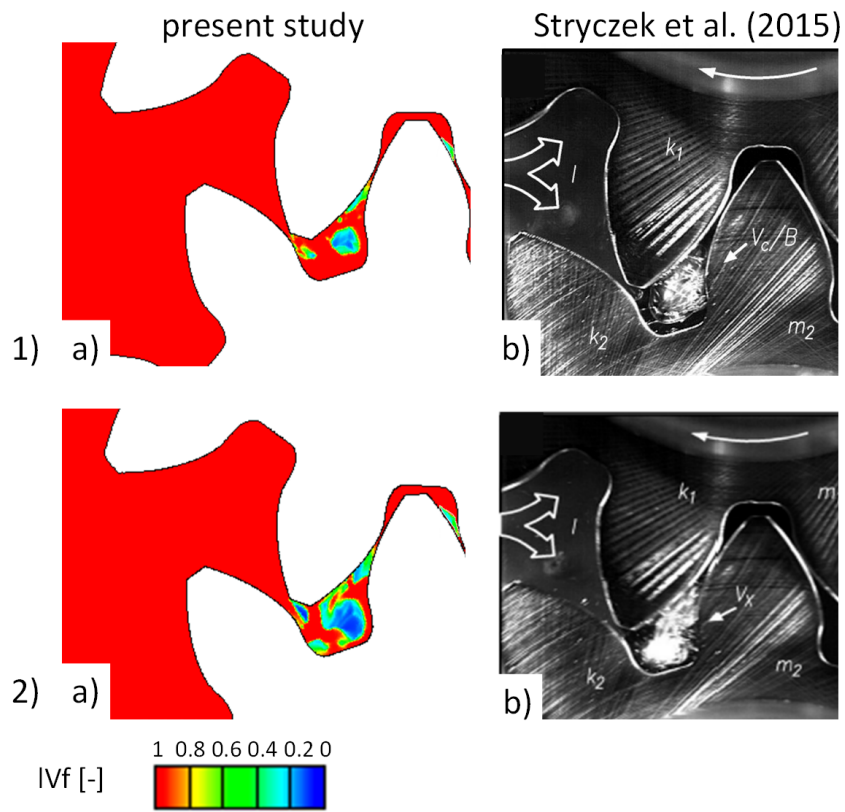


Figure 6.4: Comparison of the liquid volume fraction 1) at 500 RPM and 2) 1000 RPM; a) from the present simulation and b) from the experimental work of Stryczek et al. (10) to highlight cavitation occurring in the gap between gear teeth in the suction side.  $T_g$  is the time for one gearing period

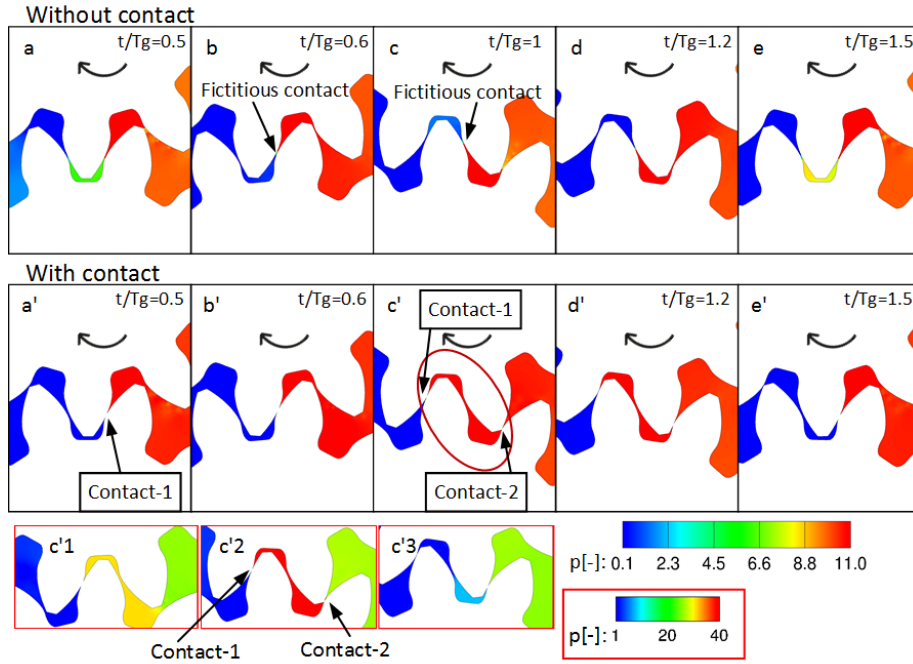


Figure 6.5: Comparison of non-dimensional absolute gauge pressure over a gearing period with (a-e) clearance between the gears and (a' - e') with contact between gears. The contours in the subset shows (c'1) the condition before the second contact, (c'2) pressure rise during two contacts in the isolated region and (c'3) the condition after the release of the first contact. Note that c' and c'2 corresponds to the same gear position. The time interval between the contour plots from a-e are not uniform; they are chosen to highlight specific events over a period

### 6.2.1 Effect of gear contact

The effect of contact between the gears on cavitation and pump performance is studied by comparing two cases, one with a clearance of  $74\mu m$  (which is very small compared to the distance between the gear centres which is  $45.1 mm$ ) between the gears and the other condition when gears are in contact. Unlike the unitary contact ratio (a ratio that defines the average number of teeth that are in contact with the mating gear during a period in which a tooth comes and goes out of contact) studied in the simulations of (136), in the present study, the contact between the gears occurs at two locations, i.e. before the first contact separates, the next pair of gears come in contact. This creates a region isolated from the inlet and outlet where very high pressures are expected in a two-dimensional simulation. In Fig. 6.5, a comparison of the development of pressure over a gearing period for two conditions considered are shown. A gradual rise in pressure from the inlet towards the outlet is observed

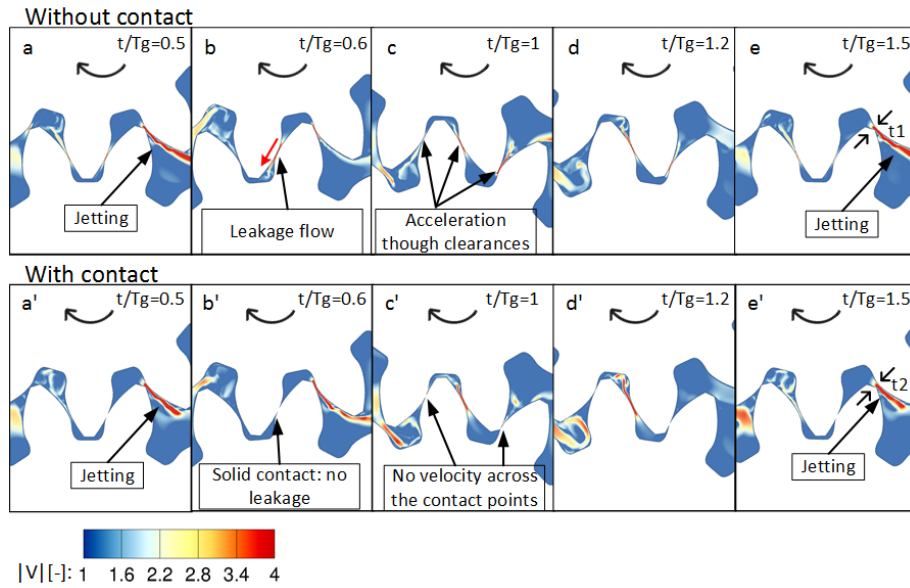


Figure 6.6: Comparison of non-dimensional velocity magnitude over a gearing period with (a-e) clearance between the gears and (a' - e') with contact between gears. The time interval between the contours from a-e are not uniform; they are chosen to highlight specific events over a period.

when a continuous clearance is present between the gears, see Fig. 6.5a. As the gear rotates, the fluid inside the pockets are compressed, and the liquid on the high-pressure side leaks towards the inlet through the small clearances as shown in (Fig. 6.5(b, c) and Fig. 6.6(b, c)). The acceleration of this leakage flow through the clearance creates a low-pressure zone and results in the formation of cavitation (Fig. 6.7). This cavity acts as a fictitious contact point that separates the inlet chamber from the outlet as also observed by (136). A sudden jump in absolute pressure across this fictitious contact can be observed in Fig. 6.5(b, c). The cavitation occurring in the clearances is highlighted using red circles in Fig. 6.7. On the other hand, when the contact between the gears are modelled, the first contact point (Contact-1) act as the barrier between the inlet and outlet which produces a sudden pressure jump across this point as can be seen from Fig. 6.5(a' - c'). Unlike the first case, the solid-solid contact does not allow flow across it, and hence no cavitation is observed at contact location (Fig. 6.6(b', c') and Fig. 6.7(b', c')). When the gears cross half-pitch rotation, the second contact is established, trapping a volume of fluid between the two contacts; Fig. 6.5c'. Further rotation of the gear raises the pressure in the trapped volume up to 30-40 times the inlet pressure Fig. 6.5(c'2). This region is of particular interest in many studies (for, e.g. (132; 119; 10)) as this pressure rise can

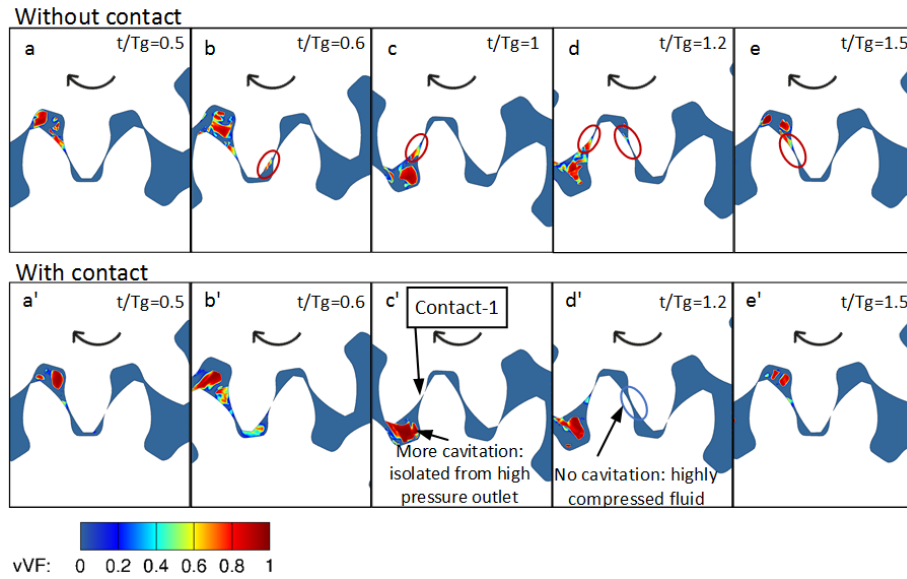


Figure 6.7: Comparison of vapour volume fraction over a gearing period with (a - e) clearance between the gears and (a' - e') with contact between gears. The time interval between the contours from a-e are not uniform; they are chosen to highlight specific events over a period

produce noise and vibration in the pump. In a real gear pump, relief grooves are provided to drain this trapped fluid to the inlet chamber to avoid excessive vibration arising from the high-pressure fluid loading on the gears. Unlike the previous case, i.e. without contact, cavitation does not appear in this region due to the pressurised fluid in the trapped volume (Fig. 6.7d) when the gears are in contact. While this is true for 2D simulations, in a real gear pump with relief grooves, the high-velocity jet from the trapped volume towards the inlet chamber through grooves can lead to erosion due to jetting. The contact between the gears at one side provides an additional clearance ( $t_2 > t_1$ ) in the backlash and hence a low-velocity jet is produced at the outlet chamber, compared to the case with clearance (Fig. 6.6(e and e')). An overall increase in cavitation is observed when the gears are in contact. This increase is mainly attributed to the increase in cavitation just ahead of the contact point where the pressure is much lower due to the isolation of the of high-pressure side from inlet by the contact point compared to the case without contact where relatively higher pressures are realised due to the continuous connection between inlet and the outlet chamber. This can be confirmed by comparing the total vapour generation over time for the two cases. In Fig. 6.8a, the time evolution of the area integral of vapour volume fraction is shown for the two cases considered. This quantity is used as a measure of cavitation generation over time. The result of the integration

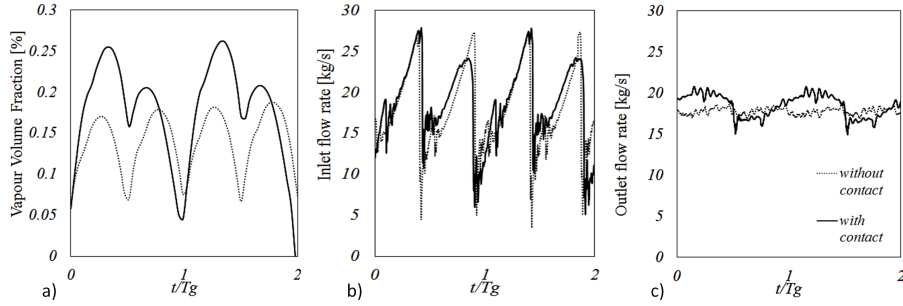


Figure 6.8: Comparison of a) area integral of vapour volume fraction normalised using the total flow area b) inlet flow rate and c) outlet flow rate over two gearing periods

plotted in Fig. 6.8a clearly shows an increase in cavitation volume (assuming unity depth) when the gears are in contact, with the mean value of vapour volume fraction at 0.19% against 0.14% without contact. The mean value of the mass flow rate plotted in Fig. 6.8c also increases approximately by  $\sim 4.5\%$  when the gears are in contact. Such an increase in flow rate with contact between the gears was also acknowledged by (9) for a unity contact ratio. They also reported that the flow fluctuation increases with the contact due to the water hammer effects caused by the sudden opening and closing of the inner teeth chamber to both the outlet and inlet. Similar to their findings, the fluctuations in the flow along with the breakage of temporal symmetry are also observed in the present simulation. The compressibility of the fluid along with the nature of gear pump operation produces these flow fluctuations which are often a source of the fluid-borne noise. The fluctuations observed in the inlet is almost half of that of the gearing period, due to the suction produced by both gears. The additional higher frequency oscillations observed in the inlet flow rate signal can be associated with cavitation occurring in the low-pressure chamber. At the outlet, the flow rate fluctuation matches with the frequency of a gearing period. A comparison of the percentage difference between the maximum outflow rate at any instant to the mean outflow rate shows a 5.5% difference when the gears are not in contact whereas this is as high as 12% when they are in contact.

### 6.2.2 Effect of gear RPM

To study the effect of gear RPM on cavitation, simulations are performed for three different rotation speeds; 500, 1000 and 2000 RPM. The results presented from this point onwards consider a contact ratio greater than unity unless mentioned otherwise. In Fig. 6.9, a comparison of cavitation occurring in the inlet chamber, represented using the contours of vapour volume fraction over a pe-



riod ( $1/11^{th}$ ) of gear rotation is shown. It is evident from the figure that the cavitation volume increases with the increase in gear RPM. At lower RPM, the formation of cavitation is observed in the gap between the gears where they expand in the inlet chamber. The strong vortical structures generated due to the expanding gears initiates this cavitation at its low-pressure core. At 1000 RPM, in addition to the vorticity induced cavitation in the expanding volume, cavitation is also formed due to the separation of the flow from the gear tips rotating towards the inlet. A further increase in rotational speed produces stronger vortices and larger separation zones resulting in increased cavitation in the inlet chamber as can be seen in column-3 of Fig. 6.9. The vortical structures generated in the domain are shown in Fig. 6.10 at  $t/T_g = 0.5$  for comparison. The structures leading to the formation of cavitation between the gears in the inlet zone and the vorticity due to the flow separation can be clearly seen from the figure. In addition to that, vortical structures are also observed at the clearance between the gear and the casing and also at the outlet chamber where the fluid is pushed out. Since the absolute pressure values at these locations are higher, being on the pressure side, cavitation does not occur here.

The area integral of the vapour volume fraction over two gearing periods reported in Fig. 6.11a, similar to the one presented in the previous sections is used to quantify the cavitation at different RPM. A comparison of this quantity confirms that the minimum cavitation occurs at 500 RPM and the maximum at 2000 RPM, with the addition of cavitation due to flow separation. With an increase in gear RPM, the net flow rate is also increased as can be seen in Fig. 6.11(b, c). It can be noticed that the maximum amplitude of fluctuations occurs at 1000 RPM, where the cavitation is more dynamic with frequent cavity creation and collapses, and minimum at 500 RPM where only less cavitation occurs. At 2000 RPM, even though the cavitation is much higher, it is less dynamic compared to the 1000 RPM with a continuous presence of stable cavities in the domain. These arguments can once again be confirmed by examining the evolution of vapour volume fraction shown in Fig. 6.11a which shows maximum fluctuations at 1000 RPM. The RMS and the maximum value of the fluctuating flow rate at different gear RPM are reported in Table 6.1. It is found that the percentage deviation between the mean and maximum flow rate reduces with the increase in RPM. This is because, at higher RPM, the gears become closer to replicate as a rotating disc with minimum fluctuations.

The development of the pressure from the inlet to the outlet at 500 RPM at a selected time instant is shown in Fig. 6.12. The time instant is selected such that two points of contact are established, and the liquid trapped between the contacts is compressed. The figure shows the non-dimensional pressure ( $p/p_{in}$ ) plotted at different locations along the curve passing from inlet to outlet through



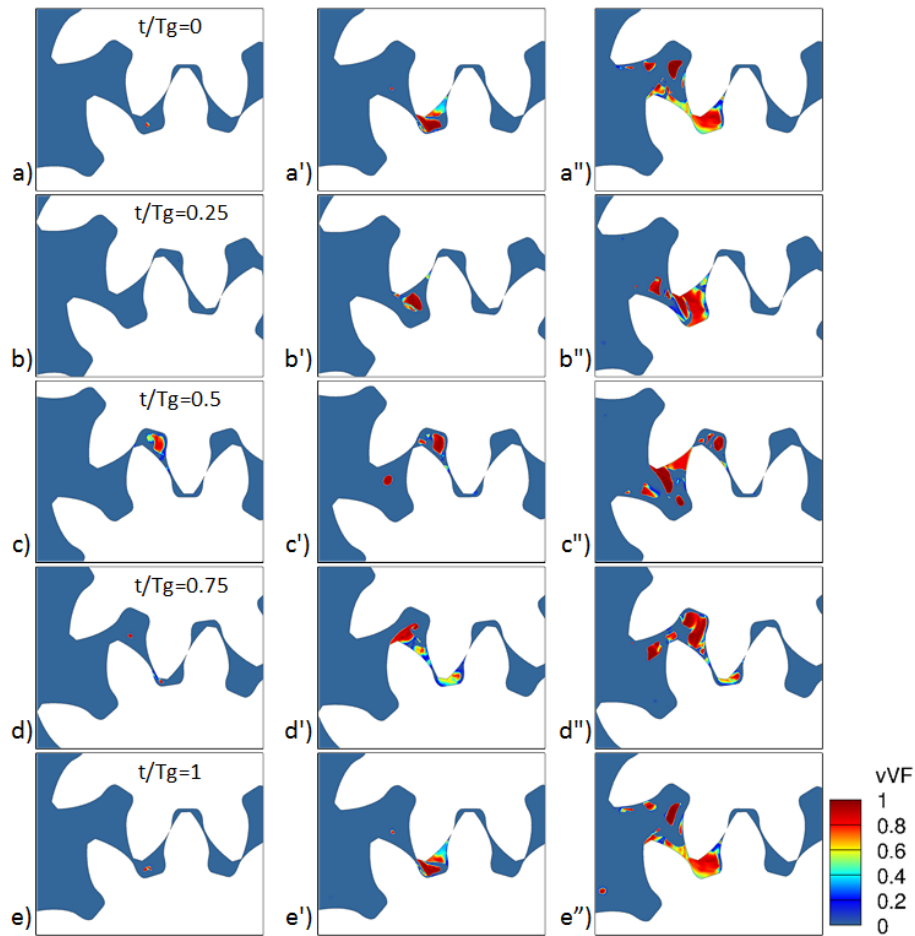


Figure 6.9: Comparison of cavitation formation at 500 RPM (a-e), 1000 RPM (a' - e') and 2000 RPM (a'' - e'') represented as contours of vapour volume fraction over one gearing period.

the gear pockets (1-15) and through to the meshing zone (5' - 13') as shown in Fig. 6.12a. The distribution of the pressure follows a stairway step profile along the line (1-15). A similar distribution was also observed by (130) in their numerical simulation. Along the path 5' - 13', which passes through the gear meshing zone, the trapped liquid gets compressed and a sudden jump in pressure between 5' and 6' is observed. The absolute pressure in this region can easily reach up to 30 times the inlet pressure as can be seen from Fig. 6.12b. The impact of this rise in pressure and the measures to avoid this unintended pressure rise were already discussed in the previous sections. The pressure rise from the inlet to outlet follows a similar trend for all other cases considered in this study, hence it is not shown here.

In Fig. 6.13, the contours of the pressure and the velocity magnitude at

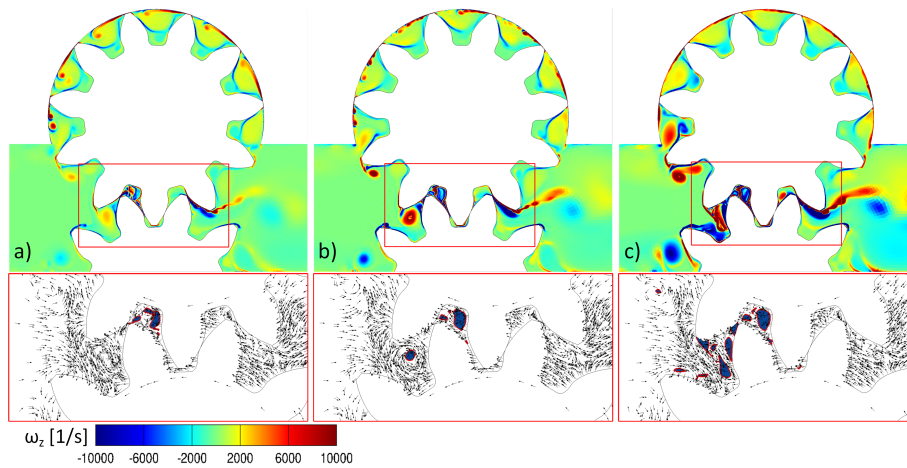


Figure 6.10: Contours of z-vorticity near the gearing zone and tip clearances at a) 500 RPM b) 1000 RPM and c) 2000 RPM. The normalised velocity vector along with 50% vapour volume fraction (blue) highlighting the two-dimensional vortex structures and locations of cavitation are given in the subset

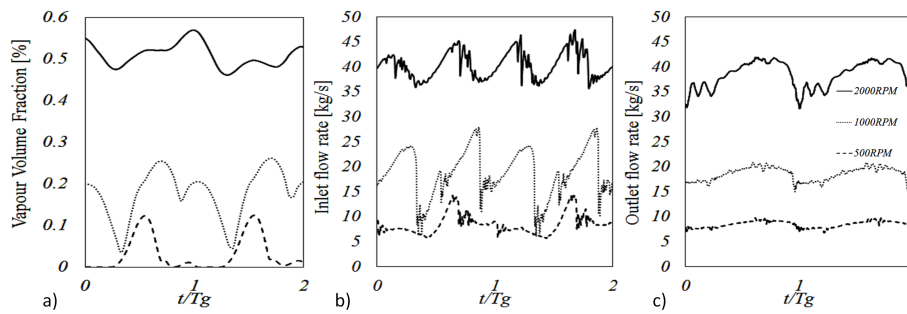


Figure 6.11: Comparison of a) area integral of vapour volume fraction normalized using the total flow area, b) inlet flow rate and c) outlet flow rate over two gearing periods at different gear RPM's

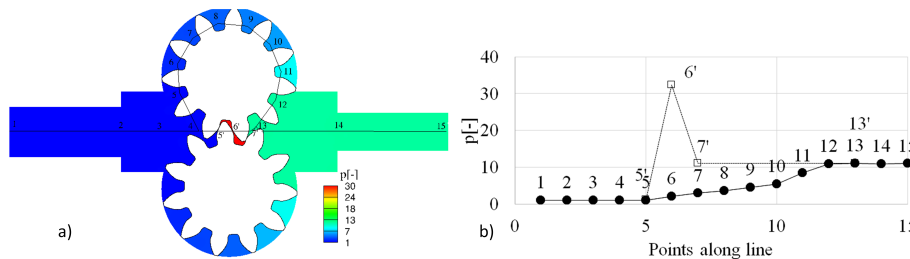


Figure 6.12: Representation of stairway pressure rise across inlet and outlet along the gear pockets at 500 RPM a) pressure contours with multiple locations along the line where the pressure is measured and b) the non-dimensional pressure at different points shown in (a)

Table 6.1: Mean and fluctuating outflow rate at different RPM

RPM	$\bar{m}_{out}(kg/s)$	$m_{out,RMS}(kg/s)$	$\dot{m}_{max}(kg/s)$	%change $\frac{(\dot{m}_{max}-\bar{m}_{out})}{\bar{m}_{out}} * 100$
500	8.36	8.39	9.71	16.1
1000	18.54	18.59	20.81	12.2
2000	38.47	38.57	41.94	9.0

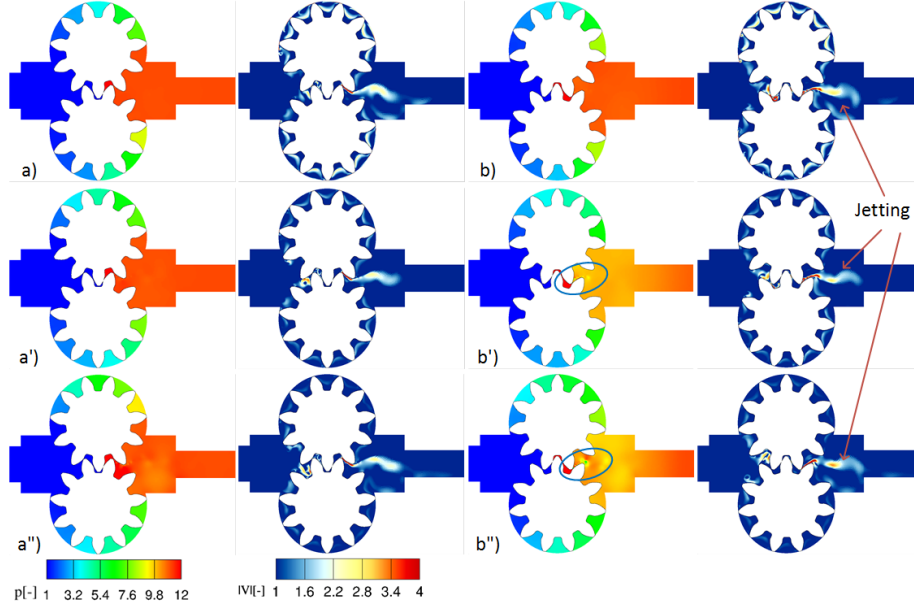


Figure 6.13: Contours of pressure and velocity magnitude 1) 500 RPM 2) 1000 RPM and 3) 2000 RPM and a)  $t/T_g=0$  ie. ( $\theta=0$ ) and b)  $t/T_g=0.5$  ie. ( $\theta=0.5 \times 2\pi/11$ )

different RPM are shown at  $t/T_g=0$  and 0.5. Jetting of fluid at the outlet chamber during the meshing of gears can be seen from the figure. The velocity of the jet increases with the increase in RPM, and this causes the pressure to drop locally near the gear tips at the outlet chamber as highlighted using blue circles in Fig. 6.13. Since this is occurring in the high-pressure chamber, the pressure drop is not sufficient to produce cavitation.

### 6.2.3 Effect of Non-condensable Gas

The effect of non-condensable gas on cavitation is studied by varying its content in water from 0% to 1% by volume at a constant rotational speed of 2000 RPM. Once again, the quantification of the cavitation corresponding to each NCG content is achieved by taking the area integral of the vapour volume fraction. A comparison of this result is presented in Fig. 6.14a over two gearing periods. It is observed that the effect of non-condensable gas is to reduce the amount of cavitation. In the absence of non-condensable gas in the fluid, a reduction in

local pressure below vapour pressure immediately causes the liquid to change its phase to vapour phase. On the other hand, in a similar situation, if a certain amount of non-condensable gas is present in the liquid, the reduction in local pressure is recovered to a certain extent by the expansion of the highly compressible gas and hence limiting cavitation. The formation of cavitation and the expansion of the NCG at the inlet chamber under different conditions are shown in Fig. 6.15. The reduction in cavitation with increasing NCG can be appreciated from this figure. In addition, a comparison of vapour contours at 0%, 0.2% and 1% NCG reveals that the core of cavitation remains the same, which is at the core of the vortices, while the spread of the vapour cavity around the core is limited by the expansion of the gas, larger volume fraction of NCG can be seen around the vapour cavities. To verify the effect of NCG on the pump performance, a comparison of the flow rate measurements at inlet and outlet is performed; the results are presented in Fig. 6.14(b, c). It is observed that the mean flow rate does not change, but the amplitude of the flow fluctuations at the inlet and outlet increases with an increase in NCG content. This increase in fluctuations could be due to the increased compressibility of the mixture in the presence of NCG. The percentage difference between the instantaneous maximum outflow rate and the mean outflow for 0%, 0.2% and 1% are shown in Table 6.2. It can be noticed that the percentage change between maximum and mean outflow increases with the increase in NCG content.

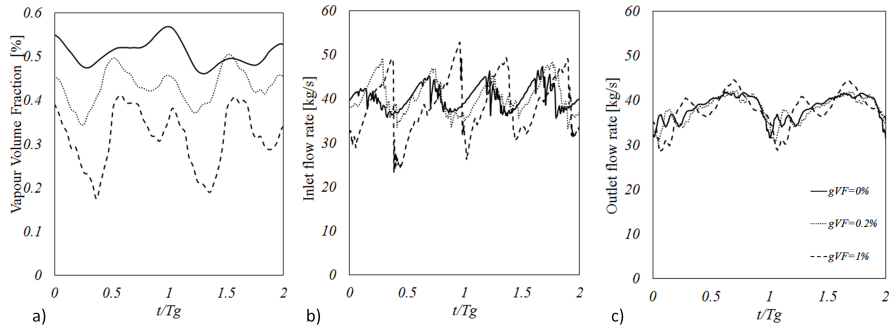


Figure 6.14: Comparison of the area integral of vapour volume fraction normalized using the total flow area over two gearing periods with different percentage of gas volume fraction at 2000 RPM.

### 6.3 Chapter summary

In this study, a numerical model for predicting cavitation in the presence of non-condensable gas along with an immersed boundary method was developed for modelling three-phase cavitation occurring in a gear pump. Such a model

Table 6.2: Mean and fluctuating outflow rate for different gas content at 2000 RPM

NCG%	$\bar{m}_{out}(kg/s)$	$m_{out,RMS}(kg/s)$	$\dot{m}_{max}(kg/s)$	%change $\frac{(\dot{m}_{max}-\bar{m}_{out})}{\bar{m}_{out}} * 100$
0%	38.47	38.57	41.94	9.03
0.2%	38.09	38.20	42.20	10.80
1%	38.07	38.28	44.68	17.35

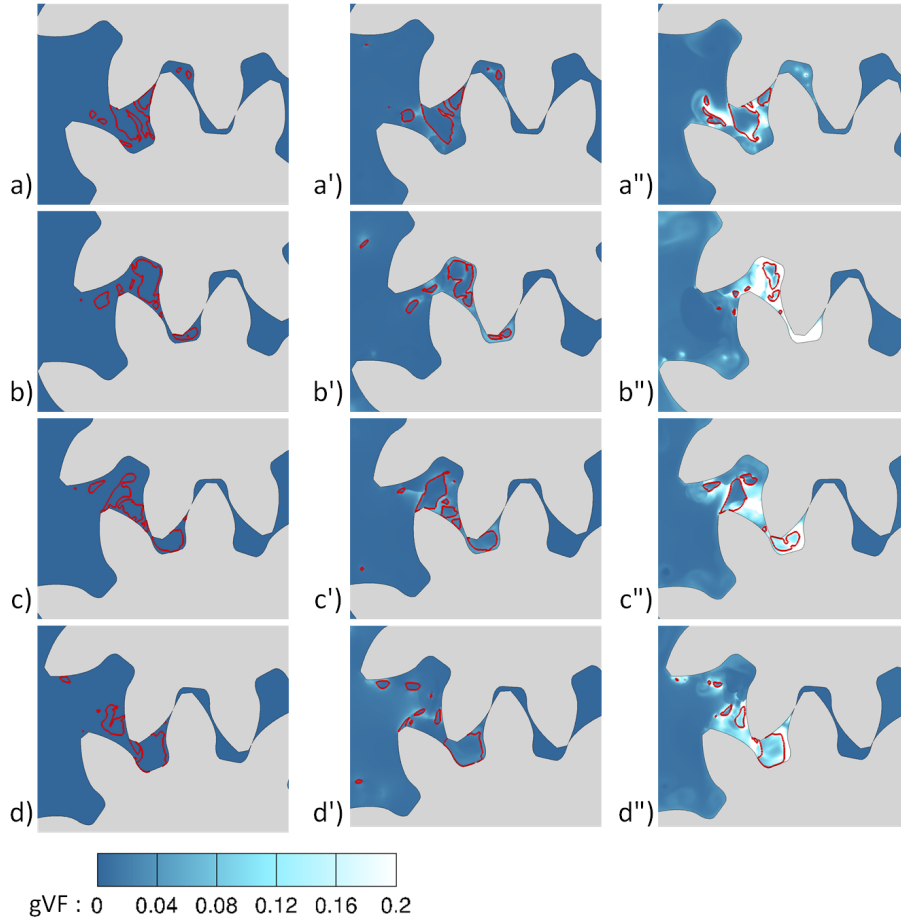


Figure 6.15: Evolution of NCG and cavitation; (a-d) for 0% NCG, (a'-d') for 0.2% and (a''-d'') for 1% NCG content. The iso-lines of 50% vapour volume fraction shown in red lines. The instances are chosen randomly to highlight main features over a gearing period

is essential for understanding the flow behaviour inside the pump in detail at different operating conditions. These details will help in efficient designing of pumps with reduced cavitation and associated energy losses. The multiphase flow model used in this study is fully compressible and utilizes the  $k - \omega - SST$  turbulence model with a user-defined correction for the turbulence viscosity. The

cavitation and the IB models are validated against numerical and experimental results from the literature. After validating the numerical model, simulations are performed on a 2D gear pump model to study the effect of contact between the gears, RPM and the amount of NCG on cavitation formation, development and collapse, as well as on pump performance. A comparison with experiments has shown that the current model could predict cavitation occurring due to vorticity in the suction chamber accurately; use of the immersed boundary approach has made the modelling of contact ratios greater than unity easier. With sufficient refinement, the approach also produces accurate results in less time as compared to other conventional re-meshing methods, as there is no mesh deformation and interpolation of data involved.

It is observed that when the gears are in contact, cavitation occurring in the suction chamber increases due to the isolation of the low-pressure side from the high-pressure chamber. As a result, more fluctuations are present in the outlet flow and a slight increase in mean flow rate is also observed as compared to the case without contact. When the contact between the gears occur at more than one location, a volume of liquid is trapped between the gears and it is compressed. The pressure in this trapped volume is observed to rise up to 30-40 times relative to the inlet pressure.

At lower RPM, cavitation is primarily observed at the core of the vortex forming between the gear teeth opening towards the inlet. With an increase in the rotational speed, vapour cavities are additionally formed at the gear tips due to flow separation. Both intensity and the total volume of cavitation increase with the gear RPM. The effect of NCG on cavitation occurring in gears pump was studied for the first time. This study is conducted by varying the gas content in the flowing liquid from 0% to 1% by volume. The results suggest that the presence of NCG reduces the formation of cavitation without having much impact on the average outlet flow rates. However, an increase in fluctuation in the outlet flow is observed with the increase in gas content.

The numerical model presented here is also validated and applied for three-dimensional gear pump simulations with side porting and radial clearances. The results obtained at 0% and 2% NCG shows that the cavitation inside the pump decreases with the increase in NCG content. The results from this study are presented in [Appendix E](#).

## Chapter 7

# Conclusions and further work

### 7.1 Conclusions

A numerical model for simulating the interaction between three phases, namely liquid, vapour and gas has been developed. The model utilises a fully compressible three-phase barotropic model; all phases are assumed to be in thermal and mechanical equilibrium. The motion of the air has been modelled using two different approaches. In the first approach, a sharp interface capturing method (VOF) has been utilised; this approach has been used for modelling the atomisation from the injector nozzle, the fuel dribbling and the external nozzle wall wetting occurring at the end of injection. In the second approach, a diffused interface mixture model approach has been tested; this was suitable for studying the effect of non-condensable gases on cavitation occurring in gear pumps. Additionally, to model complex geometric motion, an immersed boundary method based on the *continuous forcing* approach has been utilised. The application of the immersed boundary method has enabled the modelling of solid-to-solid contact easier. In addition to that, with no mesh movement/regeneration to accommodate geometric motion, a significant reduction in computational cost have been achieved which makes this model suitable for industrial applications. The validity of the numerical models developed has been assessed by comparing them against relevant experimental results.

Numerical simulations have been performed for different cases of industrial interest, such as (1) a step-nozzle, (2) a 6-hole VCO diesel injector and (3) external gear pumps. The three-phase model has been combined with the VOF model for interface capturing as well as with a wall adaptive LES model for

resolving turbulence to study the primary atomisation from a step-nozzle. The results from the simulations have been compared with the experimental results from (1). From the analysis, it has been observed that the disintegration of the liquid jet is influenced mainly by four factors: in-nozzle cavitation, the entrainment of air into the nozzle, the turbulence generated and partially due to the aerodynamic instabilities. The formation of the liquid droplets is first observed from the mushroom edge due to Rayleigh-Taylor instabilities and later from the liquid core due to the combined effect of cavitation, turbulence and Kelvin-Helmholtz instabilities. Liquid ligaments are formed when the vapour cloud collapses near the liquid-air interface. At cavitation inception, the atomization is primarily due to liquid turbulence and aerodynamic instabilities. Whereas at developing cavitation, in addition to the above parameters, the cavitation and the air entrainment into the nozzle plays the major role. The air entrainment into the nozzle is periodic when developing cavitation occurs. Due to the asymmetry in the nozzle geometry, a partial hydraulic flip occurs at 5 bar injection pressure, suppressing the vapour formation from the lower wall completely. At this condition, the atomization and the subsequent spray cone angle is drastically reduced. From the observed results, it can be concluded that the developing cavitation is the most favourable condition for effective atomization and wider spray.

The transient flow phenomena such as fuel dribbling and external nozzle wall wetting occurring during the opening and closing of the needle valve and the dwelt time between the injection have been simulated and validated against available experimental data. A six-hole VCO-type injector was used for the simulation, imposing realistic conditions of the valve movement and considering in addition to its axial motion, a time-dependent eccentric motion. The valve motion has been simulated utilising the immersed boundary method; that has allowed for predictions to be obtained at zero valve lift during the dwelt time between successive injections, where the needle remains closed. The model predicted the formation of vortex (or so-called string) cavities stretching from the needle surface till the orifice exit, along with the formation of small droplets and ligaments at the near nozzle exit region. The eccentric needle valve motion was found to be responsible for the formation of strong swirling flows inside the orifices, which not only contributes to the breakup of the injected liquid jet into ligaments but also to their backwards motion towards the external wall surface of the injector. After their splash, the liquid fragments have been found to stick to the wall due to adhesion, in agreement with relevant experimental observations. Model predictions suggest that such nozzle wall wetting phenomena are more pronounced during the closing period of the valve and the re-opening of the nozzle, due to the residual gases trapped inside the nozzle, and which contribute



to the pure atomisation of the injected fluid upon re-opening of the needle valve in subsequent injection events.

The three-phase model using the mixture approach along with the immersed boundary method was then utilised for modelling three-phase cavitation occurring in gear pumps. The numerical model was first validated against the experimental and numerical work from the literature on rotating machinery. After validating the model, simulations are performed on 2D and 3D gear pumps to study the effect of contact between the gears, the effect of increasing RPM and the effect of varying amount of NCG content in the fluid on cavitation dynamics as well as the pump performance. A comparison with experiments has shown that the current model could predict cavitation occurring due to vorticity in the suction chamber accurately; use of the immersed boundary approach has made the modelling of contact ratios greater than unity easier. With sufficient refinement, the approach also produces accurate results in less time as compared to other conventional re-meshing methods, as there is no mesh deformation and interpolation of data involved. It is observed that when the gears are in contact, cavitation occurring in the suction chamber increases due to the isolation of the low-pressure side from the high-pressure chamber. As a result, more fluctuations are present in the outlet flow and a slight increase in mean flow rate is also observed as compared to the case without contact. At lower RPM, cavitation is primarily observed at the core of the vortex forming between the gear teeth opening towards the inlet. With an increase in the rotational speed, vapour cavities are additionally formed at the gear tips due to flow separation. Both intensity and the total volume of cavitation increase with the gear RPM. The effect of NCG on cavitation occurring in gears pump was studied for the first time. This study is conducted by varying the gas content in the flowing liquid from 0% to 1% by volume. The results suggest that the presence of NCG reduces the formation of cavitation without having much impact on the average outlet flow rates. However, an increase in fluctuation in the outlet flow is observed with the increase in gas content. The study was then extended to more realistic three-dimensional gear pumps with side porting and axial clearances and validated the results with experimental observations. Simulations have been performed at high RPM's (6500) and pressure ratios and compared the difference in cavitation and pump performance at 0% and 2% NCG content. Consistent with the 2D observations, the cavitation occurring inside the pump decreases with the increasing NCG. The results are presented in the Appendix E along with the qualitative validation.

## 7.2 Further work

Despite the valuable knowledge gained throughout this project, there is a need for further work to be carried out to achieve a better understanding of the link between the non-condensable gas and cavitation. There are certain aspects of the numerical model that can be improved that would bridge gaps possibly not covered by the current project. As future work, the three-phase model could be enhanced to include the temperature capabilities into the equations of state. This way, the model could be utilised for applications in thermosensitive fluids, where the isothermal manifestation of cavitation does not hold. Furthermore, the current three-phase model assumes zero mass transfer to or from the gas phase. There is a scope for improving this approximation by adding the mass exchange between the gas and liquid/vapour by employing Henry's law (or any other empirical models). This will allow the numerical model to simulate the absorption and dissolution of gas to/from the liquid depending on the local pressure, allowing more accurate predictions. There is also scope for improving the immersed boundary approach by including the capability for predicting Fluid Structural Interaction (FSI) and material deformation. Additionally, the IBM model could be refined further to include adaptive local mesh refinement to capture the wall boundaries more accurately.

On the scope further work on the simulation front, the atomisation study using the LES was validated and simulated on a step-nozzle in this study, however, this could be extended to real size diesel injectors where experimental results are available. There is also scope for improving the wall-adhesion model used in this study, which is the default model available in the Fluent solver that requires prior knowledge to specify the contact angle. This could be extended by adding more advanced models that can handle moving interfaces or models that can compute contact angle based on the net of forces acting on the free surface of the droplet on the fly instead of specifying a fixed or temporal evolution of the contact angle. On the simulation front, the VCO nozzle simulation was performed only during the initial and final stages of the injection cycle, without considering the whole injection cycle. This involved approximating the initial flow field by performing the simulation at a fixed needle lift to establish a stable flow, this approximation will ignore the effect of needle velocity on the initial flow field. There is a scope for simulating the entire injection cycle to see if the needle velocity plays a significant role in the results predicted. Another opportunity is to simulate the effect of dissolved gas (in the released form) in the fluid on cavitation and subsequent atomisation by modelling the gas dissolution and absorption.

On the gear pump, there is an opportunity to perform three-phase flow

simulations on three-dimensional gear pump with side slots and relief groves and validate the numerical model. Since the research group at City University does not yet have the experimental facilities for studying gear pump cavitation, obtaining the experimental data could be challenging. However, in future, the continued collaboration with Rolls-Royce and the test facility at Loughborough University could bridge this gap. The numerical study conducted on the two-dimensional gear pump has shown that at the low-pressure ratio considered (10 *bar*), the increase in NCG% up to 1% does not affect the mean flow rate. This could be assessed further for its validity at higher pressure ratios and NCG%'s.

Moreover, three-phase model in combination with the immersed boundary can be utilised for studying applications with deformable bodies, such as the material deformation of gears due to contact between them, simulation of penetration of drugs into tissue during needle-less injection etc. As a starting point, these simulations could be modelled using a one-way coupling FSI, where the velocity and pressure fields from the CFD simulation will be the input for the structural solver.

## Appendix A

# Grid Resolution for LES simulation

### A.1 Validation of the estimated grid size for primary atomisation

It is known that unlike RANS, the quality of the LES simulation will improve with increasing refinement until the resolution is sufficient for a DNS. However, this is not practical for all applications due to the computational cost involved, and hence there should be some alternative way to assess the quality of the LES simulation. One approach is to perform a grid-independent study, which is again not practical when dealing with huge mesh counts and complex physics which are already computationally expensive. In this study, the quality of the LES simulation is assessed by evaluating the ratio of the resolved turbulent kinetic energy to the total kinetic energy (resolved + modelled). According to (182), if the simulation can resolve at least 80% of the turbulent kinetic energy, then the LES can be considered as well resolved. The results presented in Fig. A.1(a), shows that the ratio of the resolved to the total turbulent kinetic energy is more than 97% throughout the area of interest. This implies that the current mesh resolution is adequate for the application. Additionally, to resolve the near-wall turbulence in a wall-bounded flow, the mesh resolution near the wall should provide at least 5-8 elements in the viscous sub-layer ( $0 < y^+ < 10$ ) with the first cell having a  $y^+ < 1$ . The contour plotted in c shows  $y^+$  values less than 1.5 in most of the critical areas in the nozzle which confirms that the near-wall refinement is acceptable. This also ensures that for the other conditions considered in this study (lower injection pressures), with lower Reynolds number, the overall mesh resolution will be guaranteed. The turbulent energy spectra

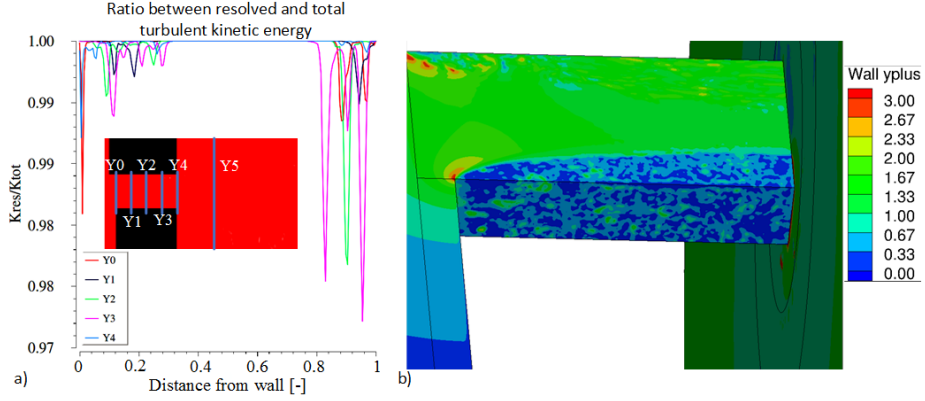


Figure A.1: LES resolution assessment (a) contour of the resolved over total turbulent kinetic energy at mid-span section and (b) along with vertical location at given locations, (c) Wall  $y^+$ . All plots are for the extreme condition considered in this study ( $P_{inj}=5\text{bar}$ ).

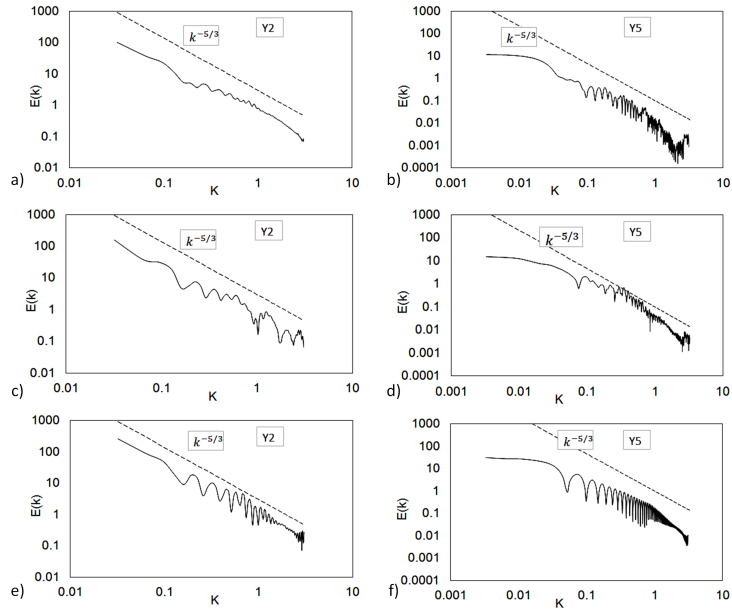


Figure A.2: Turbulent energy spectra at midsection of nozzle (left column) and 5mm downstream the nozzle-exit in spray region (right column) for (a, b) 2bar, (c, d) 3bar and (e, f) 5bar injection pressure.

calculated inside and outside of the nozzle at selected locations are shown in Fig. A.2. The spectrum obtained at both locations reproduced the Kolmogorov  $-5/3$  law, a direct consequence of resolving all the large eddies that represent the major part of the inertial subrange. At very high wavenumbers, close to the dissipative range the energy spectra show pileup of Kinetic energy which is a numerical artefact associated with the local energy transfer cut-off. Such pile-up of energy at high wavenumbers was also observed by (183; 184).

## Appendix B

# Comparison between the mixture and VoF approach for three-phase modelling and the influence of surface tension.

A two-dimensional study conducted on the same nozzle as presented in Chapter 4 with the same grid resolution with an objective to compare two different approaches for modelling the additional gas phase, the diffused interface mixture approach similar to (185) and the sharp interface VoF approach similar to (164), both implemented in Ansys Fluent. It is obvious that the interface will be better captured by the VOF approach for a given mesh resolution. However, it is also our intention here to see the effect of interfacial forces such as surface tension on the spray structure for the operating conditions considered. Owing to the objectives, a laminar flow approximation is made in order to simplify the problem. A comparison between the predictions from the two approaches (the mixture approach and the VoF approach) is given in Fig. B.1 with an injection pressure of 3bar applied at the inlet. It should be noted that the mixture model used in this study does not take into account the surface tension between the water and air. This is not a limitation of the mixture model, but a choice we made for comparing the effect of surface tension with a VoF model where surface tension of 0.0728N/m is assumed at the water-air interface. Some studies utilising the surface tension for a diffused interface mixture model can be

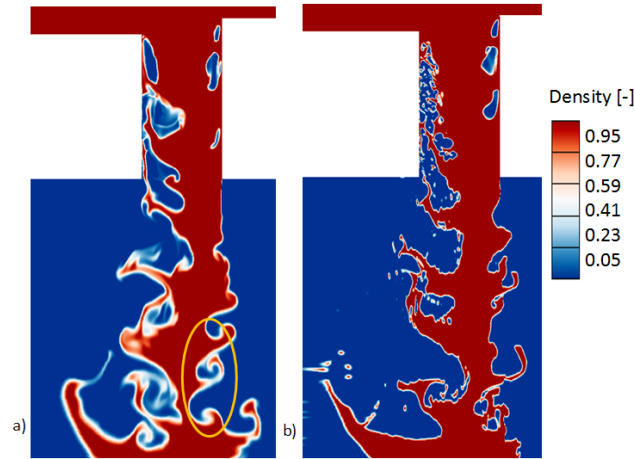


Figure B.1: Comparison between (a) mixture approach and (b) VoF approach for modelling atomization. Contours of mixture density normalized with the water density.

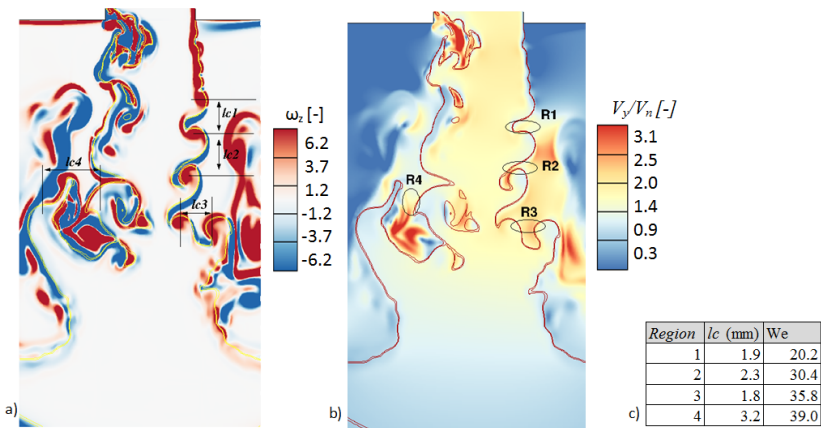


Figure B.2: Instantaneous contours of (a) vorticity and (b) velocity magnitude from two-dimensional simulation using the mixture model (without surface tension effects). (c) The calculated Weber numbers at the highlighted regions.



found in (186), (187) and (188). It is observed that the larger structures are well captured using both approaches. However, the smaller structures such as water ligaments and droplet formations are not captured well using the mixture model. The effect of surface tension is apparent in the smaller structures, where the Kelvin-Helmholtz instabilities produce shallow structures at the interface when surface tension is not present, as highlighted in Fig. B.1a, whereas more flatten edges with thin ligaments can be observed in Fig. B.1b when surface tension is present. This was further examined by estimating the local Weber number in the primary atomization region. In Fig. B.2, the contours of the instantaneous vorticity and the velocity magnitude are shown, highlighting the regions where the Weber number is calculated, and the calculated values are given as a table in Fig. B.2c. The low Webber number values calculated ( $We \sim 20$  to  $40$ ) indicates that the surface tension can have a significant effect on the spray structure, hence it is considered for the three-dimensional simulations presented in Chapter 4. The Weber number is calculated using the relation  $We = (\rho_g v^2 l_c) / (\sigma)$ , where  $l_c$  is the characteristic length,  $v$  is the local velocity magnitude and  $\sigma$  is the surface tension.

## Appendix C

# Validation of the immersed boundary model

To use the IBM for the simulation of complex multiphase phenomena with geometric motion, it is deemed necessary to validate the methodology in simpler cases before its application in more complex problems.

### C.1 Oblique impact of water jet on a planar wall

The IBM method is first validated against the theoretical results obtained by (11) for the pressure distribution when an oblique water jet impacts on a planar surface. The simulation is performed as a 2D planar steady state with VoF approach for modelling the presence of ambient gas (189). The contours of the velocity, coefficient of pressure and the liquid volume fraction after the steady state condition is reached is shown in Fig. C.1. The comparison of the pressure distribution on the wall between the current numerical model and the exact solution shows a perfect match between them as can be seen from Fig. C.2.

### C.2 Multiphase flow in an expanding chamber

In this section the validation of the IBM for moving wall problem is presented using a test case of expanding chamber (189) as shown in Fig. C.3. The 1-D chamber is  $4m$  long and is initialised with a pressure of  $650kPa$ . The domain is extended by  $0.04m$  on either sides in order to apply the immersed boundary. The domain is discretized to have a cell size of  $0.004m$ . The wall on the right side move towards the left with a velocity of  $3m/s$ . The left and right side walls are applied with fixed pressure boundary conditions. The Mix-

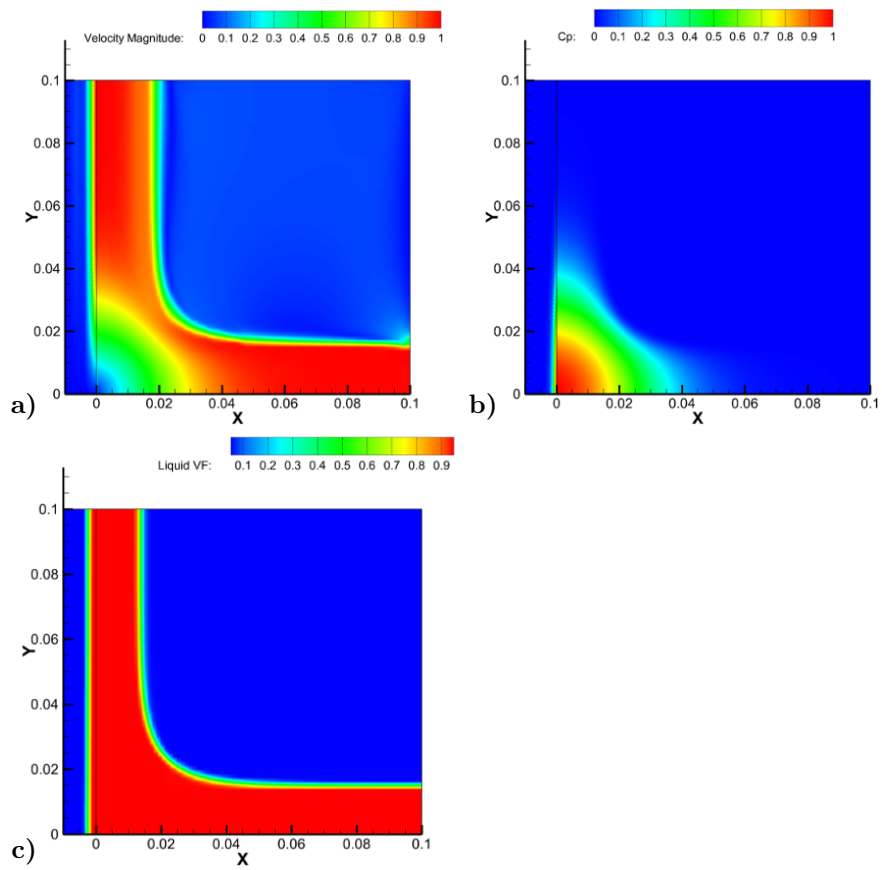


Figure C.1: Contours of a) velocity magnitude b) coefficient of pressure and c) liquid volume fraction. Flow is from right to left. The black line at  $x=0$  is the immersed boundary representation of the planar wall and  $x$ -axis is the centre of the jet.

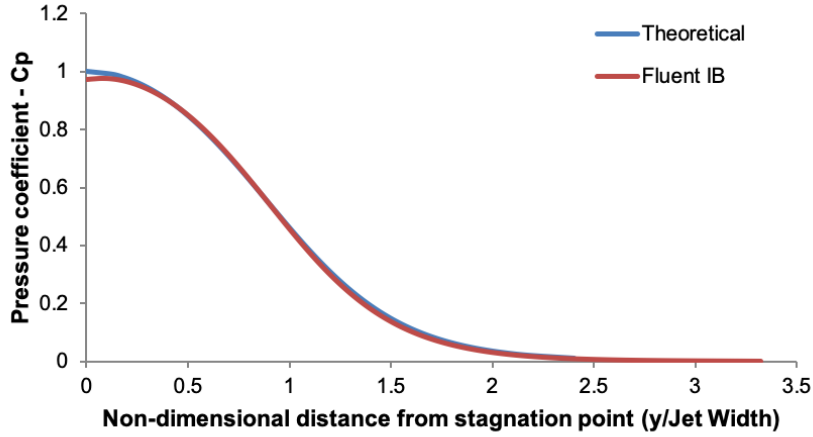


Figure C.2: Comparison of pressure coefficient along the radial direction between the IBM and the exact solution from Taylor (11)

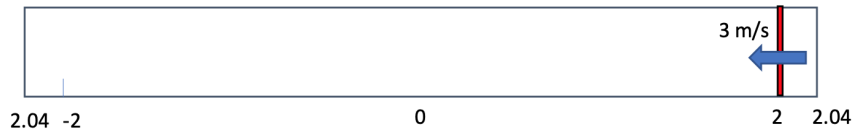


Figure C.3: Computational domain of the chamber with moving wall

ture Model implemented in Ansys Fluent solver is used for modelling the phase change. A weakly compressible diesel fuel is used as the liquid which cavitates to form diesel vapour. The liquid diesel has the properties  $P_{ref} = 19,213.09 Pa$ ,  $\rho_{ref} = 813.9227 kg/m^3$ , reference bulk modulus  $K_o = 1.513996^{+09} Pa$ , the density exponent of  $n = 7.15$  and the viscosity  $\mu = 0.0021 kg/ms$ . The diesel vapour has a density  $\rho_v = 1.234821 kg/m^3$ , viscosity  $\mu_v = 7.5^{-06} kg/ms$  and a vapour pressure of  $19,213.09 Pa$ . The simulation are performed with a fixed time step of  $50 \mu s$ . For cavitation modelling, the Zwart-Gerber-Belamri model was used with the assumptions of bubble diameter  $1 \mu m$ , nucleation site volume fraction  $5^{-04}$ , evaporation coefficient 50 and condensation coefficient 0.025. The comparison of CFD numerical results against the solution of an Arbitrary Lagrangian-Eulerian HLLC solver (ALE-HLLC) (190; 191) at  $t = 60 ms$  are presented in Fig. C.4.

### C.3 Rotating cross

In order to evaluate the implemented IBM and cavitation models for applications in rotating machinery such as pumps, a comparison is made with the

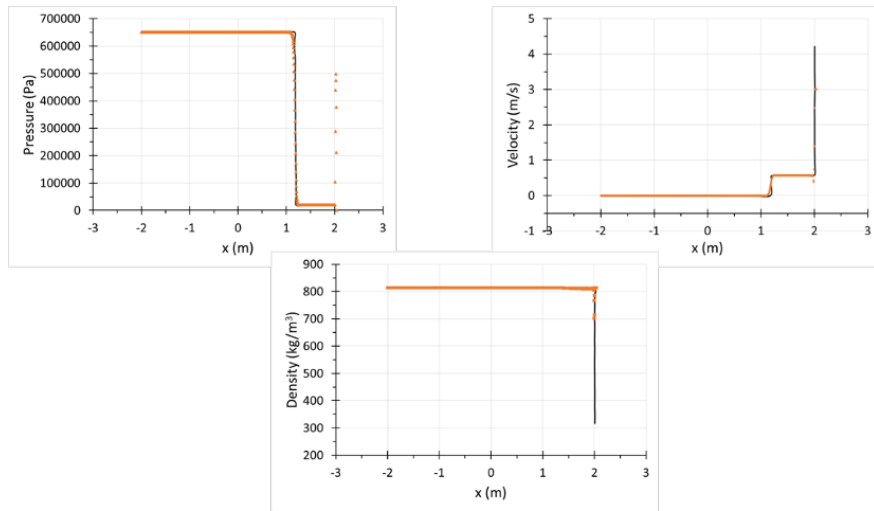


Figure C.4: Comparison of IBM CFD simulation results with the 1-D model for an expanding chamber at  $t = 60ms$

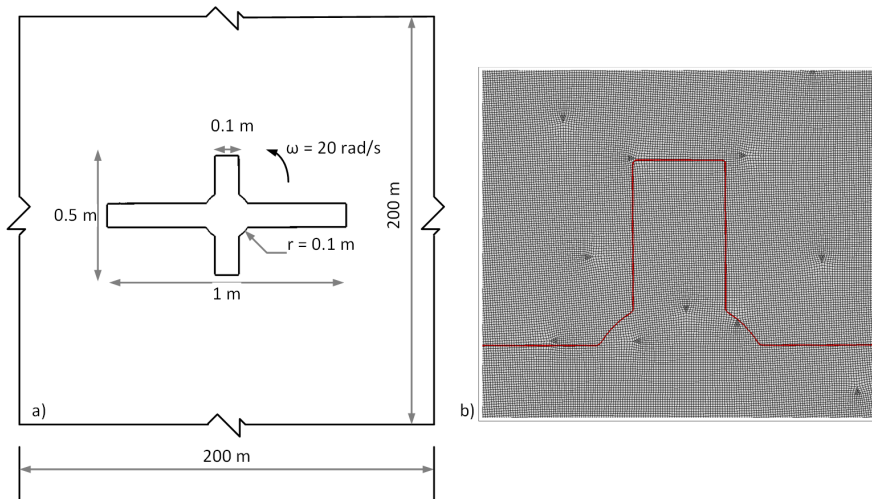


Figure C.5: a) Computational domain and b) mesh used for rotating cross simulation

test case from the published work of (12). A two-dimensional cross, rotating counter-clockwise with an angular velocity of  $20rad/sec$  in a large tank containing stationary liquid (water) is simulated. A square region of  $200m$  side is used as the computational domain to isolate any effect of the pressure waves reflected from the boundaries. The domain and the computational mesh used for simulation is shown in Fig. C.5. The mesh is refined such that there are 40 cells across the shortest side (thickness) of the cross. The flow field is initialised with  $1bar$  absolute pressure, and the liquid is held at rest. A comparison of the

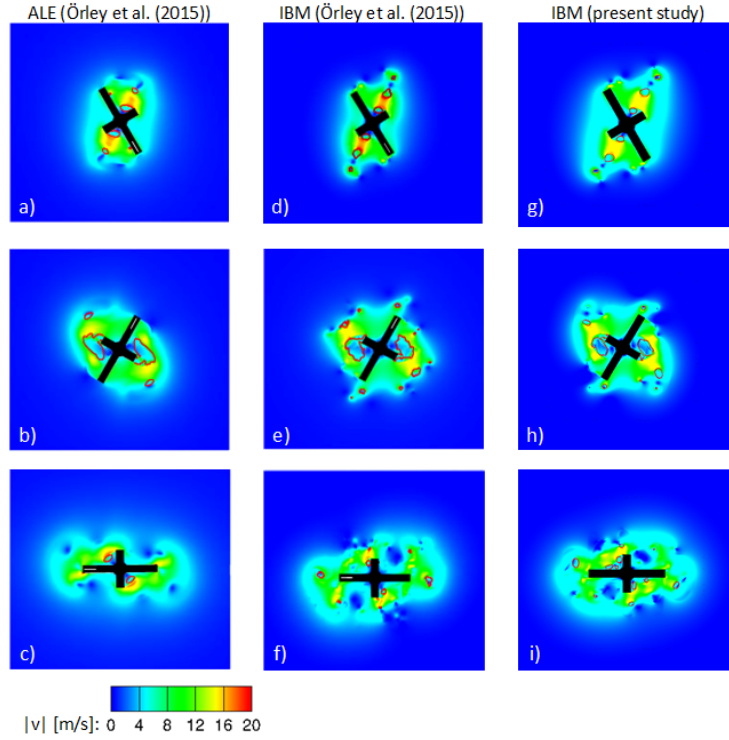


Figure C.6: Results showing comparison of instantaneous of velocity magnitude and 1% vapour volume fraction (in red) between (a-c) ALE approach and (d-f) immersed boundary approach, both from Örley et al. (12) and (g-i) current immersed boundary model; after  $120^\circ$ ,  $240^\circ$ , and  $360^\circ$  of rotation from the start

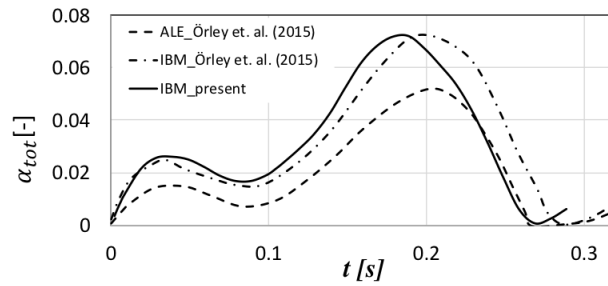


Figure C.7: Comparison of integral vapour volume fraction over time between ALE and IBM approach from Örley et al. (12) and with the current IBM model.

results obtained from the current model and that from (12) is shown in Fig. C.6. The obtained results are in good agreement when compared with both ALE (a-c) and immersed boundary approaches (d-f) used by (12). The validation of the time evolution of the integral vapour volume fraction given in Fig. C.7 also shows a very close match with the results from (12).

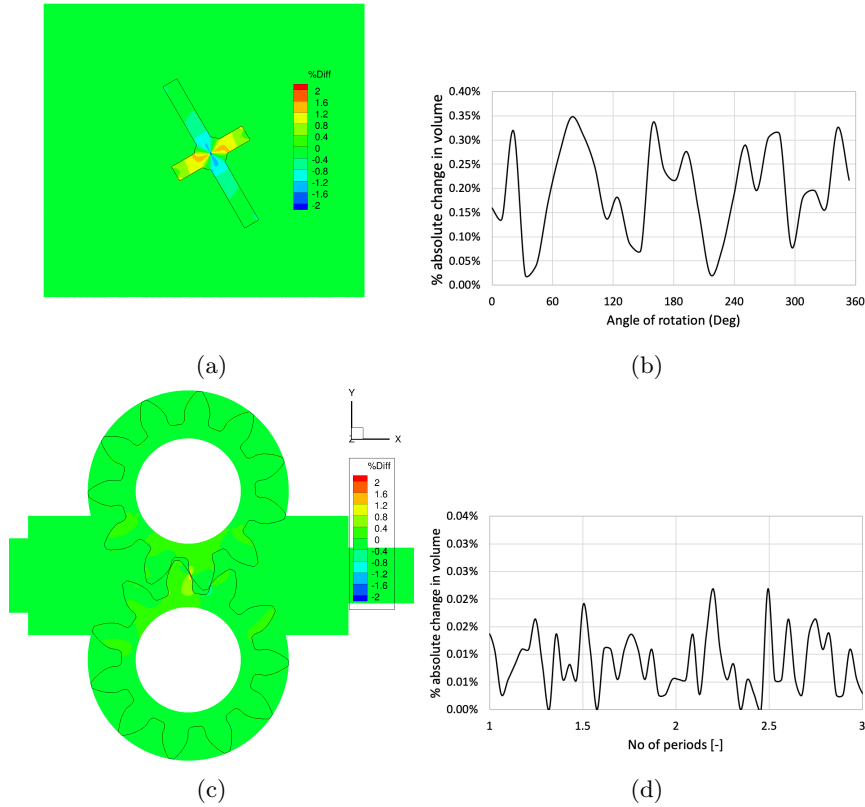


Figure C.8: Calculated percentage error between the velocity and the target velocity.

## C.4 Geometric conservativeness of the IBM model

The nature of the IBM implemented is such that although it satisfies the continuity near the solid wall, it is impossible to guarantee absolutely no penetration of flow through the walls, as the forcing term is proportional to the fluid velocity. Hence a different perspective is used for checking the correctness of the model; the mismatch between the velocity and the target velocity in cells marked as walls is evaluated in the domain. The difference between these value will be the measure of the mass leak through the wall. In most of the cases considered in this study, this value is found to be less than 2% error as can be seen from Fig. C.8(a, b). In addition, the conservation of the solid is evaluated by monitoring the change in total solid volume with respect to time for both rotating cross and gear pump as shown in Fig. C.8(c, d). The total change in solid volume (area for 2D cases) is less than 0.3% in most of the cases. Hence it is valid for practical applications.

## Appendix D

# Validation of the 3-phase mixture model approach

### D.1 Three-phase flow simulation on 2D Hydrofoil

To study the effect of NCG on cavitation formation, a two-dimensional simulation was performed on a hydrofoil geometry taken from the work of (13). The hydrofoil geometry used for the simulation is shown in Fig. D.1.

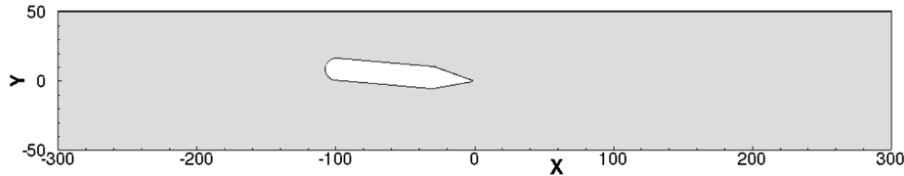


Figure D.1: Computational domain with hydrofoil geometry from the work of Dular and Coutier-Delgosha (13)

The turbulence in this study is modelled using the  $k - \epsilon - RNG$ . The initial simulations using  $k - \epsilon - RNG$  model failed in predicting cavitation cloud shedding due to overestimation of the eddy viscosity. Hence, the turbulent viscosity in the two-phase region is corrected using the relation from (64). Computations were performed by varying the NCG content from 0% to 5% keeping the inlet and outlet boundary conditions constant. Pressure boundary conditions are used at the inlet and outlet. At the inlet, the total pressure is adjusted such that the mean velocity reaches  $\sim 13m/s$  at the inlet and  $1bar$  pressure is set at the outlet boundary. The results from the simulation with 0% gas fraction is validated against the results from (13) and show a very good match between



them. Since there were no data available at non-zero gas fractions, the results for non-zero gas fractions could not be validated. However, the results obtained are inline with the understanding of the phenomena.

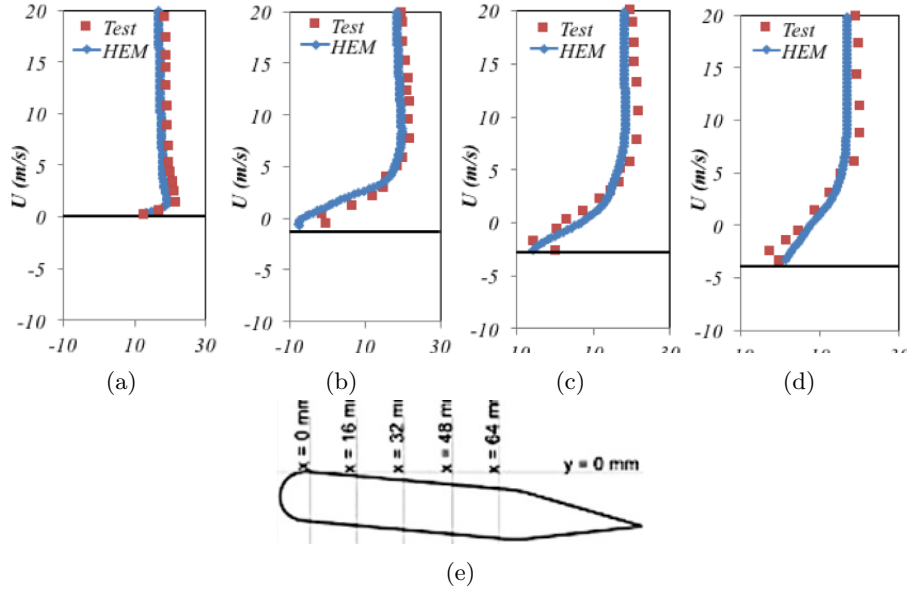


Figure D.2: Mean x-velocity profile at different locations a)  $0\text{mm}$ , b)  $16\text{mm}$ , c)  $32\text{mm}$ , d)  $48\text{mm}$  as shown in e).

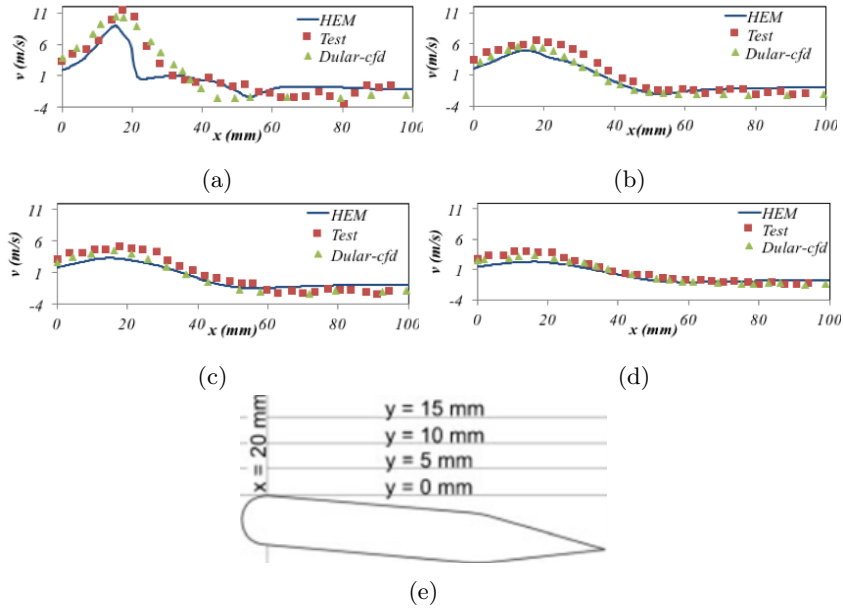


Figure D.3: Mean y-velocity profile at different locations a)  $0\text{mm}$ , b)  $5\text{mm}$ , c)  $10\text{mm}$ , d)  $15\text{mm}$  as shown in e).

Figure D.2 and Fig. D.3 shows that the mean x and y velocity profiles at different locations from the current model validated against the test results from (13). The predicted velocity profiles show good overall agreement with the experimental values. The validated two-phase model was extended to include the third phase (NCG) using a mixture approach and simulations were performed to study the effect of non-dissolved gas.

Figure D.4 shows the effect of increasing the volume fraction of NCG from 0%-5%. From Fig. D.4a, it can be noticed that the amount of gas does not have much effect on the mean velocity profiles over the hydrofoil. However, a decrease in vapour formation is observed with an increase in gas content (Fig. D.4b). This is predominant at  $x=16$  and  $x=32$  where maximum flow acceleration occurs leading to lower pressure. When the pressure in the flow drops, first the gas expands and prevents the formation of vapour. Due to this fact, even though the total void fraction increases, the void due to vapour decreases. This is evident from Fig. D.4(b and c). The mean volume fraction of vapour over the hydrofoil is shown in Fig. D.5. Based on the current results, it can be concluded that the intensity and distribution of vapour volume fraction decrease with the increase in gas content.

## D.2 Three-phase flow simulation on 2D Step-Nozzle

Two-dimensional simulations were performed using water as the working fluid to on a 2D step nozzle from the work of (14). The objective of the simulation is to check the capability of the three-phase model in predicting the jet formation and its evolution in the presence of NCG. The computational domain with the hexahedral mesh with refinement near the boundary layer is shown in Fig. D.6.

The simulations were performed assuming atmospheric pressure (1 *bar*) at the outlet and 2.6 *bar* at the inlet. At this condition, the flow separates from the inlet step and cavitation occurs in the separated shear layer. The average velocity in the nozzle at this pressure is around 15.5 *m/s* with a Reynolds number in the range of 33500. Since the default RANS model is found to stabilize the flow and was unable to predict cavitation shedding, the Reboud correction from the work of (64) for turbulent viscosity is used with the  $k - \epsilon - RNG$  turbulence model.

Figure D.7 shows the evolution of the liquid jet over time with three different compositions of NCG content in the water. The model could capture the phenomena expected during the jet evolution like leading-edge umbrella formation, Helmholtz instabilities at the interface and breakup. The results could not

be validated directly with the experiments from (14) due to the unavailability of any data presented by the authors on the particular nozzle. However, a detailed representation of the liquid jet evolution for a different nozzle geometry is presented by (15). The current results show a good match with the results presented in (15) as shown in Fig. D.8, where the liquid jet features such as the leading edge umbrella formation and the instabilities at the interfaces are observed. Since the current model used a mixture model approach with moderate grid resolution, the interfaces are not sharp. However, with a proper resolution and interface capturing method (such as the VOF approach) the current model can capture the interface more accurately. Figure D.7 also compares the effect of NCG in modifying the cavitation and jet formation, for which three different percentages of NCG is considered. The evolution of the jet structure does not seem to be much affected by the gas content. However, the break-up of the jet occurs much earlier with an increase in NCG which can be observed from Fig. D.7d.

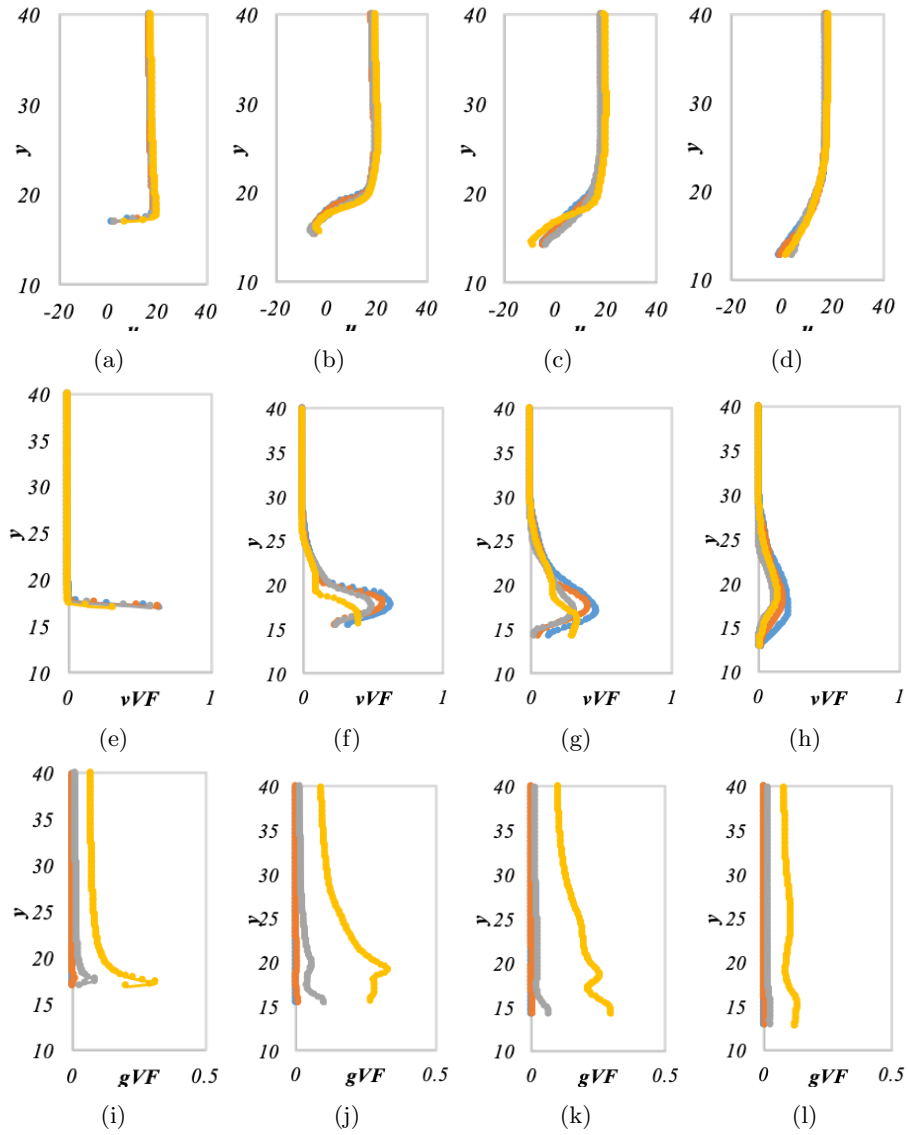


Figure D.4: Effect of NCG on the (a-d) mean u velocity (e-h) mean vapour volume fraction and (i-l) mean gas volume fraction. a, e, i) 0mm, b, f, j) 16mm, c, g, k) 32mm, d, h, l) 48mm as shown in e)

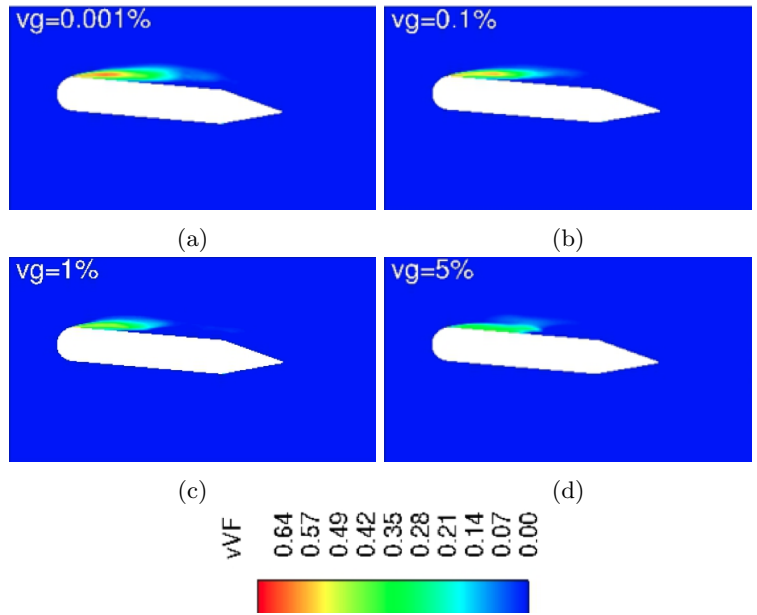


Figure D.5: Contours of mean vapour volume fraction for different gas volume fraction.

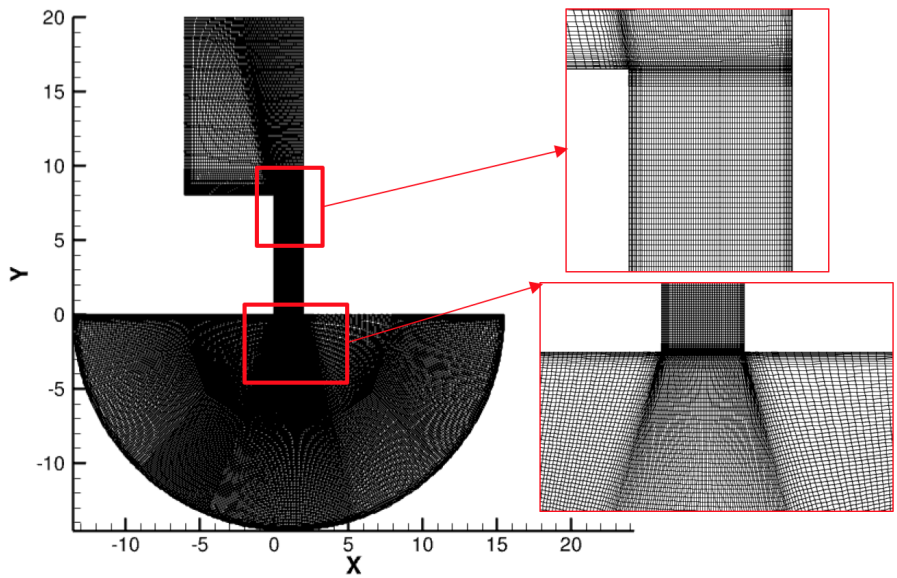


Figure D.6: The computational domain with hexahedral numerical mesh showing the extended circular. The geometry is step-nozzle is obtained from the work of Sou et al. (14).

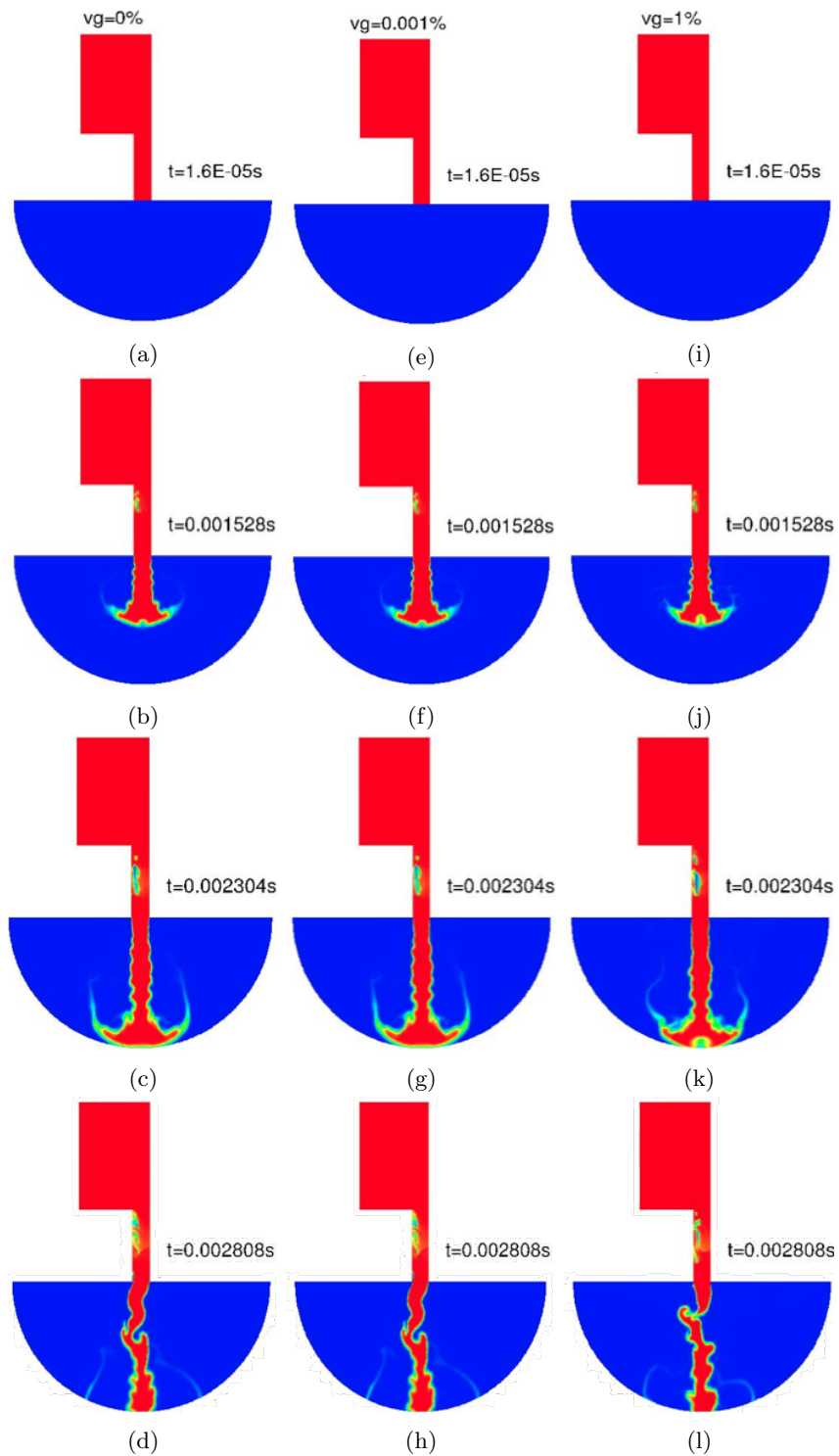


Figure D.7: Evolution of liquid jet shown using contours of mixture density at different NCG%. (a-d) 0% NCG, (e-h) 0.001%, (i-l) 1% NCG

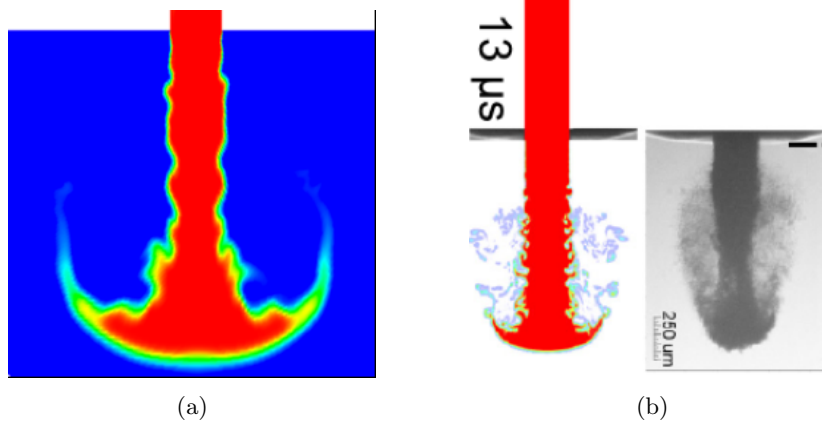


Figure D.8: Comparison of the liquid jet structure between the current simulation (a) and the results from Ghiji et al. (15)(b)

## Appendix E

# Numerical simulation of 3-phase flow in 3D gear pump

After validating the model for two-dimensional simulations, the numerical model was used for simulating 3D gear pump. The geometry of the pump and the numerical grid used for the simulation is shown in Fig. E.1. A hybrid meshing approach with hexahedral mesh in the gearing zone including the inlet and outlet chamber and a tetrahedral mesh with prism layers in the boundary immediately next to the chambers is used. The inlet and outlet domains are further extended to decouple the boundary effects from the flow in the gearing zone. The grid near the region where two gears mesh and the region near the tip of the gears are further refined to capture the flow feature in the small clearances as shown in Fig. E.1c. To reduce the computational cost, the region inside the gears, which is the solid domain, is excluded from the simulation, as shown in Fig. E.1b. The simulations are performed at 6500 RPM with an inlet pressure of 60 *psia* and a delivery pressure of 900 *psia* with water as working fluid, consistent with the relevant experimental study. The results obtained are validated against the results from the experiments (unpublished) conducted by the Rolls-Royce University Technology Centre at the Loughborough University. The numerically predicted cavitation region is in reasonable agreement with the vapour cavities observed in the experimental results as shown in Fig. E.2.

Two different simulations are performed, one with 0% NCG and the other with 2% of NCG in the water, to compare their effects on cavitation. In Fig. E.3, a comparison between the evolution of cavitation under both conditions considered are presented. It is evident from the figure that the amount of cavitation



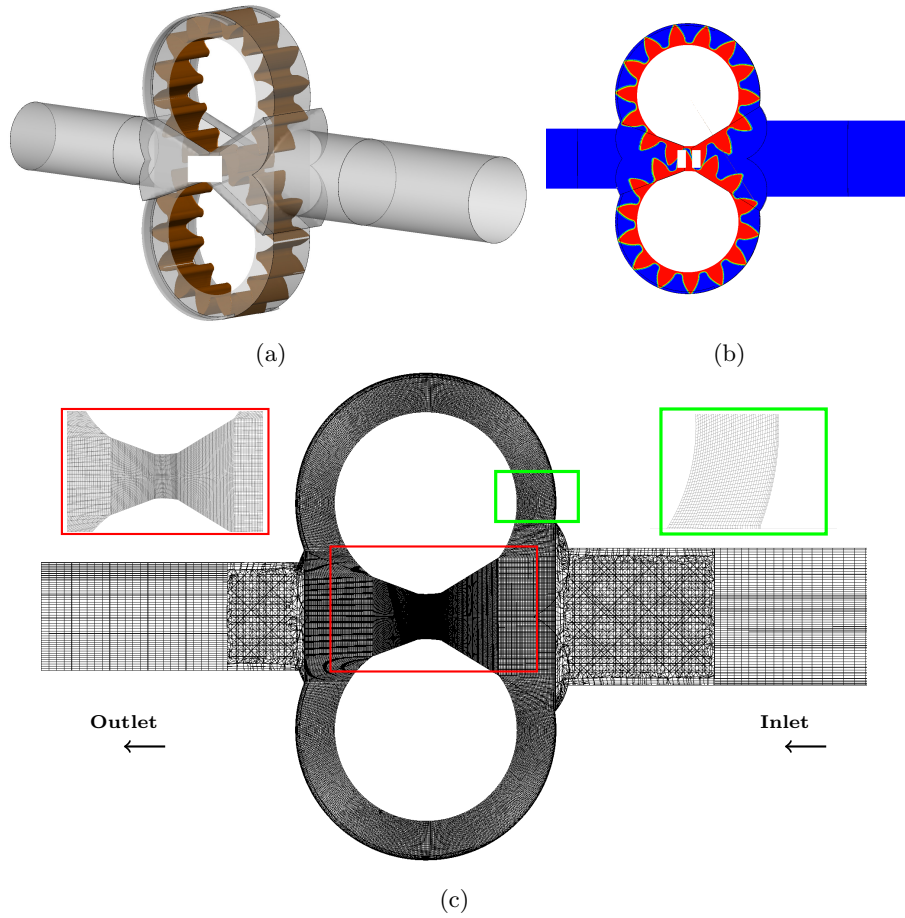


Figure E.1: a) Gear pump geometry represented using iso-surface of 50% IBM masking function b) IBM representation of gears at the mid-plane c) Numerical hybrid mesh.

decreases with the increase in NCG%. This observation is consistent with the results obtained from the 2D gear pump simulations. The reduction in cavitation is further quantified by computing the scalar integral of the vapour volume fraction in the fluid domain. A reduction in cavitation by  $\sim 30\%$  is observed with an increase in NCG content by 2% (by volume), as can be seen from Fig. E.4, caused by the expansion of gas present in the fluid.

The effect of NCG on mass flow rate at the inlet and outlet is shown in Fig. E.5. The mean flow rate predicted by the current numerical simulation ( $\sim 4.56 \text{ l/s}$ ) is in good match with the experimental flow rate, which is  $\sim 4.66 \text{ l/s}$ . The mean flow rate at the inlet and outlet does not seem to be affected by the increase in gas content. This observation is also consistent with the observation from the 2D simulation. However, more fluctuation in the flow rate is observed

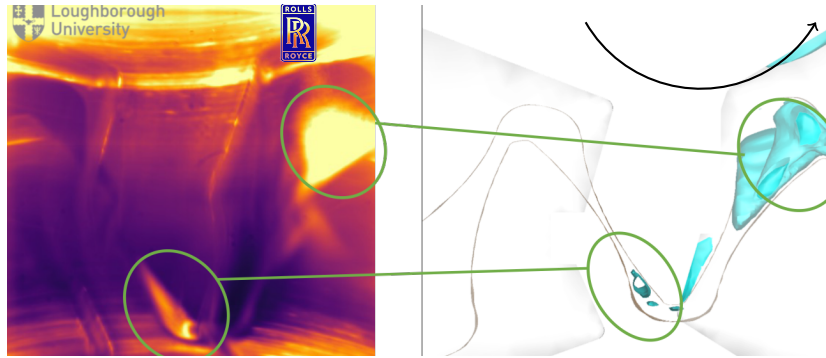


Figure E.2: Validation of the cavitation prediction from the current study with the experimental results obtained by Rolls-Royce University Technology Centre at Loughborough University. 50% vapour volume fraction shown in cyan colour.

when gas is present in the fluid.

The evolution of the pressure during one pitch rotation with 0% and 2% NCG content is shown at the mid-plane of the domain in Fig. E.6. It can be noticed that the pressure field at 2% NCG is more fluctuating than that observed at 0% NCG. This is primarily due to the increased compressibility of the mixture in the presence of gas. By comparing Fig. E.3 and Fig. E.6, one can correlate the cavitation observed in the inlet chamber with the corresponding pressure fields. It is noted that the low-pressure zones in the inlet chamber at 2% NCG is much smaller than what is observed at 0% NCG, resulting in reduced cavitation. The high-pressure spots seen near the gear surface in the contours (see Fig. E.6(e and iv)) is the consequence of the violent collapse of the vapour bubbles which can lead to material erosion due to cavitation. The non-physical rise in pressure observed in the trapped volume between two gears in a 2D simulation (ref Fig. 6.5) does not appear in the present 3D simulation, due to the presence of side porting (ports are hidden due to the geometry being an intellectual property of Rolls-Royce). During pump operation, four types of leakages are typically observed from a gear pump, leakage through the tip clearance in the radial direction, leakage through axial clearance, leakage through the bearing clearance, the leakage through the inter-tooth clearance. In the present study, the leakage through the axial and bearing clearances are not considered and only the leakage occurring through tip clearance and inter-tooth clearances are considered. The contours shown in Fig. E.7 shows the velocity distribution in the mid-plane of the pump during one pitch for 0% and 2% NCG. The velocity jetting at the outlet chamber, the liquid jet formed in the clearance region between the gears and at the tip of the gears can be seen from these figures.

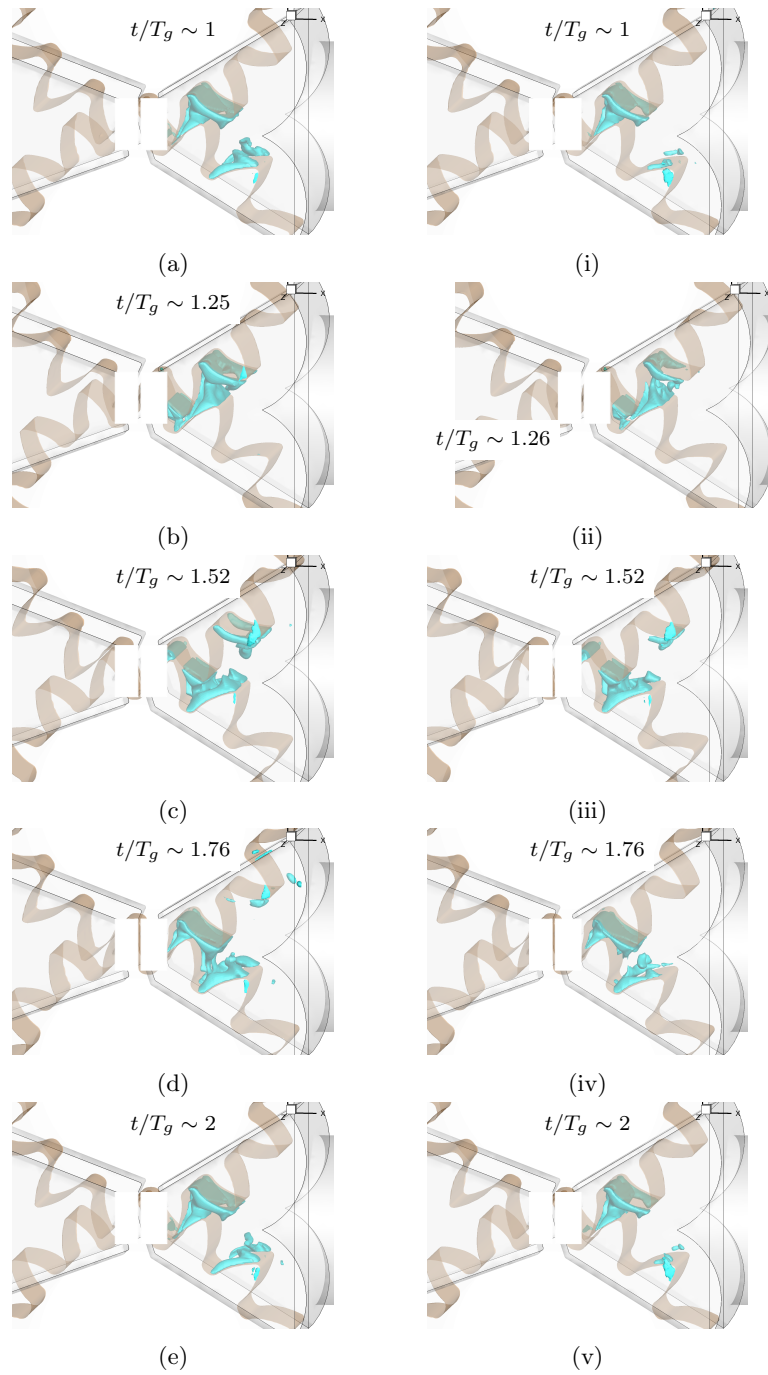


Figure E.3: Evolution of vapour volume fraction during one gearing pitch. (a-e) 0% NCG and (i-v) 2% NCG.  $T_g = 14xRPM/60$  is the term used to nondimensionalise time. 50% vapour volume fraction shown in cyan colour.

Due to the limited availability of the experimental results, this study was

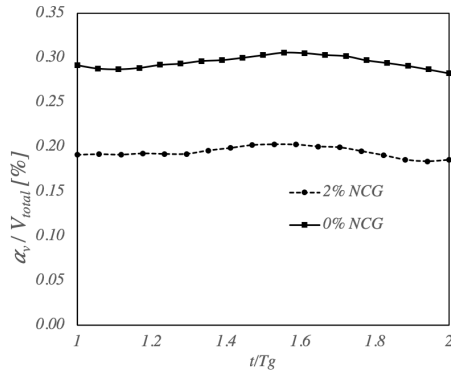


Figure E.4: Comparison of the volume integral of vapour volume fraction normalized using the total flow volume over a gearing period with 0% and 2% of gas volume fraction at 6500 RPM.

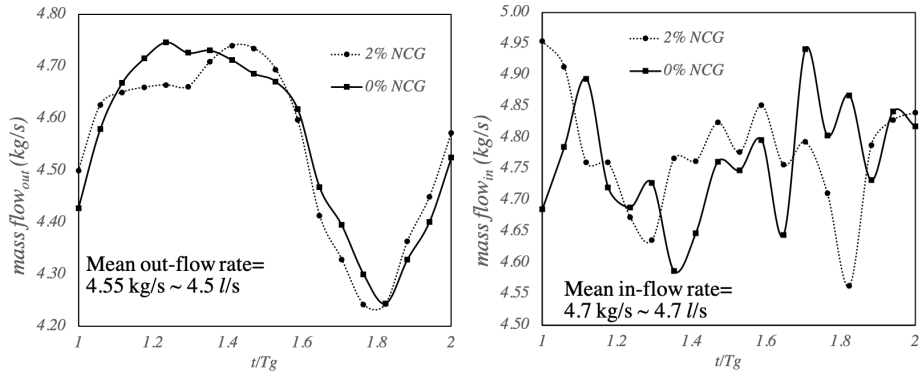


Figure E.5: Velocity contour during one gearing pitch. (a-e) 0% NCG and (i-v) 2% NCG.

limited and validated only with the qualitative predictions of vapour volume fraction at 0% NCG. However, there is a scope that this study can be further extended to validate the flow rates, flow fields and pressure fluctuations at the inlet and outlet for both degassed (0% NCG) and gassed (with some % of NCG) conditions. Further more, the CFD simulation can be further improved by increasing the mesh resolution and also including the axial clearances to the computational model.

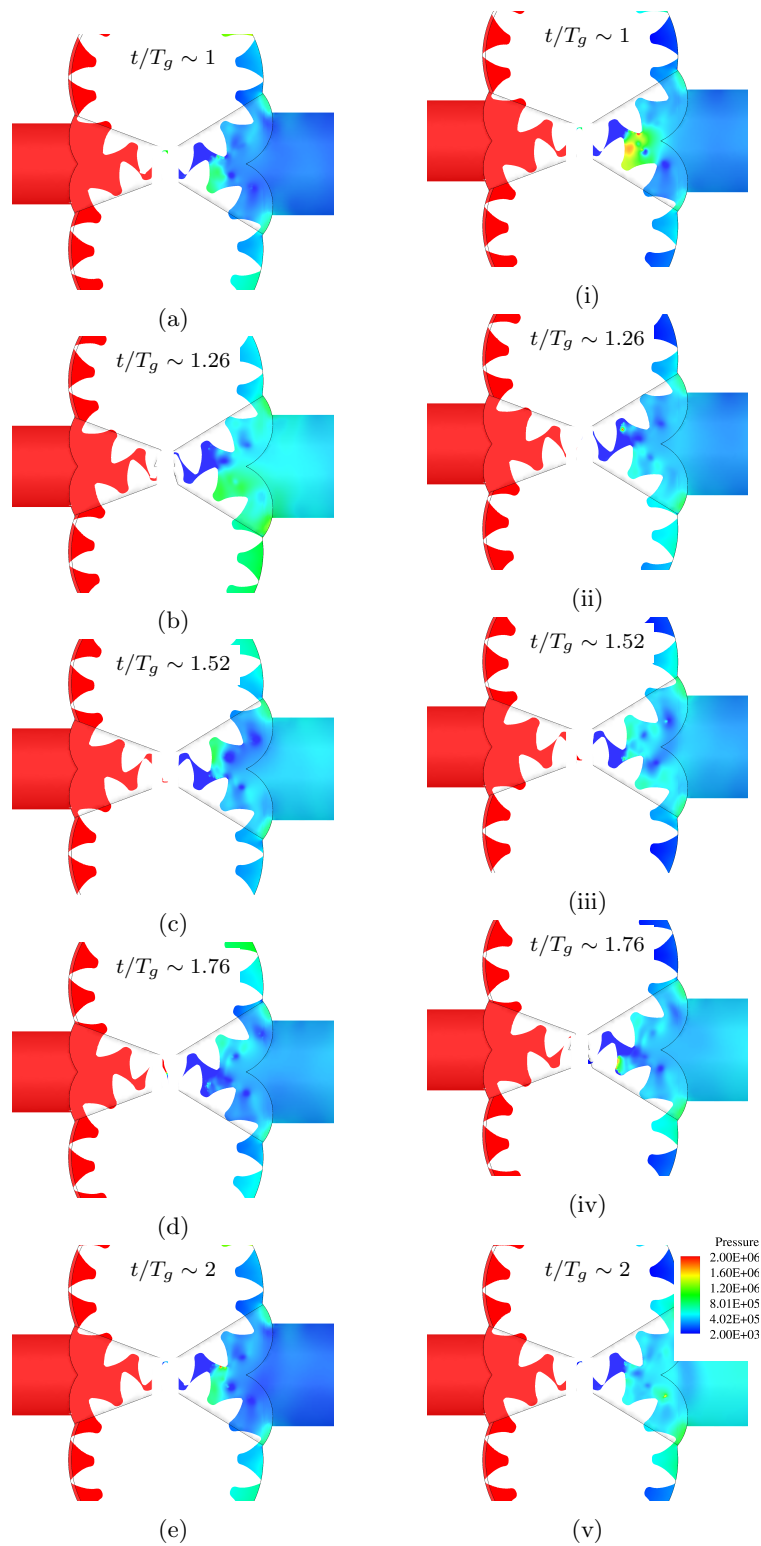


Figure E.6: Pressure distribution during one gearing pitch. (a-e) 0% NCG and (i-v) 2% NCG.

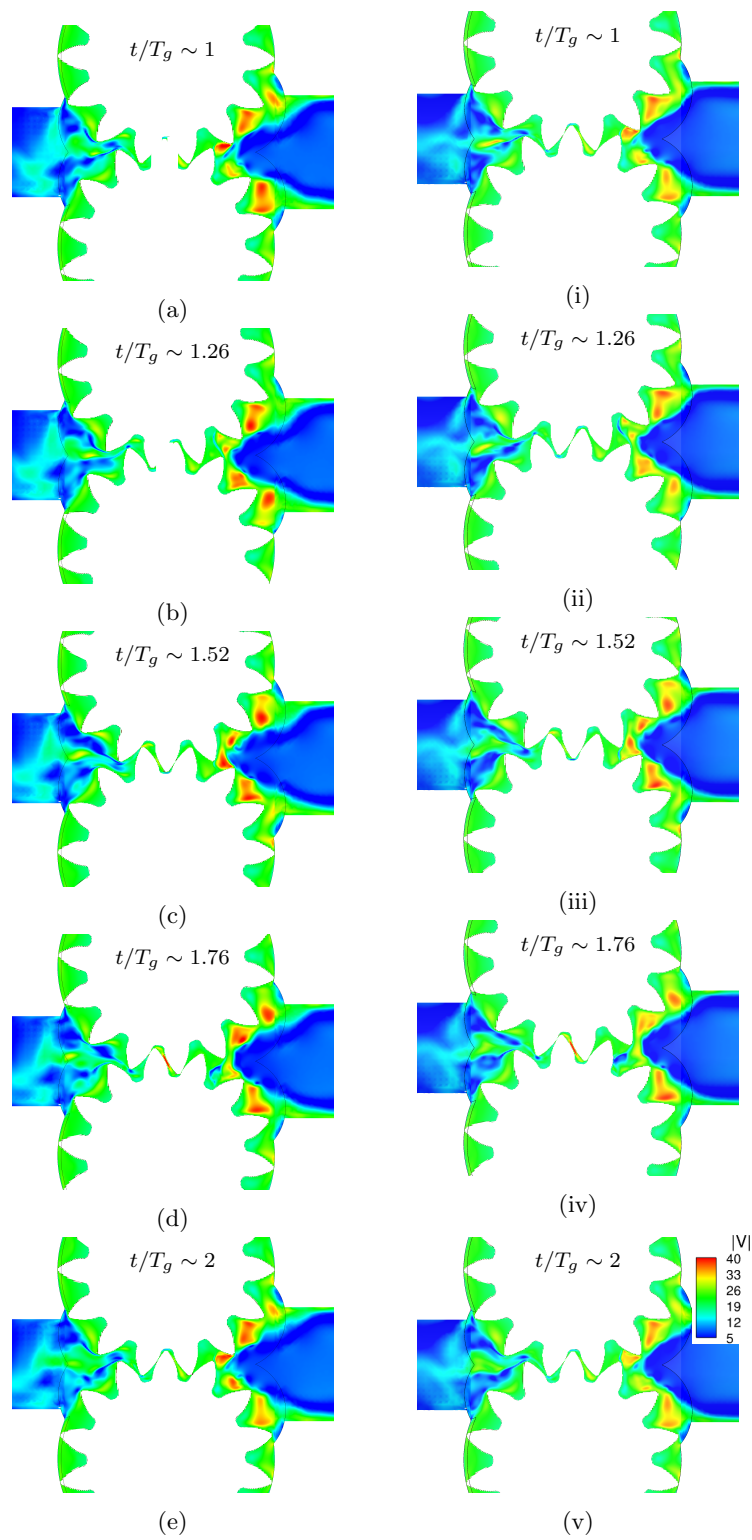


Figure E.7: Velocity contour during one gearing pitch. (a-e) 0% NCG and (i-v) 2% NCG.

# Bibliography

- [1] B. Abderrezzak, Y. Huang, A contribution to the understanding of cavitation effects on droplet formation through a quantitative observation on breakup of liquid jet, *International Journal of Hydrogen Energy* 41 (2016) 15821–15828. doi:[doi:10.1016/j.ijhydene.2016.04.209](https://doi.org/10.1016/j.ijhydene.2016.04.209).
- [2] M. Gold, R. Pearson, J. Turner, D. Sykes, V. Stetsyuk, G. de Sercey, C. Crua, **M. G. Mithun**, F. Koukouvinis, M. Gavaises, Simulation and Measurement of Transient Fluid Phenomena within Diesel Injection, 2019, pp. 1–15. URL: <https://www.sae.org/content/2019-01-0066/>. doi:[doi:10.4271/2019-01-0066](https://doi.org/10.4271/2019-01-0066).
- [3] E. Winklhofer, E. Kull, E. Kelz, A. Morozov, Comprehensive hydraulic and flow field documentation in model throttle experiments under cavitation conditions, *Proceedings of the ILASS-Europe Conference, Zurich* (2001) 574–579. doi:[doi:10.13140/2.1.1716.4161](https://doi.org/10.13140/2.1.1716.4161).
- [4] H. Naseri, *Modelling of Nozzle Cavitation in Newtonian and Viscoelastic Fluids*, Ph.D. thesis, City, University of London, UK, 2018.
- [5] P. Antoniak, J. Stryczek, Visualization study of the flow processes and phenomena in the external gear pump, *Archives of Civil and Mechanical Engineering* 18 (2018) 1103–1115. URL: <https://doi.org/10.1016/j.acme.2018.03.001><http://dx.doi.org/10.1016/j.acme.2018.03.001>. doi:[doi:10.1016/j.acme.2018.03.001](https://doi.org/10.1016/j.acme.2018.03.001).
- [6] R. Mittal, G. Iaccarino, Immersed Boundary Methods, *Annual Review of Fluid Mechanics* 37 (2005) 239–261. URL: <http://www.annualreviews.org/doi/10.1146/annurev.fluid.37.061903.175743>. doi:[doi:10.1146/annurev.fluid.37.061903.175743](https://doi.org/10.1146/annurev.fluid.37.061903.175743). [arXiv:1007.1228](https://arxiv.org/abs/1007.1228).
- [7] J. Manin, L. M. Pickett, K. Yasutomi, Transient cavitation in transparent diesel injectors, in: *ICLASS 14th Triennial International Conference on Liquid Atomization and Spray Systems*, 2018.

- [8] A. Roger Ull, Study of mesh deformation features of an open source CFD package and application to a gear pump simulation (2012). URL: <http://upcommons.upc.edu/handle/2099.1/16479>.
- [9] R. Castilla, P. Gamez-Montero, N. Ertürk, A. Vernet, M. Cousirat, E. Codina, Numerical simulation of turbulent flow in the suction chamber of a gearpump using deforming mesh and mesh replacement, *International Journal of Mechanical Sciences* 52 (2010) 1334–1342. URL: <http://linkinghub.elsevier.com/retrieve/pii/S0020740310001578>. doi:doi:10.1016/j.ijmecsci.2010.06.009.
- [10] J. Stryczek, P. Antoniak, O. Jakhno, D. Kostyuk, A. Kryuchkov, G. Belov, L. Rodionov, Visualisation research of the flow processes in the outlet chamber–outlet bridge–inlet chamber zone of the gear pumps, *Archives of Civil and Mechanical Engineering* 15 (2015) 95–108. doi:doi:10.1016/j.acme.2014.02.010.
- [11] G. Taylor, Oblique impact of a jet on a plane surface, *Philosophical Transactions of the Royal Society of London. Series A, Mathematical and Physical Sciences* 260 (1966) 96–100. doi:doi:10.1098/rsta.1966.0034.
- [12] F. Örley, V. Pasquariello, S. Hickel, N. A. Adams, Cut-element based immersed boundary method for moving geometries in compressible liquid flows with cavitation, *Journal of Computational Physics* 283 (2015) 1–22. doi:doi:10.1016/j.jcp.2014.11.028.
- [13] M. Dular, O. Coutier-Delgosha, Numerical modelling of cavitation erosion, *International Journal for Numerical Methods in Fluids* 61 (2009) 1388–1410. doi:doi:10.1002/fld.2003.
- [14] A. Sou, B. Bicer, A. Tomiyama, Numerical simulation of incipient cavitation flow in a nozzle of fuel injector, *Computers and Fluids* 103 (2014) 42–48. doi:doi:10.1016/j.compfluid.2014.07.011.
- [15] M. Ghiji, L. Goldsworthy, P. A. Brandner, V. Garaniya, P. Hield, Analysis of diesel spray dynamics using a compressible Eulerian/VOF/LES model and microscopic shadowgraphy, *Fuel* 188 (2017) 352–366. doi:doi:10.1016/j.fuel.2016.10.041.
- [16] J. Heywood, *Internal Combustion Engine Fundamentals*, McGraw-Hill, New York, 1988.
- [17] M. Gavaises, Flow in valve covered orifice nozzles with cylindrical and tapered holes and link to cavitation erosion and engine exhaust emissions,



International Journal of Engine Research 9 (2008) 435–447. URL: <http://journals.sagepub.com/doi/10.1243/14680874JER01708>. doi:doi:10.1243/14680874JER01708.

- [18] R. D. Reitz, H. Ogawa, e. Payri, IJER editorial: The future of the internal combustion engine, International Journal of Engine Research (2019) 146808741987799. URL: <http://journals.sagepub.com/doi/10.1177/1468087419877990>. doi:doi:10.1177/1468087419877990.
- [19] D. Pierpont, R. Reitz, Effects of injection pressure and nozzle geometry on DI diesel emissions and performance, SAE paper.1995-950604 950604 (1995).
- [20] C. Sayin, K. Uslu, M. Canakci, Influence of injection timing on the exhaust emissions of a dual-fuel CI engine., Renewable Energy 33 (2008) 1314–23.
- [21] D. Pierpont, D. Montgomery, R. Reitz, Reducing particulate and NOx using multiple injections and EGR in a DI diesel., SAE paper.1995;950217. (1995).
- [22] H. Durnholz, M Endres, P. Frisse, Pre-injection a measure to optimize the emission behavior of DI-diesel engine., SAE paper. 1994;940674. (1994).
- [23] S. Molina, F. Salvador, M. Carreres, D. Jaramillo, A computational investigation on the influence of the use of elliptical orifices on the inner nozzle flow and cavitation development in diesel injector nozzles, Energy Conversion and Management 79 (2014) 114–127. URL: <http://linkinghub.elsevier.com/retrieve/pii/S0196890413007917>. doi:doi:10.1016/j.enconman.2013.12.015.
- [24] W. Huang, S. Moon, Y. Gao, J. Wang, D. Ozawa, A. Matsumoto, Hole number effect on spray dynamics of multi-hole diesel nozzles: An observation from three- to nine-hole nozzles, Experimental Thermal and Fluid Science (2019). doi:doi:10.1016/j.expthermflusci.2018.12.022.
- [25] W. Huang, S. Moon, Y. Gao, Z. Li, J. Wang, Eccentric needle motion effect on near-nozzle dynamics of diesel spray, Fuel (2017). doi:doi:10.1016/j.fuel.2017.06.012.
- [26] S. Moon, W. Huang, J. Wang, First observation and characterization of vortex flow in steel micronozzles for high-pressure diesel injection, Experimental Thermal and Fluid Science (2019). doi:doi:10.1016/j.expthermflusci.2019.04.018.

- [27] I. K. Karathanassis, P. Koukouvinis, E. Kontolatis, Z. Lee, J. Wang, N. Mitroglou, M. Gavaises, High-speed visualization of vortical cavitation using synchrotron radiation, *Journal of Fluid Mechanics* (2018). doi:[doi:10.1017/jfm.2017.885](https://doi.org/10.1017/jfm.2017.885).
- [28] I. K. Karathanassis, K. Trickett, P. Koukouvinis, J. Wang, R. Barbour, M. Gavaises, Illustrating the effect of viscoelastic additives on cavitation and turbulence with X-ray imaging, *Scientific Reports* 8 (2018) 14968. URL: <http://www.nature.com/articles/s41598-018-32996-w>. doi:[doi:10.1038/s41598-018-32996-w](https://doi.org/10.1038/s41598-018-32996-w).
- [29] P. Koukouvinis, M. Gavaises, J. Li, L. Wang, Large Eddy Simulation of Diesel injector including cavitation effects and correlation to erosion damage, *Fuel* 175 (2016) 26–39. URL: <http://dx.doi.org/10.1016/j.fuel.2016.02.037>. doi:[doi:10.1016/j.fuel.2016.02.037](https://doi.org/10.1016/j.fuel.2016.02.037).
- [30] E. Giannadakis, D. Papoulias, A. Theodorakakos, M. Gavaises, Simulation of cavitation in outward-opening piezo-type pintle injector nozzles, *Proceedings of the Institution of Mechanical Engineers, Part D: Journal of Automobile Engineering* 222 (2008) 1895–1910. URL: <http://journals.sagepub.com/doi/10.1243/09544070JAUTO728>. doi:[doi:10.1243/09544070JAUTO728](https://doi.org/10.1243/09544070JAUTO728).
- [31] E. Giannadakis, M. Gavaises, C. Arcoumanis, Modelling of cavitation in diesel injector nozzles, *Journal of Fluid Mechanics* 616 (2008) 153. doi:[doi:10.1017/S0022112008003777](https://doi.org/10.1017/S0022112008003777).
- [32] R. Kolovos, Konstantinos; Kyriazis, Nikolaos; Koukouvinis, Phoevos; Gavaises, Manolis; Li, Jason; McDavid, Large-eddy simulation of turbulent cavitating flow in a Diesel injector including needle movement, in *OpenFOAM*, in: ILASS-Europe, Paris, 2-4 Sept, 2019.
- [33] M. Battistoni, Q. Xue, S. Som, E. Pomraning, Effect of Off-Axis Needle Motion on Internal Nozzle and Near Exit Flow in a Multi-Hole Diesel Injector, *SAE International Journal of Fuels and Lubricants* 7 (2014) 2014-01-1426. URL: <http://papers.sae.org/2014-01-1426/>. doi:[doi:10.4271/2014-01-1426](https://doi.org/10.4271/2014-01-1426).
- [34] L. He, F. Ruiz, Effect of cavitation on flow and turbulence in plain orifices for high-speed atomization, *Atomization and Sprays* (1995). doi:[doi:10.1615/atomizspr.v5.i6.30](https://doi.org/10.1615/atomizspr.v5.i6.30).
- [35] Z. Huang, Y. Shao, S. Shiga, H. Nakamura, Controlling mechanism and resulting spray characteristics of injection of fuel containing dissolved gas, *Journal of Thermal Science* (1994). doi:[doi:10.1007/BF02653122](https://doi.org/10.1007/BF02653122).

- [36] C. Arcoumanis, M. Gavaises, Linking nozzle flow with spray characteristics in a diesel fuel injection system, *Atomization and Sprays* (1998). doi:[doi:10.1615/AtomizSpr.v8.i3.50](https://doi.org/10.1615/AtomizSpr.v8.i3.50).
- [37] W. E. Ranz, Some experiments on orifice sprays, *The Canadian Journal of Chemical Engineering* 36 (1958) 175–181. doi:[doi:10.1002/cjce.5450360405](https://doi.org/10.1002/cjce.5450360405).
- [38] W. Bergwerk, Flow pattern in diesel nozzle spray holes, ARCHIVE: Proceedings of the Institution of Mechanical Engineers 1847-1982 (vols 1-196) 173 (1959) 655–660. doi:[doi:10.1243/PIME\\_PROC.1959.173.054.02](https://doi.org/10.1243/PIME_PROC.1959.173.054.02).
- [39] W. H. Nurick, Orifice cavitation and its effect on spray mixing, *Journal of Fluids Engineering, Transactions of the ASME* (1976). doi:[doi:10.1115/1.3448452](https://doi.org/10.1115/1.3448452).
- [40] R. D. Reitz, F. V. Bracco, Mechanism of atomization of a liquid jet, *Physics of Fluids* (1982). doi:[doi:10.1063/1.863650](https://doi.org/10.1063/1.863650).
- [41] M. Arai, M. Tabata, H. Hiroyasu, M. Shimizu, Disintegrating Process and Spray Characterization of Fuel Jet Injected by a Diesel Nozzle, in: SAE Technical Paper 840275, SAE International, 1984. URL: <http://papers.sae.org/840275/>. doi:[doi:10.4271/840275](https://doi.org/10.4271/840275).
- [42] H. Hiroyasu, A. Masataka, S. Masanori, M. Arai, M. Shimizu, Break-up Length of a Liquid Jet and Internal Flow in a Nozzle, in: NIST Special Publication, Gaithersburg, Maryland, 1991, pp. 275–282.
- [43] G. a. Ruff, P.-K. K. Wu, L. P. Bernal, G. M. Faeth, Continuous- and dispersed-phase structure of dense nonevaporating pressure-atomized sprays, *Journal of Propulsion and Power* 8 (1992) 280–289. doi:[doi:10.2514/3.23475](https://doi.org/10.2514/3.23475).
- [44] L. G. Dodge, T. W. Ryan, M. G. Ryan, Effects of different injector hole shapes on diesel sprays, in: SAE Technical Papers, 1992. doi:[doi:10.4271/920623](https://doi.org/10.4271/920623).
- [45] R. H. Spikes, G. A. Pennington, Discharge Coefficient of Small Submerged Orifices, *Proceedings of the Institution of Mechanical Engineers* (1959). doi:[doi:10.1243/pime-proc.1959.173.055.02](https://doi.org/10.1243/pime-proc.1959.173.055.02).
- [46] H. Chaves, M. Knapp, A. Kubitzek, F. Obermeier, T. Schneider, Experimental study of cavitation in the nozzle hole of diesel injectors using transparent nozzles, SAE Technical Papers (1995). doi:[doi:10.4271/950290](https://doi.org/10.4271/950290).

- [47] A. Sou, S. Hosokawa, A. Tomiyama, Effects of cavitation in a nozzle on liquid jet atomization, *International Journal of Heat and Mass Transfer* (2007). doi:[doi:10.1016/j.ijheatmasstransfer.2006.12.033](https://doi.org/10.1016/j.ijheatmasstransfer.2006.12.033).
- [48] H. K. Suh, C. S. Lee, Effect of cavitation in nozzle orifice on the diesel fuel atomization characteristics, *International Journal of Heat and Fluid Flow* 29 (2008) 1001–1009. doi:[doi:10.1016/j.ijheatfluidflow.2008.03.014](https://doi.org/10.1016/j.ijheatfluidflow.2008.03.014).
- [49] C. Soteriou, R. Andrews, M. Smith, Direct injection diesel sprays and the effect of cavitation and hydraulic flip on atomization, *SAE Technical Papers* (1995). doi:[doi:10.4271/950080](https://doi.org/10.4271/950080).
- [50] C. Arcoumanis, H. Flora, M. Gavaises, M. Badami, Cavitation in real-size multi-hole diesel injector nozzles, *SAE Technical Papers* (2000). doi:[doi:10.4271/2000-01-1249](https://doi.org/10.4271/2000-01-1249).
- [51] M. Gavaises, A. Andriotis, D. Papoulias, N. Mitroglou, A. Theodorakakos, Characterization of string cavitation in large-scale Diesel nozzles with tapered holes, *Physics of Fluids* 21 (2009) 052107. URL: <http://aip.scitation.org/doi/10.1063/1.3140940>. doi:[doi:10.1063/1.3140940](https://doi.org/10.1063/1.3140940).
- [52] F. Payri, V. Bermúdez, R. Payri, F. J. Salvador, The influence of cavitation on the internal flow and the spray characteristics in diesel injection nozzles, *Fuel* 83 (2004) 419–431. doi:[doi:10.1016/j.fuel.2003.09.010](https://doi.org/10.1016/j.fuel.2003.09.010).
- [53] H. Afzal, C. Arcoumanis, M. Gavaises, N. Kampanis, Internal flow in diesel injector nozzles: modelling and experiments, *IMEchE Paper S492/S2/99* (1999).
- [54] H. Roth, M. Gavaises, C. Arcoumanis, Cavitation initiation, its development and link with flow turbulence in diesel injector nozzles, *SAE Technical Papers* 2002 (2002). doi:[doi:10.4271/2002-01-0214](https://doi.org/10.4271/2002-01-0214).
- [55] C. Arcoumanis, M. Gavaises, J. M. Nouri, E. Abdul-Wahab, R. W. Horrocks, Analysis of the flow in the nozzle of a vertical multi-hole diesel engine injector, in: *SAE Technical Papers*, 1998. doi:[doi:10.4271/980811](https://doi.org/10.4271/980811).
- [56] M. Gavaises, A. Andriotis, Cavitation inside multi-hole injectors for large Diesel engines and its effect on the near-nozzle spray structure, in: *SAE Technical Papers*, 2006. doi:[doi:10.4271/2006-01-1114](https://doi.org/10.4271/2006-01-1114).
- [57] M. H. Arabnejad, A. Amini, M. Farhat, R. E. Bensow, Numerical and experimental investigation of shedding mechanisms from leading-edge cavitation, *International Journal of Multiphase Flow* 119 (2019) 123–143. URL: <https://doi.org/10.1016/j.ijmultiphaseflow.2019.06.010>. doi:[doi:10.1016/j.ijmultiphaseflow.2019.06.010](https://doi.org/10.1016/j.ijmultiphaseflow.2019.06.010).

- [58] L. C. Ganippa, G. Bark, S. Andersson, J. Chomiak, The structure of cavitation and its effect on the spray pattern in a single-hole diesel nozzle, in: SAE Technical Papers, 2001. doi:[doi:10.4271/2001-01-2008](https://doi.org/10.4271/2001-01-2008).
- [59] K. Sato, Y. Saito, Unstable cavitation behavior in a circular-cylindrical orifice flow, JSME International Journal, Series B: Fluids and Thermal Engineering (2002). doi:[doi:10.1299/jsmeb.45.638](https://doi.org/10.1299/jsmeb.45.638).
- [60] H. Roth, E. Giannadakis, M. Gavaises, C. Arcoumanis, K. Omae, I. Sakata, M. Nakamura, H. Yanagihara, Effect of multi-injection strategy on cavitation development in diesel injector nozzle holes, SAE Technical Papers 2005 (2005). doi:[doi:10.4271/2005-01-1237](https://doi.org/10.4271/2005-01-1237).
- [61] B. A. Reid, M. Gavaises, N. Mitroglou, G. K. Hargrave, C. P. Garner, E. J. Long, R. M. McDavid, On the formation of string cavitation inside fuel injectors, Experiments in Fluids 55 (2014) 1–8. doi:[doi:10.1007/s00348-013-1662-8](https://doi.org/10.1007/s00348-013-1662-8).
- [62] B. A. Reid, G. K. Hargrave, C. P. Garner, G. Wigley, An investigation of string cavitation in a true-scale fuel injector flow geometry at high pressure, Physics of Fluids (2010). doi:[doi:10.1063/1.3372174](https://doi.org/10.1063/1.3372174).
- [63] P. Koukouvinis, H. Naseri, M. Gavaises, Performance of turbulence and cavitation models in prediction of incipient and developed cavitation, International Journal of Engine Research 18 (2017) 333–350. doi:[doi:10.1177/1468087416658604](https://doi.org/10.1177/1468087416658604).
- [64] J. Reboud, B. Stutz, O. Coutier-Delgosha, Two phase flow structure of cavitation: experiment and modeling of unsteady effects, 3rd International Symposium on Cavitation CAV1998 26 (1998).
- [65] E. Lauer, X. Y. Hu, S. Hickel, N. A. Adams, Numerical investigation of collapsing cavity arrays, Physics of Fluids 24 (2012) 052104. doi:[doi:10.1063/1.4719142](https://doi.org/10.1063/1.4719142).
- [66] W. Yuan, G. H. Schnerr, Numerical Simulation of Two-Phase Flow in Injection Nozzles: Interaction of Cavitation and External Jet Formation, Journal of Fluids Engineering 125 (2004) 963–969. URL: <http://dx.doi.org/10.1115/1.1625687>.
- [67] A. Kubota, H. Kato, H. Yamaguchi, Finite difference analysis of unsteady cavitation on a two-dimensional hydrofoil, in: Fifth International Conference on Numerical Ship Hydrodynamics, 1990.

- [68] R. F. Kunz, D. a. Boger, D. R. Stinebring, S. Chyczewski, J. W. Lindau, H. J. Gibeling, S. Venkateswaran, T. R. Govindan, A preconditioned Navier - Stokes method for two-phase flows with application to cavitation prediction, *Computers & Fluids* 29 (2000) 849–875. doi:[doi:10.1016/S0045-7930\(99\)00039-0](https://doi.org/10.1016/S0045-7930(99)00039-0).
- [69] G. H. Schnerr, J. Sauer, Physical and Numerical Modeling of Unsteady Cavitation Dynamics, in: *Fourth International Conference on Multiphase Flow*, 2001.
- [70] P. J. Zwart, A. G. Gerber, T. Belamri, A Two-Phase Flow Model for Predicting Cavitation Dynamics, in: *ICMF 2004 International Conference on Multiphase Flow*, Yokohama, Japan, 2004. URL: <https://www.tib.eu/en/search/id/BLCP%73ACN077339909/A-Two-Phase-Flow-Model-for-Predicting-Cavitation/>.
- [71] A. Niedzwiedzka, G. H. Schnerr, W. Sobieski, Review of numerical models of cavitating flows with the use of the homogeneous approach, *Archives of Thermodynamics* 37 (2016) 71–88. doi:[doi:10.1515/aoter-2016-0013](https://doi.org/10.1515/aoter-2016-0013).
- [72] T. Goel, J. Zhao, S. Thakur, R. Haftka, W. Shyy, Surrogate Model-Based Strategy for Cryogenic Cavitation Model Validation and Sensitivity Evaluation, in: *42nd AIAA/ASME/SAE/ASEE Joint Propulsion Conference & Exhibit, Joint Propulsion Conferences*, American Institute of Aeronautics and Astronautics, 2006. doi:[doi:10.2514/6.2006-5047](https://doi.org/10.2514/6.2006-5047).
- [73] S. Gopalan, J. Katz, Flow structure and modeling issues in the closure region of attached cavitation, *Physics of Fluids* 12 (2000) 895–911. doi:[doi:10.1063/1.870344](https://doi.org/10.1063/1.870344).
- [74] C. P. Egerer, S. Hickel, S. J. Schmidt, N. A. Adams, Large-eddy simulation of turbulent cavitating flow in a micro channel, *Physics of Fluids* 26 (2014) 085102. URL: <http://aip.scitation.org/doi/10.1063/1.4891325>. doi:[doi:10.1063/1.4891325](https://doi.org/10.1063/1.4891325).
- [75] H. Lefebvre, G. M. Vincent, *Atomization and Sprays*, Second Edition, CRC Press, 2017.
- [76] X. X. Jiang, G. A. Siamas, K. Jagus, T. G. Karayiannis, Physical modelling and advanced simulations of gas-liquid two-phase jet flows in atomization and spray, *Progress in Energy and Combustion Science* 36 (2010) 131–167. URL: <http://dx.doi.org/10.1016/j.pecs.2009.09.002>. doi:[doi:10.1016/j.pecs.2009.09.002](https://doi.org/10.1016/j.pecs.2009.09.002). arXiv:[f1d.1](https://arxiv.org/abs/f1d.1).

- [77] P. Béard, J.-M. Duclos, C. Habchi, G. Bruneaux, K. Mokaddem, T. Baritaud, Extension of Lagrangian-Eulerian Spray Modeling: Application to High Pressure Evaporating Diesel Sprays, SAE International, 2000. URL: <https://doi.org/10.4271/2000-01-1893><http://papers.sae.org/2000-01-1893/>. doi:doi:10.4271/2000-01-1893.
- [78] A. M. Lippert, S. Chang, S. Are, D. P. Schmidt, Mesh Independence and Adaptive Mesh Refinement For Advanced Engine Spray Simulations, in: SAE Technical Paper 2005-01-0207, SAE International, 2005. doi:doi:10.4271/2005-01-0207.
- [79] W. Ning, R. D. Reitz, A. M. Lippert, R. Diwakar, Development of a Next-generation Spray and Atomization Model Using an Eulerian-Lagrangian Methodology, International Multidimensional Engine Modeling User's Group Meeting (2007).
- [80] A. Behzadi, R. I. Issa, H. Rusche, Modelling of dispersed bubble and droplet flow at high phase fractions, Chemical Engineering Science 59 (2004) 759–770. doi:doi:<https://doi.org/10.1016/j.ces.2003.11.018>.
- [81] V. A. Iyer, J. Abraham, V. Magi, Exploring injected droplet size effects on steady liquid penetration in a Diesel spray with a two-fluid model, International Journal of Heat and Mass Transfer 45 (2002) 519–531. URL: <http://www.sciencedirect.com/science/article/pii/S0017931001001685>. doi:doi:[https://doi.org/10.1016/S0017-9310\(01\)00168-5](https://doi.org/10.1016/S0017-9310(01)00168-5).
- [82] M. Vujanović, Z. Petranović, W. Edelbauer, J. Baleta, N. Duić, Numerical modelling of diesel spray using the Eulerian multiphase approach, Energy Conversion and Management 104 (2015) 160–169. doi:doi:10.1016/j.enconman.2015.03.040.
- [83] A. Vallet, A. A. Burluka, R. Borghi, Development of a eulerian model for the “atomization” of a liquid jet, Atomization and Sprays 11 (2001) 24. doi:doi:10.1615/AtomizSpr.v11.i6.20.
- [84] AVL, Fire Manual, 2013.
- [85] M. D. Luca, A. Vallet, R. Borghi, Pesticide atomization modeling for hollow-cone nozzle, Atomization and Sprays 19 (2009) 741–753.
- [86] M. Vujanović, Z. Petranović, W. Edelbauer, N. Duić, Modelling spray and combustion processes in diesel engine by using the coupled Eulerian-Eulerian and Eulerian-Lagrangian method, Energy Conversion and

- Management 125 (2016) 15–25. URL: <http://www.sciencedirect.com/science/article/pii/S0196890416302084>. doi:doi:<https://doi.org/10.1016/j.enconman.2016.03.072>.
- [87] Y. Wang, W. G. Lee, R. D. Reitz, R. Diwakar, Numerical Simulation of Diesel Sprays Using an Eulerian-Lagrangian Spray and Atomization (ELSA) Model Coupled with Nozzle Flow, SAE International, 2011. URL: <https://doi.org/10.4271/2011-01-0386><http://papers.sae.org/2011-01-0386/>. doi:doi:10.4271/2011-01-0386.
- [88] A. Berlemont, Z. Bouali, J. Cousin, P. Desjonquieres, M. Doring, T. Menard, E. Noel, Simulation of liquid/gas interface break-up with a coupled Level Set/VOF/Ghost Fluid method, in: ICCFD7, Big Island, Hawaii, 2012.
- [89] M. Arienti, X. Li, M. C. Soteriou, C. A. Eckett, M. Sussman, R. J. Jensen, Coupled Level-Set/Volume-of-Fluid Method for Simulation of Injector Atomization, *Journal of Propulsion and Power* 29 (2013) 147–157. doi:doi:10.2514/1.B34198.
- [90] R. Saurel, F. Petitpas, R. Abgrall, Modelling phase transition in metastable liquids: application to cavitating and flashing flows, volume 607, 2008. doi:doi:10.1017/S0022112008002061.
- [91] Y. Wang, L. Qiu, R. D. Reitz, R. Diwakar, Simulating cavitating liquid jets using a compressible and equilibrium two-phase flow solver, *International Journal of Multiphase Flow* 63 (2014) 52–67. doi:doi:10.1016/j.ijmultiphaseflow.2014.03.006.
- [92] F. Örley, T. Trummler, S. Hickel, M. S. Mihatsch, S. J. Schmidt, N. A. Adams, Large-eddy simulation of cavitating nozzle flow and primary jet break-up, *Physics of Fluids* 27 (2015) 086101. doi:doi:10.1063/1.4928701.
- [93] O. Ubbink, Numerical Prediction of Two Fluid Systems With Sharp Interfaces, Phd thesis, Imperial College of Science, Technology and Medicine, 1997.
- [94] R. Marcer, P. Le Cottier, H. Chaves, B. Argueyrolles, C. Habchi, B. Barbeau, B. B. R. Marcer, P. Le Cottier, H. Chaves, B. Argueyrolles, C. Habchi, A Validated Numerical Simulation of Diesel Injector Flow Using a VOF Method, in: SAE Technical Paper 2000-01-2932, SAE International, 2000. doi:doi:10.4271/2000-01-2932.
- [95] J. Ishimoto, F. Sato, G. Sato, Computational Prediction of the Effect of Microcavitation on an Atomization Mechanism in a Gasoline Injector



- Nozzle, *Journal of Engineering for Gas Turbines and Power* 132 (2010) 082801. doi:[doi:10.1115/1.4000264](https://doi.org/10.1115/1.4000264).
- [96] W. Edelbauer, Numerical simulation of cavitating injector flow and liquid spray break-up by combination of Eulerian-Eulerian and Volume-of-Fluid methods, *Computers and Fluids* 144 (2017) 19–33. doi:[doi:10.1016/j.compfluid.2016.11.019](https://doi.org/10.1016/j.compfluid.2016.11.019).
- [97] H. Yu, L. Goldsworthy, P. A. Brandner, V. Garaniya, Development of a compressible multiphase cavitation approach for diesel spray modelling, *Applied Mathematical Modelling* 45 (2017) 705–727. doi:[doi:10.1016/j.apm.2017.01.035](https://doi.org/10.1016/j.apm.2017.01.035).
- [98] D. P. Schmidt, C. J. Ruland, M. L. Corradini, A Fully Compressible Model of Small, High Speed Cavitating Nozzle Flows, *Atomization and Sprays* 9 (1999) 255–276.
- [99] N. Mitroglou, M. Gavaises, J. M. Nouri, C. Arcoumanis, Cavitation Inside Enlarged And Real-Size Fully Transparent Injector Nozzles And Its Effect On Near Nozzle Spray Formation, in: G. E. Cossali, S. Tonini (Eds.), *Proceedings of the DIPSI Workshop 2011. Droplet Impact Phenomena & Spray Investigations*, Dip. Ingegneria industriale. Università degli studi di Bergamo, Bergamo, 2011, pp. 33–45. URL: <http://openaccess.city.ac.uk/1507/>.
- [100] N. Mitroglou, M. McLorn, M. Gavaises, C. Soteriou, M. Winterbourne, Instantaneous and ensemble average cavitation structures in Diesel micro-channel flow orifices, *Fuel* (2014). doi:[doi:10.1016/j.fuel.2013.08.060](https://doi.org/10.1016/j.fuel.2013.08.060).
- [101] J. W. Lee, K. D. Min, K. Y. Kang, C. S. Bae, E. Giannadakis, M. Gavaises, C. Arcoumanis, Effect of piezo-driven and solenoid-driven needle opening of common-rail diesel injectors on internal nozzle flow and spray development, *International Journal of Engine Research* 7 (2006) 489–502. URL: <http://journals.sagepub.com/doi/10.1243/14680874JER00806>. doi:[doi:10.1243/14680874JER00806](https://doi.org/10.1243/14680874JER00806).
- [102] **M. G. Mithun**, P. Koukouvinis, M. Gavaises, Numerical simulation of cavitation and atomization using a fully compressible three-phase model, *Physical Review Fluids* 3 (2018) 064304. URL: <https://link.aps.org/doi/10.1103/PhysRevFluids.3.064304>. doi:[doi:10.1103/PhysRevFluids.3.064304](https://doi.org/10.1103/PhysRevFluids.3.064304).
- [103] C. Arcoumanis, M. Gavaises, E. Abdul-Wahab, V. Moser, Modeling of Advanced High-Pressure Fuel Injection Systems for Passenger Car Diesel

- Engines, 1999. URL: <https://www.sae.org/content/1999-01-0910/>. doi:doi:10.4271/1999-01-0910.
- [104] F. Brusiani, D. Ph, G. M. Bianchi, D. Ph, Evaluation of Air / Cavitation Interaction Inside a Vane Pump (2009).
- [105] M. Gavaises, D. Papoulias, E. Giannadakis, A. Andriotis, N. Mitroglou, A. Theodorakakos, Comparison of cavitation formation and development in Diesel VCO nozzles with cylindrical and converging tapered holes, in: Thermo- and Fluid-Dynamic Processes in Diesel Engines (THIESEL 2008), Valencia, 2008.
- [106] F. Örley, S. Hickel, S. J. Schmidt, N. A. Adams, LES of cavitating flow inside a Diesel injector including dynamic needle movement, *Journal of Physics: Conference Series* 656 (2015) 012097. doi:doi:10.1088/1742-6596/656/1/012097.
- [107] F. Örley, S. Hickel, S. J. Schmidt, N. A. Adams, Large-Eddy Simulation of turbulent, cavitating fuel flow inside a 9-hole Diesel injector including needle movement, *International Journal of Engine Research* (2016) 146808741664390. URL: <http://journals.sagepub.com/doi/10.1177/1468087416643901>. doi:doi:10.1177/1468087416643901.
- [108] S. Kook, L. Pickett, M. Musculus, K. Kattke, R. Gehmlich, Liquid-phase diesel spray penetration during end-of-injection transient, *Proceedings of the 7th International Conference on Modeling and Diagnostics for Advanced Engine Systems, COMODIA 2008* (2008) 413–420.
- [109] M. P. Musculus, Entrainment waves in decelerating transient turbulent jets, *Journal of Fluid Mechanics* 638 (2009) 117–140. doi:doi:10.1017/S0022112009990826.
- [110] S. Kook, L. M. Pickett, M. P. Musculus, Influence of Diesel Injection Parameters on End-of-Injection Liquid Length Recession, *SAE International Journal of Engines* 2 (2009) 2009–01–1356. URL: <http://papers.sae.org/2009-01-1356/>. doi:doi:10.4271/2009-01-1356.
- [111] A. B. Swantek, D. Duke, F. Z. Tilocco, N. Sovis, C. F. Powell, End of Injection , Mass Expulsion Behaviors in Single Hole Diesel Fuel Injectors, in: *Proceedings of ILASS Americas*, May, 2014.
- [112] J.-S. Han, T. C. Wang, X. B. Xie, M.-C. Lai, N. A. Henein, D. L. Harrington, J. Pinson, P. C. Miles, Dynamics of Multiple-Injection Fuel Sprays

- in a Small-bore HSDI Diesel Engine, in: SAE Technical Papers 2000-01-1256, 2000. URL: <http://papers.sae.org/2000-01-1256/>. doi:doi:10.4271/2000-01-1256.
- [113] W. E. Eagle, M. P. B. Musculus, Cinema - Stereo Imaging of Fuel Dribble after the End of Injection in an Optical Heavy - Duty Diesel Engine, in: Thermo- and Fluid-Dynamic Processes in Diesel Engines (THIESEL 2014), 2014.
- [114] S. Moon, W. Huang, Z. Li, J. Wang, End-of-injection fuel dribble of multi-hole diesel injector: Comprehensive investigation of phenomenon and discussion on control strategy, *Applied Energy* 179 (2016) 7–16. URL: <http://dx.doi.org/10.1016/j.apenergy.2016.06.116>. doi:doi:10.1016/j.apenergy.2016.06.116.
- [115] M. Battistoni, A. L. Kastengren, C. F. Powell, S. Som, Fluid Dynamics Modeling of End-of-Injection, ILASS 2014 - 26th Annual Conference on Liquid Atomization and Spray Systems (2014).
- [116] N. Papadopoulos, P. Aleiferis, Numerical Modelling of the In-Nozzle Flow of a Diesel Injector with Moving Needle during and after the End of a Full Injection Event, in: SAE Paper 2015-24-2472, 2015.
- [117] O. Chiavola, F. Palmieri, Modeling Needle Motion Influence on Nozzle Flow in High Pressure Injection System, 2007. URL: <http://papers.sae.org/2007-01-0250/>. doi:doi:10.4271/2007-01-0250.
- [118] M. Spathopoulou, D. Papoulias, E. Giannadakis, M. Gavaises, A. Theodorakakos, Influence of the Spatially Resolved Nozzle Hole Exit Flow Distribution on Diesel Spray Development, 2007. URL: <http://papers.sae.org/2007-24-0025/>. doi:doi:10.4271/2007-24-0025.
- [119] M. Eaton, P. S. Keogh, K. A. Edge, The Modelling, Prediction, and Experimental Evaluation of Gear Pump Meshing Pressures with Particular Reference to Aero-Engine Fuel Pumps, *Proceedings of the Institution of Mechanical Engineers, Part I: Journal of Systems and Control Engineering* 220 (2006) 365–379. URL: <http://journals.sagepub.com/doi/10.1243/09596518JSCE183>. doi:doi:10.1243/09596518JSCE183. arXiv:0803973233.
- [120] M. P. Wernet, Development of digital particle imaging velocimetry for use in turbomachinery, *Experiments in Fluids* (2000). doi:doi:10.1007/s003480050015.

- [121] R. Castilla, J. Wojciechowski, P. J. Gamez-Montero, A. Vernet, E. Codina, Analysis of the turbulence in the suction chamber of an external gear pump using Time Resolved Particle Image Velocimetry, *Flow Measurement and Instrumentation* 19 (2008) 377–384. URL: <http://dx.doi.org/10.1016/j.flowmeasinst.2008.06.005>. doi:doi:10.1016/j.flowmeasinst.2008.06.005.
- [122] N. Ertürk, A. Vernet, R. Castilla, P. J. Gamez-Montero, J. A. Ferre, Experimental analysis of the flow dynamics in the suction chamber of an external gear pump, *International Journal of Mechanical Sciences* 53 (2011) 135–144. doi:doi:10.1016/j.ijmecsci.2010.12.003.
- [123] T. E. Beacham, High-Pressure Gear Pumps, *Proceedings of the Institution of Mechanical Engineers* 155 (1946) 417–452. URL: [https://doi.org/10.1243/PIME{}\\_PROC{}\\_1946{}\\_155{}\\_058{}\\_02](https://doi.org/10.1243/PIME{}_PROC{}_1946{}_155{}_058{}_02)[http://journals.sagepub.com/doi/10.1243/PIME{}\\_PROC{}\\_1946{}\\_155{}\\_058{}\\_02](http://journals.sagepub.com/doi/10.1243/PIME{}_PROC{}_1946{}_155{}_058{}_02). doi:doi:10.1243/PIME\_PROC\_1946\_155\_058\_02.
- [124] N. D. Manring, S. B. Kasaragadda, The Theoretical Flow Ripple of an External Gear Pump, *Journal of Dynamic Systems, Measurement, and Control* 125 (2003) 396. doi:doi:10.1115/1.1592193.
- [125] M. Borghi, B. Zardin, E. Specchia, External Gear Pump Volumetric Efficiency: Numerical and Experimental Analysis, 2009. URL: <http://papers.sae.org/2009-01-2844/>. doi:doi:10.4271/2009-01-2844.
- [126] A. Vacca, M. Guidetti, Modelling and experimental validation of external spur gear machines for fluid power applications, *Simulation Modelling Practice and Theory* 19 (2011) 2007–2031. URL: <http://dx.doi.org/10.1016/j.simpat.2011.05.009><http://linkinghub.elsevier.com/retrieve/pii/S1569190X11001018>. doi:doi:10.1016/j.simpat.2011.05.009.
- [127] J. Zhou, A. Vacca, P. Casoli, A novel approach for predicting the operation of external gear pumps under cavitating conditions, *Simulation Modelling Practice and Theory* 45 (2014) 35–49. URL: <http://dx.doi.org/10.1016/j.simpat.2014.03.009>. doi:doi:10.1016/j.simpat.2014.03.009.
- [128] D. Bruce, M. Wilson, S. Generalis, Flow Field Analysis of Both the Trilobal Element and Mixing Disc Zones within a Closely Intermeshing, Co-Rotating Twin-Screw Extruder, *International Polymer Processing* 12 (1997) 323–330. URL: <http://www.hanser-elibrary.com/doi/abs/10.3139/217.970323><https://doi.org/10.3139/217.970323>. doi:doi:10.3139/217.970323.

- [129] K. Riemsdagh, J. Vierendeels, E. Dick, An arbitrary Lagrangian–Eulerian finite-volume method for the simulation of rotary displacement pump flow, *Applied Numerical Mathematics* 32 (2000) 419–433. URL: <http://www.sciencedirect.com/science/article/pii/S0168927499000616>. doi:doi:[https://doi.org/10.1016/S0168-9274\(99\)00061-6](https://doi.org/10.1016/S0168-9274(99)00061-6).
- [130] G. Houzeaux, R. Codina, A finite element method for the solution of rotary pumps, *Computers and Fluids* 36 (2007) 667–679. doi:doi:[10.1016/j.compfluid.2006.02.005](https://doi.org/10.1016/j.compfluid.2006.02.005).
- [131] W. Strasser, CFD Investigation of Gear Pump Mixing Using Deforming/Agglomerating Mesh, *Journal of Fluids Engineering* 129 (2006) 476–484. URL: <http://fluidsengineering.asmedigitalcollection.asme.org/article.aspx?articleid=1431150http://dx.doi.org/10.1115/1.2436577>. doi:doi:[10.1115/1.2436577](https://doi.org/10.1115/1.2436577).
- [132] R. Castilla, P. J. Gamez-Montero, D. del Campo, G. Raush, M. Garcia-Vilchez, E. Codina, Three-Dimensional Numerical Simulation of an External Gear Pump With Decompression Slot and Meshing Contact Point, *Journal of Fluids Engineering* 137 (2015) 041105. URL: <http://dx.doi.org/10.1115/1.4029223http://fluidsengineering.asmedigitalcollection.asme.org/article.aspx?doi=10.1115/1.4029223>. doi:doi:[10.1115/1.4029223](https://doi.org/10.1115/1.4029223).
- [133] A. Kovacevic, N. Stosic, I. K. Smith, Three Dimensional Numerical Analysis of Screw Compressor Performance, *Journal of Computational Methods in Sciences and Engineering* 3 (2003) 259–284. URL: <https://www.medra.org/servlet/aliasResolver?alias=iospress{&}doi=10.3233/JCM-2003-3206>. doi:doi:[10.3233/JCM-2003-3206](https://doi.org/10.3233/JCM-2003-3206).
- [134] G. Bianchi, S. Rane, A. Kovacevic, R. Cipollone, S. Murgia, G. Contaldi, Grid generation methodology and CFD simulations in sliding vane compressors and expanders, *IOP Conference Series: Materials Science and Engineering* 232 (2017) 012053. URL: <http://stacks.iop.org/1757-899X/232/i=1/a=012053?key=crossref.c8e9e514b447726cb7d01cd47dd74666>. doi:doi:[10.1088/1757-899X/232/1/012053](https://doi.org/10.1088/1757-899X/232/1/012053).
- [135] G. Singh, S. Sun, A. Kovacevic, Q. Li, C. Bruecker, Transient flow analysis in a Roots blower: Experimental and numerical investigations, *Mechanical Systems and Signal Processing* 134 (2019) 106305. URL: <https://doi.org/10.1016/j.ymsp.2019.106305>. doi:doi:[10.1016/j.ymsp.2019.106305](https://doi.org/10.1016/j.ymsp.2019.106305).

- [136] D. del Campo, R. Castilla, G. A. Raush, P. J. Gamez Montero, E. Codina, Numerical Analysis of External Gear Pumps Including Cavitation, *Journal of Fluids Engineering* 134 (2012) 081105. URL: <http://dx.doi.org/10.1115/1.4007106http://fluidsengineering.asmedigitalcollection.asme.org/article.aspx?articleid=1484255>. doi:doi:10.1115/1.4007106.
- [137] D. del Campo, R. Castilla, G. Raush, P. Gamez-Montero, E. Codina, Pressure effects on the performance of external gear pumps under cavitation, *Proceedings of the Institution of Mechanical Engineers, Part C: Journal of Mechanical Engineering Science* 228 (2014) 2925–2937. URL: <http://journals.sagepub.com/doi/10.1177/0954406214522990>. doi:doi:10.1177/0954406214522990.
- [138] A. King, R. Plant, A. Kovacevic, Improved design of gear pump porting through CFD simulation., in: *International conference on compressors and their systems.*, London, 2009, pp. 387–394.
- [139] E. Frosina, A. Senatore, M. Rigosi, Study of a High-Pressure External Gear Pump with a Computational Fluid Dynamic Modeling Approach, *Energies* 10 (2017) 1113. URL: <http://www.mdpi.com/1996-1073/10/8/1113>. doi:doi:10.3390/en10081113.
- [140] A. K. Singhal, M. M. Athavale, H. Li, Y. Jiang, Mathematical Basis and Validation of the Full Cavitation Model, *Journal of Fluids Engineering* 124 (2002) 617. URL: <http://fluidsengineering.asmedigitalcollection.asme.org/article.aspx?articleid=1429576>. doi:doi:10.1115/1.1486223.
- [141] D. Yan, A. Kovacevic, Q. Tang, S. Rane, Numerical investigation of cavitation in twin-screw pumps, *Proceedings of the Institution of Mechanical Engineers, Part C: Journal of Mechanical Engineering Science* 232 (2018) 3733–3750. doi:doi:10.1177/0954406217740927.
- [142] Y. Yoon, B. H. Park, J. Shim, Y. O. Han, B. J. Hong, S. H. Yun, Numerical simulation of three-dimensional external gear pump using immersed solid method, *Applied Thermal Engineering* 118 (2017) 539–550. doi:doi:10.1016/j.applthermaleng.2017.03.014.
- [143] C. Kato, M. Kaiho, A. Manabe, An Overset Finite-Element Large-Eddy Simulation Method With Applications to Turbomachinery and Aeroacoustics, *Journal of Applied Mechanics* 70 (2003) 32. URL: <http://dx.doi.org/10.1115/1.1530637http://>

[//appliedmechanics.asmedigitalcollection.asme.org/article.aspx?articleid=1414752](http://appliedmechanics.asmedigitalcollection.asme.org/article.aspx?articleid=1414752). doi:doi:10.1115/1.1530637.

- [144] C. S. Peskin, Flow patterns around heart valves: A numerical method, *Journal of Computational Physics* 10 (1972) 252–271. doi:doi:10.1016/0021-9991(72)90065-4.
- [145] D. Goldstein, R. Handler, L. Sirovich, Modeling a No-Slip Flow Boundary with an External Force Field, *Journal of Computational Physics* 105 (1993) 354–366. URL: <http://www.sciencedirect.com/science/article/pii/S0021999183710818><http://linkinghub.elsevier.com/retrieve/pii/S0021999183710818>. doi:doi:10.1006/jcph.1993.1081.
- [146] G. Iaccarino, G. Kalitzin, C. Elkins, Numerical and experimental investigation of the turbulent flow in a ribbed serpentine passage, Technical Report, Stanford, CA, 2003.
- [147] G. Iaccarino, R. Verzicco, Immersed boundary technique for turbulent flow simulations, *Applied Mechanics Reviews* 56 (2003) 331. URL: <http://appliedmechanicsreviews.asmedigitalcollection.asme.org/article.aspx?articleid=1397637>. doi:doi:10.1115/1.1563627.
- [148] J. Pei, M. K. Osman, W. Wang, D. Appiah, T. Yin, Q. Deng, A Practical Method for Speeding up the Cavitation Prediction in an Industrial Double-Suction Centrifugal Pump, *Energies* 12 (2019) 2088. doi:doi:10.3390/en12112088.
- [149] S. O. Unverdi, G. Tryggvason, A front-tracking method for viscous, incompressible, multi-fluid flows, *Journal of Computational Physics* (1992). doi:doi:10.1016/0021-9991(92)90307-K.
- [150] L. J. Fauci, A. McDonald, Sperm motility in the presence of boundaries, *Bulletin of Mathematical Biology* (1995). doi:doi:10.1007/BF02461846.
- [151] R. P. Beyer, R. J. Leveque, Analysis of a one-dimensional model for the immersed boundary method, *SIAM Journal on Numerical Analysis* (1992). doi:doi:10.1137/0729022.
- [152] E. M. Saiki, S. Biringen, Numerical simulation of a cylinder in uniform flow: Application of a virtual boundary method, *Journal of Computational Physics* (1996). doi:doi:10.1006/jcph.1996.0036.
- [153] P. Angot, C. H. Bruneau, P. Fabrie, A penalization method to take into account obstacles in incompressible viscous flows, *Numerische Mathematik* (1999). doi:doi:10.1007/s002110050401.

- [154] K. Khadra, P. Angot, S. Parneix, J. P. Caltagirone, Fictitious domain approach for numerical modelling of Navier-Stokes equations, *International Journal for Numerical Methods in Fluids* (2000). doi:[doi:10.1002/1097-0363\(20001230\)34:8\(651::AID-FLD61\)3.0.CO;2-D](https://doi.org/10.1002/1097-0363(20001230)34:8<651::AID-FLD61>3.0.CO;2-D).
- [155] R. Mittal, C. Bonilla, H. Udaykumar, Cartesian Grid Methods For Simulating Flows With Moving Boundaries, *WIT Transactions on Modelling and Simulation* 33 (2003) 10. doi:[doi:10.2495/CMEM030551](https://doi.org/10.2495/CMEM030551).
- [156] R. Mittal, V. Seshadri, H. S. Udaykumar, Flutter, tumble and vortex induced autorotation, *Theoretical and Computational Fluid Dynamics* (2004). doi:[doi:10.1007/s00162-003-0101-5](https://doi.org/10.1007/s00162-003-0101-5).
- [157] S. J. Shin, H. J. Sung, Three-dimensional simulation of a valveless pump, *International Journal of Heat and Fluid Flow* (2010). doi:[doi:10.1016/j.ijheatfluidflow.2010.05.001](https://doi.org/10.1016/j.ijheatfluidflow.2010.05.001).
- [158] M. Specklin, A versatile immersed boundary method for pump design, *Sulzer Technical Review* (2018).
- [159] **M. G. Mithun**, P. Koukouvinis, I. K. Karathanassis, M. Gavaises, Numerical simulation of three-phase flow in an external gear pump using immersed boundary approach, *Applied Mathematical Modelling* (2019). doi:[doi:10.1016/j.apm.2019.03.022](https://doi.org/10.1016/j.apm.2019.03.022).
- [160] A. H. Koop, Numerical simulation of unsteady three-dimensional sheet cavitation, Ph.D. thesis, University of Twente, Enschede, The Netherlands, 2008. doi:[doi:10.3990/1.9789036527019](https://doi.org/10.3990/1.9789036527019).
- [161] A. Kumar, Investigation of in-nozzle flow characteristics of fuel injectors of ic engines, Ph.D. thesis, City, University of London, 2017. URL: <http://openaccess.city.ac.uk/id/eprint/17583>.
- [162] B. Christopher E, Cavitation and Bubble Dynamics, volume 9, Cambridge University Press, Cambridge, 2013. URL: <http://ebooks.cambridge.org/ref/id/CB09781107338760><http://arjournals.annualreviews.org/doi/abs/10.1146/annurev.fl.09.010177.001045>. doi:[doi:10.1017/CBO9781107338760](https://doi.org/10.1017/CBO9781107338760).
- [163] J.-P. Franc, J.-M. Michel, Fundamentals of Cavitation, volume 76 of *Fluid Mechanics and Its Applications*, Kluwer Academic Publishers, Dordrecht, 2005. URL: <http://link.springer.com/10.1007/1-4020-2233-6>. doi:[doi:10.1007/1-4020-2233-6](https://doi.org/10.1007/1-4020-2233-6). [arXiv:arXiv:1011.1669v3](https://arxiv.org/abs/1011.1669v3).



- [164] C. W. Hirt, B. D. Nichols, Volume of fluid (VOF) method for the dynamics of free boundaries, *Journal of Computational Physics* 39 (1981) 201–225. doi:[doi:https://doi.org/10.1016/0021-9991\(81\)90145-5](https://doi.org/10.1016/0021-9991(81)90145-5).
- [165] J. U. Brackbill, D. B. Kothe, C. J. Zemach, A Continuum Method for Modeling Surface Tension, *Comput. Phys.* 100 (1992) 335–354.
- [166] F. Ducros, F. Nicoud, Subgrid-scale stress modelling based on the square of the velocity gradient tensor, *Flow, Turbulence and Combustion* 62 (1999) 1–36.
- [167] H. Naseri, P. Koukouvinis, M. Gavaises, Evaluation of Turbulence Models Performance in Predicting Incipient Cavitation in an Enlarged Step-Nozzle, *Journal of Physics: Conference Series* 656 (2015) 012095. doi:[doi:10.1088/1742-6596/656/1/012095](https://doi.org/10.1088/1742-6596/656/1/012095).
- [168] D. Wilcox, *Turbulence modeling for CFD*, La Canada Flintridge, CA: D C W Industries (2006).
- [169] J. Reboud, Numerical simulation of unsteady cavitating flows: some applications and open problems, ... on Cavitation, ... (2003) 1–10. URL: <http://flow.me.es.osaka-u.ac.jp/Cav2003/ILpaper/Cav03-IL-10.pdf>.
- [170] W. Egler, J. R. Giersch, F. Boecking, J. Hammer, J. Hlousek, P. Mattes, Fuel injection systems, in: K. Mollenhauer, H. Tschoke (Eds.), *Handbook of diesel engines*, 1 ed., Heidelberg: Springer-Verlag, Berlin, 2010, pp. 127–174.
- [171] M. A. Green, C. W. Rowley, G. Haller, Detection of Lagrangian coherent structures in three-dimensional turbulence, *Journal of Fluid Mechanics* 572 (2007) 111–120.
- [172] G. Haller, An objective definition of a vortex, *Journal of Fluid Mechanics* 525 (2005) 1–26.
- [173] H. Grosshans, *Large Eddy Simulation of Atomizing Sprays*, Ph.D. thesis, LUND, 2013.
- [174] K. Sasak, S. Naoya, D. Akamatsu, H. Saito, K. Sasaki, N. Suzuki, D. Akamatsu, H. Saito, Rayleigh-Taylor instability and mushroom-pattern formation in a two-component Bose-Einstein condensate, *Physical Review A - Atomic, Molecular, and Optical Physics* 80 (2009) 1–4. doi:[doi:10.1103/PhysRevA.80.063611](https://doi.org/10.1103/PhysRevA.80.063611). [arXiv:0910.1440](https://arxiv.org/abs/0910.1440).

- [175] J. Shinjo, A. Umemura, Detailed simulation of primary atomization mechanisms in Diesel jet sprays (isolated identification of liquid jet tip effects), *Proceedings of the Combustion Institute* 33 (2011) 2089–2097. doi:[doi:10.1016/j.proci.2010.07.006](https://doi.org/10.1016/j.proci.2010.07.006).
- [176] P.-K. Wu, G. M. Faeth, A. Arbor, Aerodynamic Effects on Primary Breakup of Turbulent Liquids, *Atomization and Sprays* 3 (1993) 289. doi:[doi:10.1615/AtomizSpr.v3.i3.20](https://doi.org/10.1615/AtomizSpr.v3.i3.20).
- [177] M. Gavaises, D. Papoulias, A. Andriotis, E. Giannadakis, A. Theodorakakos, Link Between Cavitation Development and Erosion Damage in Diesel Injector Nozzles, in: *SAE Paper 2007-01-0246*, 2007. URL: <http://papers.sae.org/2007-01-0246/>. doi:[doi:10.4271/2007-01-0246](https://doi.org/10.4271/2007-01-0246).
- [178] S. Som, A. I. Ramirez, D. E. Longman, S. K. Aggarwal, Effect of nozzle orifice geometry on spray, combustion, and emission characteristics under diesel engine conditions, *Fuel* 90 (2011) 1267–1276. URL: <http://dx.doi.org/10.1016/j.fuel.2010.10.048>. doi:[doi:10.1016/j.fuel.2010.10.048](https://doi.org/10.1016/j.fuel.2010.10.048).
- [179] G. Bark, M. Grekula, R. E. Bensow, N. Berchiche, On some physics to consider in numerical simulation of erosive cavitation, in: *Seventh International Symposium on Cavitation*, 2009. URL: <http://hdl.handle.net/2027.42/84223>.
- [180] E. Gavaises, M. Mirshahi, J. M. Nouri, Y. Yan, Link between in-nozzle cavitation and jet spray in a gasoline multi-hole injector, in: *ILASS 2013 - 25th Annual Conference on Liquid Atomization and Spray Systems*, 2013. URL: <http://openaccess.city.ac.uk/14407/>.
- [181] **M. G. Mithun**, P. Koukouvnis, I. K. Karathanassis, M. Gavaises, Simulating the Effect of In-Nozzle Cavitation on Liquid Atomisation Using a Three-Phase Model, in: J. Katz (Ed.), *Proceedings of the 10th International Symposium on Cavitation (CAV2018)*, ASME, New York, NY, 2018. URL: [http://dx.doi.org/10.1115/1.861851\\_ch175](http://dx.doi.org/10.1115/1.861851_ch175).
- [182] S. B. Pope, Ten questions concerning the large-eddy simulation of turbulent flows, *New Journal of Physics* 6 (2004) 35–35. URL: <http://stacks.iop.org/1367-2630/6/i=1/a=035http://stacks.iop.org/1367-2630/6/i=1/a=035?key=crossref.52a7b24a34f388e291ce7d86a724556b>. doi:[doi:10.1088/1367-2630/6/1/035](https://doi.org/10.1088/1367-2630/6/1/035).
- [183] L. Davidson, Large Eddy Simulations: How to evaluate resolution, *International Journal of Heat and Fluid Flow* 30 (2009) 1016–1025. doi:[doi:10.1016/j.ijheatfluidflow.2009.06.006](https://doi.org/10.1016/j.ijheatfluidflow.2009.06.006).

- [184] M. Vanella, U. Piomelli, E. Balaras, Effect of grid discontinuities on large-eddy simulation statistics and flow fields, *Journal of Turbulence* 9 (2008) N32. URL: <https://www.tandfonline.com/doi/full/10.1080/14685240802446737>. doi:doi:10.1080/14685240802446737.
- [185] A. Prosperetti, G. Tryggvason, Computational methods for multiphase flow, 2009. URL: <http://www.cambridge.org/9780521847643>.
- [186] G. Perigaud, R. Saurel, A compressible flow model with capillary effects, *Journal of Computational Physics* 209 (2005) 139–178.
- [187] S. Le Martelot, R. Saurel, B. Nkonga, Towards the direct numerical simulation of nucleate boiling flows, *International Journal of Multiphase Flow* 66 (2014) 62–78.
- [188] K. Schmidmayer, F. Petitpas, E. Daniel, N. Favrie, S. Gavriluk, A model and numerical method for compressible flows with capillary effects., *Journal of Computational Physics* 334 (2017) 468–496.
- [189] I. Malgarinos, Simulation of cavitation and erosion in FUEL injection SYSTEMS of medium/heavy duty Diesel engines at injection pressures reaching 3000bar, Technical Report, 2013.
- [190] C. Hirt, A. Amsden, J. Cook, An Arbitrary Lagrangian–Eulerian Computing Method for All Flow Speeds, *Journal of Computational Physics* 135 (1997) 203–216. doi:doi:10.1006/jcph.1997.5702.
- [191] E. F. Toro, *Riemann Solvers and Numerical Methods for Fluid Dynamics*, Springer Berlin Heidelberg, Berlin, Heidelberg, 2009. URL: <http://link.springer.com/10.1007/b79761>. doi:doi:10.1007/b79761.